

ARTIFICIAL LATERAL LINE SYSTEMS FOR FEEDBACK CONTROL OF  
UNDERWATER ROBOTS

By

Ahmad Taha Abdulsadda

A DISSERTATION

Submitted to  
Michigan State University  
in partial fulfillment of the requirements  
for the degree of

DOCTOR OF PHILOSOPHY

Electrical Engineering

2012

## ABSTRACT

# ARTIFICIAL LATERAL LINE SYSTEMS FOR FEEDBACK CONTROL OF UNDERWATER ROBOTS

By

**Ahmad Taha Abdulsadda**

A lateral line system, consisting of arrays of flow-sensing neuromasts, allows fish and amphibians to probe their ambient environment and plays a vital role in their behaviors spanning predator/prey detection, schooling, rheotaxis, courtship and communication. The feats of biological lateral lines have inspired an increasing interest in engineering a similar sensing module for underwater robots and vehicles. Often known as artificial lateral lines, these sensors could potentially enable an underwater robot to detect and identify moving or stationary objects, and exploit ambient flow energy for efficient locomotion. Despite the advances made in this area, realizing a practical artificial lateral line still faces significant challenges in both signal processing and flow sensor fabrication.

In this dissertation we describe our effort in developing signal processing methods for hydrodynamic object localization and tracking using an artificial lateral line (ALL). We consider two types of objects, a vibrating sphere and a non-vibrating cylinder, both of which are of interest in underwater applications. A vibrating sphere, known as a dipole source, is widely used in the study of biological lateral lines and it emulates the rhythmic body or fin movement. A non-vibrating cylinder (with unknown cross-section shape), on the other hand, represents a general moving or stationary object underwater with a 2D flow profile.

First, a novel bio-inspired artificial lateral line system is proposed for underwater robots and vehicles by exploiting the inherent sensing capability of ionic polymermetal composites (IPMCs). Analogous to its biological counterpart, the IPMC-based lateral line processes

the sensor signals through a neural network, and we demonstrate the performance of this approach in the localization of a dipole source.

Second, with an assumption of potential flows, we formulate nonlinear estimation problems for the localization and tracking of a dipole source based on analytical flow models, and propose and compare several algorithms for solving the problem. For the case of a moving cylinder, we use conformal mapping to represent a general cross-section profile, and explore the use of Kalman-filtering-type techniques in the tracking and size/shape estimation of the object.

We have conducted extensive experiments to validate the developed algorithms with an artificial lateral line prototype made of millimeter-scale IPMC sensors, with sensor-to-sensor separation of 2 cm, which is determined through an optimization process based on the Cramer-Rao bound (CRB) analysis.

Finally, we experimentally explore the use of IPMC sensors for estimating the hydrodynamic parameters involved in a Kármán vortex street that is created by a stationary cylinder in a flow. We validate that the vortex shedding frequency, which can be extracted from the sensor signal, shows clear correlation with the flow speed and the obstacle size.

Copyright by  
AHMAD TAHA ABDULSADDA  
2012

## DEDICATION

To Mom, Dad, and My Family

## ACKNOWLEDGMENTS

I am grateful to my advisor, Dr. Xiaobo Tan, for his thoughtful guidance during the course of my PhD study. He inspired me with his expertise and guided me with his patience in the novel field of artificial lateral lines for feedback control of underwater robots.

I would like to thank my committee members, Dr. Hassan Khalil, Dr. Fathi Salem, and Dr. Guoming (George) Zhu for providing helpful suggestions and comments. Thanks also go to my colleagues for their help and discussion, in particular, John Thon, Hong Lie, and Fetain Zhang.

I am grateful for the financial support of my study from Ministry of Higher Education in Iraq and my research from the Office of Naval Research (ONR: Grant N000140810640, N000141210149) and National Science Foundation (NSF: ECCS 0547131, CCF 0820220, CNS 0751155, DBI-0939454, IIS 0916720).

I would like to thank all members in Iraqi Cultural Office in Washington DC. Finally, I would like to thank my family for their patience, understanding and support during this study.

# TABLE OF CONTENTS

<b>List of Tables</b> . . . . .	<b>x</b>
<b>List of Figures</b> . . . . .	<b>xii</b>
<b>Chapter 1 Introduction</b> . . . . .	<b>1</b>
1.1 Research Background . . . . .	1
1.2 Research Objective . . . . .	5
1.3 Contributions . . . . .	6
1.3.1 An Artificial Lateral Line System Using IPMC Sensor Arrays . . . . .	6
1.3.2 Localization of a Fixed Dipole Using Neural Network . . . . .	8
1.3.3 Nonlinear Estimation-based Dipole Source Localization . . . . .	8
1.3.4 Localization of a Moving Dipole Source Underwater . . . . .	9
1.3.5 Underwater Tracking and Size-Estimation of a Moving Object . . . . .	10
1.3.6 Localization and Identification of an Stationary Obstacle Underwater . . . . .	11
1.4 Organization of This Dissertation . . . . .	12
<b>Chapter 2 Dipole Source Localization Using Neural Networks</b> . . . . .	<b>14</b>
2.1 Hydrodynamic Model for an IPMC Sensor Under Oscillatory Flow . . . . .	15
2.2 Source Localization Using Neural Network Processing . . . . .	19
2.3 Optimum Design of the Neural Network Using Genetic Algorithm . . . . .	22
2.4 Experimental Setup and Sensor Characterization . . . . .	23
2.5 Experimental Results on Diploe Source Localization . . . . .	29
2.6 Chapter Summary . . . . .	32
<b>Chapter 3 Nonlinear Estimation-based Dipole Source Localization</b> . . . . .	<b>37</b>
3.1 Problem Formulation . . . . .	38
3.2 Estimation Algorithms . . . . .	42
3.2.1 Gauss-Newton Algorithm . . . . .	43
3.2.2 Newton-Raphson Algorithm . . . . .	44
3.2.3 Beamforming Algorithm . . . . .	45
3.2.4 Cramer-Rao Bound Analysis . . . . .	46
3.3 Simulation Results . . . . .	49
3.3.1 CRB-based Optimal Design of Lateral Line Sensor . . . . .	49

3.3.2	Localization of Dipole Source with Unknown Vibration Amplitude and Orientation . . . . .	51
3.3.3	Further CRB Analysis on Performance . . . . .	53
3.4	Experimental Setup and Flow Model Verification . . . . .	58
3.4.1	Experimental Setup . . . . .	58
3.4.2	Flow Model Validation . . . . .	59
3.4.3	Calibration of IPMC Sensors . . . . .	61
3.4.4	Experimental Results on Dipole Source Localization . . . . .	64
3.5	Chapter Summary . . . . .	70
<b>Chapter 4</b>	<b>Localization of a Moving Dipole Source . . . . .</b>	<b>72</b>
4.1	Localization of a Traveling Dipole Source: Problem Formulation . . . . .	73
4.2	The Sliding Discrete Fourier Transform (SDFT) Algorithm . . . . .	76
4.3	The Gauss-Newton Method for Solving the Estimation Problem . . . . .	78
4.4	Simulation Results . . . . .	79
4.5	Experimental Setup and Results . . . . .	83
4.5.1	Experimental Setup . . . . .	83
4.5.2	Experimental Results on Moving Dipole Source Localization . . . . .	86
4.6	Chapter Summary . . . . .	87
<b>Chapter 5</b>	<b>Underwater Tracking and Size-Estimation of a Moving Object . . . . .</b>	<b>96</b>
5.1	Flow Model and Problem Formulation . . . . .	97
5.2	Nonlinear Filtering . . . . .	101
5.2.1	Extended Kalman Filter . . . . .	102
5.2.2	Unscented Kalman Filter . . . . .	103
5.2.3	Particle Filter . . . . .	105
5.3	Simulation Results . . . . .	109
5.3.1	Recursive Information Matrix . . . . .	109
5.3.2	Simulation Results on Nonlinear Filtering . . . . .	111
5.4	Experimental Results . . . . .	115
5.5	Chapter Summary . . . . .	118
<b>Chapter 6</b>	<b>Exploration of IPMC Sensors in Vortex Street Sensing . . . . .</b>	<b>127</b>
6.1	Stationary Vortex and Kármán Vortex Street . . . . .	128
6.2	Localization of an Obstacle: Problem Formulation . . . . .	133
6.3	Experimental Setup and Results . . . . .	137
6.3.1	Swim Tunnel Flow Calibration . . . . .	137
6.3.2	Differentiation of Steady and Unsteady Flow . . . . .	139
6.3.3	Differentiation of Obstacle Size . . . . .	142
6.3.4	Differentiation of Flow Velocity . . . . .	143
6.3.5	Two IPMC Sensors . . . . .	143
6.4	Chapter Summary . . . . .	144
<b>Chapter 7</b>	<b>Conclusion . . . . .</b>	<b>152</b>

<b>Chapter 8</b>	<b>Future Work</b>	<b>155</b>
<b>Appendices</b>		<b>158</b>
<b>Appendix A</b>	<b>Artificial Lateral Line Design: CRB</b>	<b>159</b>
<b>Appendix B</b>	<b>Appendix for Chapter5</b>	<b>161</b>
B.1	Derivation of CRB	161
B.2	More Results for One-stage Extended Kalman Filtering Scheme	164
<b>Bibliography</b>		<b>169</b>

## LIST OF TABLES

Table 3.1	Experimental results: maximum and average estimation errors under different algorithms. “BF (0.02)” stands for beamforming with $0.02 \times 0.02 \text{ cm}^2$ grid, and similar interpretations apply for “BF (0.05)” and “BF (0.1)”. Note that vibration amplitude and orientation are assumed known for the BF algorithms. . . . .	68
Table 3.2	Average computational time per localization point for different algorithms. . . . .	70
Table 4.1	Simulation results: Estimated velocity ( $v_m$ ), vibrating amplitude ( $A$ ). . . . .	85
Table 4.2	Experimental results: Estimated velocity ( $v_m$ ), vibrating amplitude ( $A$ ). . . . .	87
Table 5.1	Simulation results: Estimated velocity, size parameter, and shape parameter under different process noise variances. Two-stage extended Kalman filtering is used. . . . .	114
Table 5.2	Simulation results: Estimated velocity, size parameter, and shape parameter under different measurement noise variances. Estimation is done with two-stage extended Kalman filtering. . . . .	114
Table 5.3	Simulation results: Estimated velocity, size parameter, and shape parameter under three nonlinear filtering algorithms. . . . .	115
Table 5.4	Cylindrical object experimental results: Estimated velocity and size parameter. . . . .	117
Table 5.5	Ellipsoidal object experimental results: Estimated velocity, size parameter, and shape parameter. . . . .	117
Table 6.1	Simulation results: Setup parameters. . . . .	132

Table B.1	One-stage scheme: Estimated velocity, size parameter, and shape parameter under different process noise variances. . . . .	164
Table B.2	One-stage scheme: Estimated velocity, size parameter, and shape parameter under different measurement noise variances. . . . .	167

## LIST OF FIGURES

Figure 1.1	(a) Illustration of the structure of a neuromast (image credit: C. H. Mallery); (b) distribution of superficial (small dots) and canal neuromasts (dots within shaded areas) on the Lake Michigan mottled sculpin [20]. For interpretation of the references to color in this and all other figures, the reader is referred to the electronic version of this dissertation. . . . .	3
Figure 1.2	Illustration of the potential use of an artificial lateral line system on a robotic fish. . . . .	6
Figure 1.3	Illustration of IPMC sensing principle. . . . .	7
Figure 1.4	Benefit of exploiting vortex streets (adapted from [57]): (a) Exploiting flow due to vortex streets of leading fish; (b) harvesting energy from oncoming vortices. . . . .	12
Figure 2.1	Illustration of the beam dynamics of an IPMC sensor in flow. . . . .	16
Figure 2.2	Schematic of the dipole source localization problem. . . . .	19
Figure 2.3	Schematic of the MLP neural network for signal processing of the IPMC lateral line. . . . .	20
Figure 2.4	A prototype of IPMC-based lateral line system. . . . .	23
Figure 2.5	The schematic of circuit for measuring the short-circuit current generated by the IPMC sensor. . . . .	24
Figure 2.6	Experimental setup: (a) Experimental tank equipped with a DPIV system; (b) the mini-shaker-based dipole source. . . . .	25

Figure 2.7	Flow field around one IPMC sensor under a dipole stimulation: (a) Dipole-sensor separation 10 cm, with maximum flow amplitude of 9.3 mm/s in the field; (b) dipole-sensor separation 45 cm, with maximum flow amplitude of 4.1 mm/s in the field. . . . .	26
Figure 2.8	Typical IPMC sensor signals: (a) Signal from sensor #2, which is close to the dipole source; (b) signal from sensor #4. . . . .	27
Figure 2.9	Sensor characterization, measured sensor signal magnitude as a function of source location, The dipole vibration axis is: (a) Parallel to the IPMC beam plane; (b) perpendicular to the IPMC beam plane. . . . .	28
Figure 2.10	Evolution of the fitness function (the mean square error $J$ ) over generations, in the genetic algorithm-based training phase. This example involves all six sensors and 180 training points. . . . .	30
Figure 2.11	Localization of the dipole source using all six sensors of the lateral line: (a) With 90 training points; (b) with 50 training points. . . . .	31
Figure 2.12	Localization error at 16 validation points when all six sensors are used: (a) With 90 training points; (b) with 50 training points. . . . .	32
Figure 2.13	Localization of the dipole source using four sensors of the lateral line: (a) With 90 training points; (b) with 50 training points. . . . .	34
Figure 2.14	Localization of the dipole source using two sensors of the lateral line: (a) With 90 training points; (b) with 50 training points. . . . .	35
Figure 2.15	Error in localization of the dipole source using the lateral line: (a) Maximum error along the track; (b) average error along the track. . . . .	36
Figure 3.1	Illustration of the problem setup. The dipole source is located at $(x_s, y_s)$ . . . . .	40
Figure 3.2	CRB-based cumulative uncertainty in localization as a function of intra-sensor spacing. . . . .	51
Figure 3.3	Illustration of the simulation setup, where 19 points as indexed in the figure will be localized. . . . .	53
Figure 3.4	Simulation results: (a) Estimation of source locations; (b) localization errors at the 19 points. . . . .	54

Figure 3.5	Simulation results: Estimation of the source vibration amplitudes. . . . .	55
Figure 3.6	Simulation results: Estimation of the source vibration orientations. . . . .	56
Figure 3.7	Simulation results: Comparison of square-root of empirical estimation variances (a) $\sigma_x$ and (b) $\sigma_y$ with the corresponding CRBs. . . . .	57
Figure 3.8	Experimental setup: Schematic of the experimental system. . . . .	60
Figure 3.9	Experimental results: Comparison of DPIV-measured flow velocity with the model prediction. . . . .	61
Figure 3.10	Illustration of IPMC sensor calibration. . . . .	63
Figure 3.11	Experimental results: (a) Estimation of source locations; (b) localization errors at the 19 points. . . . .	65
Figure 3.12	Experimental results: (a) Estimation of the source vibration amplitudes; (b) estimation of the source vibration orientations. . . . .	66
Figure 3.13	Experimental results: Constructed energy-like map when the dipole is located at point #3 ( $0.1 \times 0.1 \text{ cm}^2$ grid). . . . .	67
Figure 3.14	Experimental results: Localization of the dipole source using the beamforming algorithm: (a) Estimation of the source locations; (b) localization errors at the 19 points. . . . .	69
Figure 4.1	Illustration of the problem setup for the localization of a moving dipole source. . . . .	74
Figure 4.2	Illustration of the simulation setup. . . . .	80
Figure 4.3	Simulation results: Time trajectories of the flow velocities at the sensor locations. . . . .	81
Figure 4.4	Simulation results: Magnitude trajectories of the DC component at the sensor sites. . . . .	82
Figure 4.5	Simulation results: Magnitude trajectories of the AC component at the sensor sites. . . . .	83

Figure 4.6	Simulation results on the estimation of the source location: (a) Localization; (b) tracking error. . . . .	84
Figure 4.7	Simulation results on the estimation of the source location, vibration amplitude changing with the time: (a) Localization; (b) tracking error.	88
Figure 4.8	Simulation results of the source vibration amplitude. . . . .	89
Figure 4.9	An experimental prototype of IPMC-based lateral line system. . . . .	89
Figure 4.10	Experimental setup of the moving dipole source: Schematic. . . . .	90
Figure 4.11	Experimental setup of the moving dipole source: Picture of the experimental setup. . . . .	91
Figure 4.12	Calibration of an IPMC sensor. . . . .	91
Figure 4.13	Experimental results: Time trajectories of the flow velocities at the sensor locations. . . . .	92
Figure 4.14	Experimental results: Magnitude trajectories of the DC component at the sensor sites. . . . .	93
Figure 4.15	Experimental results: Magnitude trajectories of the AC component at the sensor sites. . . . .	94
Figure 4.16	Experimental results on the estimation of the source location: (a) Localization; (b) tracking error. . . . .	95
Figure 5.1	Illustration of the Laurent series expansion : (a) Circle $\zeta(z) = z$ ; (b) the shape fingerprint $\zeta(z) = z + 1/(2z)$ ; (c) the shape fingerprint $\zeta(z) = z + 1/(2z) + 1/(6z^2)$ ; (d) the shape fingerprint $\zeta(z) = z + 1/(2z) + 1/(6z^2) + 1/(12z^3)$ (adapted from [11]). . . . .	99
Figure 5.2	Illustration of the problem setup for the tracking and estimation of a moving object. . . . .	100
Figure 5.3	Illustration of the two-stage filtering scheme. . . . .	108
Figure 5.4	$\sqrt{CRB}$ for: (a) Moving object $x_s$ coordinate; (b) moving object $y_s$ coordinate; (c) size parameter $R$ ; (d) shape parameter $\lambda_1$ . . . . .	110

Figure 5.5	Simulation setup for tracking of a moving cylinder. . . . .	111
Figure 5.6	Simulated time trajectories of sensor measurements. . . . .	112
Figure 5.7	Simulation results on tracking the ellipsoidal cylinder using two-stage extended Kalman filtering: (a) The estimation of the moving object location for different variance values for the process noises; (b) localization error at each $x$ -coordinate of the object. The measurement noise variance is held at $0.01 \text{ cm}^2/\text{s}^2$ . . . . .	113
Figure 5.8	Simulation results on tracking the ellipsoidal cylinder using the two-stage extended Kalman filtering: (a) The estimation of the moving object location for different variance values for the measurement noises; (b) localization error at each $x$ -coordinate of the object. The process noise variance is held at 0.3 (in its respective unit for each state component). . . . .	119
Figure 5.9	Simulation results on tracking the ellipsoidal cylinder for three nonlinear filters: The process noise variance is held at 0.3 (in its respective unit for each state component) and the measurement noise variance is held at $0.01 \text{ cm}^2/\text{s}^2$ . . . . .	120
Figure 5.10	Experimental setup: Schematic. . . . .	121
Figure 5.11	Experimental setup: (a) Picture of the experimental setup with a circular cylinder; (b) picture of the experimental setup with an ellipsoidal cylinder. . . . .	122
Figure 5.12	Comparison of DPIV-measured flow velocity with the model prediction.	123
Figure 5.13	Measured flow velocities by six IPMC sensors: (a) DC motor driving the cylindrical object, with digital low pass filter ( $f_c = 42$ ) Hz; (b) AC motor driving ellipsoidal object, with digital low pass filter ( $f_c = 4$ ) Hz.	124
Figure 5.14	Experimental results on tracking a cylinder with circular profile with two-stage extended Kalman filtering: (a) The estimation of the object location; (b) localization error at each $x$ -coordinate of the object. . . . .	125
Figure 5.15	Ellipsoidal object experimental results on tracking an ellipse: (a) The estimation of the object location; (b) localization error at each $x$ -coordinate of the object. . . . .	126

Figure 6.1	Illustration of the analytical model for cylinder-shed vorticity. . . . .	129
Figure 6.2	Visualization of the flow around a cylinder. . . . .	130
Figure 6.3	Illustration of the analytical model for cylinder-shed Kármán vortex street. . . . .	130
Figure 6.4	Visualization of a Kármán vortex street flow filed around: (a) Circular cylinder; (b) ellipsoidal cylinder. . . . .	133
Figure 6.5	Illustration of the problem setup. The obstacle is located at $(x_o, y_o)$ . . . . .	134
Figure 6.6	Simulation results: 3D illustration of flow velocity behind the obstacles: (a) Along the $x$ -direction; (b) along the $y$ -direction. In each subfigure, the left plot shows the velocity for the circular cylinder while the right plot shows the velocity for the ellipsoidal cylinder. . . . .	136
Figure 6.7	Loligo Systems swim tunnel: (a) Side view; (b) top view. . . . .	138
Figure 6.8	Rotor-X flow sensor for swim tunnel calibration: (a) Side view; (b) top view; (c) calibration curve . . . . .	139
Figure 6.9	IPMC sensor in a uniform flow in the absence of the obstacle: (a) Sensor at $t_o$ ; (b) sensor at $t_1$ , (b) sensor at $t_2$ . . . . .	141
Figure 6.10	IPMC sensor right behind obstacle (predominantly negative flow): (a) Illustration; (b) typical sensor configuration. . . . .	141
Figure 6.11	IPMC sensor behind obstacle but shifted from center (predominantly positive flow): (a) Illustration; (b) typical sensor configuration. . . . .	142
Figure 6.12	Typical IPMC sensor signals and frequency spectrum of the response under different flow conditions with nominal flow velocity of 10.6 cm/s: (a) Running water (free flow); (b) predominantly negative flow (suction region), frequency = 0.61 Hz; (c) predominantly positive flow (vortex region), frequency = 0.67 Hz. . . . .	145
Figure 6.13	IPMC sensor was attached behind of the: (a) 6 cm diameter cylindrical obstacle; (b) 4 cm diameter cylindrical obstacle. . . . .	146

Figure 6.14	Typical IPMC sensor signals for different-size cylindrical obstacles with diameter: (a) 6 cm, theoretical / measured $f_{sh}$ : 0.56/0.6 Hz; (b) 4 cm, theoretical / measured $f_{sh}$ : 0.73/0.79 Hz. . . . .	147
Figure 6.15	Typical IPMC sensor signals under 6 cm upstream cylinder, the nominal flow velocity of: (a) 7.5 cm/s, Theoretical / Measured $f_{sh}$ :0.4/0.61 Hz;(b) 10.6 cm/s, Theoretical / Measured $f_{sh}$ : 0.56/0.67 Hz. . . . .	148
Figure 6.16	Typical IPMC sensor signals to the human fingers that moved alongside the two IPMC sensors with velocity of about 25 cm/s, direction of the movement: (a) Toward positive $x$ -axis; (b) toward negative $x$ -axis. . . . .	149
Figure 6.17	Two IPMC sensors were attached behind a 6 cm cylinder: (a) Setup at time $t_o$ ; (b) sensor #1 sucked toward the obstacle, while sensor#2 repelled from the obstacle at time $t_1$ . . . . .	150
Figure 6.18	Signals from the two IPMC sensors and their frequency spectra: (a) Sensor #1, dominant frequency = 0.55 Hz; (b) sensor #2, dominant frequency = 0.73 Hz. . . . .	151
Figure 8.1	Illustration of the $n$ -stages nonlinear filtering scheme. . . . .	156
Figure B.1	Simulation results on tracking the ellipsoidal cylinder for one-stage scheme: (a) The estimation of the moving object location for different variance values for the process noises; (b) localization error at each $x$ -coordinate of the object. The measurement noise variance is held at $0.01 \text{ cm}^2/\text{s}^2$ . . . . .	165
Figure B.2	Simulation results on tracking the ellipsoidal cylinder for one-stage scheme: (a) The estimation of the moving object location for different variance values for the measurement noises; (b) localization error at each $x$ -coordinate of the object. The process noise variance is held at 0.3 (in its respective unit for each state component). . . . .	166

# Chapter 1

## Introduction

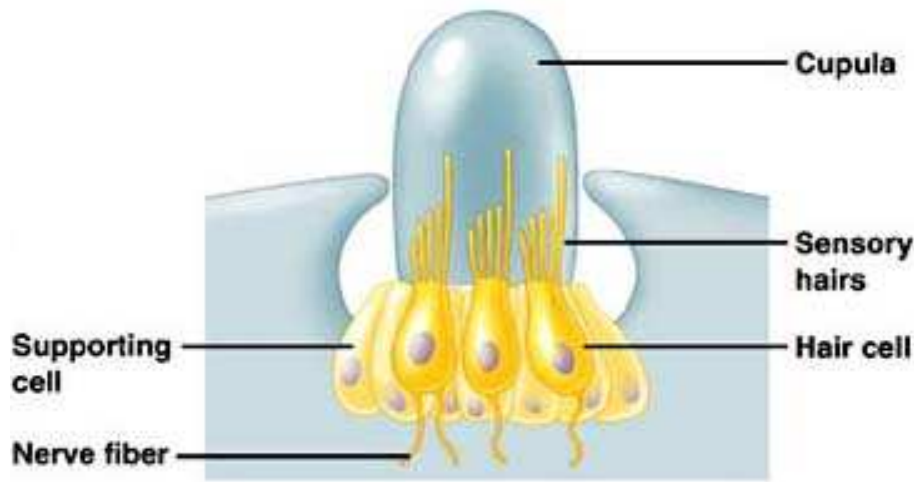
### 1.1 Research Background

Most fish and aquatic amphibians use the lateral line system as an important sensory organ to probe their environment [20, 21]. A lateral line consists of arrays of hair cell sensors, known as neuromasts. Each neuromast contains bundles of sensory hairs, encapsulated in a gelatinous structure called cupula, as illustrated in Fig. 1.1(a). An impinging flow deflects the cupula, and thus the hairs inside, eliciting firing of the hair cell neurons. Neuromasts can be divided into two types, superficial neuromasts, which are distributed on the skin surface, and canal neuromasts, which are recessed in the scales or in bony canals underneath the skin (Fig. 1.1(b)). With the same basic structure, the two types of neuromasts show distinct sensing characteristics [52]. The lateral line system allows an aquatic animal to identify near-field objects of interest and perform hydrodynamic imaging of the environment, typically within one to two Body Lengths (BLs) of the animal. Consequently, the lateral line is involved in various behaviors of aquatic animals, such as prey/predator detection [70], schooling [69],

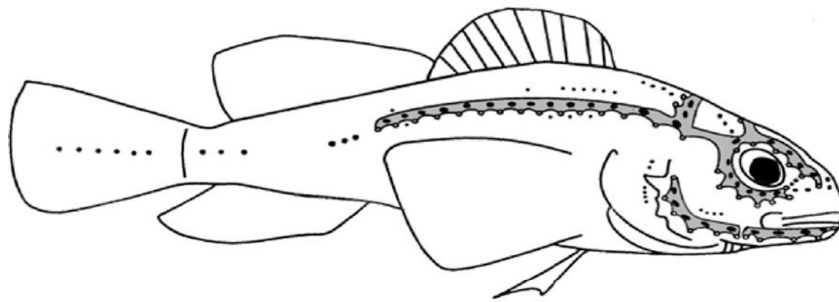
rheotaxis [36], courtship and communication [21]. In addition to the qualitative roles the lateral line plays in behaviors, there have been studies on how probed information is encoded and decoded in the nervous systems [26]. For example, Fishes frequently exploit unsteady forcing of wake flows to extract energy for efficient locomotion and maneuvering. The researchers in [56, 55] observed that, when trout perform Kármán gaiting to hold station in the wake of vortices shed from a cylindrical obstacle, their muscle activity is significantly reduced comparing to swimming in steady flow. The role of the lateral line organ in such behavior is further described in [93].

An engineering equivalent of a biological lateral line is of great interest to the navigation and control of underwater robots and vehicles. In particular, an artificial lateral line will represent a new, noiseless sensing modality for underwater applications that is complementary to traditional sensors such as vision and sonar [20, 59]. A number of micromachined flow sensors, inspired by neuromasts in fish lateral lines [74, 31, 96, 60] or by wind receptor hairs in insects [67, 29], have been reported in the last decade. These sensors typically have an out-of-plane beam structure that bends or deforms during the interaction with a flow. The bending or deformation, which carries information about the flow, is captured via resistance change [67, 92, 74, 31, 60, 97] or capacitance change [78, 29]. Hair cell-inspired sensors have also been developed at slightly larger scales, exploiting optical transduction [50] or novel sensing materials such as ionic polymer-metal composites (IPMCs) [1, 2] and gel-supported lipid bilayers [80].

Extensive behavioral and neurophysiological studies have been conducted by biologists to understand how hydrodynamic stimuli are encoded and processed in the lateral line system [26, 24, 94, 9, 22, 23], which could potentially provide insight into information processing



(a)



(b)

Figure 1.1: (a) Illustration of the structure of a neuromast (image credit: C. H. Mallery); (b) distribution of superficial (small dots) and canal neuromasts (dots within shaded areas) on the Lake Michigan mottled sculpin [20]. For interpretation of the references to color in this and all other figures, the reader is referred to the electronic version of this dissertation.

for artificial lateral lines. Theoretical work on flow modeling in the context of lateral lines is often instrumental in both explaining hydrodynamic imaging by fish and guiding the information extraction in artificial lateral lines. For example, Hassan modeled the flow field around a fish when the latter passes by or approaches an obstacle [40], moves in open water or approaches a plane surface [41], glides alongside or above a plane surface [42], and is near an oscillating sphere (also known as dipole) [43]. Ren and Mohseni derived the pressure

field around a flat body as well as the flow inside a trunk canal in the presence of vortex street and explored its implications in vortex sensing [75]. Sichert *et al.* explored the use of hydrodynamic multipole expansion to explain how aquatic animals distinguish shapes of moving objects [83], and in another work Sichert and van Hemmen investigated the shape influence of a submerged moving object on the lateral line perception using the conformal mapping theory [84]. Bouffanais *et al.* performed analytical and numerical studies on the pressure field around a cylindrical object in a uniform flow and examined the estimation of location, size, and cross-section shape of the object based on the measured pressure field [11]. There has also been experimental work in exploring the strategies for vortex sensing [50, 4, 91] and object tracking and recognition [33].

Barring some of the aforementioned research in vortex sensing and object imaging, much of the work in information processing for biological and artificial lateral lines has been focused on dipole source localization. The dipole source emulates the rhythmic movement of fins and body appendages, and has been widely used as a stimulus (playing the role of predator, prey, or conspecific) in the study of biological lateral lines [26, 22, 23, 39]. Dipole source localization has also become a benchmark problem in the development of artificial lateral lines, for demonstration of the latter's capability in mimicking their biological counterpart. In addition, for underwater applications, localization of dipole sources has implications in detecting and estimating nearby fish-like robots and therefore is relevant to robot coordination and control.

Dagamseh *et al.* proposed the use of characteristic points (zero-crossings, maxima, etc.) in the measured velocity profile along the lateral line for dipole source localization [27], similar to what was proposed by Franosch *et al.* for modeling the localization by the clawed

frog *Xenopus* [34]. However, this approach would require prohibitively many sensors to determine the characteristic points, and it is limited to a maximum detection distance of  $1/\sqrt{2}$  body length (BL). Fransch *et al.* also suggested a maximum-likelihood estimator-type model for dipole localization by *Xenopus* [34], although no algorithms were presented to solve for the optimal source location. Data-matching/table-lookup approaches were presented by Pandya *et al.*, where the measured signal pattern was compared with a large, pre-obtained set of templates or an empirical model fitted with sufficient amount of data [68]. These approaches suffered from the need for excessive computing and storage resources, or the difficulty in system-level implementation [68]. Recently, a beamforming algorithm for array signal processing was used to localize a dipole source and a tail-flicking crayfish, and showed better performance than the matched filter [98].

## 1.2 Research Objective

Inspired by the sensing capabilities of biological lateral lines, our goal in this dissertation is to investigate signal processing approaches for an artificial lateral line, which will be ultimately mounted on an underwater robot such as a robotic fish (Fig. 1.2). Realization of this goal could have significant implications. First, it will directly benefit many underwater applications. For example, autonomous underwater vehicles can navigate in narrow spaces with a near-field sensing capability. Second, by learning the mechanisms used by most fish and underwater species, we will be able to develop new algorithms for sensor signal processing that will find use beyond hydrodynamic sensing.

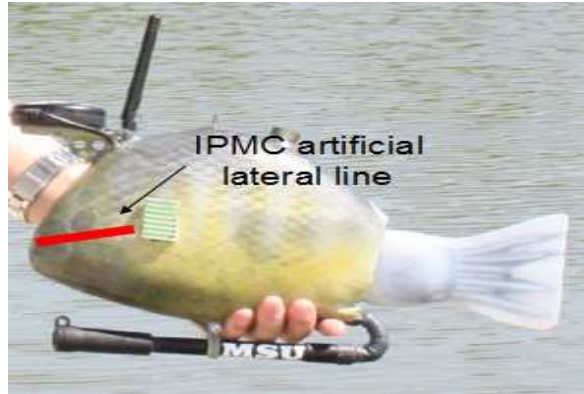


Figure 1.2: Illustration of the potential use of an artificial lateral line system on a robotic fish.

## 1.3 Contributions

### 1.3.1 An Artificial Lateral Line System Using IPMC Sensor Arrays

The first contribution of this dissertation is a novel approach to the realization of artificial lateral lines, which exploits the inherent sensing properties of ionic polymer-metal composites (IPMCs)[81, 19, 58]. As illustrated in Fig. 1.3, An IPMC has three layers, with an ion-exchange polymer membrane sandwiched by metal electrodes. Inside the polymer, (negatively charged) anions covalently fixed to polymer chains are balanced by mobile, (positively charged) cations. Deformation under a mechanical perturbation redistributes the cations, producing a detectable electric signal (e.g., short-circuit current) that is well correlated with the mechanical stimulus, which explains the sensing principle of an IPMC. Conversely, under an applied voltage, transport of hydrated cations and water molecules within the membrane, together with the associated electrostatic interactions, leads to bending motion

of the IPMC sample. Many researchers have studied the fabrication [49, 6, 18], characterization, and modeling [63, 86, 10, 17, 14, 28, 71, 72, 73, 100] of IPMC sensors and actuators. Recent years have seen significant interest in using IPMC materials for underwater actuation [87, 15, 7, 99, 12, 48, 88], sensing [35], and energy harvesting [8].

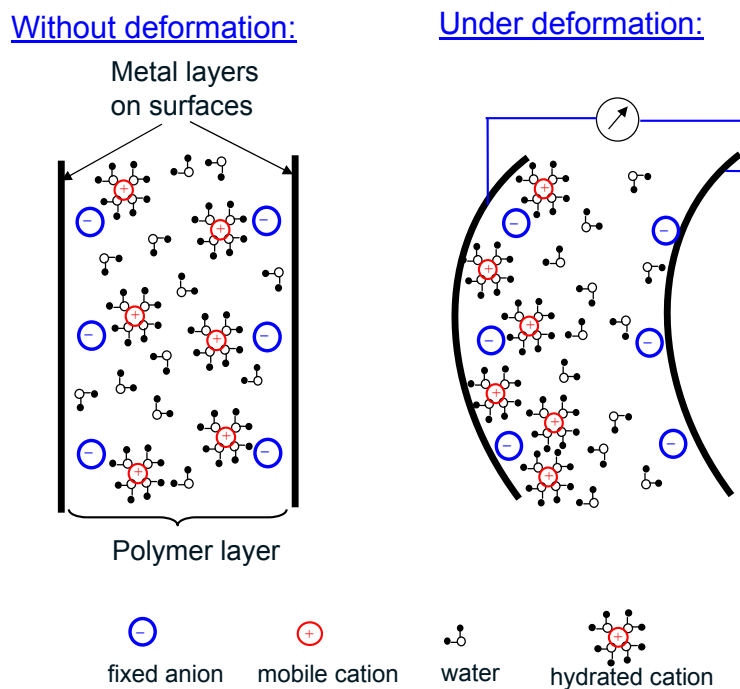


Figure 1.3: Illustration of IPMC sensing principle.

We have chosen the IPMC material for creating artificial lateral line in this work for several reasons. First, IPMC works well in water and has direct mechanosensory property, which makes it relatively easy to construct the sensor and its readout circuitry. Another advantage of IPMC sensors (over, e.g., hot-wire flow sensors) is that they automatically capture the flow polarity. Furthermore, the softness of IPMC material allows it to respond to small flows and thus attain high measurement sensitivity. Finally, the fabrication processes for IPMCs are relatively simple and have been studied extensively over the past decade. In particular, for millimeter-scale and above, one can fabricate an IPMC sheet using well known

processes [49] and then cut into any desired sizes.

### **1.3.2 Localization of a Fixed Dipole Using Neural Network**

In this dissertation, we propose an artificial neural network-based scheme for processing the signals from IPMC sensor arrays, to localize a dipole source. In general, the relationship between the source location and the resulting flow field (and thus the sensor outputs) is highly nonlinear and complex. While there is an analytical but nonlinear model for a dipole-generated flow field under ideal assumptions [53], this model may not capture the flow field well under more realistic conditions, an example of which is the frequent scenario that involves fluid-structure interactions. Artificial neural networks are capable of approximating nonlinear mappings, and in particular, when such mappings are unknown, there are established methods for training the approximating neural networks [79]. For this reason, we have adopted a neural network-based scheme for the dipole-source localization. The concept of an IPMC lateral line and its neural network-based processing scheme are examined experimentally. A prototype comprising six millimeter-scale IPMC sensors, with a body length (BL) of 10 cm, is constructed. The localization experiments are conducted for a dipole source that is vibrating at 40 Hz. Note that this frequency is consistent with the typical range of dipole frequencies adopted in the study of biological and artificial lateral lines (e.g., 50 Hz in [24] and 45 Hz in [98, 65]).

### **1.3.3 Nonlinear Estimation-based Dipole Source Localization**

An engineering equivalent of a biological lateral line is of great interest to the navigation and control of underwater robots and vehicles. A vibrating sphere, also known as a dipole source,

can emulate the rhythmic movement of fins and body appendages, and has been widely used as a stimulus in the study of biological lateral lines. Dipole source localization has also become a benchmark problem in the development of artificial lateral lines. In this dissertation we present two novel iterative schemes, called Gauss-Newton (GN) and Newton-Raphson (NR) algorithms, for simultaneously localizing a dipole source and estimating its vibration amplitude and orientation, based on the analytical model for a dipole-generated flow field. The performance of the GN and NR methods is first confirmed with simulation results and the Cramer-Rao bound (CRB) analysis. Experiments are further conducted on an artificial lateral line prototype, consisting of six millimeter-scale ionic polymer-metal composite (IPMC) sensors with intra-sensor spacing optimized with CRB analysis. Consistent with simulation results, the experimental results show that both GN and NR schemes are able to simultaneously estimate the source location, vibration amplitude and orientation with comparable precision. Specifically, the maximum localization error is less than 5% of the body length (BL) when the source is within the distance of one BL. Experimental results have also shown that the proposed schemes are superior to the beamforming method, one of the most competitive approaches reported in literature, in terms of accuracy and computational efficiency.

### **1.3.4 Localization of a Moving Dipole Source Underwater**

We further investigate the problem of localizing a moving dipole source using an artificial lateral line (ALL). Such a moving source could represent a swimming fish or robotic fish, which demonstrates a combination of translational motion and oscillatory body/fin motion. First, we formulate a nonlinear estimation problem based on an analytical model for the

moving dipole-generated flow field, where we assume that the source location, vibration amplitude, and moving speed are unknown. We also assume that the amplitudes of the flow velocities at the DC and dipole vibration frequencies are available as measurements. Such amplitudes can be obtained by conducting sliding digital Fourier transform (SDFT) of the measured signal in the time domain. The estimation problem is solved recursively with the Gauss-Newton method, and we illustrate the proposed approach with simulation and experimental results.

### **1.3.5 Underwater Tracking and Size-Estimation of a Moving Object**

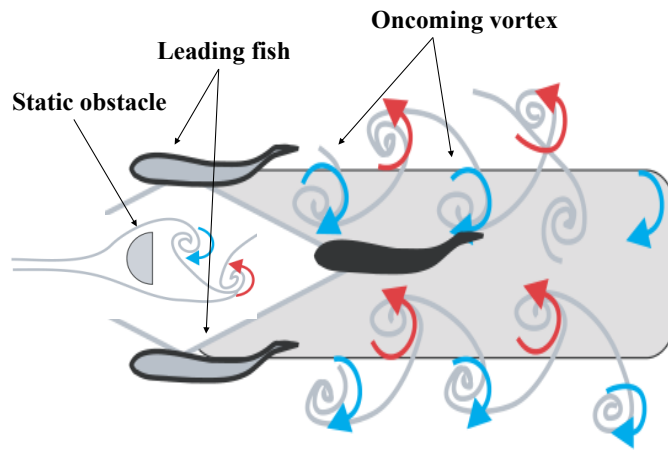
We investigate the problem of tracking a moving but non-vibrating cylindrical object and estimating its size and shape using an artificial lateral line system. Instead of using pressure sensing as done in the literature for similar problems [11, 33, 91], we consider the measurement of flow velocities as is believed to be what is adopted in biological lateral lines. Based on a nonlinear analytical model for the moving object-induced flow field, two-stage nonlinear filtering algorithms are proposed to estimate the location, velocity, size, and shape of the object. Using two-stage filtering instead of one stage is motivated partly by the progressive information extraction conjectured for biological lateral lines [11], and partly by computational efficiency. The approach is first illustrated with simulation results, where a moving cylinder with ellipsoidal cross-section is tracked and its shape parameter estimated. Experimental validation is then conducted with an artificial lateral line prototype comprising six IPMC flow sensors. Experimental results show that the proposed approach is able to track the movement of a cylindrical and an ellipsoidal objects with a circular profile and provide

an estimate of the object size, and shape, respectively.

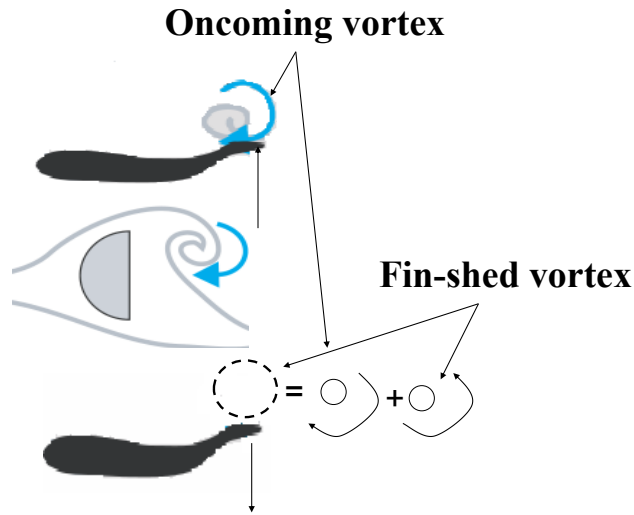
### 1.3.6 Localization and Identification of an Stationary Obstacle Underwater

Fish exploits the vortex streets generated by leading fish (schooling behaviors) or by a static obstacle in flow. First, a fish swimming between the vortex streets created by two leading fish will experience a flow assisting its forward motion (Fig. 1.4(a)) [95]. Second, a fish can extracting energy from oncoming vortices. For example, if the caudal fin counter-spins a vortex shed by leading fish or a static obstacle, the energy wasted in the wake can be minimized (Fig. 1.4(b)) [90]. Such a strategy for autonomous underwater vehicles will require detecting, tracking and manipulating oncoming vortices using artificial lateral lines.

For a robot-like fish or an underwater vehicle, the information sensed via the artificial lateral line reflects the combined effect of an unknown number of vortices, the flow due to its own motions, and other disturbances. Biologically, fish are able to easily identify stimuli of interest in a noisy environment through its lateral line system [20]. We experimentally explore the use of IPMC sensors for estimating the hydrodynamic parameters involved in a Kármán vortex street that is created by a stationary cylinder in a flow. We validate that the vortex shedding frequency, which can be extracted from the sensor signal, shows clear correlation with the flow speed and the obstacle size.



(a)



(b)

Figure 1.4: Benefit of exploiting vortex streets (adapted from [57]): (a) Exploiting flow due to vortex streets of leading fish; (b) harvesting energy from oncoming vortices.

## 1.4 Organization of This Dissertation

The remainder of this dissertation is organized as follows. Chapter 2 presents a complete development of an IPMC artificial lateral line. Using IPMC sensors designed and fabricated

by our Smart Microsystems Laboratory in Michigan State University (MSU), we assemble and model the response of an IPMC sensor array, and conduct the sensor calibration. We then perform fast Fourier transform to analyze the signal spectrum and/or extract signal amplitudes at frequencies of interest. The performance of the system is demonstrated and tested through a range of experiments involving various hydrodynamic stimuli. We further demonstrate the performance of the IPMC lateral line in localizing a dipole source, where an artificial neural network is used for signal processing. Chapter 3 first reviews an analytical model for a dipole-generated flow field. The digital particle image velocimetry (DPIV) system (LaVision, Ypsilanti, MI) and Cramer-Rao bound optimization technique are also introduced in this chapter. New nonlinear estimation algorithms are investigated for localizing a dipole source with unknown vibration amplitude and orientation. Both simulation and experimental are presented to support the proposed methods. Chapter 4 and Chapter 5 focus on tracking of a moving dipole source and a moving but non-vibrating object, respectively. For the moving dipole case, we demonstrate in both simulation and experimentation that the Gauss-Newton scheme is able to successfully accomplish the localization and tracking task. For a moving but non-vibrating cylinder, we propose several two-stage Kalman-filtering-type algorithms, and conduct simulation and experiments to examine their performance. Chapter 6 presents the experimental results on how an IPMC lateral line might be used for hydrodynamic imaging of vortex streets shed by a stationary object in a flow. Chapter 7 draws conclusions on the research, while the recommendations for future work on the project are proposed in Chapter 8.

## Chapter 2

# Dipole Source Localization Using Neural Networks

The signals from IPMC sensors of the artificial lateral line are complex functions of the source location. Even for the dipole stimulation, the flow field measured with digital particle image velocimetry (DPIV) deviates appreciably from the theoretical predictions, because of nonideal fluid conditions and interactions of fluid with structures (e.g., with the IPMC beams and the walls of the tank). In addition, the sensing characteristics of individual sensors could be different from each other in practice because of imperfect fabrication processes. The sensor outputs are further contaminated with noises due to ambient water movement and thermal fluctuations [35]. As a result, it is difficult to decode the sensor signals analytically.

Biological fish are faced with similar challenges in extracting relevant sensing information from vast amount of data that are corrupted by noises. However, they manage to accomplish source localization and other missions robustly through neural network-based information processing. Taking this biological inspiration, we construct an (artificial) neural network to

process the signals acquired by the IPMC-based lateral line.

The remainder of the chapter is organized as follows. The model for an IPMC sensor interacting with a flow is first discussed in Section 2.1. The neural network-based processing scheme and the optimal design of the neural network using genetic algorithm are described in Section 2.2 and Section 2.3, respectively. The experimental setup and basic sensor characterization are presented in Section 2.4. Experimental results on the localization of a dipole source are shown in Section 2.5. Finally, concluding remarks are provided in Section 2.6.

## 2.1 Hydrodynamic Model for an IPMC Sensor Under Oscillatory Flow

In a biological lateral line system, under an AC flow, the flow field around the cilium is very different from what it would be under a DC flow. Due to a viscous flow, a boundary layer symmetric about the cilium will develop at the substrate (Fig. 2.1), and the drag force acting on the cilium will have some phase shift along the length. As the starting point of this analysis, we assume that there is an oscillatory flow with angular frequency  $\omega$ , and the local fluid velocity at the  $i$ th sensor site is denoted as  $v(x_i, y_i)$ , where sensor  $i$  has dimensions of  $h \times W \times t$  (height, width, thickness) and is located at  $(x_i, y_i)$ . Under the small-deflection assumption, the Euler-Bernoulli equation for the IPMC beam is given as,

$$YJ \frac{\partial^4 q}{\partial y^4} + \bar{\rho}_m \frac{\partial^2 q}{\partial t^2} + c_1 \left( \frac{\partial q}{\partial t} - U \right) + \bar{\rho}_a \left( \frac{\partial^2 q}{\partial t^2} - \frac{\partial U}{\partial t} \right) = \bar{\rho}_w \frac{\partial U}{\partial t}, \quad (2.1)$$

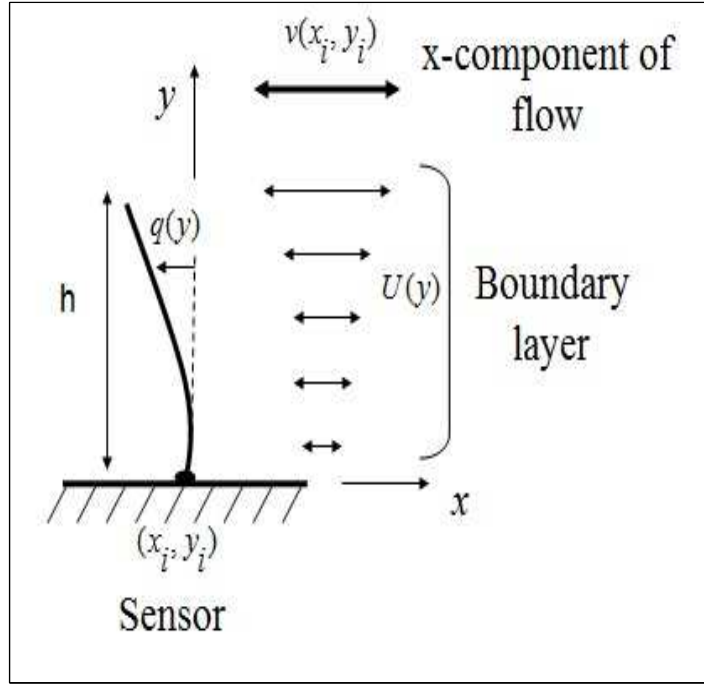


Figure 2.1: Illustration of the beam dynamics of an IPMC sensor in flow.

where the first term represents elastic force ( $F_e$ ) acting on the beam [45]:

$$F_e = YJ \frac{\partial^4 q}{\partial y^4}, \quad (2.2)$$

$Y$  is the Yong's modulus of the IPMC beam,  $J$  is the second moment of inertia  $J = \frac{2}{3}Wt^3$ .

The second term in (2.1) represents the inertial force  $F_m$ , given as [61]

$$F_m = \bar{\rho}_m \frac{\partial^2 q}{\partial t^2}, \quad (2.3)$$

where  $\bar{\rho}_m = \rho_m Wt$ , and  $\rho_m$  is the density of the IPMC material. The model treats the stimulus as an oscillating pressure field and we can calculate the flow near the boundary

over the flat surface as [38]

$$U = v(x_i, y_i) \left( 1 - e^{\left(\frac{-y}{\delta}\right)} \cos\left(\frac{-y}{\delta}\right) \right), \quad (2.4)$$

where  $\delta$  is the boundary layer thickness. This is calculated by [38]

$$\delta = \sqrt{\frac{2\mu}{\rho_w \omega}}, \quad (2.5)$$

where  $\rho_w$  and  $\mu$  are the density and dynamic viscosity of water, respectively. The viscous drag force  $F_u$ , on an element of the IPMC beam, is given as the third term in (2.1) [61]

$$F_u = c_1 \left( \frac{\partial q}{\partial t} - U \right), \quad (2.6)$$

where  $c_1 = 4\pi\mu k$ , and  $k$  is a viscous drag coefficient, which is calculated as

$$k = \frac{L}{L^2 + (\pi/4)^2}, \quad (2.7)$$

where  $L$  is the hydrodynamic force coefficient.  $L$  can be calculated as

$$L = \gamma + \ln\left(\frac{W}{\sqrt{2\delta}}\right), \quad (2.8)$$

where  $\gamma$  is Euler's constant ( $\gamma \approx 0.5772$ ). The acceleration reaction force  $F_a$ , is represented as the fourth term in (2.1) [37]

$$F_a = \bar{\rho}_a \left( \frac{\partial^2 q}{\partial t^2} - \frac{\partial U}{\partial t} \right). \quad (2.9)$$

Pressure field that develops around the IPMC beam as flow accelerates results in a buoyant force,  $F_b$ , that can be calculated as

$$F_b = \bar{\rho}_w \frac{\partial U}{\partial t}, \quad (2.10)$$

where  $\bar{\rho}_w = \rho_w W t$ . By converting the equation (2.1) from the time-domain to the Laplace ( $s$ ) domain, we can derive the transfer function that relates the beam tip deformation  $q_1$  to the local velocity  $v$ . With typical parameters, the transfer function turns out to be approximated well by

$$\frac{q_1(s)}{v(s)} = \frac{c_a}{s}, \quad (2.11)$$

where  $c_a$  is constant. On the other hand, Chen *et al.* [16] have developed a dynamic for IPMC sensors, where the transfer function from the tip displacement  $q_1$  to IPMC current output  $I$  can be approximated as

$$\frac{I(s)}{q_1(s)} = c_b s, \quad (2.12)$$

where  $c_b$  is a constant. The overall approximate model from local velocity  $v$  to the IPMC current output  $I$  is then given as

$$\frac{I}{v(s)} = \eta, \quad (2.13)$$

where  $\eta = c_a c_b$  is constant gain that will be calibrated in experiments. Note that the approximations used to arrive at (2.11) and (2.12) are only valid for an intermediate frequency range, where the IPMC sensor behaves like a band-pass filter. For DC or high-frequency range, the sensor model will need to be adapted appropriately.

## 2.2 Source Localization Using Neural Network Processing

We consider the localization of a dipole source in a two-dimensional (2D) plane with coordinates  $(x, y)$ . The proposed approach can be extended readily to the localization in a 3D space, although that will require more training points for the neural network. Fig. 2.2 illustrates the problem setup. Here  $(x, y)$  denotes the location of the source, and the IPMC sensor arrays are placed at a known location. As illustrated in Fig. 2.3, we adopt the

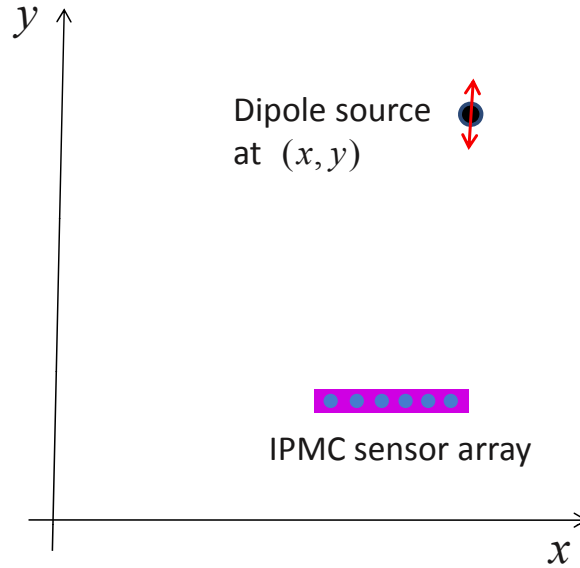


Figure 2.2: Schematic of the dipole source localization problem.

multilayer perceptron (MLP) architecture for the neural network. An MLP network consists of an input layer, a hidden layer, and an output layer, and is the most widely used network structure for nonlinear classification and prediction applications [79].

One could use different features extracted from the sensor output data as the input to the neural network. In this work, we use the signal amplitude at the stimulus frequency

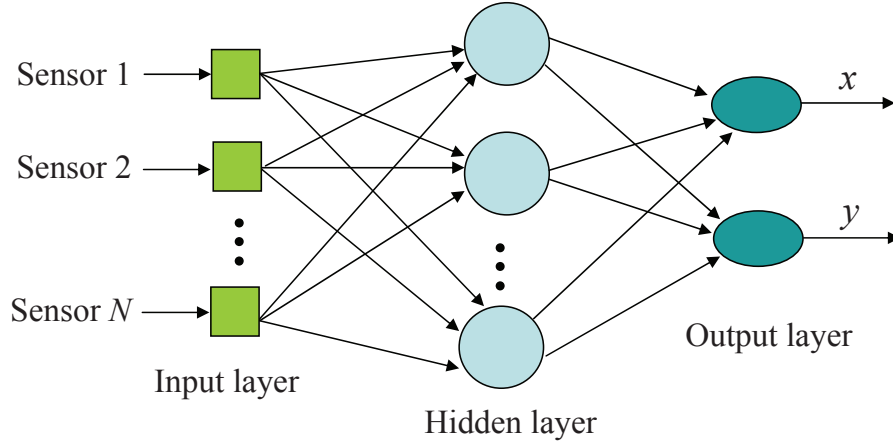


Figure 2.3: Schematic of the MLP neural network for signal processing of the IPMC lateral line.

because of its robustness to measurement noises. The amplitude is obtained through fast Fourier transform (FFT) of the raw sensor signal. The number of inputs is the same as the number of IPMC sensors considered. For comparison purposes, in this work we investigate the performance of the artificial lateral line when different numbers of sensors are adopted. The number of the hidden-layer nodes is chosen through a genetic algorithm (GA)-based optimization process, which will be further described below. Each hidden layer node represents the operation of nonlinear activation, which takes the form of a sigmoid function. The output layer has two nodes, representing the  $x$  and  $y$  coordinates of the vibrating source.

The number of hidden-layer nodes and the connective weights between the layers are determined through a two-phase training procedure, using the software NeuroSolutions [64]. The training data are obtained by placing the stimulus at known locations  $(x_i, y_i)$ ,  $1 \leq i \leq M$ , measuring the corresponding sensor outputs and computing the signal amplitudes. In the first training phase, a genetic algorithm is used to find an appropriate value for the number of hidden-layer nodes and a reasonable set of values for the connective weights. In particular, each genome encodes both the number of hidden-layer nodes and the weights of

all connecting edges. The maximum number of hidden-layer nodes is limited to 24 based on the numbers of network inputs and outputs. We consider a population size of 25 genomes and run 40 generations of evolution (crossover/mutation). The fitness function (or more appropriately, the cost function) used in the selection process is the mean square error  $J$ :

$$J = \frac{1}{2M} \sum_{i=1}^M (x_i - \hat{x}_i)^2 + (y_i - \hat{y}_i)^2, \quad (2.14)$$

where  $(\hat{x}_i, \hat{y}_i)$  denotes the predicted value for  $(x_i, y_i)$  under the current network structure and weights.

The values of the connective weights obtained in the first training phase then serve as the initial condition for weights refinement in the second phase, where the network structure is fixed as determined in the first phase. Delta-bar-delta learning [79], with adaptive learning rate, is used for weights optimization. Let  $K$  be the total number of weights. For each weight  $w_k$ ,  $1 \leq k \leq K$ , the update rule is

$$w_k^{\text{new}} = w_k^{\text{old}} - \eta_k^{\text{new}} \frac{\partial J}{\partial w_k^{\text{old}}}, \quad (2.15)$$

where the adaptive learning rate  $\eta_k$  is updated as

$$\eta_k^{\text{new}} = \begin{cases} \eta_k^{\text{old}} + a, & \text{if } \frac{\partial J}{\partial w_k^{\text{old}}} > 0 \\ b\eta_k^{\text{old}}, & \text{if } \frac{\partial J}{\partial w_k^{\text{old}}} \leq 0 \end{cases}, \quad (2.16)$$

and  $a, b$  are constants satisfying  $0 < a, b < 1$ .

## 2.3 Optimum Design of the Neural Network Using Genetic Algorithm

The genetic algorithm (GA) is a search technique, based on an abstraction of biological evolution, used to find solutions of optimization problems. In GA, a population of chromosomes, which are represented as binary vectors, evolves into a new population of chromosomes using the natural selection forces of crossover and mutation. Some chromosomes are selected and allowed to reproduce and the more “fit” chromosomes produce more offspring. Recombination is achieved via the crossover operator, which exchanges parts of two chromosomes. Mutation can randomly change some segments in the chromosome. Chromosomes are used to encode possible solutions to an optimization problem. The quality of a solution is represented by its fitness, which is the objective function to be optimized. In our case, the objective function is the mean-square error. The GA is implemented according to the following steps: (i) Randomly generate an initial chromosome population; (ii) calculate the minimum square error to indicate the fitness function value for each chromosome in the population; (iii) create a new chromosome population from mating of current chromosomes and applying mutation and recombination; (iv) select a fixed number of chromosomes such that more fit chromosomes are more likely to be selected; (v) compute the fitness of the new population; (vi) increment the current number of generation. Finally, if not (end-test) go to step (iii), or else stop and return the best chromosome. We use the genetic algorithm to determine the optimal initial weights and the optimum number of nodes in the hidden layer of the neural network. The optimal initial weights will guarantee a faster convergence to the global minimum of the objective function, and the optimum number of nodes in the

hidden layer will avoid the bias-variance dilemma of neural networks. Given a data set, it is known that a small number of nodes in the hidden layer captures the data trend only in a small region of the pattern, whereas a large number of nodes in the hidden layer results in overfitting the data [79].

## 2.4 Experimental Setup and Sensor Characterization

Fig. 2.4 shows the constructed lateral line prototype, consisting of six IPMC sensors. Each sensor, with dimensions  $8 \text{ mm} \times 2 \text{ mm} \times 200 \text{ }\mu\text{m}$ , has been cut from an IPMC sheet fabricated by the Smart Microsystems Laboratory at Michigan State University, following a recipe similar to the one described in [49]. The IPMC material contains lithium ions ( $\text{Li}^+$ ) as cations. The sensor-to-sensor separation is 2 cm, resulting in a total span of 10 cm, which will be regarded as the Body Length (BL) in later discussions.

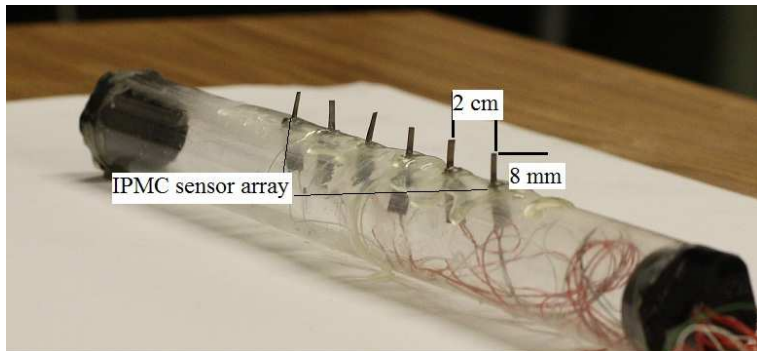


Figure 2.4: A prototype of IPMC-based lateral line system.

Under a mechanical stimulus, an open-circuit voltage or a short-circuit current can be measured across the two electrodes of an IPMC. We have chosen to take the short-circuit current as the sensor output because current measurement is less susceptible to noises. Fig. 2.5 shows the schematic of the measurement circuit, which consists of two cascaded operational

amplifiers (op-amps)[35]. A low-noise, low-bias precision op-amp (OPA 124 from Texas Instruments) is adopted for the first-tier amplification, to reduce both the noise and the spurious DC bias in the sensor output induced by the leakage current. Since the “-” terminal of Op-amp 1 is virtually the ground (following standard op-amp circuit analysis), the two electrodes of IPMC can be considered short-circuited. The sensing current generated under this configuration,  $i(t)$ , is proportional to the voltage output  $v_1(t) = R_1 i(t)$ . The second op-amp is introduced for gain adjustment, where the resistor  $R_3$  is tunable. The output  $v_2(t)$  is related to the current signal  $i(t)$  via  $v_2(t) = \frac{R_3 R_1}{R_2} i(t)$ . In the circuit we used,  $R_1 = 470 \text{ k}\Omega$ ,  $R_2 = 10 \text{ k}\Omega$ , and  $R_3$  was adjustable from 0 to 50 k $\Omega$ . Acquisition and processing of the IPMC sensor output are conducted through a dSPACE system (DS1104, dSPACE Inc., Germany). A digital low-pass filter with cutoff frequency 55 Hz is further implemented to remove high-frequency noises from the sensor signals .

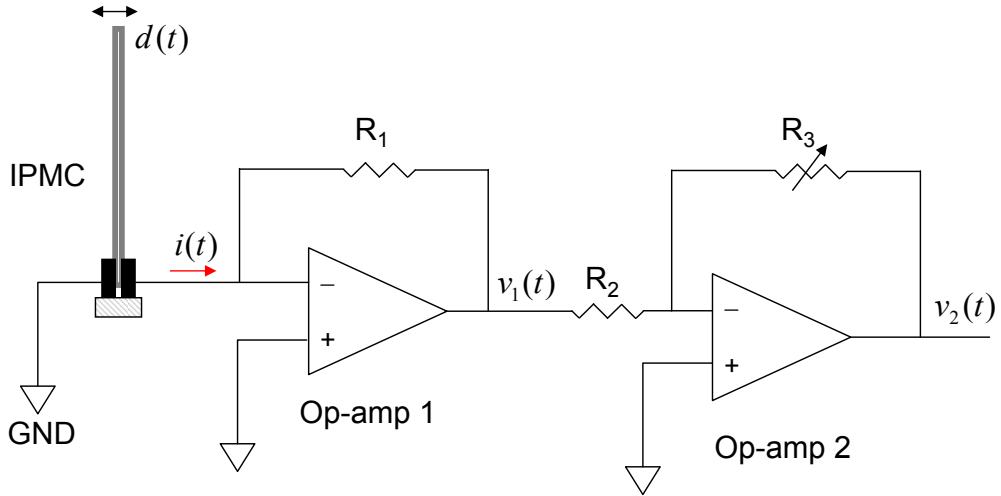


Figure 2.5: The schematic of circuit for measuring the short-circuit current generated by the IPMC sensor.

All experiments are conducted in a water tank, shown in Fig. 2.6(a). The tank measures  $6 \times 2 \times 2 \text{ ft}^3$ , and is equipped with a digital particle image velocimetry (DPIV) system

(LaVision, Ypsilanti, MI). In a DPIV system, small particles are dispersed in a fluid and a laser sheet is created in the fluid to illuminate the particles. Processing of images taken in quick successions can reveal the movement of particles and thus provide information about the flow field. In our experiments, the DPIV system is used for preliminary characterization of the flow field under the stimulating source. A dipole source is created with a mini-shaker (4810, Brüel & Kjaer, Denmark) (Fig. 2.6(b)), the vibration amplitude and frequency of which can be readily controlled through a voltage input to the shaker. A lightweight bar firmly attached to the mini-shaker then translates the vibration to a sphere rigidly coupled to the bar. The sphere, which is a steel ball, has a diameter of 19 mm. The frequency range of the dipole spans DC–20 kHz. The source location and vibration direction with respect to the IPMC lateral line can be adjusted by moving the stand holding the IPMC lateral line or by moving the source itself.

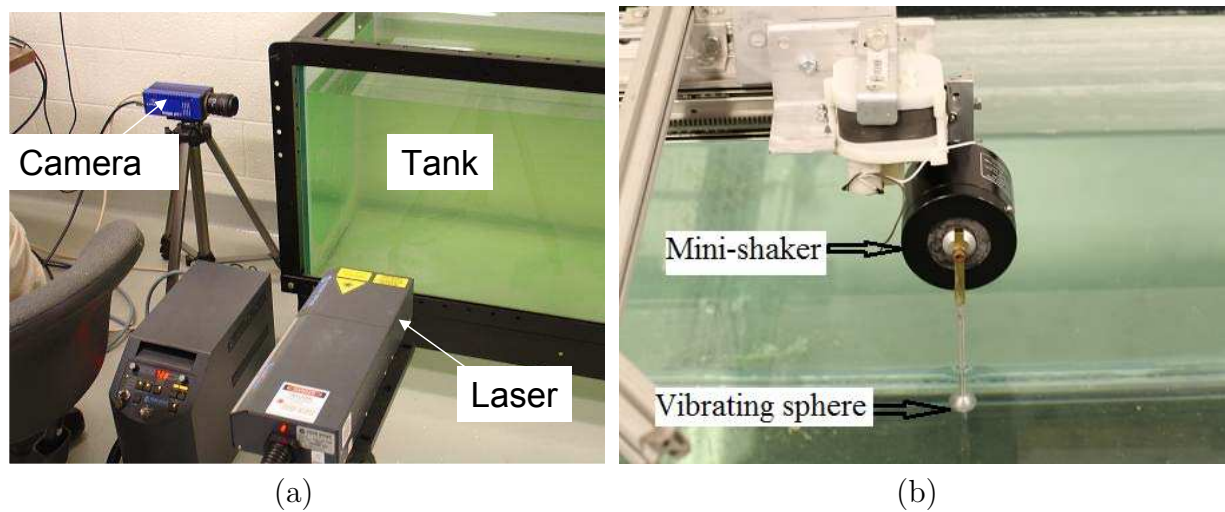


Figure 2.6: Experimental setup: (a) Experimental tank equipped with a DPIV system; (b) the mini-shaker-based dipole source.

DPIV experiments have been conducted to observe the flow field around the IPMC sensors, for different source-sensor separation, to get a sense of the flow magnitude un-

der the stimuli. For example, Fig. 2.7 shows the flow fields around an IPMC sensor for a  $19 \text{ mm} \times 14 \text{ mm}$  window, under a 20 Hz stimulus produced with a dipole source described in [35], where both the source vibration axis and the illuminated plane are perpendicular to the IPMC beam plane. In other words, the IPMC beam would bend left and right in Fig. 2.7, although the IPMC thickness did not look to scale because of laser light scattering around the beam. Fig. 2.7(a) and (b) correspond to dipole-IPMC separations of 10 and 45 cm, respectively, which clearly indicates that the flow velocity decreases as the separation between source and sensor increases.

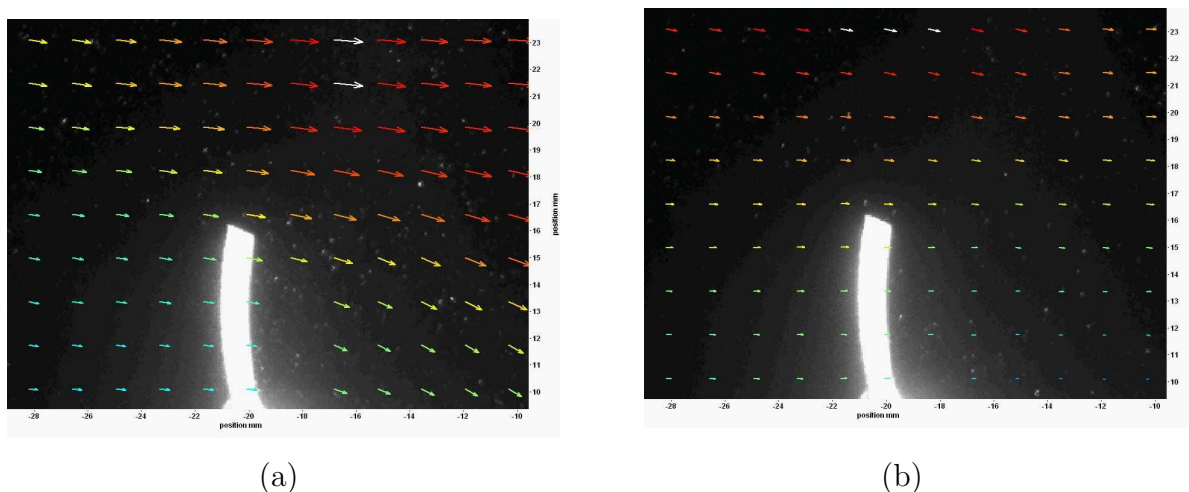
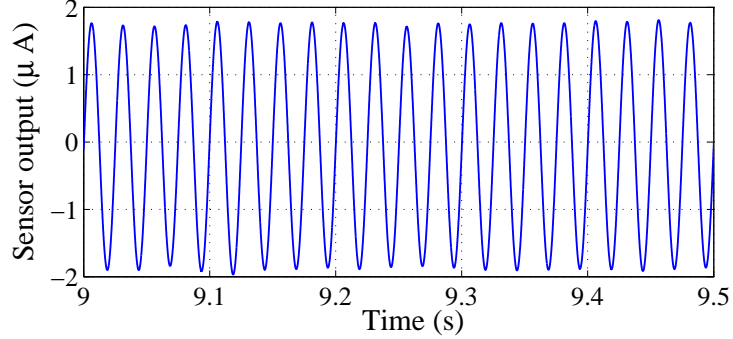


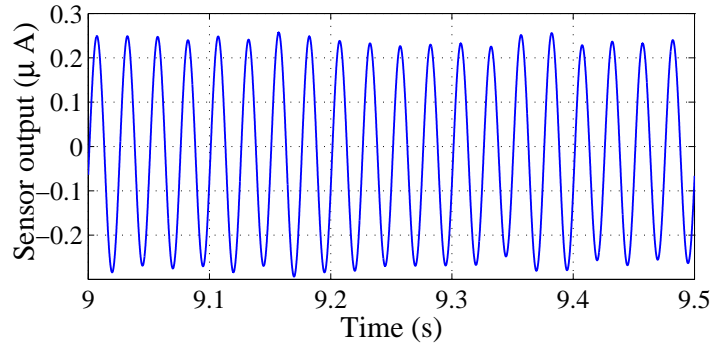
Figure 2.7: Flow field around one IPMC sensor under a dipole stimulation: (a) Dipole-sensor separation 10 cm, with maximum flow amplitude of 9.3 mm/s in the field; (b) dipole-sensor separation 45 cm, with maximum flow amplitude of 4.1 mm/s in the field.

Fig. 2.8 shows typical sensor responses under the mini-shaker-based stimulation (40Hz), indicating that the current output from the IPMC sensor is at the order of  $\mu\text{A}$ , which can be captured very well by the sensing circuit. Fig. 2.8(a) shows the signal from sensor #2 of the IPMC lateral line, when the source is 1 cm away from this sensor, while Fig. 2.8(b) shows the response from sensor #4 (4 cm from sensor #2) under the same stimulus. In this

experiment the lateral line axis is perpendicular to the vibration axis of the dipole source, and perpendicular to the beam plane of each sensor.



(a)



(b)

Figure 2.8: Typical IPMC sensor signals: (a) Signal from sensor #2, which is close to the dipole source; (b) signal from sensor #4.

Fig. 2.9 shows the amplitude of the signal from one IPMC, located at  $(7,0)$ , as a function of the location  $(x,y)$  of the mini-shaker-based dipole stimulus vibrating parallel and perpendicular to the IPMC beam plane. It can be seen that, while in general the signal gets stronger when the source gets closer, the overall amplitude landscape has a sophisticated profile. The results in Fig. 2.9 clearly illustrate the challenge in underwater localization. In particular, it would be difficult to localize unambiguously a source with a single sensor;

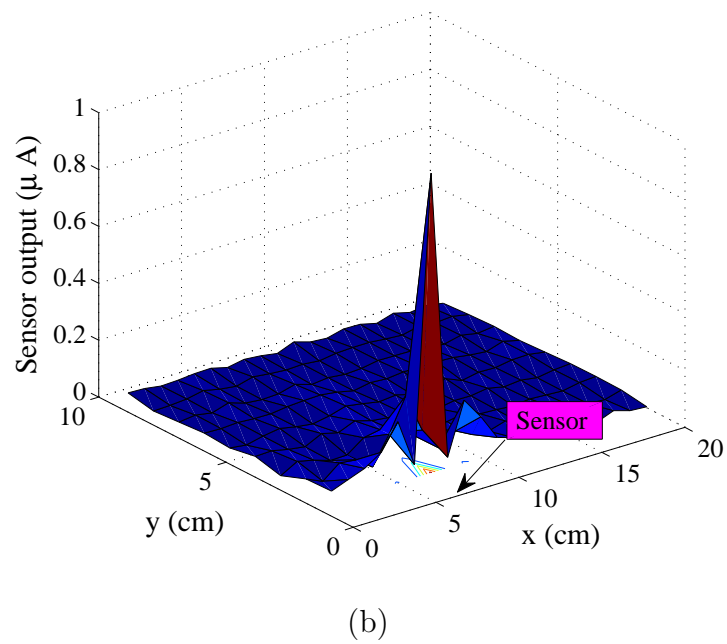
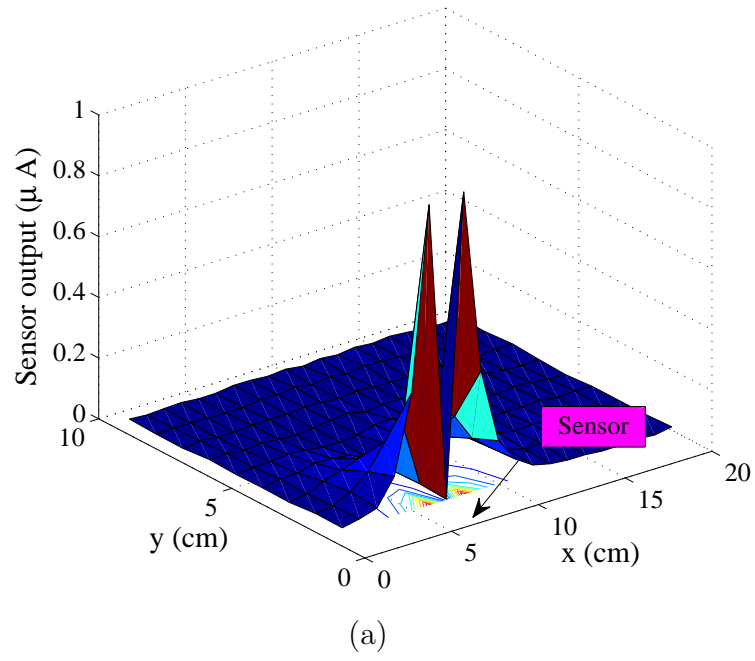


Figure 2.9: Sensor characterization, measured sensor signal magnitude as a function of source location, The dipole vibration axis is: (a) Parallel to the IPMC beam plane; (b) perpendicular to the IPMC beam plane.

instead, a lateral line-like array structure will be needed.

## 2.5 Experimental Results on Dipole Source Localization

As shown in Fig. 2.11, a working area of about  $20 \times 10 \text{ cm}^2$  is used in the experiments. The frequency of the dipole source is 40 Hz, the vibration is along the  $y$  direction with an amplitude of 1.91 mm. The lateral line is placed in parallel with the  $x$ -axis, at  $y = 0$  and spanning from  $x = 5 \text{ cm}$  to  $x = 15 \text{ cm}$ . The beam plane of each IPMC sensor is perpendicular to the lateral line direction. Both the dipole source and the lateral line are placed 6 cm underwater. First, for the purpose of training the neural network, we define a grid of  $1 \times 1 \text{ cm}^2$  lattices in the working area, resulting in a total of 180 grid points. The dipole source is placed at each grid point, where the amplitude of the signal from each IPMC sensor in the lateral line is obtained. Subsets of these data are used to train the neural network in different cases. Fig. 2.10 shows the evolution of the cost function  $J$  in (2.14) during the first, genetic algorithm-based training phase, for the case involving six sensors and 180 training points. It can be seen that the cost function converges to a steady-state value as the number of generations approaches 40. As explained in Section 2.2, the connective weights obtained in the first training phase are then refined in the second phase using delta-bar-delta learning. To test the performance of the lateral line, we place the dipole source at each of 16 points along an elliptical track centered at  $(10, 5.5)$ , obtain the amplitudes of sensor signals from the lateral line and feed them to the trained neural network, and compare the output of the network to the actual location.

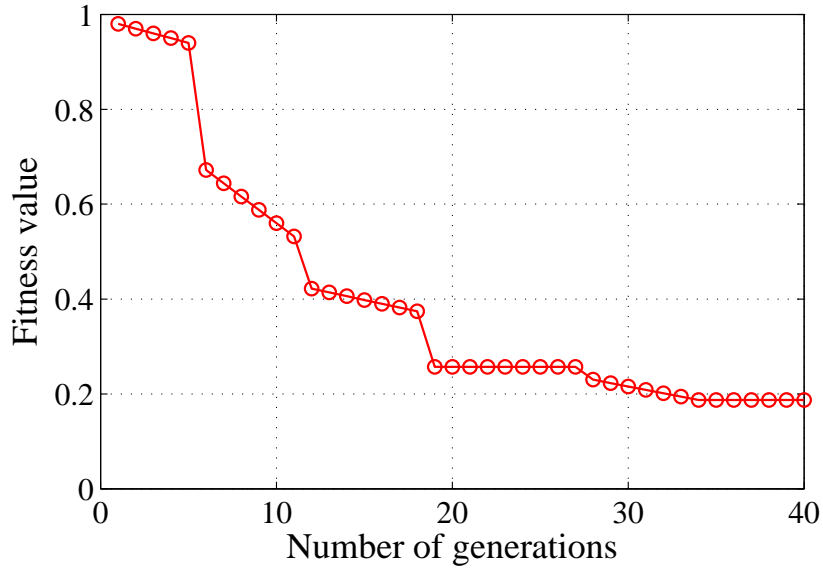
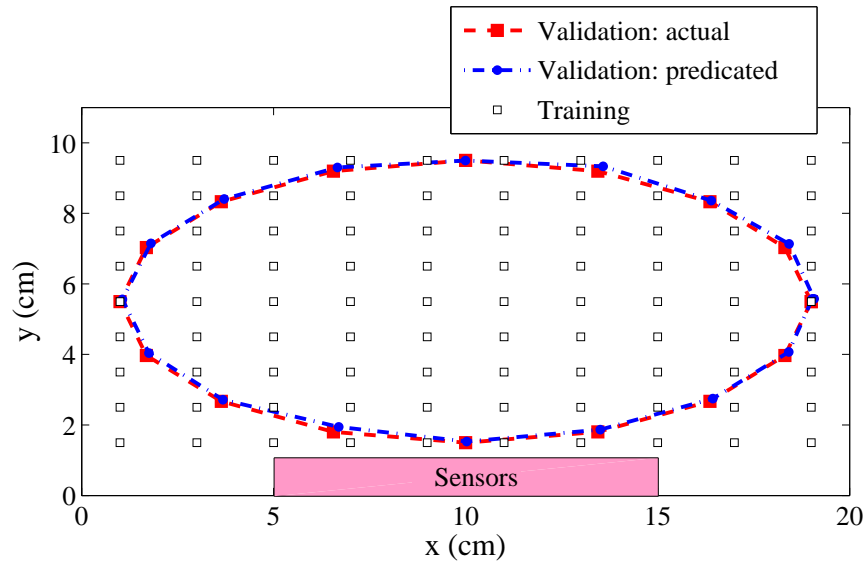


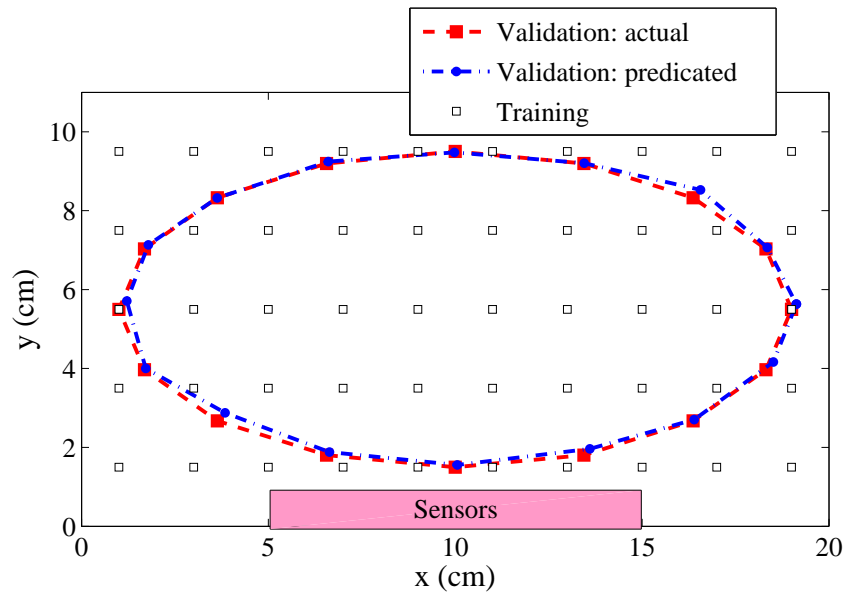
Figure 2.10: Evolution of the fitness function (the mean square error  $J$ ) over generations, in the genetic algorithm-based training phase. This example involves all six sensors and 180 training points.

Fig. 2.11(a) and (b) show the localization results when all six sensors are used, where 90 ( $2 \times 1$  cm<sup>2</sup> lattices) and 50 ( $2 \times 2$  cm<sup>2</sup> lattices) training points are utilized, respectively. The locations of the training points are denoted with squares in the figures. Fig. 2.12(a) and (b) further show the actual localization errors at all 16 validation points for the two cases. It is clear from Fig. 2.12(b) that, for a training grid of  $2 \times 2$  cm<sup>2</sup> lattices (50 points), the maximum localization error is 0.3 cm. The maximum error drops to 0.2 cm when the number of training points is increased to 90 (Fig. 2.12(a)). Note that the resulting neural networks are different when different numbers of training points (or different numbers of sensors) are used. For example, the neural network has 13 hidden nodes for the case in Fig. 2.11(a), while it has 10 hidden nodes for the case in Fig. 2.11(b).

In order to examine the effect of the number of sensors on the localization performance, we have repeated the localization with four and two sensors of the lateral line, as shown



(a)

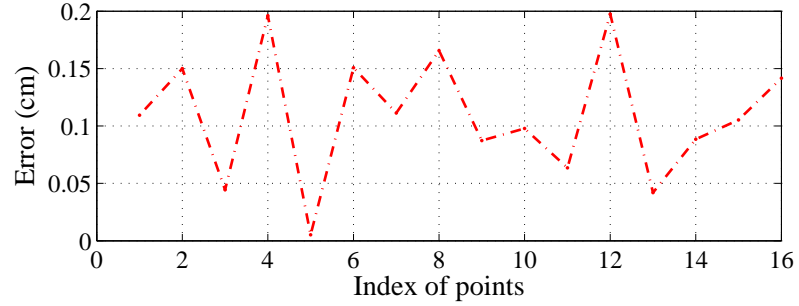


(b)

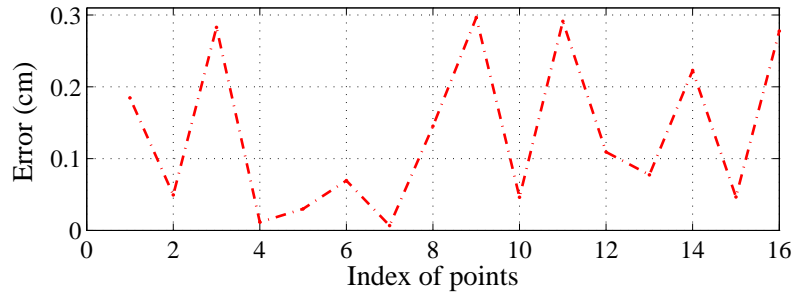
Figure 2.11: Localization of the dipole source using all six sensors of the lateral line: (a) With 90 training points; (b) with 50 training points.

in Figs. 2.13 and 2.14, respectively. In each case, the sensors are taken from the middle section of the lateral line. It is clear that with fewer sensors, the localization error increases.

Fig. 2.15 further shows the maximum and average localization errors when different numbers



(a)



(b)

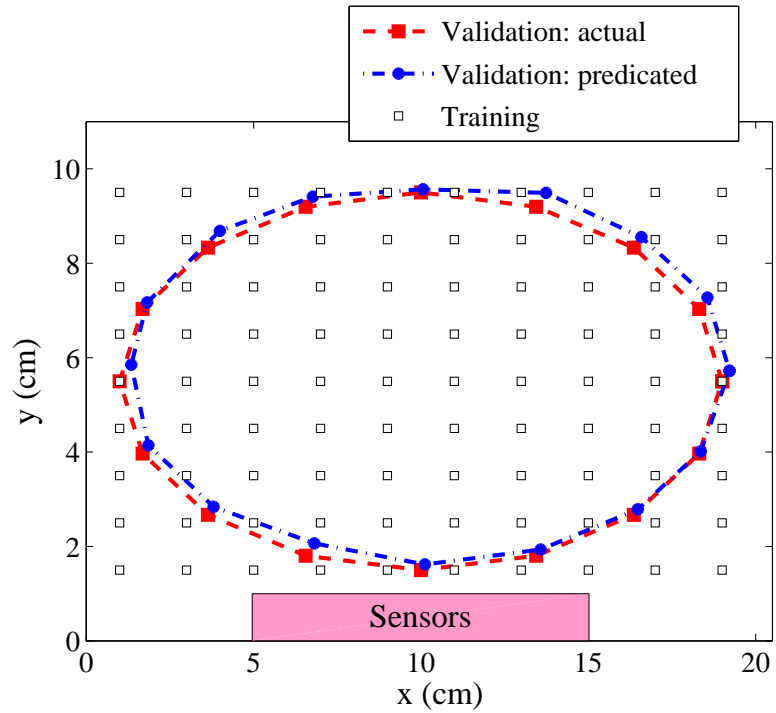
Figure 2.12: Localization error at 16 validation points when all six sensors are used: (a) With 90 training points; (b) with 50 training points.

of sensors and training points are used. From the figure, we can see that the localization performance with four sensors becomes comparable to that with six sensors when the number of training points is quadrupled (from  $2 \times 2 \text{ cm}^2$  lattices to  $1 \times 1 \text{ cm}^2$  lattices). And for two sensors, even with all 180 training points, the maximum localization error is bigger than that with all six sensors when only 25 training points are used.

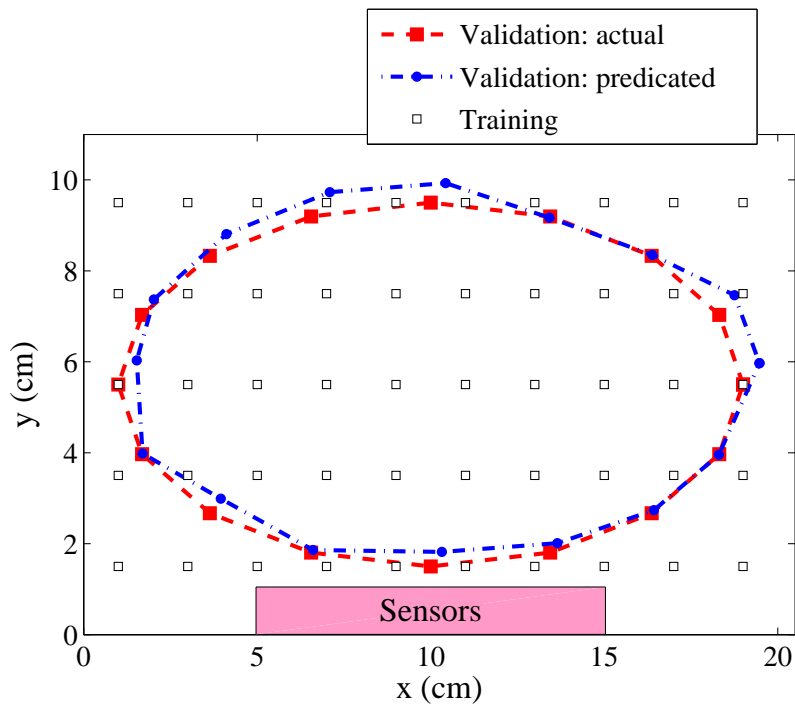
## 2.6 Chapter Summary

In this chapter, we investigated a new approach to the realization of artificial lateral lines for underwater robots and vehicles, including both the proposal of using IPMC materials as

sensing elements and the neural network-based signal processing algorithm. The effectiveness of the proposed approach was validated in experiments involving localization of a dipole source. Experimental results show that the IPMC-based lateral line can localize the dipole source 1-2 BLs away, with a maximum localization error of 0.3 cm, when the data for training the neural network are collected from a grid of 2 cm by 2 cm lattices. The performance of the lateral line using fewer sensors is also studied, and it is found that, with fewer sensors, more training data are needed to achieve a given localization precision. For example, when four sensors are used, it requires training data on a grid of 1 cm by 1 cm lattices to yield the same level of localization accuracy as achieved by six sensors with training data from  $2 \times 2 \text{ cm}^2$  lattices. These results have not only demonstrated the feasibility of using arrays of IPMC sensors as artificial lateral lines, but also provided interesting insight into the tradeoffs in design and implementation.

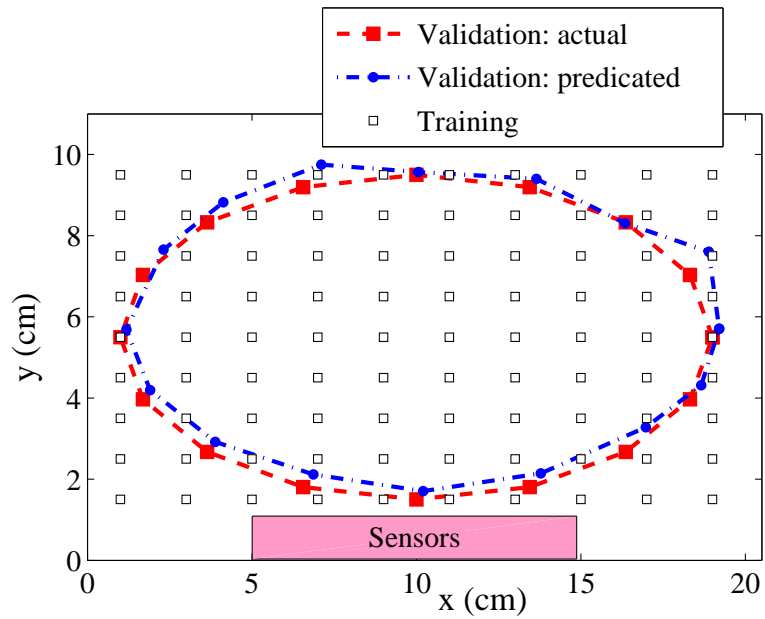


(a)

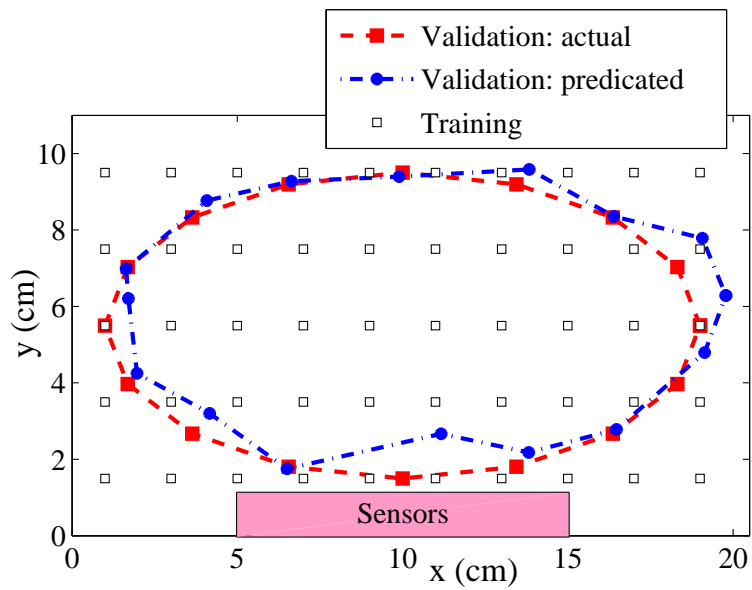


(b)

Figure 2.13: Localization of the dipole source using four sensors of the lateral line: (a) With 90 training points; (b) with 50 training points.

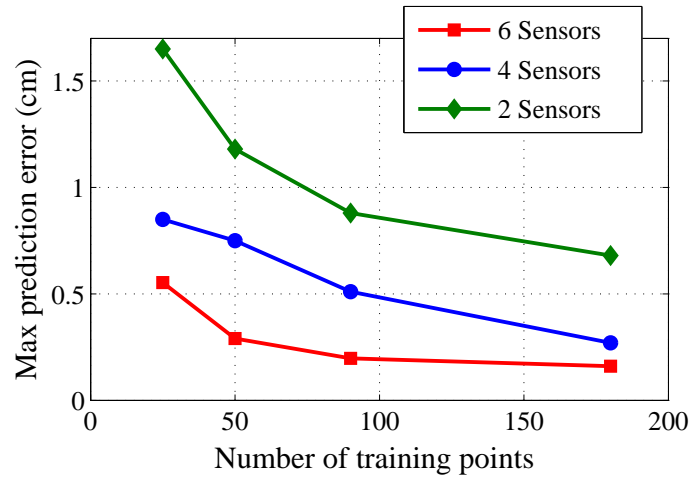


(a)

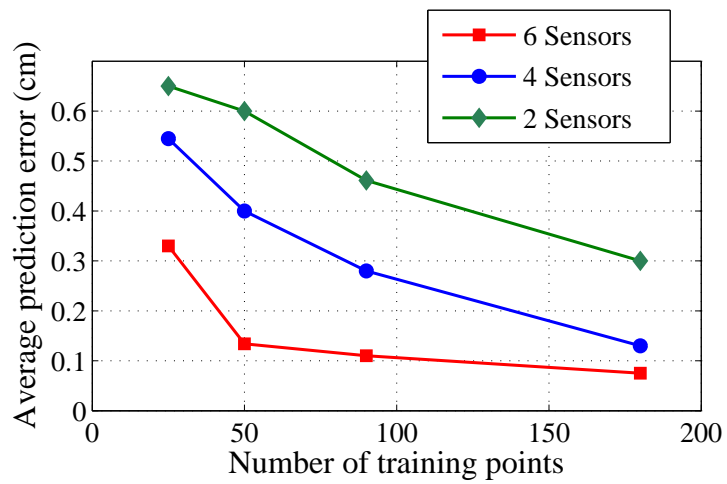


(b)

Figure 2.14: Localization of the dipole source using two sensors of the lateral line: (a) With 90 training points; (b) with 50 training points.



(a)



(b)

Figure 2.15: Error in localization of the dipole source using the lateral line: (a) Maximum error along the track; (b) average error along the track.

## Chapter 3

# Nonlinear Estimation-based Dipole Source Localization

Most existing work deals with a dipole source that has fixed vibration amplitude and orientation. In this chapter we consider the dipole localization problem where both the vibration amplitude and vibration orientation are unknown. When the vibration amplitude is varying, the problem becomes challenging, partly because a source far away but with large vibration and another source nearby but with small vibration could produce signals of similar amplitudes. If we consider the scenario of one fish detecting a predator using its lateral line system, the solution to the aforementioned problem would imply that the fish not only knows where the predator is, but also which way it is swimming toward. There are similar implications for artificial lateral line systems.

To solve these problems, we treat the source location, vibration amplitude, and orientation of vibration axis as unknowns of a nonlinear estimation problem, and then present two recursive algorithms. In the first scheme, we solve a linearized estimation problem with the

Gauss-Newton (GN) method. In the second scheme, we solve the nonlinear equations corresponding to the first-order optimality condition using the Newton-Raphson (NR) method. We will also compare the proposed methods with the beamforming method proposed by [98], which is among the most competitive methods reported in the literature. In this chapter we also exploit the Cramer-Rao Bound (CRB) for the assessment of estimation performance.

The remainder of the chapter is organized as follows. The estimation problem is formulated in Section 3.1. The GN, NR, and beamforming algorithms are described in Section 3.2, along with the CRB analysis. Simulation and experimental results are presented in Section 3.3 and Section 3.4, respectively. Finally, chapter conclusions are provided in Section 3.5.

## 3.1 Problem Formulation

As widely assumed in the literature [46, 39, 43], we consider a potential flow generated by a vibrating sphere, the dipole source. The velocity potential  $\varphi$  at a spatial point can be expressed as [53]

$$\varphi(\mathbf{r}) = \frac{a^3(\mathbf{v}_d \cdot \mathbf{r})}{2\|\mathbf{r}\|^3}, \quad (3.1)$$

where  $a$  is the diameter of vibrating sphere,  $\mathbf{v}_d$  is the instantaneous velocity of the dipole source,  $\mathbf{r}$  represents the relative location of the point of interest with respect to the dipole, and  $\|\cdot\|$  denotes the Euclidean norm of a vector. At the point  $\mathbf{r}$ , the flow velocity  $\mathbf{v}(\mathbf{r})$  is

$$\mathbf{v}(\mathbf{r}) = -\nabla\varphi(\mathbf{r}) = \frac{a^3(3(\mathbf{v}_d \cdot \mathbf{r})\mathbf{r} - \|\mathbf{r}\|^2\mathbf{v}_d)}{2\|\mathbf{r}\|^5}. \quad (3.2)$$

Since our goal in this dissertation is to localize the dipole source, we redefine  $\mathbf{r}$  hereafter as the location of the dipole source with respect to a known point. Note that the formula (3.2) for the dipole-generated velocity field remains valid under the new definition of  $\mathbf{r}$ , because  $\mathbf{v}(-\mathbf{r}) = \mathbf{v}(\mathbf{r})$ .

To ease the discussion, we will focus on the case where the lateral line sensor and the dipole source are located in the same plane (denoted as the  $x - y$  plane) in which the axis of dipole oscillation lies; see Fig. 3.1 for illustration. This is a scenario widely adopted in the study of biological and artificial lateral lines, and our proposed method will extend to the more general, three-dimensional case in a straightforward manner. As depicted in Fig. 3.1, the dipole source is located at  $(x_s, y_s)$  and vibrates with velocity  $v^d$ , where the angle between the vibration axis and the  $x$ -axis is  $\phi$ . Let an array of  $N$  sensors be located in parallel to the  $x$ -axis, with their locations assumed to be known and denoted as  $(x_i, y_i)$ ,  $0 \leq i \leq N - 1$ . We assume that the presence of sensors has negligible effect on the flow distribution as characterized in (3.2); further discussion on sensor-flow interactions will be provided in Subsection 3.4.3. We assume that each sensor is able to provide a noisy measurement of the local flow velocity  $v$  along one direction, which, without loss of generality, is taken to be the  $x$ -direction in this dissertation. The latter consideration is motivated by the fact that most beam-like flow sensors [92, 74, 31, 60, 97, 78, 29, 1] can only sense one component of the flow velocity. In the absence of noise, from (3.2), we get

$$v(x_i, y_i) = \frac{a^3 v^d}{2 \|\mathbf{r}_i\|^5} ((2(x_i - x_s)^2 - (y_i - y_s)^2) \cos \phi + 3(x_i - x_s)(y_i - y_s) \sin \phi), \quad (3.3)$$

where  $\mathbf{r}_i = (x_i - x_s, y_i - y_s)^T$ , with “ $T$ ” denoting the transpose. Let the sphere vibrate

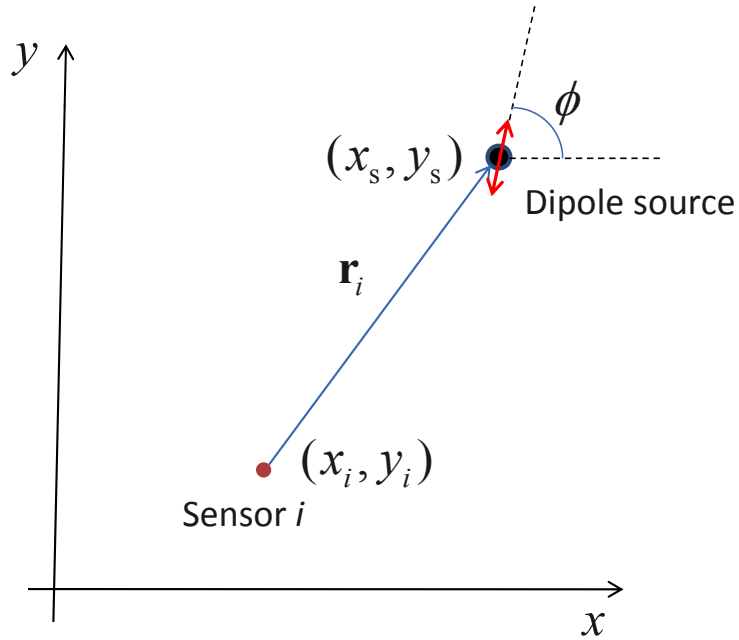


Figure 3.1: Illustration of the problem setup. The dipole source is located at  $(x_s, y_s)$ .

with angular frequency  $\omega$  and amplitude  $A$ , i.e.,

$$v^d = A \sin(\omega t).$$

Furthermore, due to the periodic nature of the dipole-generated flow, we consider extracting the signal amplitude at frequency  $\omega$  from each sensor as the *measurement*. In particular, given the raw signals from time  $n_1$  to  $n_2$ ,  $\{s_i(n)\}_{n=n_1}^{n_2}$ , the signal amplitude at  $\omega$  can be readily obtained through techniques such as fast Fourier transform (FFT) [66] or sliding discrete Fourier transform (SDFT) [44, 82], and this inherent filtering process greatly reduces the noise contained in the raw sensor signal. For sensor  $i$ , the measurement  $M_i$  can then be

written as

$$M_i = \left| \frac{a^3((2(x_i - x_s)^2 - (y_i - y_s)^2)\alpha_1 + 3(x_i - x_s)(y_i - y_s)\alpha_2)}{2\|\mathbf{r}_i\|^5} + d_i \right|, \quad (3.4)$$

where  $\alpha_1 = A \cos \phi$ ,  $\alpha_2 = A \sin \phi$ , and  $d_i$  is the (amplitude) measurement noise for sensor  $i$ . Note that, to accommodate the nonnegativity constraint for the extracted amplitude, we have placed the noise  $d_i$  inside  $|\cdot|$ , since in general the noise could be positive or negative. The noises  $\{d_i\}_{i=0}^{N-1}$  are assumed to have zero means and be uncorrelated with each other.

Based on the sensor measurements, we are interested in estimating the location  $(x_s, y_s)$ , vibration amplitude  $A$ , and vibration direction  $\phi$  of the dipole source. For ease of presentation, for  $i = 0, \dots, N-1$ , define

$$f_i(\theta) = \frac{a^3}{2\|\mathbf{r}_i\|^5}((2(x_i - x_s)^2 - (y_i - y_s)^2)\alpha_1 + 3(x_i - x_s)(y_i - y_s)\alpha_2), \quad (3.5)$$

where  $\theta = (\alpha_1, \alpha_2, x_s, y_s)$  represents the set of parameters to be estimated. Once  $\theta$  is obtained, we can find the vibration amplitude  $A = \sqrt{\alpha_1^2 + \alpha_2^2}$  and vibration orientation  $\phi = \arctan(\alpha_2/\alpha_1)$ . We further define

$$\begin{aligned} M &\triangleq (M_0, \dots, M_{N-1})^T, \\ f(\theta) &\triangleq (f_0(\theta), \dots, f_{N-1}(\theta))^T, \\ d &\triangleq (d_0, \dots, d_{N-1})^T. \end{aligned}$$

We then have

$$M = |f(\theta) + d|, \quad (3.6)$$

where  $|\cdot|$  denotes the component-wise absolute value of the vector. The estimation problem is formulated as follows. Let the dipole diameter  $a$ , frequency  $\omega$ , and the sensor locations  $\{(x_i, y_i)\}_{i=0}^{N-1}$  be known. Given the sensor measurement  $M$ , provide an estimate  $\hat{\theta}$  for the parameter  $\theta$ , such that

$$J(\hat{\theta}) = \left( M - |f(\hat{\theta})| \right)^T \left( M - |f(\hat{\theta})| \right) \quad (3.7)$$

is minimized, where  $|f(\hat{\theta})|$  is the predicted measurement based on the estimated parameters.

Before presenting the estimation algorithms, we briefly comment on the assumptions made on the knowledge of  $a$ ,  $\omega$ , and  $\{(x_i, y_i)\}_{i=0}^{N-1}$ . Clearly, it is natural to assume knowing  $\{(x_i, y_i)\}_{i=0}^{N-1}$ . If the frequency  $\omega$  is not given *a priori*, it can be identified through FFT of the sensor signals and scan to capture the frequency that has a maximum magnitude. Finally, if  $a$  is unknown, one will be able to estimate  $a^3 A$  as a lump parameter, since that is how  $a$  and  $A$  collectively affect the flow field.

## 3.2 Estimation Algorithms

In this dissertation we propose and compare two recursive algorithms to obtain the parameter estimate  $\hat{\theta}$  for minimizing the cost function  $J$  in (3.7). The function  $f(\theta)$  is linear in  $\hat{\alpha}_1$  and  $\hat{\alpha}_2$ , but highly nonlinear in  $(\hat{x}_s, \hat{y}_s)$ . In the first algorithm, briefly summarized in Subsection 3.2.1,  $|f(\theta)|$  is linearized at each intermediate parameter estimate, and the estimate at the next iteration is obtained by solving a standard least-squares problem. This algorithm is also known as the Gauss-Newton method [47]. In the second algorithm, described in Subsection 3.2.2, we first derive the (nonlinear) equation capturing the first-order necessary

condition for minimizing  $J$ , and then solve the equation using the Newton-Raphson method [47].

We will further compare our proposed algorithms experimentally with the beamforming algorithm, which was one of the most competitive algorithms reported for dipole localization [98]. The algorithm will be briefly reviewed in Subsection 3.2.3.

The Cramer-Rao bound (CRB) [25] establishes the lower limit for the variance of any unbiased estimator, and we have conducted CRB analysis for both the optimal design of a lateral line sensor and the evaluation of the proposed algorithms. The CRB analysis is presented in Subsection 3.2.4.

### 3.2.1 Gauss-Newton Algorithm

Linearizing the function  $|f(\hat{\theta})|$  about some nominal point  $\bar{\theta}$ , we have

$$|f(\hat{\theta})| \approx f_{\text{L}}(\hat{\theta}) \triangleq |f(\bar{\theta})| + B(\bar{\theta})(\hat{\theta} - \bar{\theta}), \quad (3.8)$$

where

$$B(\bar{\theta}) = \left. \frac{\partial |f(\theta)|}{\partial \theta} \right|_{\theta=\bar{\theta}}.$$

The estimation problem is then converted to finding  $\hat{\theta}$ , such that

$$J_1(\hat{\theta}) = \left( M - f_{\text{L}}(\hat{\theta}) \right)^T \left( M - f_{\text{L}}(\hat{\theta}) \right)$$

is minimized. This becomes a standard least squares estimation problem, the solution of which is

$$\hat{\theta} = \bar{\theta} + \lambda \left( B(\bar{\theta})^T B(\bar{\theta}) \right)^{-1} B^T(\bar{\theta}) (M - |f(\bar{\theta})|), \quad (3.9)$$

where  $\lambda$  is a stepping parameter. To minimize the impact of error introduced by the linearization, a recursive version of (3.9) is used, where  $\bar{\theta}$  is replaced by the estimate at the previous iteration:

$$\hat{\theta}_{k+1} = \hat{\theta}_k + \lambda \left( B(\hat{\theta}_k)^T B(\hat{\theta}_k) \right)^{-1} B^T(\hat{\theta}_k) (M - |f(\hat{\theta}_k)|), \quad (3.10)$$

with  $\hat{\theta}_1 = \theta_0$ , an initial guess for the parameters. The algorithm is stopped when  $\|\hat{\theta}_{k+1} - \hat{\theta}_k\| \leq \epsilon$ , where  $\epsilon > 0$  is a specified tolerance.

### 3.2.2 Newton-Raphson Algorithm

The necessary condition for minimizing (3.7) is

$$\frac{\partial J}{\partial \hat{\theta}} = 0, \quad (3.11)$$

which implies

$$g(\hat{\theta}) \triangleq \left( \frac{\partial |f|}{\partial \hat{\theta}} \right)^T (M - |f(\hat{\theta})|) = 0. \quad (3.12)$$

An estimate of the parameter  $\theta$  can then be obtained by solving the nonlinear equation (3.12) using the Newton-Raphson method:

$$\hat{\theta}_{k+1} = \hat{\theta}_k - \lambda G^{-1}(\hat{\theta}_k)g(\hat{\theta}_k), \quad (3.13)$$

where  $\lambda$  is stepping parameter, and  $G(\hat{\theta})$  denotes  $\frac{\partial g}{\partial \hat{\theta}}$  and can be evaluated as

$$G(\hat{\theta}) = \sum_{i=0}^{N-1} \left( M_i - |f_i(\hat{\theta})| \right) \frac{\partial^2 |f_i|}{\partial \hat{\theta}^2} - \left( \frac{\partial |f_i|}{\partial \hat{\theta}} \right)^T \left( \frac{\partial |f_i|}{\partial \hat{\theta}} \right).$$

The starting value  $\hat{\theta}_1$  in (3.13) is set to be  $\theta_0$ , an initial guess of the parameters. Similar to the Gauss-Newton method, the iteration in (3.13) is stopped when  $\|\hat{\theta}_{k+1} - \hat{\theta}_k\| \leq \epsilon$  for a prespecified  $\epsilon$ .

### 3.2.3 Beamforming Algorithm

The beamforming algorithm based on Capon's method was used by Yang *et al.* to estimate a five-dimensional (5D) dipole state (3D location and 2D vibration orientation) [98]. In our dipole localization setup, the dipole state is fully captured by the 4D parameter vector  $\theta$ . Given the raw sensor signals for instantaneous flow velocities (projected into the sensing axes), denoted as  $\{s_0(n), \dots, s_{N-1}(n)\}_{n=n_1}^{n_2}$ , one constructs an energy-like map  $E(\hat{\theta})$ , which indicates how likely the actual dipole state is  $\hat{\theta}$ . The optimal estimate of  $\theta$  is then obtained as

$$\hat{\theta}^* = \arg \max_{\hat{\theta}} E(\hat{\theta}). \quad (3.14)$$

In order to evaluate  $E(\hat{\theta})$ , one first evaluates the correlation matrix  $R$  based on the

measurements from all sensors:

$$R = \frac{1}{n_2 - n_1} \sum_{n=n_1}^{n_2} S(n)S^T(n),$$

where  $S(n) = [s_0(n), s_1(n), \dots, s_{N-1}(n)]^T$ . The energy-like function  $E$  is then computed as

$$E(\hat{\theta}) = \frac{1}{|f(\hat{\theta})|^T R^{-1} |f(\hat{\theta})|}. \quad (3.15)$$

To search for the maximizing  $\hat{\theta}$  for  $E$ , one typically scans through the space for the dipole state [98]. The latter involves creating a discrete grid of dipole state components, and the resulting total number of grid points increases exponentially with the dimension of the dipole state.

### 3.2.4 Cramer-Rao Bound Analysis

Consider (3.4). For the Cramer-Rao bound (CRB) analysis, we assume that the noise  $d_i$  from each sensor is Gaussian with zero mean and variance  $\sigma_m^2$ . Given the dipole state  $\theta$ , the probability for the sensors to have the measurement  $M = (M_0, \dots, M_{N-1})^T$  is expressed as

$$P(M, \theta) = \prod_{i=0}^{N-1} \frac{1}{(2\pi\sigma_m^2)^{1/2}} \left( e^{\frac{-1}{2\sigma_m^2}(M_i - f_i(\theta))^2} + e^{\frac{-1}{2\sigma_m^2}(-M_i - f_i(\theta))^2} \right), \quad (3.16)$$

$$= \prod_{i=0}^{N-1} \frac{2}{(2\pi\sigma_m^2)^{1/2}} \left( e^{\frac{-M_i^2}{2\sigma_m^2}} e^{\frac{-f_i^2(\theta)}{2\sigma_m^2}} \cosh \frac{M_i f_i(\theta)}{\sigma_m^2} \right). \quad (3.17)$$

The log-likelihood function is then

$$\begin{aligned} \ln P(M, \theta) &= N \frac{2}{(2\pi\sigma_m^2)^{1/2}} - \frac{1}{2\sigma_m^2} \sum_{i=0}^{N-1} M_i^2 - \frac{1}{2\sigma_m^2} \sum_{i=0}^{N-1} f_i^2(\theta) \\ &\quad + \sum_{i=0}^{N-1} \ln \left( \cosh \frac{M_i f_i(\theta)}{\sigma_m^2} \right). \end{aligned} \quad (3.18)$$

Taking the first derivative,

$$\frac{\partial \ln P(M, \theta)}{\partial \theta} = \frac{1}{\sigma_m^2} \sum_{i=0}^{N-1} \left\{ -f_i(\theta) \frac{\partial f_i(\theta)}{\partial \theta} + \tanh \left( \frac{M_i f_i(\theta)}{\sigma_m^2} \right) M_i \frac{\partial f_i(\theta)}{\partial \theta} \right\},$$

and consequently,

$$\begin{aligned} \frac{\partial^2 \ln P(M, \theta)}{\partial \theta^2} &= \frac{1}{\sigma_m^2} \sum_{i=0}^{N-1} \left\{ -f_i(\theta) \frac{\partial^2 f_i(\theta)}{\partial \theta^2} - \left[ \frac{\partial f_i(\theta)}{\partial \theta} \right] \left[ \frac{\partial f_i(\theta)}{\partial \theta} \right]^T \right. \\ &\quad + \tanh \left( \frac{M_i f_i(\theta)}{\sigma_m^2} \right) M_i \frac{\partial^2 f_i(\theta)}{\partial \theta^2} + \frac{M_i^2}{\sigma_m^2} \left[ \frac{\partial f_i(\theta)}{\partial \theta} \right] \left[ \frac{\partial f_i(\theta)}{\partial \theta} \right]^T \\ &\quad \left. \times \left[ 1 - \tanh^2 \frac{M_i f_i(\theta)}{\sigma_m^2} \right] \right\}. \end{aligned} \quad (3.19)$$

Taking the negative expectation on (3.19) results in

$$\begin{aligned}
& - \mathbf{E} \left\{ \frac{\partial^2 \ln P(M, \theta)}{\partial \theta^2} \right\} = -\frac{1}{\sigma_m^2} \mathbf{E} \left\{ \sum_{i=0}^{N-1} \left\{ -f_i(\theta) \frac{\partial^2 f_i(\theta)}{\partial \theta^2} - \left[ \frac{\partial f_i(\theta)}{\partial \theta} \right] \left[ \frac{\partial f_i(\theta)}{\partial \theta} \right]^T \right. \right. \\
& \quad \left. \left. + \tanh \left( \frac{M_i f_i(\theta)}{\sigma_m^2} \right) M_i \frac{\partial^2 f_i(\theta)}{\partial \theta^2} + \frac{M_i^2}{\sigma_m^2} \left[ \frac{\partial f_i(\theta)}{\partial \theta} \right] \left[ \frac{\partial f_i(\theta)}{\partial \theta} \right]^T \right. \right. \\
& \quad \left. \left. \left[ 1 - \tanh^2 \frac{M_i f_i(\theta)}{\sigma_m^2} \right] \right\} \right\} \\
& = \frac{1}{\sigma_m^2} \sum_{i=0}^{N-1} \left\{ f_i(\theta) \frac{\partial^2 f_i(\theta)}{\partial \theta^2} + \left[ \frac{\partial f_i(\theta)}{\partial \theta} \right] \left[ \frac{\partial f_i(\theta)}{\partial \theta} \right]^T \right. \\
& \quad \left. - \mathbf{E} \left\{ \tanh \left( \frac{M_i f_i(\theta)}{\sigma_m^2} \right) M_i \frac{\partial^2 f_i(\theta)}{\partial \theta^2} + \frac{M_i^2}{\sigma_m^2} \left[ \frac{\partial f_i(\theta)}{\partial \theta} \right] \left[ \frac{\partial f_i(\theta)}{\partial \theta} \right]^T \right. \right. \\
& \quad \left. \left. \left[ 1 - \tanh^2 \frac{M_i f_i(\theta)}{\sigma_m^2} \right] \right\} \right\},
\end{aligned}$$

The Fisher information matrix  $I(\theta)$  can then be derived as

$$\begin{aligned}
I(\theta) & = -\mathbf{E} \left[ \frac{\partial^2 \ln P(M; \theta)}{\partial \theta^2} \right] \\
& = \frac{1}{\sigma_m^2} \sum_{i=0}^{N-1} \left\{ f_i(\theta) \frac{\partial^2 f_i(\theta)}{\partial \theta^2} + \left[ \frac{\partial f_i(\theta)}{\partial \theta} \right] \left[ \frac{\partial f_i(\theta)}{\partial \theta} \right]^T \right. \\
& \quad \left. - \int_{M_i=0}^{\infty} g_i(M_i, \theta) P_i(M_i, \theta) dM_i \right\}, \tag{3.20}
\end{aligned}$$

where  $\mathbf{E}[\cdot]$  denotes the expectation,

$$\begin{aligned}
g_i(M_i, \theta) & \triangleq \tanh \left( \frac{M_i f_i(\theta)}{\sigma_m^2} \right) M_i \frac{\partial^2 f_i(\theta)}{\partial \theta^2} \\
& \quad + \frac{M_i^2}{\sigma_m^2} \left[ \frac{\partial f_i(\theta)}{\partial \theta} \right] \left[ \frac{\partial f_i(\theta)}{\partial \theta} \right]^T \left[ 1 - \tanh^2 \frac{M_i f_i(\theta)}{\sigma_m^2} \right], \tag{3.21}
\end{aligned}$$

$$P_i(M_i, \theta) = \frac{1}{(2\pi\sigma_m^2)^{1/2}} \left\{ e^{\frac{-1}{2\sigma_m^2}(M_i - f_i(\theta))^2} + e^{\frac{-1}{2\sigma_m^2}(-M_i - f_i(\theta))^2} \right\}. \tag{3.22}$$

Note that  $I^{-1}(\theta)$  represents the lower bound (CRB) on the estimation variance for any unbiased estimator of  $\theta$ ; specifically, the variance of the  $j$ -th component of  $\hat{\theta}$ , denoted as  $\hat{\theta}_{[j]}$ , satisfies

$$\text{Var}(\hat{\theta}_{[j]}) \geq \left[ I^{-1}(\theta) \right]_{j,j}, \quad j = 1, \dots, 4. \quad (3.23)$$

In Section 3.3, we will illustrate the use of (3.23), with  $j = 1, 2$ , for the optimal design of a lateral line sensor (with given vibration amplitude and orientation) and for the localization performance evaluation of the proposed estimation algorithms. Appendix A provides the first and second derivatives of the  $f_i(\cdot)$ .

### 3.3 Simulation Results

#### 3.3.1 CRB-based Optimal Design of Lateral Line Sensor

The CRB analysis presented in Subsection 3.2.4 can be used for the optimal design of a lateral line system, including both the number of flow sensors and the geometric arrangement of these sensors. The latter point is illustrated here with an example of optimizing the intra-sensor spacing, which is later adopted in the construction of an experimental prototype. We consider a working area of  $20 \times 10 \text{ cm}^2$  ( $-10 \leq x \leq 10, 0 < y \leq 10$ ), and assume that the lateral line consists of 6 flow sensors, uniformly distributed along the  $x$ -axis and centered at the origin. We would like to determine the sensor-to-sensor spacing that minimizes the localization error, in a sense that will be described next.

Additional parameters for the optimization problem, largely motivated by our experimental setup, include sphere diameter  $a = 1.9 \text{ cm}$ , vibration axis angle  $\phi = 0^\circ$ , vibration frequency 40 Hz, and vibration amplitude  $A = 0.191 \text{ cm}$ . In order to ensure good lo-

calization performance when the dipole is at different locations within the working area, we divide the area into a grid of  $1 \times 1 \text{ cm}^2$  cells, resulting in a total of 210 grid points ( $x = 0, \pm 1, \dots, \pm 10, y = 1, 2, \dots, 10$ ). For a given intra-sensor spacing, for each grid point  $(x(k), y(k))$ ,  $1 \leq k \leq 210$ , we evaluate the corresponding CRBs  $C_x(k)$  and  $C_y(k)$  for the estimation variances  $\sigma_x^2(k)$  and  $\sigma_y^2(k)$ , assuming that the dipole is located at  $(x(k), y(k))$ . Note that  $C_x(k)$  and  $C_y(k)$  represent the minimum uncertainty in estimating  $x(k)$  and  $y(k)$ , respectively. There are two potential ways to define a single quantity characterizing the localization uncertainty. The first criterion is based on the so-called D-optimality [30] and it represents the area of the ellipsoidal region of maximum confidence and can be evaluated using the determinant of the corresponding  $2 \times 2$  sub-matrix of  $I^{-1}(\theta)$ . This criterion could be misleading, especially when the ellipsoidal region is thin. Therefore, we have adopted an alternative based on A-optimality and capture the bound on the localization uncertainty using  $U(k) = \pi (C_x(k) + C_y(k))$ . The cumulative uncertainty for a given intra-sensor spacing is then obtained as  $U_c = \sum_k U(k)$ . Fig. 3.2 shows the cumulative uncertainty  $U_c$  as a function of the intra-sensor spacing, for three different noise variances  $\sigma_m^2$  for the measurement noise. Here  $m_1 = 0.0065 \text{ cm}^2/\text{s}^2$  represents a typical value of variance for our IPMC prototype flow sensors. It is clear that there is an optimal range (around 2 cm) for the intra-sensor distance where the cumulative localization uncertainty is minimized. Larger or smaller spacing leads to bigger uncertainty. This can be explained as follows. When the sensors are too packed, they cannot pick up sufficiently distinct signals (think about the extreme case of all sensors stacked together) and cannot cover a wide area with large signal-to-noise ratio. On the other hand, when the sensors are very far apart, some sensors become too distant from the dipole source and their signal-to-noise ratios become very low, negatively impacting the localization

performance. Another interesting observation from Fig. 3.2 is that, the optimal intra-sensor spacing is not sensitive to the value of the noise variance. This is a positive news for the design, since it is often difficult to know the precise value of  $\sigma_m^2$  in practice.

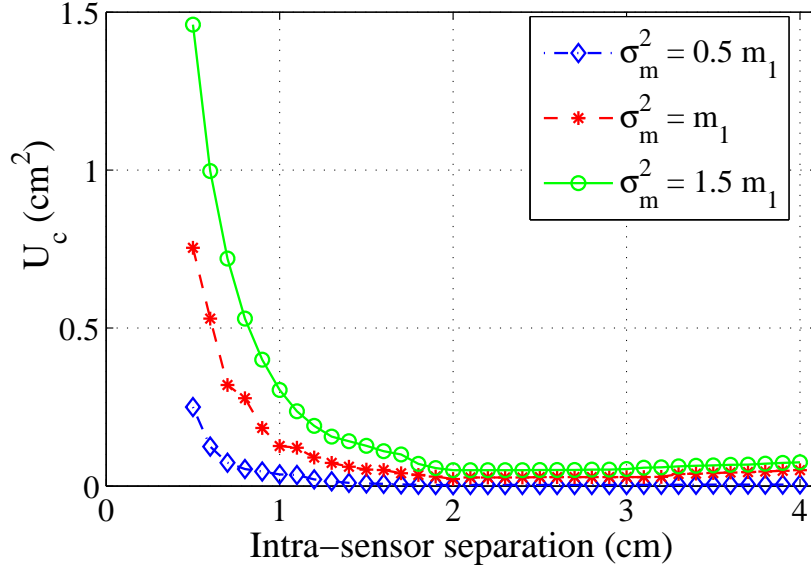


Figure 3.2: CRB-based cumulative uncertainty in localization as a function of intra-sensor spacing.

### 3.3.2 Localization of Dipole Source with Unknown Vibration Amplitude and Orientation

We now present simulation results on the performance of the proposed Gauss-Newton and Newton-Raphson schemes on localizing a dipole source with unknown vibration amplitude and orientation. Fig. 3.3 illustrates the simulation setup. The lateral line system, consisting of 6 flow sensors with intra-sensor spacing of 2 cm, is placed parallel to the  $x$ -axis and centered at the origin. The dipole source is placed at 19 different locations along an ellipsoidal

track that is centered at (0, 6) cm. Specifically, the dipole locations are prescribed by

$$(x_s(k), y_s(k)) = (10 \cos \psi(k), 6 + 4 \sin \psi(k)), \quad k = 1, 2, \dots, 19, \quad (3.24)$$

where  $\psi(k) = \frac{(k-1)\pi}{9}$ . Note that point 1 and point 19 overlap, as shown in Fig. 3.3. In order to test the algorithms' capability in estimating vibration amplitude  $A$  and orientation  $\phi$  in addition to the source location, we vary  $A$  (in cm) and  $\phi$  along the track as follows:

$$A(k) = 0.191 - 0.01(k - 1), \quad (3.25)$$

$$\phi(k) = \frac{(k - 1)\pi}{9}. \quad (3.26)$$

The sphere diameter  $a$ , vibration frequency, and the measurement noise variance  $\sigma_m^2$  are set to be 1.9 cm, 40 Hz, and  $m_1$  ( $0.0065 \text{ cm}^2/\text{s}^2$ ), respectively. The stopping criterion  $\epsilon$  for both the Gauss-Newton algorithm and the Newton-Raphson algorithm is chosen to be 0.01.

Fig. 3.4(a) shows the actual and estimated source locations under the Gauss Newton (GN) method and the Newton Raphson (NR) method for a typical run. It can be seen the localization is well accomplished under both schemes. Furthermore, Fig. 3.4(b) shows the localization error for each of the 19 points on the track, where the error is defined as the Euclidean distance between the actual and estimated locations. The two proposed methods have comparable performance in terms of the localization error. The maximum error under the GN method is 0.38 cm and that under the NR method is 0.39 cm.

Fig. 3.5 shows the estimated source vibration amplitudes and the estimation errors for both methods. The maximum amplitude error is 0.0013 cm and 0.0015 cm for the GN and NR methods, respectively. Fig. 3.6 shows the estimated source vibration orientations and

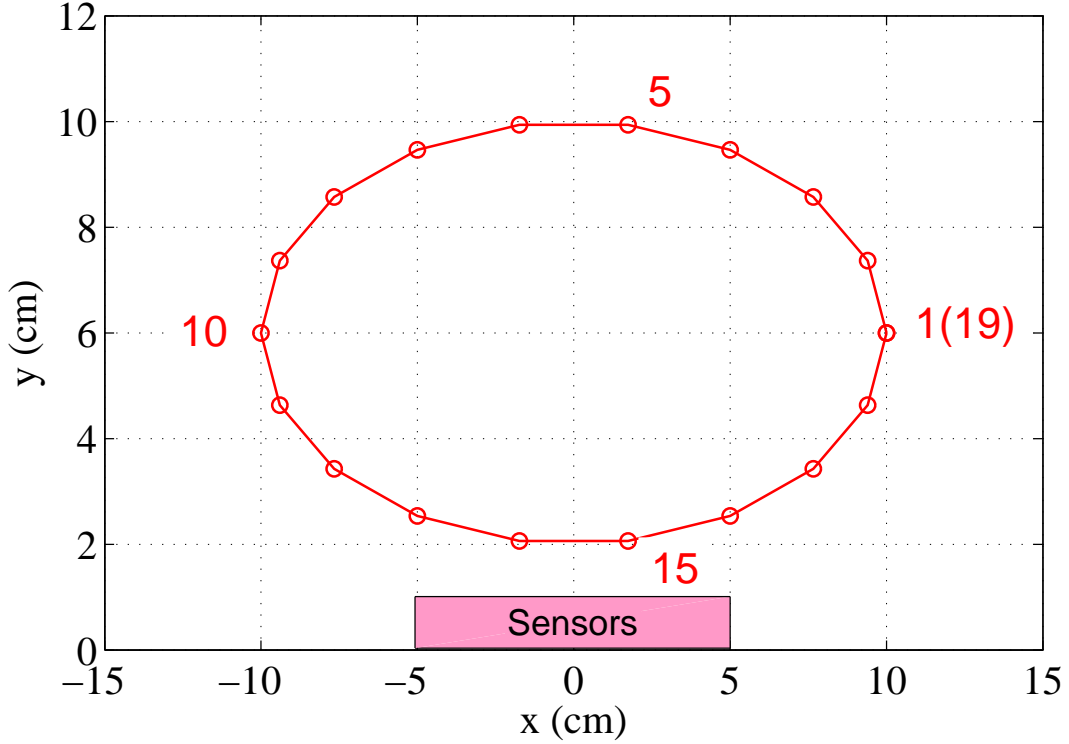


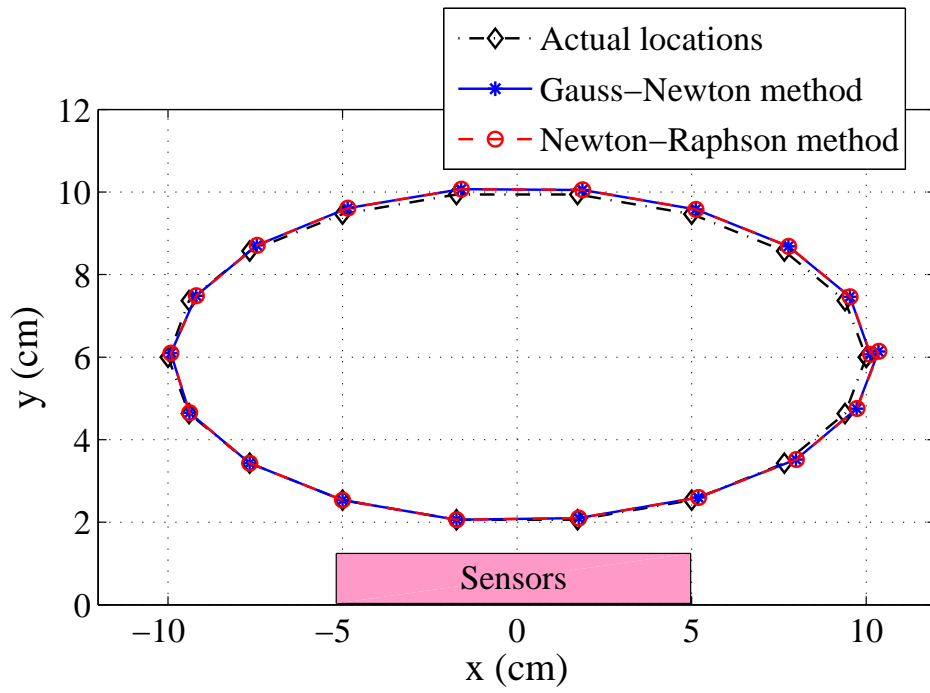
Figure 3.3: Illustration of the simulation setup, where 19 points as indexed in the figure will be localized.

the corresponding errors. The maximum orientation error is 0.12 rad and 0.13 rad for the GN and NR methods, respectively.

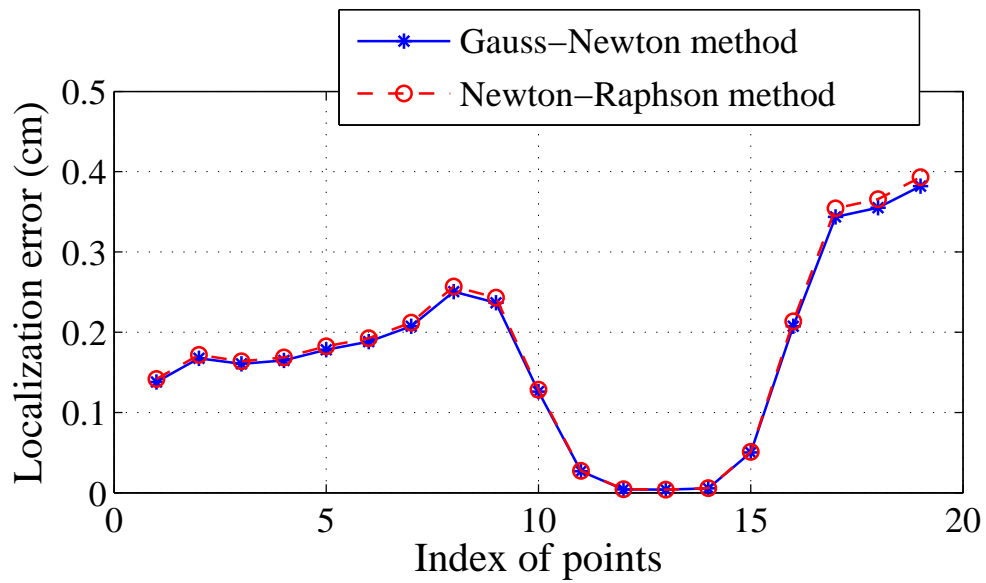
From Figs. 3.4, 3.5, and 3.6, we can see that both the GN and NR methods are able to simultaneously estimate the location, vibration amplitude, and vibration orientation successfully. In addition, while the GN method has slightly higher estimation accuracy for all variables, the overall performances of the two methods are quite close.

### 3.3.3 Further CRB Analysis on Performance

We have further used the CRB analysis to evaluate the localization performance of our proposed methods. In this evaluation, a similar setup as in Subsection 3.3.2 is considered,



(a)



(b)

Figure 3.4: Simulation results: (a) Estimation of source locations; (b) localization errors at the 19 points.

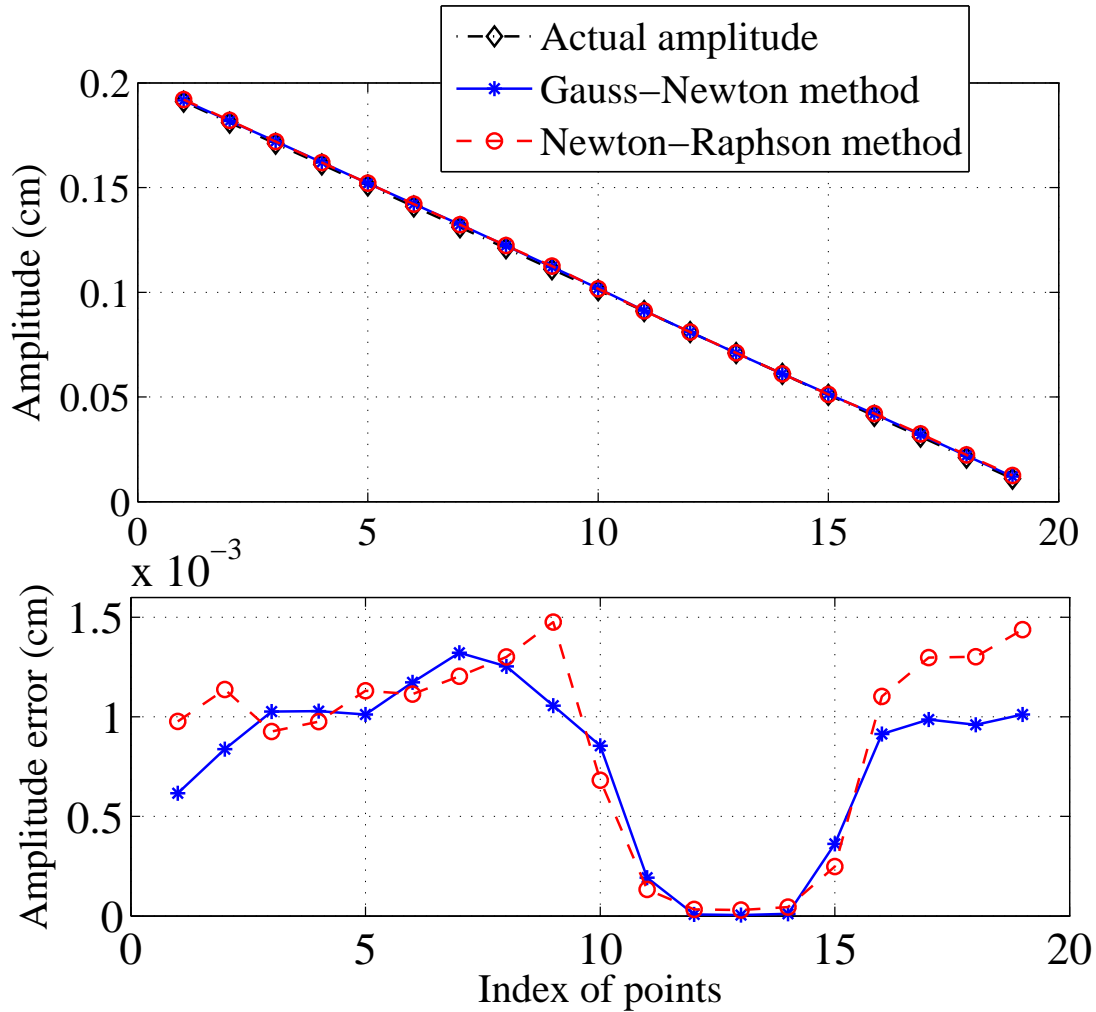


Figure 3.5: Simulation results: Estimation of the source vibration amplitudes.

except that we fix the vibration amplitude and orientation at all points to be 0.191 cm and  $0^\circ$ , respectively, and treat them as known. We run the simulation of localizing the 19 points using the GN and NR algorithms for 20 times, based on which the empirical estimation variances  $\sigma_x^2$  and  $\sigma_y^2$  for  $x_s$  and  $y_s$  are obtained. Fig. 3.7 shows the comparison of the square-roots of empirical variances with the corresponding CRBs. It is clear that the CRBs are lowest when the source location is closest to the lateral line (points # 13–16), which is explained the highest signal-to-noise ratio (SNR) at those locations. The empirical

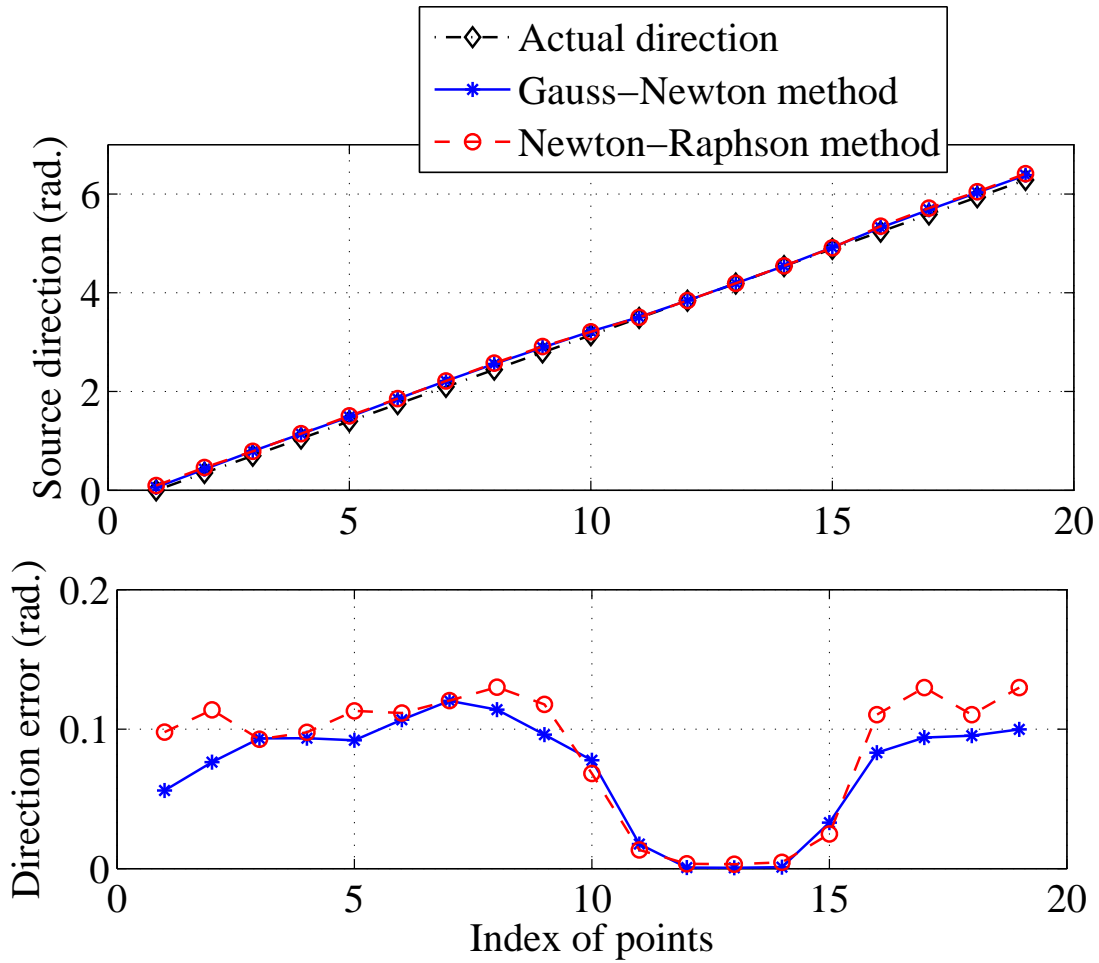
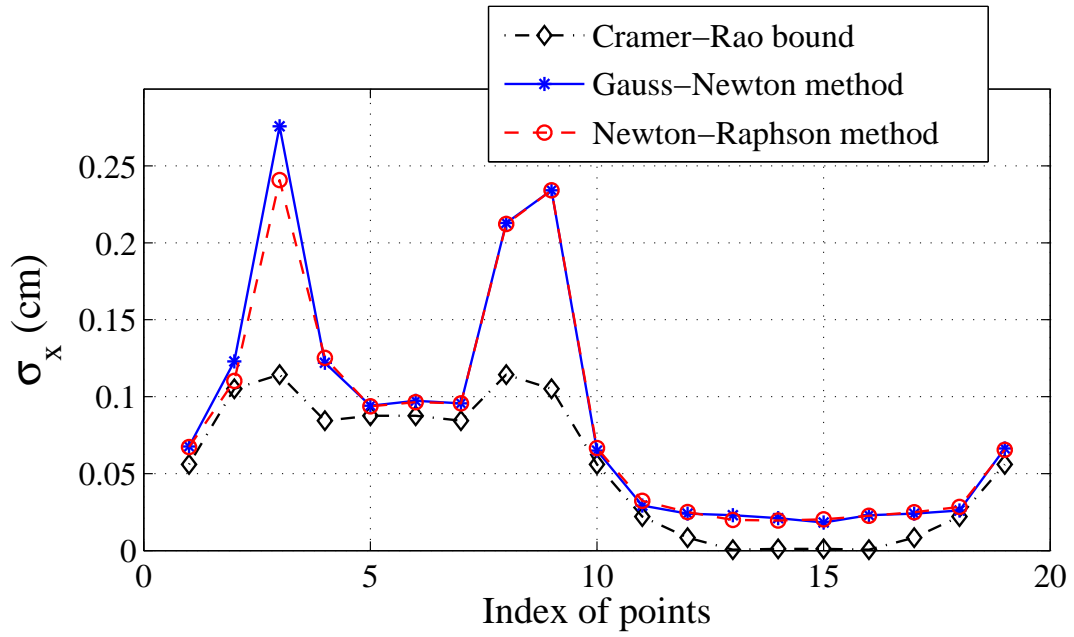
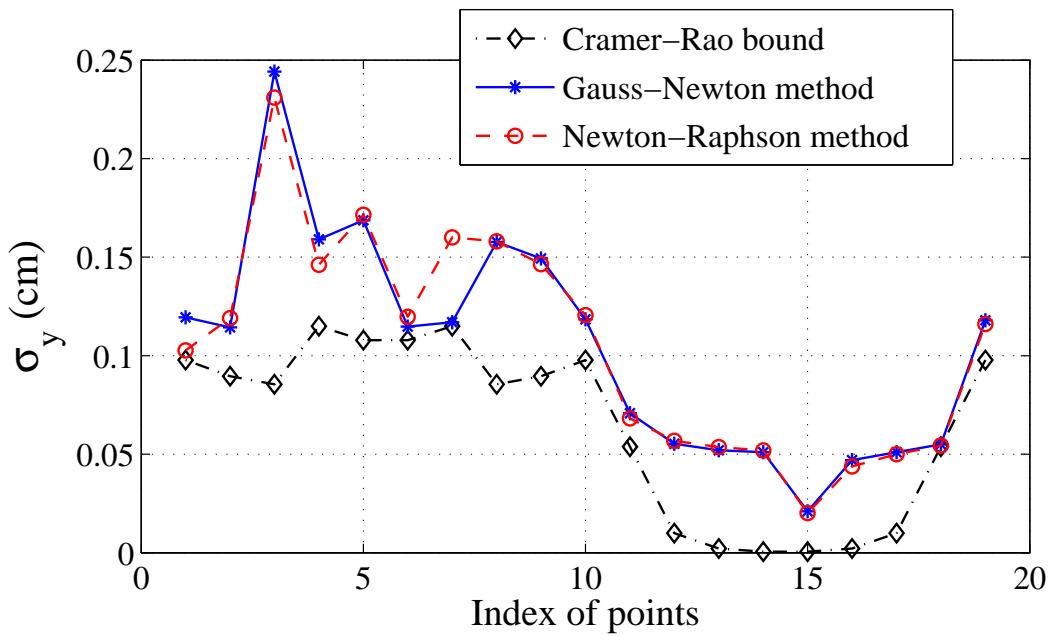


Figure 3.6: Simulation results: Estimation of the source vibration orientations.

estimation variances under both schemes are higher than the CRBs; however, the differences are not big, especially at the points where the SNR is large. This analysis confirms that the proposed GN and NR schemes deliver close-to-optimal estimation performance.



(a)



(b)

Figure 3.7: Simulation results: Comparison of square-root of empirical estimation variances (a)  $\sigma_x$  and (b)  $\sigma_y$  with the corresponding CRBs.

## 3.4 Experimental Setup and Flow Model Verification

### 3.4.1 Experimental Setup

We have experimentally examined the performance of the proposed GN and NR algorithms and the beamforming algorithm reported in the literature, using an artificial lateral line prototype consisting of six ionic polymer-metal composite (IPMC) sensors, shown in Fig. 2.4. An IPMC has three layers, with an ion-exchange polymer membrane sandwiched by metal electrodes. Inside the polymer, (negatively charged) anions covalently fixed to polymer chains are balanced by mobile, (positively charged) cations. Deformation under a mechanical perturbation redistributes the cations, producing a detectable electric signal (e.g., short-circuit current) that is well correlated with the mechanical stimulus, which explains the sensing principle of an IPMC [81]. Each sensor in our lateral line prototype, measuring 8 mm long, 2 mm wide, and 200  $\mu\text{m}$  thick, was cut from an IPMC sheet fabricated by the Smart Microsystems Laboratory at Michigan State University, following a recipe similar to the one described in [49]. Based on the optimization results from CRB analysis (Subsection 3.2.4), the intra-sensor separation was set to be 2 cm, resulting in a total span of 10 cm for the sensor. The latter can be considered as the Body Length (BL) of the lateral line system, and we will test its capability in localizing a dipole source within a distance of about one BL, which is the typical working range for biological lateral lines. All sensors can bend in the direction that is parallel to the lateral line, thus measuring the flow component in the same direction.

Fig. 3.8(a) illustrates the experimental setup. Experiments are conducted in a tank that is 6 feet long, 2 feet wide, and 2 feet deep. The short-circuit current output of each

IPMC sensor is amplified with a two-stage amplification circuit, the details of which can be found in [35]. Acquisition and processing of the IPMC sensor output are conducted through a dSPACE system (DS1104, dSPACE Inc., Germany). A digital low-pass filter is further implemented to remove high-frequency noises from the sensor signals. The dipole source is created with a mini-shaker (Model 4810, Brüel & Kjaer, Denmark)(Fig. 2.6(b)), the vibration amplitude and frequency of which can be readily controlled through a voltage input to the mini-shaker. A lightweight bar firmly attached to the mini-shaker then translates the vibration to a sphere rigidly coupled to the bar. The sphere, which is a aluminum ball, has a diameter of 1.9 cm. The sphere and the IPMC sensors are submerged underwater, about 5 cm from the water surface. The dipole source location and vibration direction with respect to the IPMC lateral line can be adjusted by moving the stand holding the IPMC lateral line. The dipole frequency is chosen to be 40 Hz, which is in the typical range for the study of biological and artificial lateral lines. The vibration amplitude of the sphere is measured with a laser displacement sensor (OADM 20I6441/S14F, Baumer Electric).

### 3.4.2 Flow Model Validation

The basis of our estimation algorithms is the analytical model (3.5) for a dipole source-generated flow field. It is thus of interest to examine the validity of this model experimentally. The validation has been conducted using a digital particle image velocimetry (DPIV) system (LaVision, Ypsilanti, MI). In a DPIV system, small particles are dispersed in a fluid and a laser sheet is created in the fluid to illuminate the particles. Processing of images taken in quick successions can reveal the movement of particles and thus provide information about the flow field.

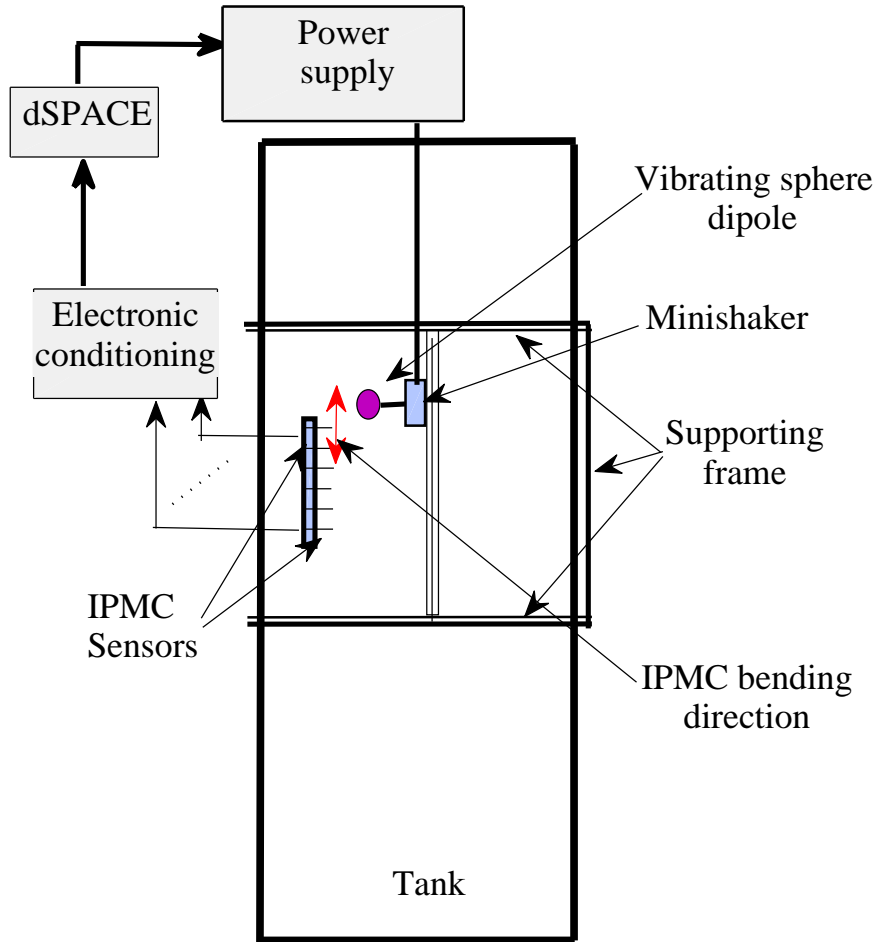


Figure 3.8: Experimental setup: Schematic of the experimental system.

We measured the  $x$ -component of the flow velocity at the origin when a dipole source, enabled with a slightly different mechanism from that in Fig. 3.8(b) [3], was placed at eight different locations:  $(\pm 1.5, 1.5)$  cm,  $(\pm 3, 1.5)$  cm,  $(\pm 1.5, 3)$  cm, and  $(\pm 3, 3)$  cm. Since the DPIV system has a measurement frequency of 15 Hz, we have obtained the velocity amplitude by taking the maximum measurement over a sufficiently long period (over 10 s). Fig. 3.9 shows the comparison of the DPIV measurement with the prediction from the theoretical model (3.5). As can be seen, the match between the model and the experimental

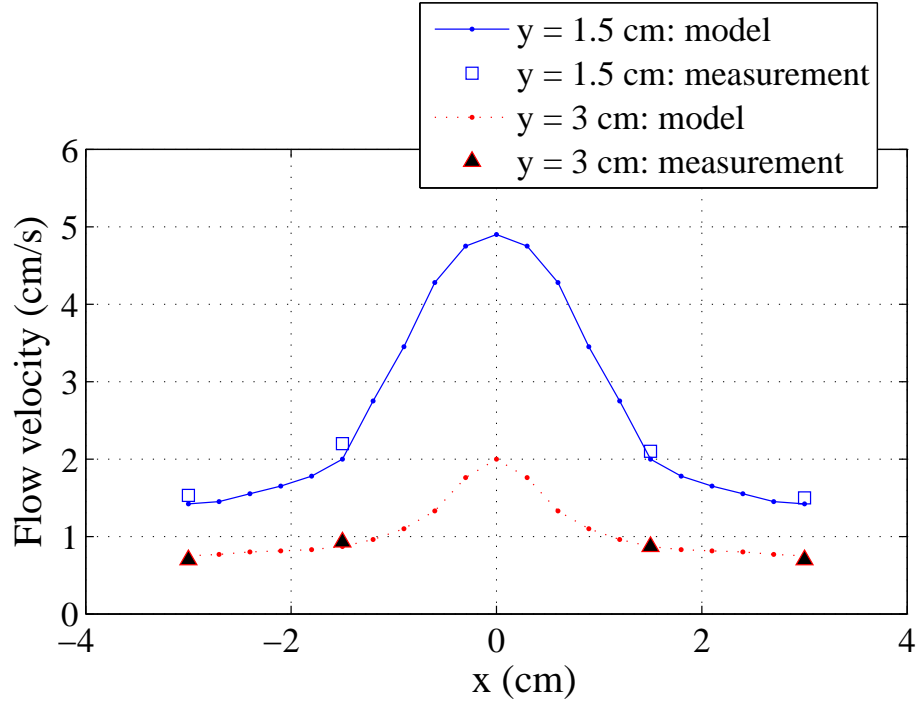


Figure 3.9: Experimental results: Comparison of DPIV-measured flow velocity with the model prediction.

measurement is good, with the maximum error being 0.2 cm/s among the eight sampled points.

### 3.4.3 Calibration of IPMC Sensors

The relationship between the current output  $I$  of an IPMC sensor and the local flow velocity  $v$  can be captured by the cascaded connection of fluid-structure interaction dynamics  $G_1$  and IPMC transduction dynamics  $G_2$ , both of which can be treated as linear when the flow is relatively small. The dynamics  $G_1$  describes how the tip displacement  $q$  of the sensor beam responds to the flow  $v$ , and can be modeled following the approach presented by McHenry *et al.* in modeling the interactions between a superficial neuromast and the ambient flow [61].

The dynamics  $G_2$ , on the other hand, relates the current output  $I$  to the tip displacement  $q$  and can be captured with a physics-based model [16]. It can be shown that, based on the physical parameters for the IPMC sensors and the operating frequency in our experiments, the transfer function  $G_1(s)$  can be approximated by [61]

$$G_1(s) = \frac{q(s)}{v(s)} = \frac{c_1}{s}, \quad (3.27)$$

and  $G_2$  by [13]

$$G_2(s) = \frac{I(s)}{q(s)} = c_2 s, \quad (3.28)$$

where  $s$  is the Laplace variable, and  $c_1$  and  $c_2$  are lumped physical constants. The detailed derivation and approximation of  $G_1$  and  $G_2$  are explained earlier in Chapter 2.

From (3.27) and (3.28), the short-circuit current output of an IPMC sensor is (approximately) proportional to the instantaneous local flow velocity. The proportionality constant can vary from sensor to sensor because of the spatial inhomogeneity in the fabricated IPMC material, difference in exact sensor dimensions, and discrepancy across different channels of the sensing circuit. The constant is identified through a calibration procedure described next. We put the mini-shaker-based dipole source at different locations with respect to each sensor and extracted the amplitude of sensing current with FFT. The theoretical value of the flow velocity at the location of the sensor was obtained using (3.5). Fig. 3.10 shows the IPMC signal amplitude versus the theoretical local velocity for one IPMC sensor, from which an approximately linear relationship between the sensor output  $I$  and the flow velocity  $v$  parallel to the lateral line can be observed. The proportional constant  $\eta = \frac{I}{v}$  is identified

using the Matlab command `polyfit(·, ·, 1)`.

The proportionality constants identified for the six IPMC sensors are  $\eta_1 = 0.49 \mu\text{A}/(\text{cm} \cdot \text{s}^{-1})$ ,  $\eta_2 = 0.21 \mu\text{A}/(\text{cm} \cdot \text{s}^{-1})$ ,  $\eta_3 = 0.165 \mu\text{A}/(\text{cm} \cdot \text{s}^{-1})$ ,  $\eta_4 = 0.23 \mu\text{A}/(\text{cm} \cdot \text{s}^{-1})$ ,  $\eta_5 = 0.24 \mu\text{A}/(\text{cm} \cdot \text{s}^{-1})$ , and  $\eta_6 = 0.3 \mu\text{A}/(\text{cm} \cdot \text{s}^{-1})$ . Given  $\eta_i$ , the flow velocity at the site of sensor  $i$  is calculated from the sensor output  $I_i$  via

$$v_i = \frac{I_i}{\eta_i}.$$

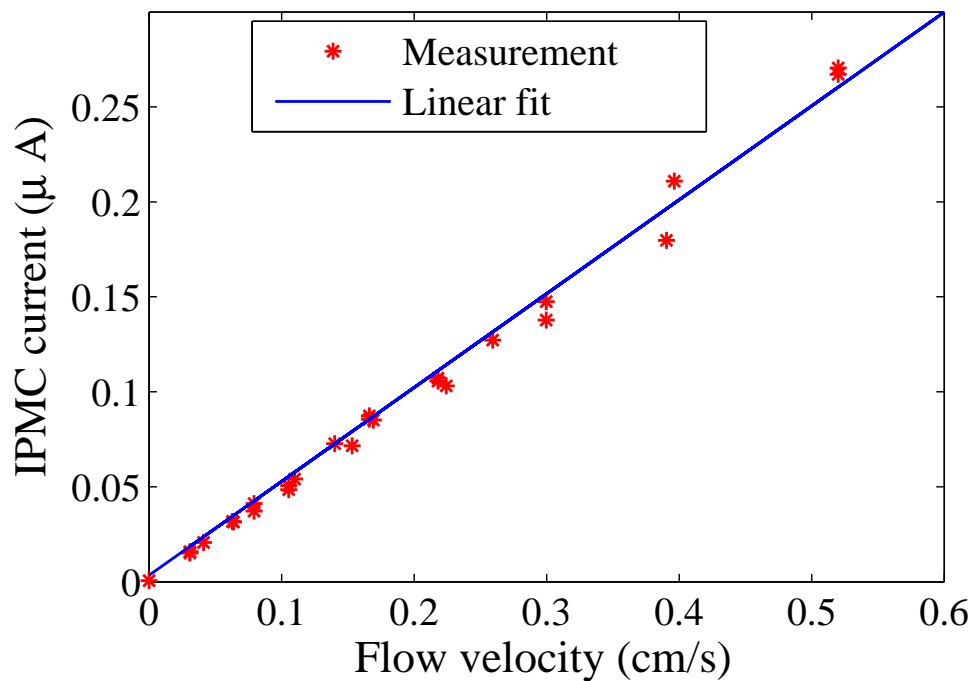


Figure 3.10: Illustration of IPMC sensor calibration.

### 3.4.4 Experimental Results on Dipole Source Localization

We have conducted localization experiments in a very similar setup as for the simulation (see Fig. 3.3). Specifically, we have placed the dipole source (relative to the lateral line) at 19 points along an ellipsoidal track centered at (0, 6) cm, as prescribed by (3.24). The vibration amplitude at each point varies according to (3.25). Due to the difficulty in precisely orienting the dipole vibration axis, we have chosen to use only two different orientations, 0 and  $\frac{\pi}{2}$  rad.

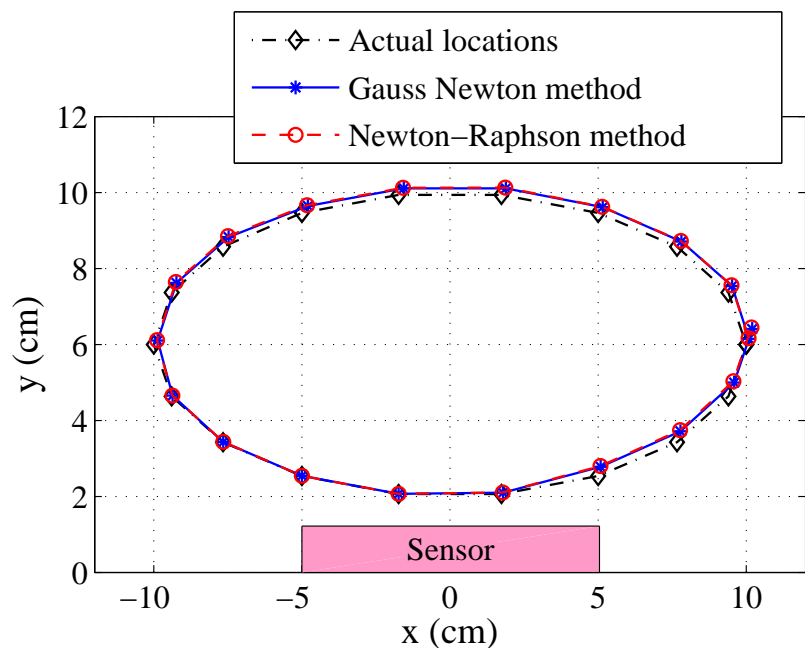
In particular, we set

$$\phi(k) = \begin{cases} 0, & k = 1, \dots, 10 \\ \frac{\pi}{2}, & k = 11, \dots, 19 \end{cases}$$

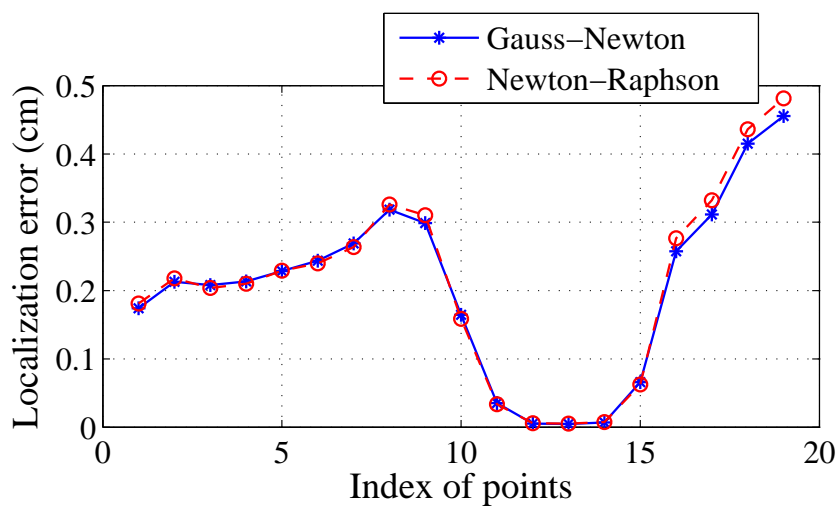
For each location, sensor outputs of 10 s are acquired at a sampling rate of 1 kHz. FFT is performed on the data to extract the signal amplitudes, which are then used for estimation with the GN and NR methods. For comparison purposes, the same (raw) sensor data have been used for estimation using the beamforming algorithm; see the description in Subsection 3.2.3.

Fig. 3.11 shows the experimental results on the localization. It is notable that the localization performance has only slightly degraded from that in simulation (Fig. 3.4). The maximum localization errors for the GN and NR methods are 0.46 cm and 0.48 cm, respectively, which occur at point #19, where the vibration amplitude is the smallest. Fig. 3.12(a) and (b) show the estimated source vibration amplitudes and source vibration directions at the 19 points. For both methods, the maximum errors in the amplitude estimation are around 0.002 cm, about 50% larger than those in simulation. The maximum errors in the orientation estimation are around 0.12 rad, which are almost the same as those in simulation; this might be explained by the fact that only two different orientations were tested in the

experiments. Another observation is that, in consistency with the simulation results, the GN method has demonstrated slightly better performance than the NR method.



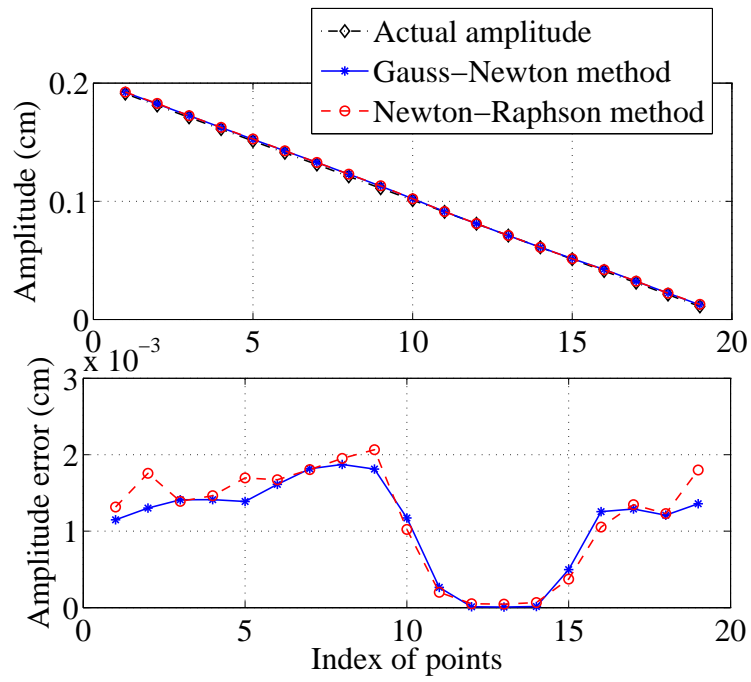
(a)



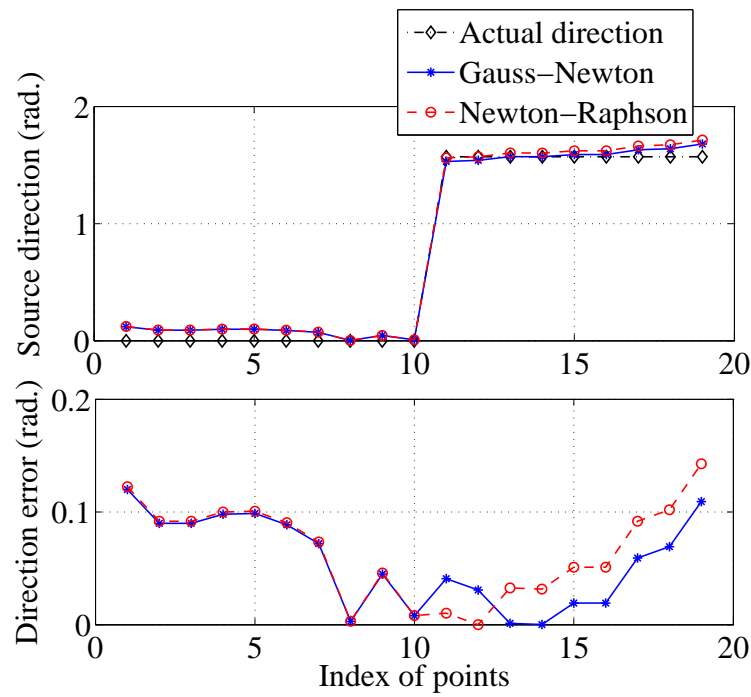
(b)

Figure 3.11: Experimental results: (a) Estimation of source locations; (b) localization errors at the 19 points.

We have further examined the performance of the beamforming algorithm on the same



(a)



(b)

Figure 3.12: Experimental results: (a) Estimation of the source vibration amplitudes; (b) estimation of the source vibration orientations.

data. In order to create the energy-like map for each dipole state, one needs to discretize the space for the dipole state (location, vibration amplitude, and vibration orientation). Clearly, the resolution of the discretization has a direct impact on the estimation performance; a finer grid is expected to produce more accurate resolution (sharper map), but at the cost of computational time. To ease the computation, we have assumed that the vibration amplitude and orientation at each location are known, and thus focused on only the estimation of source location. We have used three different resolutions for discretizing the working area,  $0.02 \times 0.02 \text{ cm}^2$ ,  $0.05 \times 0.05 \text{ cm}^2$ , and  $0.1 \times 0.1 \text{ cm}^2$ . The dipole location is estimated by visually finding the maximum of the energy-like map. As an illustration, Fig. 3.13 shows the energy-like map when the dipole source was placed at point #3, with the  $0.1 \times 0.1 \text{ cm}^2$  discretization grid, where the peak is clearly visible.

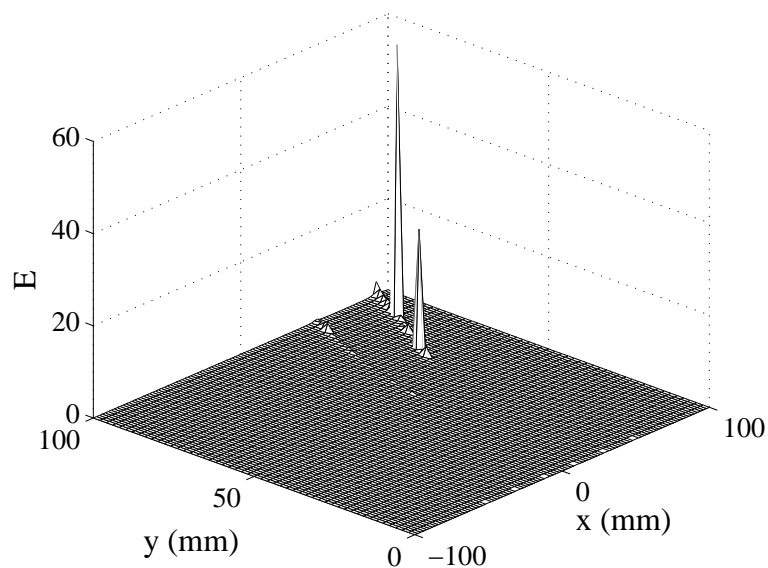


Figure 3.13: Experimental results: Constructed energy-like map when the dipole is located at point #3 ( $0.1 \times 0.1 \text{ cm}^2$  grid).

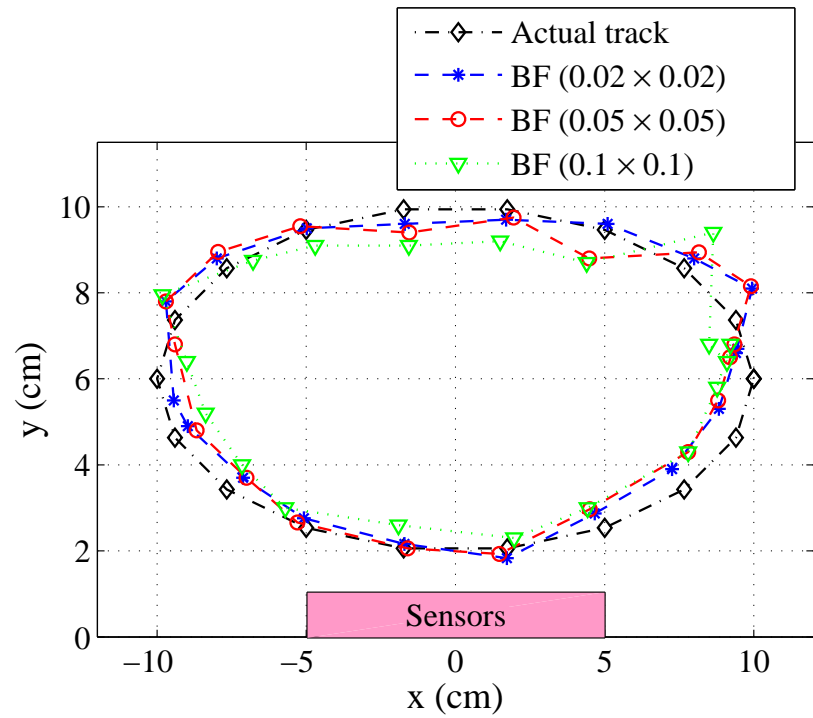
Fig. 3.14 shows the localization results corresponding to the three discretization schemes

Table 3.1: Experimental results: maximum and average estimation errors under different algorithms. “BF (0.02)” stands for beamforming with  $0.02 \times 0.02$  cm<sup>2</sup> grid, and similar interpretations apply for “BF (0.05)” and “BF (0.1)” . Note that vibration amplitude and orientation are assumed known for the BF algorithms.

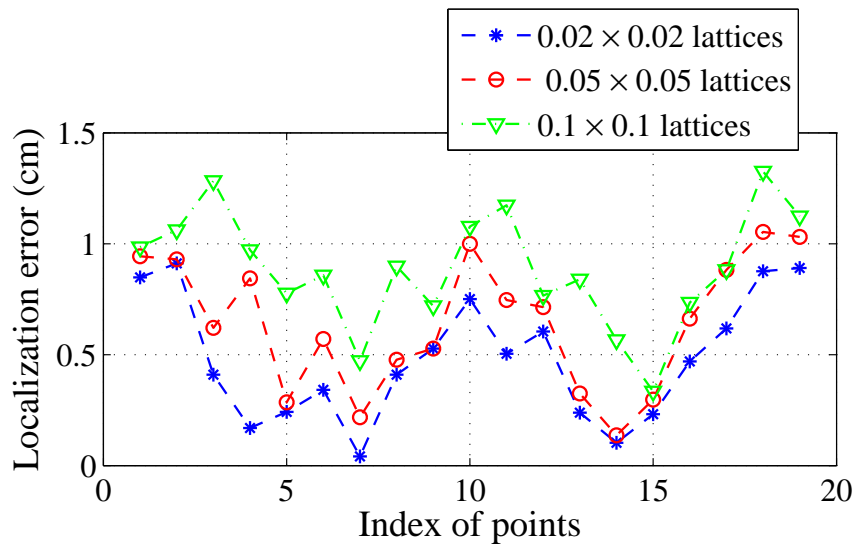
Algorithms	GN	NR	BF (0.02)	BF (0.05)	BF (0.1)
Average localization error (cm)	0.21	0.21	0.48	0.65	0.89
Max. localization error (cm)	0.46	0.48	0.91	1.1	1.33
Average amplitude error (cm)	0.0014	0.0014	-	-	-
Max. amplitude error (cm)	0.0019	0.0021	-	-	-
Average orientation error (rad)	0.1	0.1	-	-	-
Max. orientation error (rad)	0.12	0.14	-	-	-

under the beamforming approach. As one would expect, the localization error decreases as the grid gets finer; however, the error does not scale linearly with the grid resolution. The maximum localization errors for the three discretization schemes (finer to coarser) are 0.91 cm, 1.1 cm, and 1.33 cm, respectively. For a more clear comparison, Table 3.1 summarizes the average and maximum localization errors for the 19 points, for the Gauss-Newton (GN), Newton-Raphson (NR), and three beamforming (BF) algorithms. It can be seen that, with the finest grid ( $0.02 \times 0.02$  cm<sup>2</sup>), the BF algorithm results in an average/maximum localization error that is twice as much as what is resulted from the GN and NR algorithms.

To put the comparison in perspective, we have further recorded the computation time taken by each algorithm. All algorithms have been run on Samsung laptop with a 2.53 GHz processor and 4 GB RAM. The localization problem at all 19 points is executed under each algorithm for seven times, and Table 3.2 summarizes the average time per point taken by each algorithm. Note that for GN and NR, the computation includes FFT and executing the recursive update until convergence, and for the beamforming algorithm, the computation



(a)



(b)

Figure 3.14: Experimental results: Localization of the dipole source using the beamforming algorithm: (a) Estimation of the source locations; (b) localization errors at the 19 points.

Table 3.2: Average computational time per localization point for different algorithms.

Algorithms	Average time (s)
GN	1.1
NR	1.2
BF ( $0.02 \times 0.02 \text{ cm}^2$ )	11.2
BF ( $0.05 \times 0.05 \text{ cm}^2$ )	2.1
BF ( $0.1 \times 0.1 \text{ cm}^2$ )	1.26

includes evaluating the correlation matrix and constructing the energy-like map. From Table 3.2, it can be seen that GN is slightly more efficient than NR. With a discretization grid of  $0.02 \times 0.02 \text{ cm}^2$ , the beamforming algorithm takes a comparable amount of computation time as GN or NR; however, from Table 3.1, the corresponding maximum localization error is three times as much. Considering that the GN and NR algorithms simultaneously estimate four variables while the beamforming algorithm only does two (in this setup), we can conclude that the proposed GN and NR algorithms are more accurate and computationally efficient than the beamforming algorithm. One likely reason that the beamforming algorithm produces larger estimation error is the noise in the raw signals from IPMC sensors, which would have a lesser impact for the GN and NR schemes because of the FFT procedure.

### 3.5 Chapter Summary

In this chapter, using the analytical model for a dipole-generated flow field, we formulate a nonlinear estimation problem and present two novel iterative schemes for simultaneously localizing a dipole source and estimating its vibration amplitude and orientation. The first scheme, which is based on the Gauss-Newton (GN) method, solves the nonlinear estimation problem through iterative linearization. In the second scheme, the Newton-Raphson (NR)

method is used to solve the nonlinear equation resulting from the first-order optimality condition. The flow model, with measurement noise properly incorporated, is also used to derive the Cramer-Rao bound (CRB). Analysis based on the CRB is subsequently exploited for the optimal design of intra-sensor spacing of the lateral line. Simulation is conducted to localize a dipole source placed at different points along an ellipsoidal track, with its vibration amplitude and orientation varying from one point to next. Simulation results have shown that both the GN and NR algorithms are able to simultaneously estimate the source location, vibration amplitude and orientation with comparable precision. Furthermore, the comparison with the CRB shows that the algorithms achieve near-optimal performance at many points.

We have further validated the algorithms using an experimental prototype of lateral line that is comprised of six millimeter-scale ionic polymer-metal composite (IPMC) flow sensors. With excellent agreement with the simulation results, the experimental results confirm that the GN and NR schemes have comparable performance in accuracy and computational efficiency with the GN scheme having a slight advantage. Specifically, for the body length (BL) of 10 cm, the maximum localization error is less than 5% of BL when the source is within the distance of one BL. Experimental results have also shown that the proposed schemes are superior to the beamforming method; when the beamforming method is only required to determine the dipole location (with vibration amplitude/orientation given), its maximum (average, resp.) localization error is three (four, resp.) times of those under the GN and NR schemes while consuming comparable computing time.

# Chapter 4

## Localization of a Moving Dipole

### Source

Existing studies on artificial lateral lines (ALLs) have been mostly focused on the localization of a fixed underwater vibrating sphere (dipole source). In this chapter we introduce a novel analytical model for the problem of localizing a moving dipole source using an ALL. Such a moving source could represent a swimming fish or robotic fish, which demonstrates a combination of translational motion and oscillatory body/fin motion.

First, we formulate a nonlinear estimation problem based on an analytical model for the moving dipole-generated flow field, where we assume that the source location, vibration amplitude, and moving speed are unknown. We also assume that the amplitudes of the flow velocities at the DC and dipole vibration frequencies are available. Such amplitudes can be obtained by conducting sliding digital Fourier transform (SDFT) of the measured signal in the time domain. The estimation problem is solved recursively with the Gauss-Newton method, and we illustrate the proposed approach with simulation and experimental results.

The remainder of the chapter is organized as follows. The localization of the traveling dipole source is formulated in Section 4.1. The sliding discrete Fourier transformation algorithm is described in Section 4.2, and the Gauss-Newton recursive estimation algorithm is presented in Section 4.3. Simulation and experimental results are presented in Section 4.4 and Section 4.5, respectively. Finally, concluding remarks are provided in Section 4.6.

## 4.1 Localization of a Traveling Dipole Source: Problem Formulation

We now formulate the problem of localizing a moving dipole source in the two-dimensional  $x - y$  plane. Consider Fig. 4.1, where an ALL comprising  $N$  sensors is located in parallel to the  $x$ -axis, with the sensor locations denoted as  $(x_i, y_i)$ ,  $0 \leq i \leq N - 1$ . We denote the location of a dipole source at time  $t$  by  $(x_s(t), y_s(t))$ . The source is assumed to move with a constant speed  $v_m$  parallel to the ALL, and vibrating with a velocity  $v^d$  with the vibration axis perpendicular to the ALL. We further assume that the presence of sensors has negligible effect on the flow distribution generated by the moving source. Each sensor is assumed to provide a (noisy) measurement of the local flow velocity  $v$  along the  $x$ -direction.

Under an assumption of ideal flows, the flow velocity ( $x$ -component) at the site of sensor  $i$  can be derived as [53]

$$v(x_i, y_i, t) = \frac{a^3}{2\|\mathbf{r}_i(t)\|^5} \left( (2(x_i - x_s(t))^2 - (y_i - y_s(t))^2)v_m + 3(x_i - x_s(t))(y_i - y_s(t))v^d(t) \right), \quad (4.1)$$

where  $\mathbf{r}_i(t) = (x_s(t) - x_i, y_s(t) - y_i)^T$ ,  $a$  represents the radius of the sphere, and  $T$  denotes

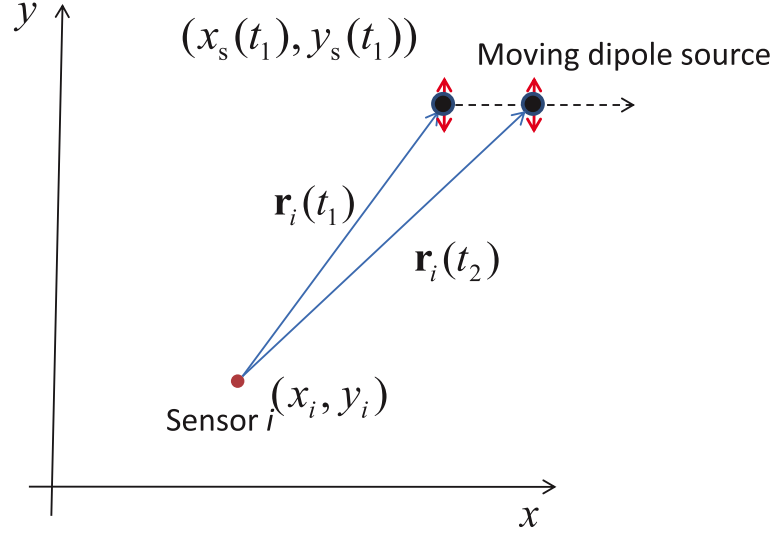


Figure 4.1: Illustration of the problem setup for the localization of a moving dipole source.

the transpose. Assume that the sphere vibrates with angular frequency  $\omega$  and amplitude  $A$ :

$$v^d(t) = A \sin(\omega t).$$

When the source location  $(x_s(t), y_s(t))$  is changing relatively slowly with respect to the dipole motion  $v^d(t)$ , Eq. (4.1) can be viewed as the sum of a constant term and an oscillatory term, corresponding to the source translation and vibration motions, respectively. Denote the amplitudes of the two terms as  $m_{1,i}$  and  $m_{2,i}$ , respectively; namely,

$$m_{1,i} \triangleq \frac{a^3}{2\|\mathbf{r}_i\|^5} (2(x_i - x_s)^2 - (y_i - y_s)^2) v_m, \quad (4.2)$$

$$m_{2,i} \triangleq \frac{a^3}{2\|\mathbf{r}_i\|^5} (3(x_i - x_s)(y_i - y_s)A), \quad (4.3)$$

where  $\theta = (v_m, A, x_s, y_s)$  represents the set of parameters to be estimated. Note that  $\theta$  will have a dependence on  $t$  since the source location  $(x_s(t), y_s(t))$  changes over time, the

magnitude of these components namely  $f_{1,i} = |m_{1,i}|$ , and  $f_{2,i} = |m_{2,i}|$ . We assume that noise-corrupted measurements of  $m_{1,i}$ ,  $m_{2,i}$ ,  $i = 0, 1, \dots, N-1$ , are available:

$$\begin{aligned}\hat{m}_{1,i} &= |m_{1,i} + d_{1,i}|, \\ \hat{m}_{2,i} &= |m_{2,i} + d_{2,i}|,\end{aligned}$$

where  $d_{1,i}$  and  $d_{2,i}$  are noises associated with the sensor  $i$ . We assume the noises  $\{d_{1,i}, d_{2,i}\}_{i=0}^{N-1}$  are of zero mean and not correlated with each other. We further define

$$\begin{aligned}m_1 &\triangleq (m_{1,0}, \dots, m_{1,N-1})^T, \\ m_2 &\triangleq (m_{2,0}, \dots, m_{2,N-1})^T, \\ \hat{m}_1 &\triangleq (\hat{m}_{1,0}, \dots, \hat{m}_{1,N-1})^T, \\ \hat{m}_2 &\triangleq (\hat{m}_{2,0}, \dots, \hat{m}_{2,N-1})^T, \\ f_1(\theta) &\triangleq (f_{1,0}(\theta), \dots, f_{1,N-1}(\theta))^T, \\ f_2(\theta) &\triangleq (f_{2,0}(\theta), \dots, f_{2,N-1}(\theta))^T,\end{aligned}$$

The estimation problem is formulated as follows. Let the sphere diameter  $a$ , the sensor locations  $\{(x_i, y_i)\}_{i=0}^{N-1}$ , and the frequency  $\omega$  be known. Given the sensor measurements  $\hat{m}_1$  and  $\hat{m}_2$  at the time  $t$ , provide an estimate of the parameter  $\theta(t)$ ,  $\hat{\theta}(t) = (\hat{v}_m, \hat{A}, \hat{x}_s(t), \hat{y}_s(t))$ , such that

$$J(\hat{\theta}) = \beta(\hat{m}_1 - f_1(\hat{\theta}))^T(\hat{m}_1 - f_1(\hat{\theta})) + (1 - \beta)(\hat{m}_2 - f_2(\hat{\theta}))^T(\hat{m}_2 - f_2(\hat{\theta})) \quad (4.4)$$

is minimized, where  $\beta \in [0, 1]$  is a parameter weighing the importance of the DC term relative to the oscillatory term.

## 4.2 The Sliding Discrete Fourier Transform (SDFT)

### Algorithm

Since the actual sensor output is a discrete-time signal, discrete Fourier transform (DFT) can be used to extract the signal amplitudes at different frequencies. However, because the target is moving, the amplitudes  $m_1$  and  $m_2$  evolve with the time index  $n$  and it is thus not practical to collect a large sequence of sensor data and perform DFT to extract the measurements  $\hat{m}_1$  and  $\hat{m}_2$ . The SDFT algorithm [44, 82] is particularly suitable for computing a specific spectral bin in real-time application based on a sliding window of time samples. For this reason, the SDFT algorithm has been adopted to compute the two frequency components of interest in this paper.

For a window of  $M$  time samples,  $\{x[n - (M - 1)], \dots, x[n]\}$ , we can evaluate the  $p$ -th spectral bin using DFT:

$$X_p[n] = \sum_{i=0}^{M-1} x[n - M + 1 + i] e^{-2j\pi pi/M}, \text{ for } 0 \leq p \leq M - 1. \quad (4.5)$$

Recall (4.1). In our target localization problem, there are two frequencies that are of interest, the DC signal (spectral bin  $p = 0$ ) and the signal with angular frequency  $\omega$  (spectral bin  $p = \left\lceil \frac{\omega M}{2\pi F_s} \right\rceil$ ), where  $\lceil \cdot \rceil$  denotes rounding to the nearest integer and  $F_s$  is the sampling frequency for obtaining sensors signals  $x[\cdot]$ . Exploiting the fact that all elements but one in neighboring windows are identical, the SDFT algorithm can efficiently evaluate  $X_p[n]$

recursively:

$$X_p[n] = e^{-j\omega_0}(X_p[n-1] - x[n-N] + x[n]), \quad (4.6)$$

where  $\omega_0 = 2\pi p/M$ .

For  $p = 0$ , from (4.5), we can see that  $X_0[n]$  essentially sums up the  $M$  signal samples in the window. Consequently, the magnitude of the DC component for  $\{x[\cdot]\}$  is  $\frac{|X_0[n]|}{M}$ . For the AC component ( $p = \left\lceil \frac{\omega M}{2\pi F_s} \right\rceil$ ) is given as

$$\begin{aligned} X_p[n] &= \sum_{i=0}^{M-1} m_2 \sin(\omega_0(n - M + 1 + i)) e^{-2j\pi p i/M} \\ &= \frac{m_2 e^{-j\omega_0(M-n)}}{2j} \sum_{i=0}^{M-1} (1 - e^{-2j\omega_0 i}) \\ &= \frac{m_2 e^{-j\omega_0(M-n)}}{2j} \left( M - \left( \frac{1 - e^{-2j\omega_0 M}}{1 - e^{-2j\omega_0}} \right) \right) \\ &= \frac{m_2 e^{-j\omega_0(N-n)}}{2j} M \end{aligned} \quad (4.7)$$

where  $e^{-2j\omega_0 M} - 1 = 0$ , because  $p$  is an integer number. Taking the norm for both sides:

$$|X_p[n]| = \left| \frac{m_2 M}{2} \right| \quad (4.8)$$

Then, the corresponding AC component is

$$f_2 = |m_2| = \frac{|2X_p[n]|}{M} \quad (4.9)$$

### 4.3 The Gauss-Newton Method for Solving the Estimation Problem

While  $f_1(\theta)$  and  $f_2(\theta)$  are linear in  $v_m$  and  $A$ , they are highly nonlinear in  $(x_s, y_s)$ . To efficiently solve the estimation problem, we adopt the Gauss-Newton method. First we approximate  $f_1$  and  $f_2$  by linearizing them around some nominal point  $\bar{\theta}$ :

$$\begin{aligned}\bar{f}_1(\theta) &= f_1(\bar{\theta}) + B_1(\bar{\theta})(\theta - \bar{\theta}), \\ \bar{f}_2(\theta) &= f_2(\bar{\theta}) + B_2(\bar{\theta})(\theta - \bar{\theta}),\end{aligned}$$

where

$$B_1(\bar{\theta}) = \left. \frac{\partial f_1}{\partial \theta} \right|_{\theta=\bar{\theta}}, \quad B_2(\bar{\theta}) = \left. \frac{\partial f_2}{\partial \theta} \right|_{\theta=\bar{\theta}}.$$

Accordingly, we modify the cost function for the estimation problem from (4.4) to

$$J(\hat{\theta}) = \beta(\hat{m}_1 - \bar{f}_1(\hat{\theta}))^T(\hat{m}_1 - \bar{f}_1(\hat{\theta})) + (1 - \beta)(\hat{m}_2 - \bar{f}_2(\hat{\theta}))^T(\hat{m}_2 - \bar{f}_2(\hat{\theta})), \quad (4.10)$$

which becomes a standard least squares estimation problem. A solution to this problem is

$$\begin{aligned}\hat{\theta} &= \bar{\theta} + \lambda_1 \left( \beta B_1(\bar{\theta})^T B_1(\bar{\theta}) + (1 - \beta) B_2(\bar{\theta})^T B_2(\bar{\theta}) \right)^{-1} \\ &\quad \left( \beta B_1^T(\bar{\theta})(\hat{m}_1 - f_1(\bar{\theta})) + (1 - \beta) B_2^T(\bar{\theta})(\hat{m}_2 - f_2(\bar{\theta})) \right),\end{aligned} \quad (4.11)$$

where  $\lambda_1$  is a stepping parameter for the DC component.

In order to minimize the impact of error introduced by linearization, we use a recursive

version of (4.11) to update the estimate:

$$\hat{\theta}_{k+1} = \hat{\theta}_k + \lambda_1 \left( \beta B_1(\hat{\theta}_k)^T B_1(\hat{\theta}_k) + (1 - \beta) B_2(\hat{\theta}_k)^T B_2(\hat{\theta}_k) \right)^{-1} \left( \beta B_1^T(\hat{\theta}_k)(\hat{m}_1 - f_1(\hat{\theta}_k)) + (1 - \beta) B_2^T(\hat{\theta}_k)(\hat{m}_2 - f_2(\hat{\theta}_k)) \right), \quad (4.12)$$

where the initial estimate  $\hat{\theta}_0$  is chosen properly. When  $\beta = 0$  (i.e., considering the oscillatory component only), the algorithm (4.12) is simplified to

$$\hat{\theta}_{k+1} = \hat{\theta}_k + \lambda_1 \left( B_2(\hat{\theta}_k)^T B_2(\hat{\theta}_k) \right)^{-1} \left( B_2^T(\hat{\theta}_k)(\hat{m}_2 - f_2(\hat{\theta}_k)) \right). \quad (4.13)$$

The iteration is stopped when  $\|\hat{\theta}_{k+1} - \hat{\theta}_k\| \leq \epsilon$ , where  $\epsilon > 0$  is a specified tolerance.

## 4.4 Simulation Results

Fig. 4.2 illustrates the simulation setup. The lateral line system is placed parallel to the  $x$ -axis and centered at  $(0, 5)$  cm. It consists of 6 sensors, with the sensor-to-sensor separation of 2 cm. The dipole source (sphere diameter 1.9 cm) vibrates at 40 Hz with amplitude  $A = 0.191$  cm. The source moves from left to right with a constant speed of 1.5 cm/s. The initial location of the source is  $(0, 2)$  cm, and the time duration for the movement is 6.667 s, resulting in a terminal location of  $(10, 2)$  cm.

Fig. 4.3 shows the simulated flow velocities ( $x$ -component) at each sensor site. Figs. 4.4 and 4.5 show the magnitudes of the DC and AC components, respectively, obtained through SDFT. The sampling frequency used is 20 kHz, and the sliding window size is 500 samples (25 ms).

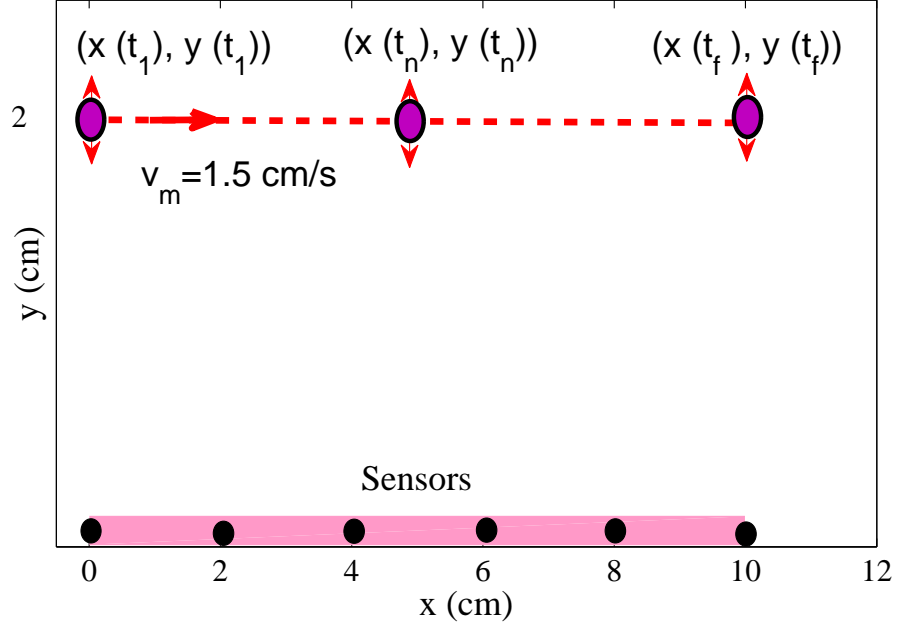


Figure 4.2: Illustration of the simulation setup.

It is clear from Figs. 4.4 and 4.5 that both the DC and AC components contain relevant information for localizing the source, as can be seen from the shifting magnitude profiles in the figures. We assume a zero-mean Gaussian noise with a variance of  $0.0065 \text{ (cm}^2/\text{s}^2)$  for the sensors.

It is of interest to investigate how the weighting parameter  $\beta$  in (4.4) impacts the estimation performance. Fig. 4.6 shows the actual and estimated source locations and the tracking error at each point under the proposed method for a typical run, where the stopping criterion  $\epsilon$  is chosen to be 0.01, and at period time  $\Delta = 0.2 \text{ s}$  over the period (10 s), we have estimated the source locations and the other parameters. The maximum tracking errors are 0.044 cm for  $\beta = 0$  and 0.0441 for  $\beta = 0.5$ , respectively. Table 4.1 summarizes the averages of the estimates for other parameters ( $v_m$  and  $A$ ), where each average is obtained by taking the mean of the estimated values over the period  $[0.2, 10] \text{ s}$ . When  $\beta = 0$ , we do not have direct

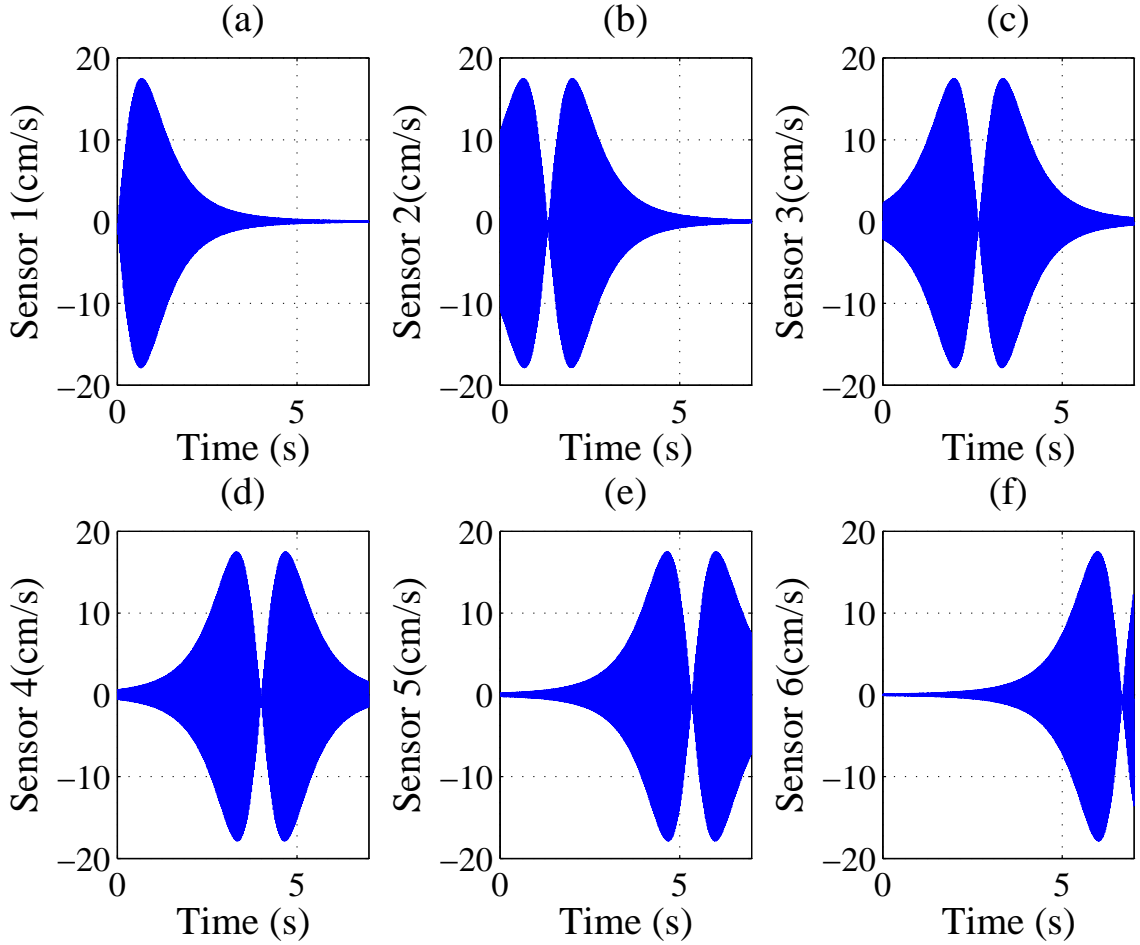


Figure 4.3: Simulation results: Time trajectories of the flow velocities at the sensor locations.

information to estimate the moving velocity, so we have used an indirect method to do so by defining  $\bar{v}_m$  as:

$$\bar{v}_{m,k} = \frac{\hat{x}_k - \hat{x}_{k-1}}{\Delta}, \quad (4.14)$$

where  $k$  is the discrete time index. It is clear from Table 4.1 that, the difference between  $\bar{v}_m$  and  $\hat{v}_m$  is small, which will be our justification for using just the AC-component in the experimental section.

We have further examined the case where the amplitude of vibration varies while the

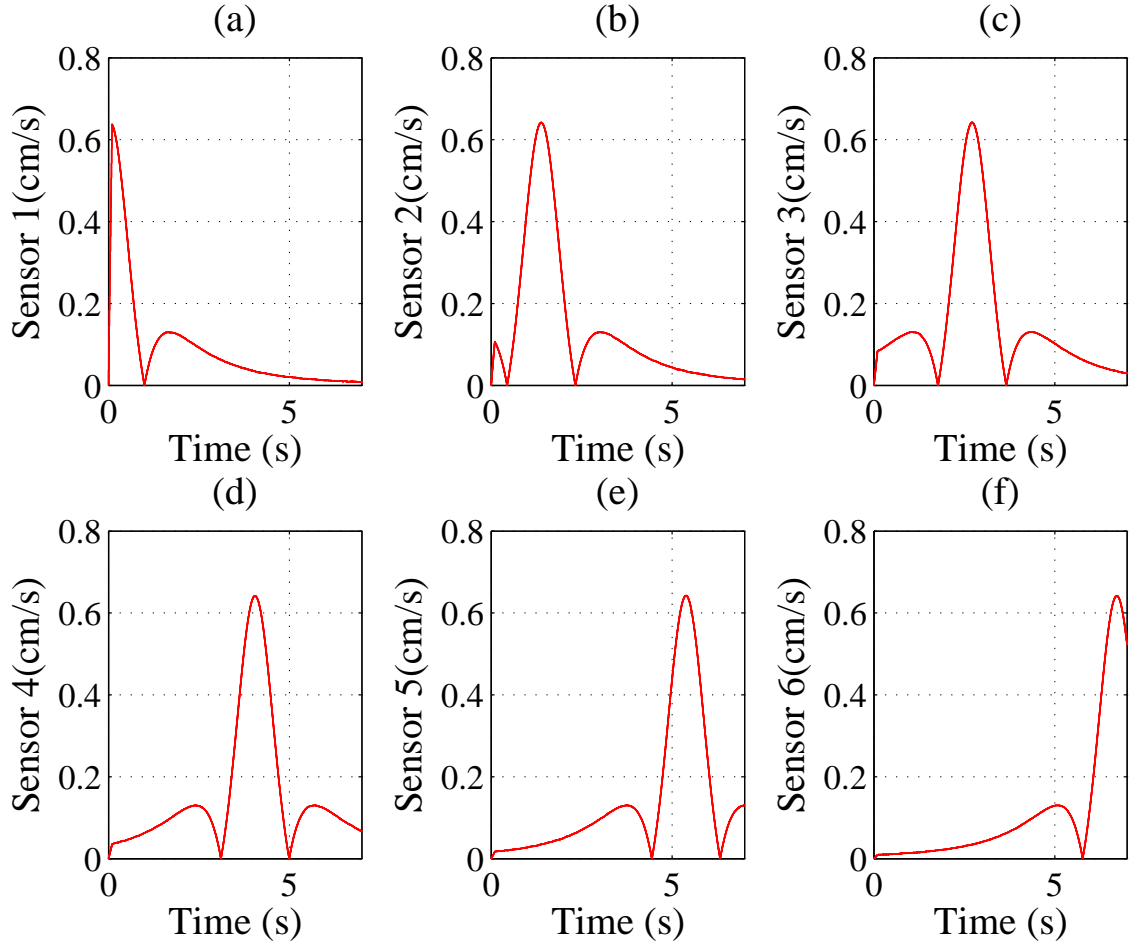


Figure 4.4: Simulation results: Magnitude trajectories of the DC component at the sensor sites.

sphere is moving. Fig. 4.7 shows the actual and estimated locations under a typical run, where the moving velocity is 3 cm/s and the vibration amplitude changes with the time as shown in Fig. 4.8. From Figs. 4.7 and 4.8, the proposed scheme can effectively estimate both the location and the vibration amplitude of the dipole. The estimated dipole traveling speed is  $\bar{v}_m = 2.87$  cm/s, which is close to the actual value of 3 cm/s.

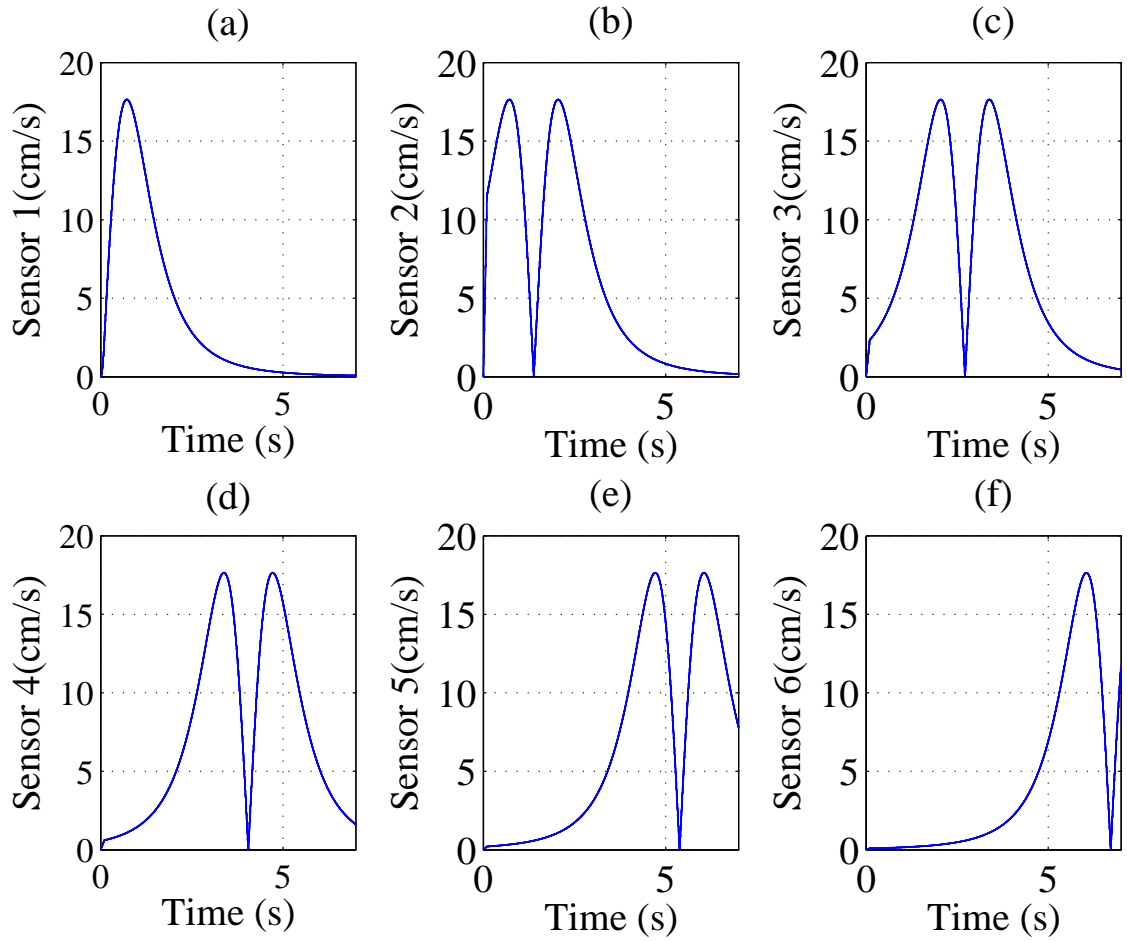


Figure 4.5: Simulation results: Magnitude trajectories of the AC component at the sensor sites.

## 4.5 Experimental Setup and Results

### 4.5.1 Experimental Setup

The artificial lateral line prototype consists of six IPMC sensors as shown in Fig. 4.9. Each sensor has dimensions  $8 \text{ mm} \times 2 \text{ mm} \times 200 \text{ }\mu\text{m}$ . The sensor-to-sensor separation was 2 cm, resulting in a total span of 10 cm. Each sensor is mounted in such a way that it would bend in the direction parallel to the sensor array, which is denoted as  $x$ -direction.

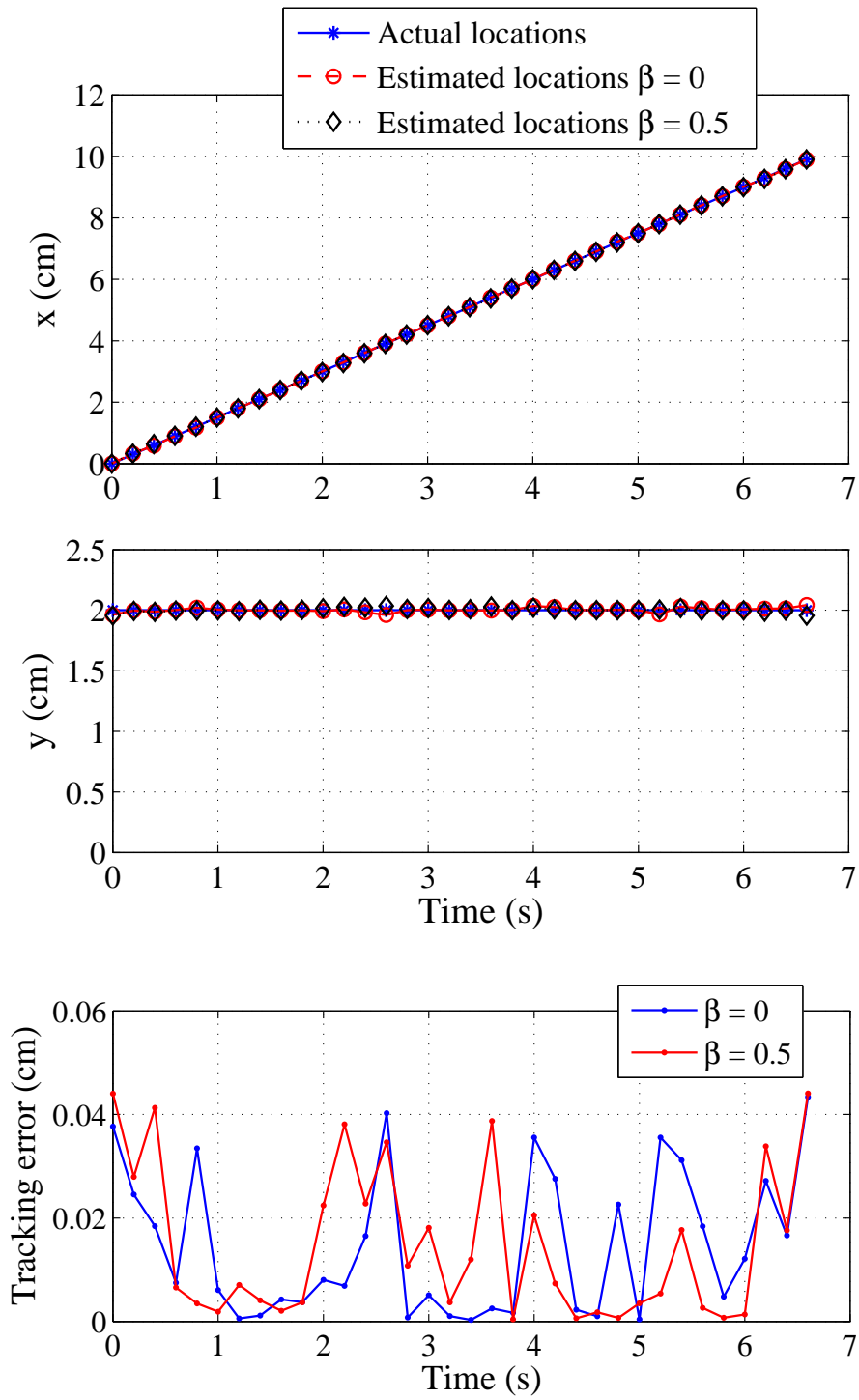


Figure 4.6: Simulation results on the estimation of the source location: (a) Localization; (b) tracking error.

Table 4.1: Simulation results: Estimated velocity ( $v_m$ ), vibrating amplitude ( $A$ ).

Parameter	Actual	$\bar{v}_m(\beta = 0)$	$\bar{v}_m(\beta = 0.5)$	$\hat{v}_m(\beta = 0.5)$
Velocity (cm/s)	1.5	1.41	1.414	1.46
Amplitude (mm)	1.91	1.87	-	1.86

Fig. 4.10 shows the schematic of the experimental setup, while Fig. 4.11 shows the picture of the actual experimental system. The experiments were conducted in a water tank measuring 6 ft long, 2 ft wide, and 2 ft deep. A custom-built, DC motor-driven conveyor was used to move a moving dipole in the water. The conveyor track was separated from the lateral line system by 2 cm. The signals from the IPMC sensors were conditioned and amplified before the acquisition and processing by a PC equipped with dSPACE (DS 1104, dSPACE). The relationship between the current output  $I$  of an IPMC sensor and the local flow velocity of the AC component  $m_2$  can be captured by the cascaded connection of fluid-structure interaction dynamics  $G_1$  and IPMC transduction dynamics  $G_2$ , both of which can be treated as linear when the flow-induced beam deformation is relatively small. The short-circuit current output of an IPMC sensor is (approximately) proportional to the instantaneous local flow velocity; the detailed derivation and approximation of  $G_1$  and  $G_2$  are explained earlier in Chapter 2. The proportionality constant can vary from sensor to sensor because of the spatial inhomogeneity in the fabricated IPMC material, difference in exact sensor dimensions, and discrepancy across different channels of the sensing circuit. The constant is identified through a calibration procedure described next. We put the mini-shaker-based dipole source at different locations with respect to each sensor and extracted the amplitude of sensing current with DFT. The theoretical value of the flow velocity at the location of the sensor is obtained using (4.3). Fig. 4.12 shows the IPMC signal ampli-

tude versus the theoretical local velocity for one IPMC sensor, from which an approximately linear relationship between the sensor output  $I$  and the flow velocity  $f_2$  parallel to the lateral line can be observed. The proportional constant  $\eta = \frac{I}{f_2}$  is identified using the Matlab command `polyfit(·, ·, 1)`. The proportionality constants identified for the six IPMC sensors are  $\eta_1 = 0.4 \mu\text{A}/(\text{cm} \cdot \text{s}^{-1})$ ,  $\eta_2 = 0.25 \mu\text{A}/(\text{cm} \cdot \text{s}^{-1})$ ,  $\eta_3 = 0.22 \mu\text{A}/(\text{cm} \cdot \text{s}^{-1})$ ,  $\eta_4 = 0.33 \mu\text{A}/(\text{cm} \cdot \text{s}^{-1})$ ,  $\eta_5 = 0.28 \mu\text{A}/(\text{cm} \cdot \text{s}^{-1})$ , and  $\eta_6 = 0.23 \mu\text{A}/(\text{cm} \cdot \text{s}^{-1})$ . Given  $\eta_i$ , the flow velocity at the site of sensor  $i$  is calculated from the sensor output  $I_i$  via

$$v_i = \frac{I_i}{\eta_i}.$$

## 4.5.2 Experimental Results on Moving Dipole Source Localization

For a typical run, the dipole source vibrates at 40 Hz with amplitude  $A = 0.191$  cm. The source moves from left to right with a constant speed of 1.5 cm/s. The initial location of the source is (0, 2) cm, and the time duration for the movement is 6.667 s, resulting in a terminal location of (10, 2) cm. During experiments both the IPMC sensors and the vibrating sphere are completely submerged underwater with a depth of approximately 5 cm. Fig. 4.13 shows the measured flow velocities ( $x$ -component) at each sensor site.

Fig. 4.14 and 4.15 show the experimental magnitudes of the DC and AC components, respectively, obtained through SDFIT. The sampling frequency used is 20 kHz, and the sliding window size is 500 samples (25 ms). It is clear from Fig. 4.14 that the magnitude trajectories of the DC flow component at the sensor sites are subject to uncertain drifts. Therefore, in the following experimental localization results, we take  $\beta = 0$  so that only the

AC component is used.

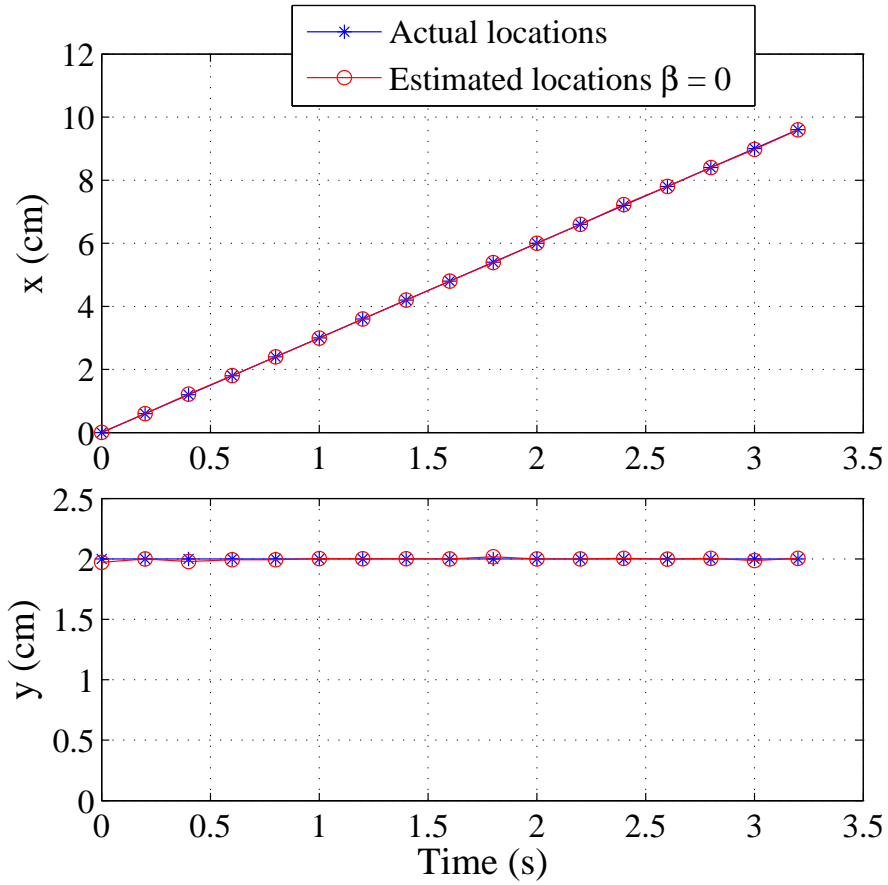
Fig. 4.16 shows the actual and estimated source locations and the tracking error at each point under the Gauss Newton method for a typical run. Table 4.2 lists the estimated moving speed and vibrating amplitude. The maximum tracking error was 0.33 cm and the errors in estimating  $v_m$  and  $A$  were less than 10%, which demonstrates the effectiveness of the proposed estimation approach.

Table 4.2: Experimental results: Estimated velocity ( $v_m$ ), vibrating amplitude ( $A$ ).

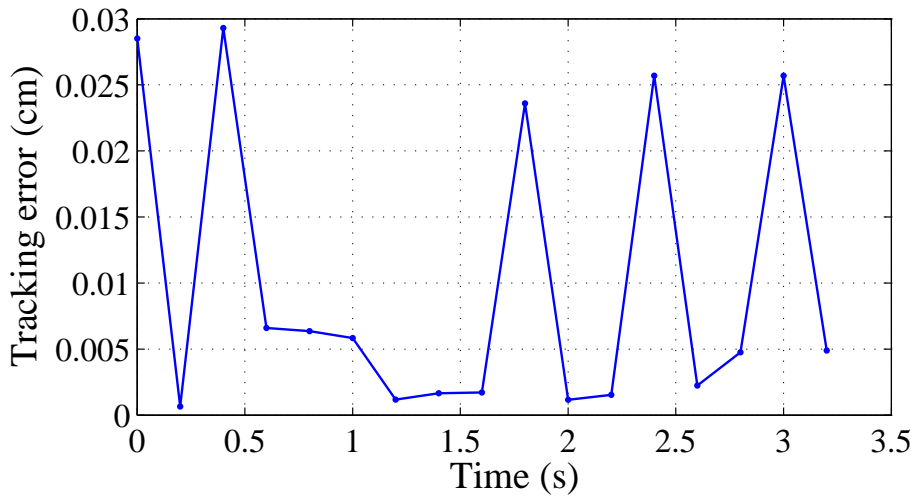
Parameter	Actual	Estimated	Error
Velocity (cm/s)	1.5	1.4	0.1
Vibrating amplitude (mm)	1.91	2.1	0.19

## 4.6 Chapter Summary

In this chapter we investigated an analytical model-based estimation approach to the localization of a moving dipole source using an artificial lateral line consisting of an array of flow sensors. The moving speed, vibration amplitude, and location of the moving source were assumed to be unknown, and we proposed a Gauss-Newton algorithm to solve the nonlinear estimation problem based on the evolving signal magnitudes obtained with SDFT. The effectiveness of the approach was illustrated with simulation and experimental results.



(a)



(b)

Figure 4.7: Simulation results on the estimation of the source location, vibration amplitude changing with the time: (a) Localization; (b) tracking error.

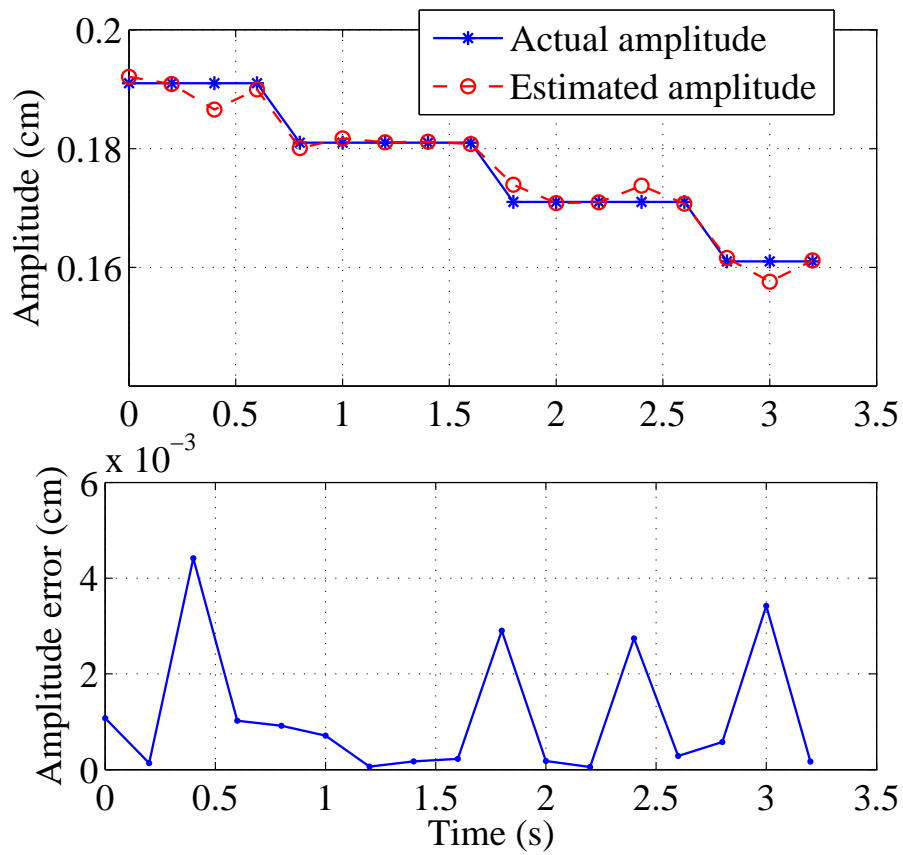


Figure 4.8: Simulation results of the source vibration amplitude.

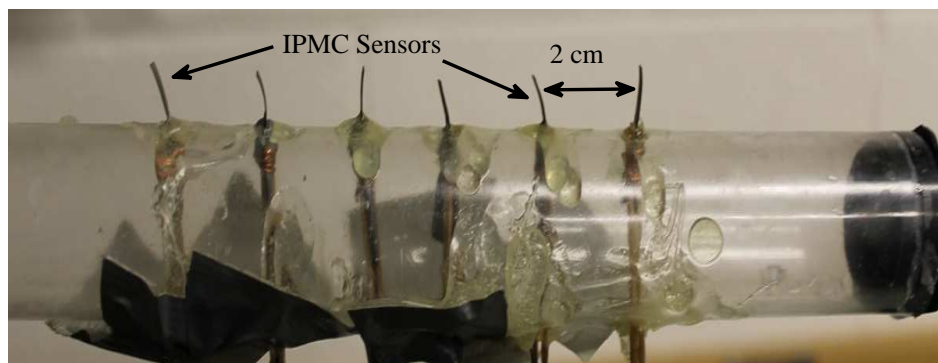


Figure 4.9: An experimental prototype of IPMC-based lateral line system.

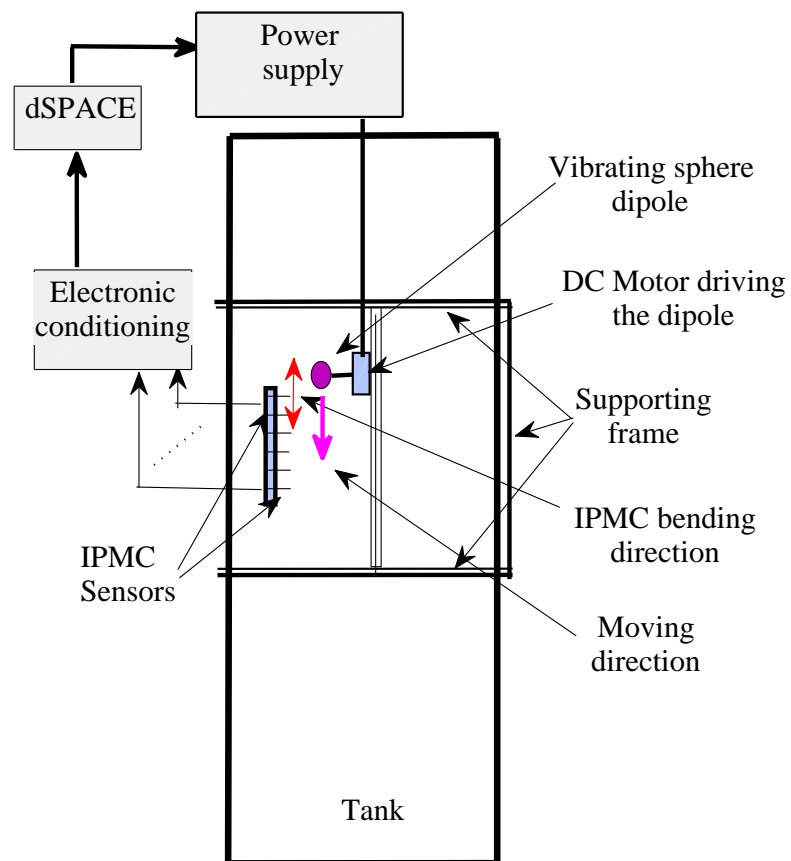


Figure 4.10: Experimental setup of the moving dipole source: Schematic.

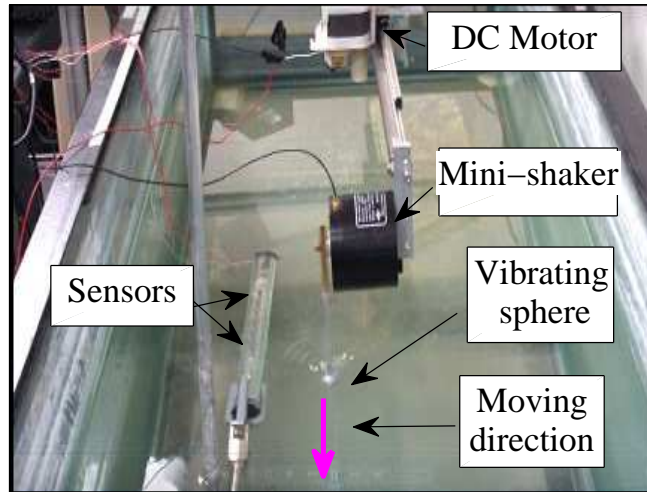


Figure 4.11: Experimental setup of the moving dipole source: Picture of the experimental setup.

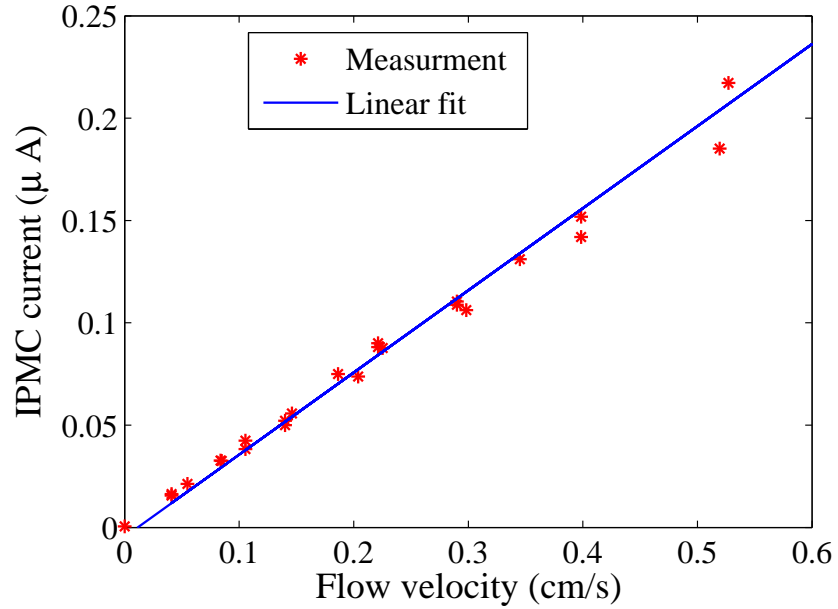


Figure 4.12: Calibration of an IPMC sensor.

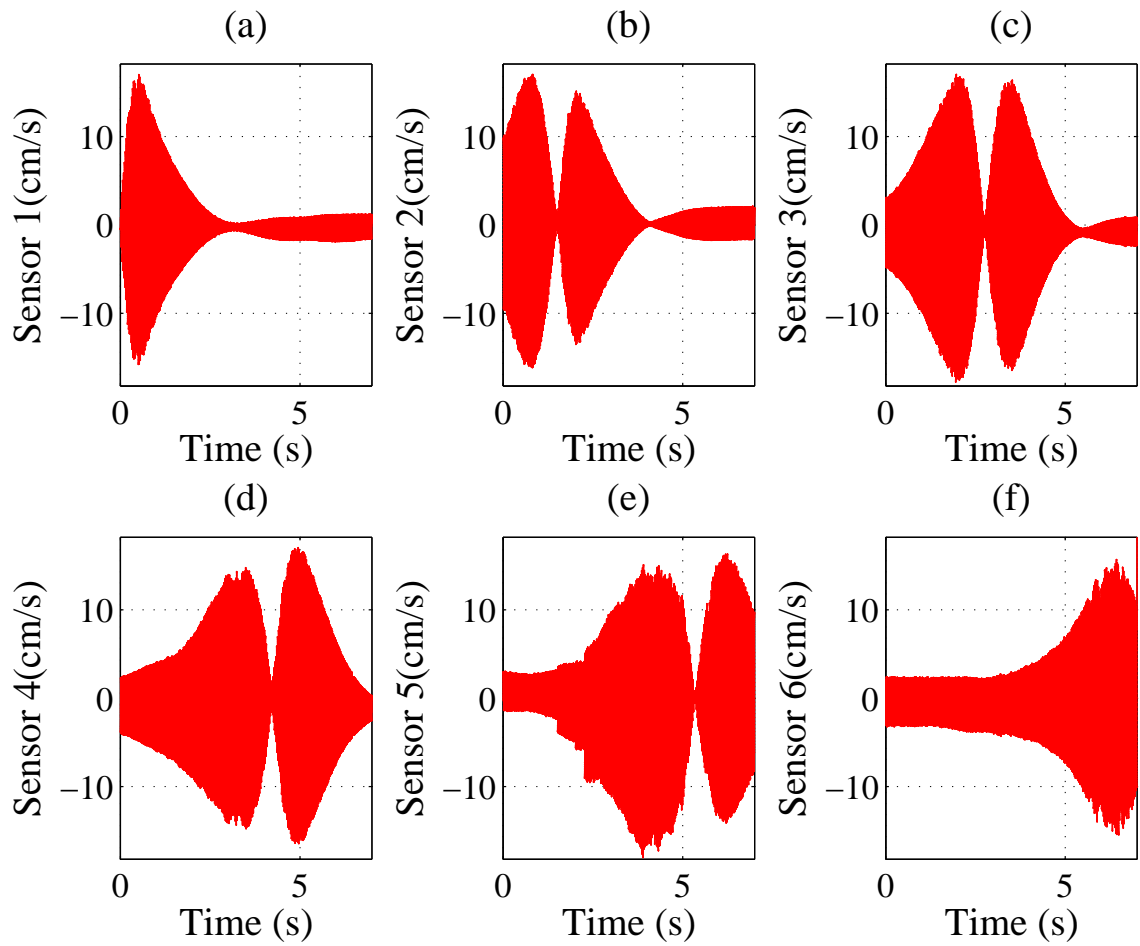


Figure 4.13: Experimental results: Time trajectories of the flow velocities at the sensor locations.

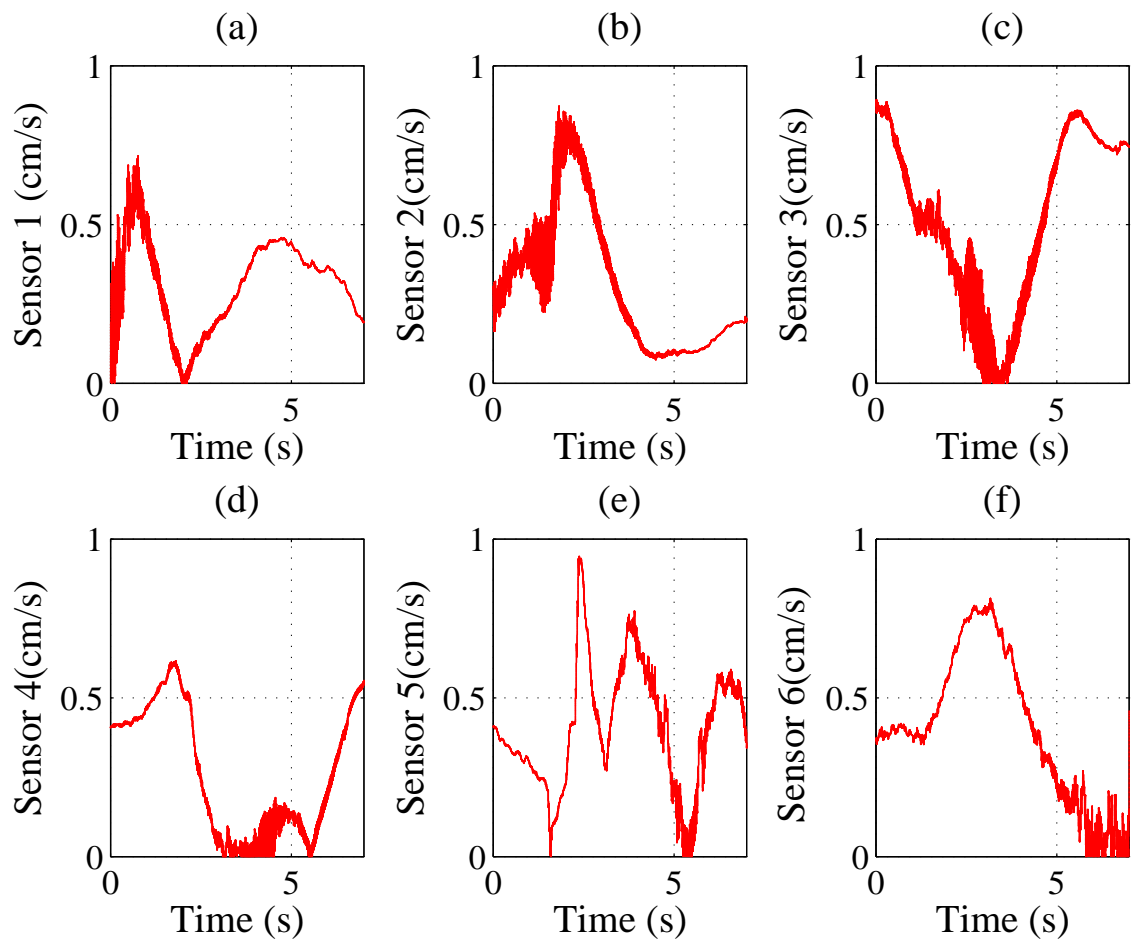


Figure 4.14: Experimental results: Magnitude trajectories of the DC component at the sensor sites.

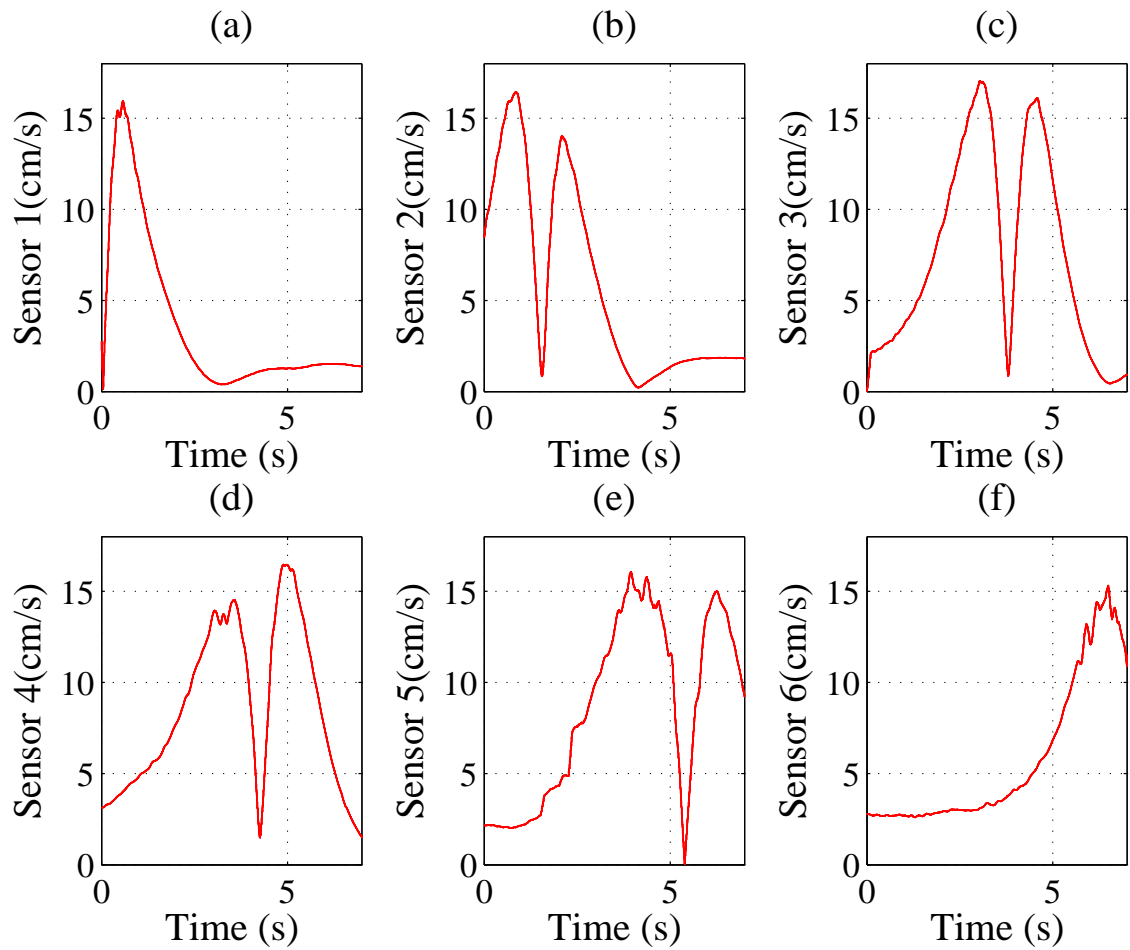
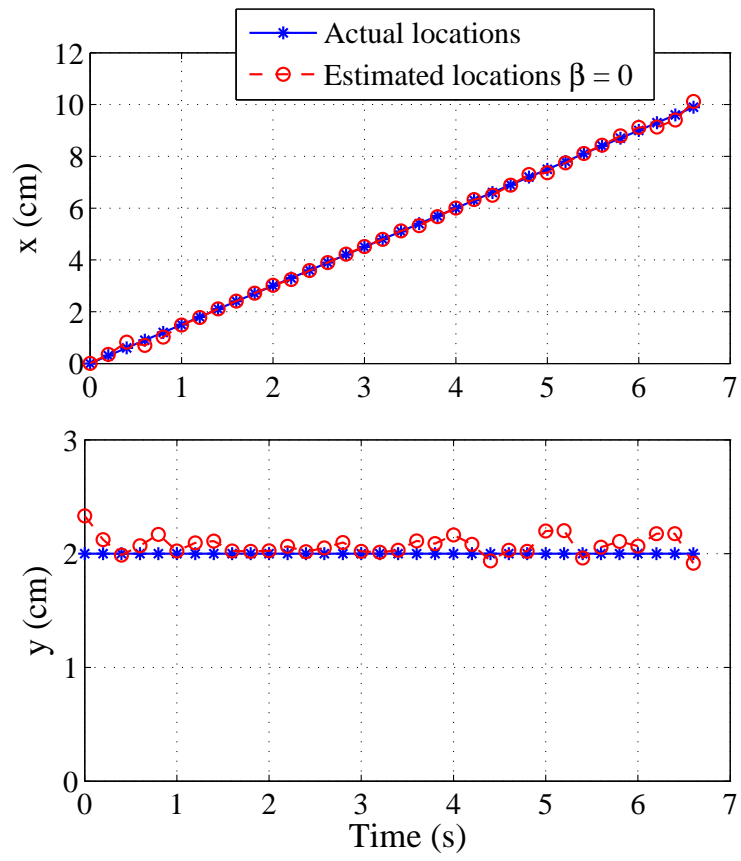
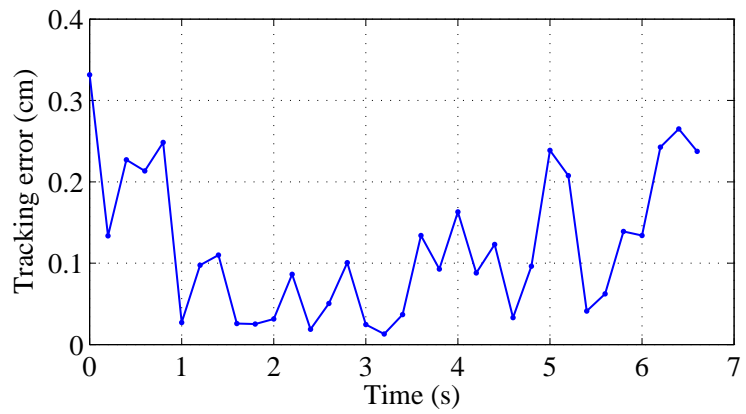


Figure 4.15: Experimental results: Magnitude trajectories of the AC component at the sensor sites.



(a)



(b)

Figure 4.16: Experimental results on the estimation of the source location: (a) Localization; (b) tracking error.

## Chapter 5

# Underwater Tracking and Size-Estimation of a Moving Object

In this chapter we investigate the problem of tracking a moving but non-vibrating cylindrical object and estimating its size and shape using an artificial lateral line system. Based on a nonlinear analytical model for the moving object-induced flow field, a two-stage extended Kalman filter is proposed to estimate the location, velocity, size, and shape of the object. For comparison purposes, unscented Kalman filtering and particle filtering are also explored. The flow model is validated with digital particle image velocimetry (DPIV) measurement. Simulation results on tracking a cylinder with ellipsoidal cross-section are presented to illustrate the approach. The approach has been further verified experimentally with an artificial lateral line prototype consisting of six ionic polymer metal composite (IPMC) flow sensors.

The remainder of this chapter is organized as follows. We first present the model for the flow field generated by a moving object in a two-dimensional (2D) potential flow, and formulate the estimation problem in Section 5.1. The filtering schemes are described in

Section 5.2, followed by the simulation example in Section 5.3 . The experimental setup and results are presented in Section 5.4. Finally concluding remarks are provided in Section 5.5.

## 5.1 Flow Model and Problem Formulation

In this dissertation we assume a two-dimensional (2D) potential flow. Consider a cylindrical object moving through an otherwise still fluid. We first present the special case of circular cross-section, and then generalize the model to an arbitrary cross-section profile using the conformal mapping theory.

Consider the 2D plane  $z = x + iy$ . Without the loss of generality, assume that the cylinder is moving along  $x$ -direction with its cross-section lying in the  $x - y$  plane. The complex potential  $w^c(z)$ , where  $z$  is outside the region occupied by the cylinder, is given by [77]

$$w^c(z) = v_x \frac{R^2}{z - z_1}, \quad (5.1)$$

where the superscript  $c$  indicates the case of a circular profile,  $v_x$  denotes the moving speed,  $R$  is a radius of the circular cross-section, and  $z_1 = x_s + iy_s$  denotes the center of the moving cylinder. The corresponding complex flow velocity  $W^c$  is then given by

$$W^c(z) = \frac{dw^c(z)}{dz} = -v_x \frac{R^2}{(z - z_1)^2}. \quad (5.2)$$

If we write  $W^c(z) = v_x^c + i v_y^c$ , then

$$v_x^c = -\frac{v_x R^2((x - x_s)^2 - (y - y_s)^2)}{((x - x_s)^2 + (y - y_s)^2)^2}, \quad (5.3)$$

$$v_y^c = \frac{2v_x R^2(y - y_s)(x - x_s)}{((x - x_s)^2 + (y - y_s)^2)^2}. \quad (5.4)$$

For a cylinder with a general shape (Fig. 5.1), its cross-section profile can be obtained by mapping the circular profile with the Laurent series expansion [11]:

$$\zeta(z) = (z - z_1) + \frac{\lambda_1}{(z - z_1)} + \frac{\lambda_2}{(z - z_1)^2} + \dots, \quad (5.5)$$

where  $\lambda_1, \lambda_2, \dots$ , are the shape parameters. When the shape parameters are real, the obtained shape will be symmetric with respect to the  $x$ -direction. It can be shown that the complex flow velocity  $W^g(z)$  around the moving object with a general profile is

$$\begin{aligned} W^g(z) &= \frac{dw^c(z)}{dz} \frac{dz}{d\zeta} \\ &= \underbrace{v_x \left( -\frac{R^2}{(z - z_1)^2} \right)}_{W^c(z)} \underbrace{\left( 1 - \frac{\lambda_1}{(z - z_1)^2} - \dots \right)^{-1}}_{\frac{dz}{d\zeta}}. \end{aligned} \quad (5.6)$$

In (5.6),  $z \in D$ , the domain exterior to the object with the general profile. Since the impact of higher-order terms in (5.5) decays quickly with the distance from the object [11], in this chapter, we consider the case of ellipsoidal profile only, namely,  $\lambda_1 \neq 0$ ,  $\lambda_i = 0$ ,  $\forall i > 1$ . Furthermore, we assume that  $\lambda_1$  is real. Using (5.6), we can derive the complex flow velocity

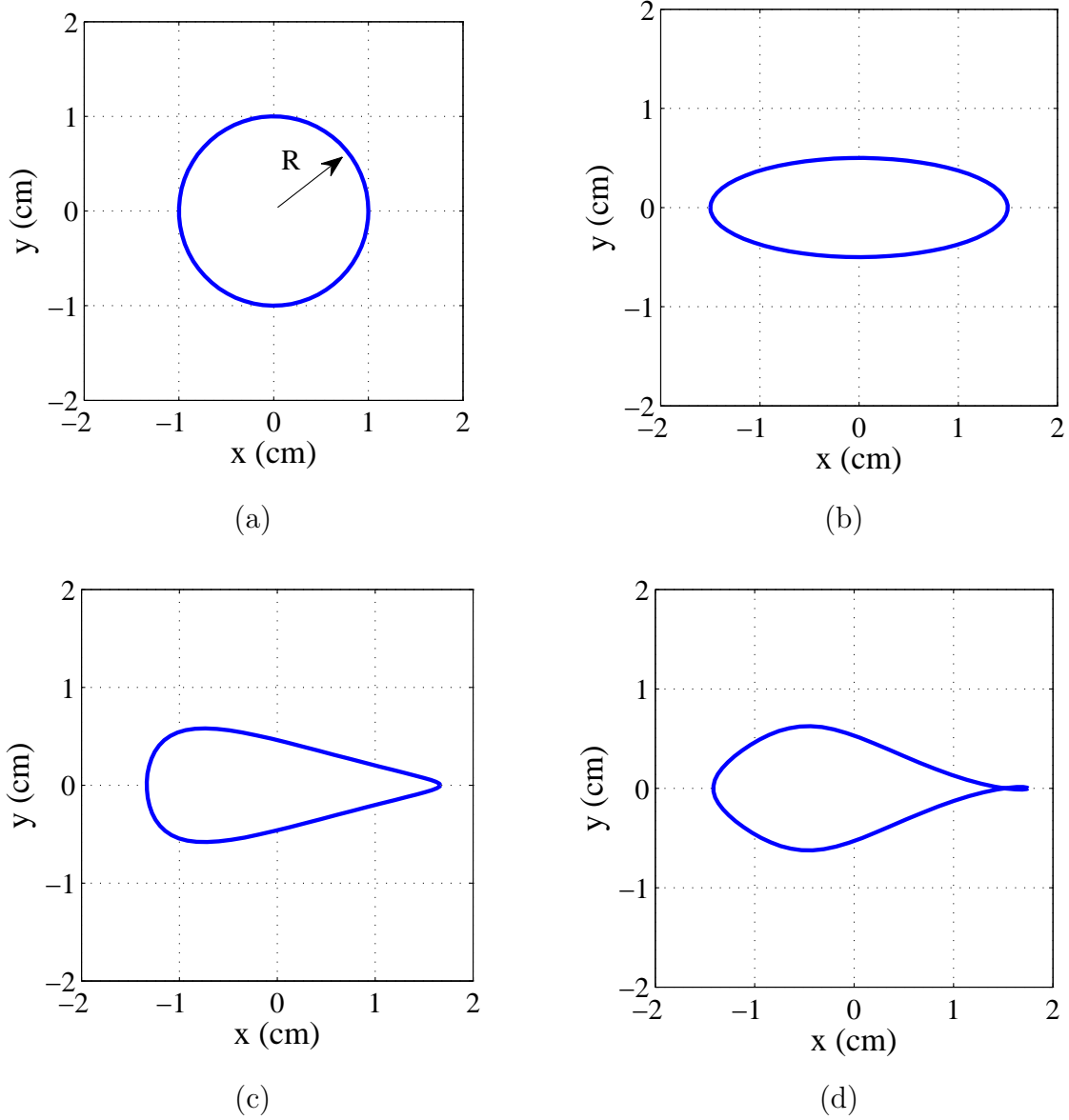


Figure 5.1: Illustration of the Laurent series expansion : (a) Circle  $\zeta(z) = z$ ; (b) the shape fingerprint  $\zeta(z) = z + 1/(2z)$ ; (c) the shape fingerprint  $\zeta(z) = z + 1/(2z) + 1/(6z^2)$ ; (d) the shape fingerprint  $\zeta(z) = z + 1/(2z) + 1/(6z^2) + 1/(12z^3)$ (adapted from [11]).

$W^e(z)$  around an ellipsoidal cylinder:

$$W^e(z) = v_x \left( -\frac{R^2}{(z - z_1)^2} \right) \left( 1 - \frac{\lambda_1}{(z - z_1)^2} \right)^{-1}. \quad (5.7)$$

If we write  $W^e(z) = v_x^e + i v_y^e$ , then

$$v_x^e = -\frac{v_x R^2 ((x - x_s)^2 - (y - y_s)^2 - \lambda_1)}{((x - x_s)^2 - (y - y_s)^2 - \lambda_1)^2 + 4(x - x_s)^2 (y - y_s)^2}, \quad (5.8)$$

$$v_y^e = \frac{2v_x R^2 (y - y_s)(x - x_s)}{((x - x_s)^2 - (y - y_s)^2 - \lambda_1)^2 + 4(x - x_s)^2 (y - y_s)^2}. \quad (5.9)$$

We now formulate the problem of localizing a moving object with ellipsoidal profile and estimating its size/shape in the  $x - y$  plane using an array of flow sensors. Consider Fig. 5.2, where an artificial lateral line comprising  $N$  sensors is located in parallel to the  $x$ -axis, with the sensor locations denoted as  $(x_i, y_i)$ ,  $0 \leq i \leq N - 1$ . We denote the center of the moving cylinder at time  $t$  by  $(x_s(t), y_s(t))$ . The object is assumed to move with a constant speed  $v_x$  parallel to the lateral line. We further assume that the presence of sensors has negligible effect on the flow field generated by the moving object. Each sensor is assumed to provide

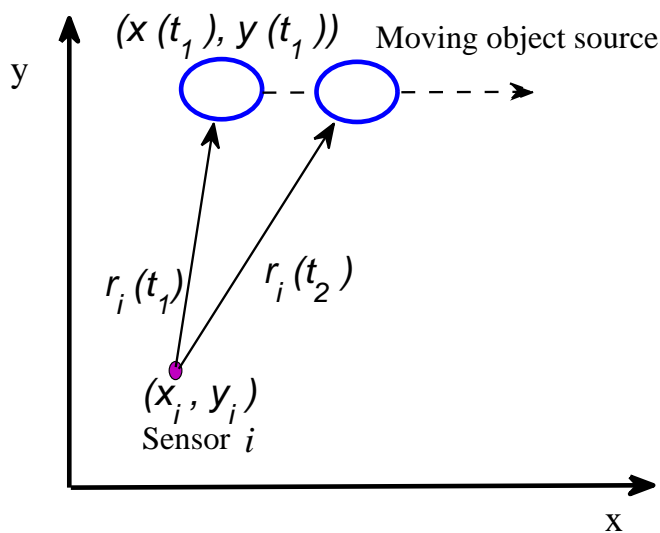


Figure 5.2: Illustration of the problem setup for the tracking and estimation of a moving object.

a noisy measurement of the local flow velocity  $v_x$  along the  $x$ -direction. In particular, the measurement  $m_i(t)$  by sensor  $i$  at time  $t$  is given by

$$m_i(t) = f^e(x_i, y_i, x_s(t), y_s(t), v_x, R, \lambda_1) + d_i(t), \quad (5.10)$$

where the function  $f^e$  follows from (5.8), and  $d_i$  is the measurement noise. We introduce a compact notation for the measurements from all sensors,

$$M(t) = [m_1(t) \ \cdots \ m_N(t)]^T = F^e(x_s(t), y_s(t), v_x, R, \lambda_1) + d(t),$$

where  $T$  denotes transpose,

$$F^e(x_s, y_s, v_x, R, \lambda_1) \triangleq \begin{bmatrix} f^e(x_1, y_1, x_s, y_s, v_x, R, \lambda_1) & \cdots \\ & f^e(x_N, y_N, x_s, y_s, v_x, R, \lambda_1) \end{bmatrix}^T,$$

and  $d(t) = [d_1(t) \ \cdots \ d_N(t)]^T$ .

The estimation problem is then formulated as: given the measurements from the artificial lateral line,  $M(\cdot)$ , determine the object location  $(x_s(t), y_s(t))$ , speed  $v_x$ , size parameter  $R$ , and shape parameter  $\lambda_1$ .

## 5.2 Nonlinear Filtering

Several filtering schemes will be explored in this chapter, including extended Kalman filtering, unscented Kalman filtering, and particle filtering. We first provide a brief review of each method.

### 5.2.1 Extended Kalman Filter

In this chapter we propose to solve the tracking and estimation problem with extended Kalman filtering. We first provide a brief review of extended Kalman filtering, when the measurement equation involves nonlinearities [76]. The discrete-time setting is considered in this work, where the time index is denoted by  $k$ . Suppose that the system dynamics is given by

$$\begin{aligned} X_k &= A_{k-1}X_{k-1} + w_{k-1}, \\ M_k &= f(X_k) + d_k. \end{aligned} \tag{5.11}$$

where  $X_k \in \mathbb{R}^n$  denotes the state vector,  $A_{k-1}$  has dimensions  $n \times n$ ,  $M_k \in \mathbb{R}^p$  denotes the measurement,  $f(\cdot)$  is a nonlinear function, and  $w_{k-1} \in \mathbb{R}^n$  and  $d_k \in \mathbb{R}^p$  denote the process noise and the measurement noise, respectively. It is assumed that  $w_{k-1}$  and  $d_k$  are white, zero-mean, Gaussian noises, with covariance matrices denoted as  $Q_k$  and  $C_k$ , respectively. It is also assumed that  $w_{k-1}$  and  $d_k$  are uncorrelated with each other.

Since  $f(X_k)$  is a nonlinear function, in extended Kalman filtering, it is linearized at  $\hat{X}_{k|k-1}$ , the prediction for  $X_k$  at time  $k - 1$ . In particular,  $f(X_k)$  is approximated by

$$f(X_k) \approx f(\hat{X}_{k|k-1}) + \hat{H}_k(X_k - \hat{X}_{k|k-1}), \tag{5.12}$$

where  $\hat{H}_k$  is the Jacobin matrix of  $f(\cdot)$  evaluated at  $\hat{X}_{k|k-1}$ :

$$\hat{H}_k = \left. \frac{\partial f(X_k)}{\partial X_k} \right|_{X_k = \hat{X}_{k|k-1}}. \tag{5.13}$$

At  $k = 0$ , the initial state estimate  $\hat{X}_{0|0} = X_0$  is a random vector with known mean  $\mu_0 = E[X_0]$ , and the initial covariance matrix is given by  $P_{0|0} = E[(X_0 - \mu_0)(X_0 - \mu_0)^T]$ . The main steps in an extended Kalman filter are outlined next. The state prediction is given by

$$\hat{X}_{k|k-1} = A_{k-1}\hat{X}_{k-1|k-1}. \quad (5.14)$$

For  $k \geq 1$ , the prediction of state covariance matrix follows

$$P_{k|k-1} = A_{k-1}P_{k-1|k-1}A_{k-1}^T + Q_{k-1}, \quad (5.15)$$

and the optimal gain matrix  $K_k$  is given by

$$K_k = P_{k|k-1}\hat{H}_k^T \left( C_k + \hat{H}_k P_{k|k-1} \hat{H}_k^T \right)^{-1}. \quad (5.16)$$

Finally, the estimates of the state and its covariance matrix are updated via

$$\hat{X}_{k|k} = \hat{X}_{k|k-1} + K_k \left( M_k - f \left( \hat{X}_{k|k-1} \right) \right), \quad (5.17)$$

$$P_{k|k} = (I - K_k \hat{H}_k) P_{k|k-1}, \quad (5.18)$$

where  $I$  denotes the identity matrix.

## 5.2.2 Unscented Kalman Filter

Unlike the EKF, the Unscented Kalman Filter (UKF) does not approximate nonlinear function  $f(X_k)$ . Instead, it approximates the posterior  $p(X_k | M_k)$  by a Gaussian density, which is represented by a set of deterministically chosen sample points [76]. Consider the non-

linear filtering problem defined by (5.11). The assumption is that the posterior density at time  $k - 1$  is Gaussian:  $p(X_{k-1} | M_{k-1}) = \mathcal{N}(X_{k-1}; \hat{X}_{k-1|k-1}, P_{k-1|k-1})$ . The first step is to represent this density by a set of  $N_s$  sample points  $\mathcal{X}_{k-1|k-1}^i$  and their weights  $W_{k-1}^i$ ,  $i = 0, \dots, N_s - 1$ . The prediction step is then performed as follows:

$$\hat{X}_{k|k-1} = \sum_{i=0}^{N_s-1} W_{k-1}^i \cdot \mathcal{X}_{k-1|k-1}^i, \quad (5.19)$$

$$P_{k|k-1} = Q_{k-1} + \sum_{i=0}^{N_s-1} W_{k-1}^i \left[ \mathcal{X}_{k-1|k-1}^i - \hat{X}_{k|k-1} \right] \left[ \mathcal{X}_{k-1|k-1}^i - \hat{X}_{k|k-1} \right]^T. \quad (5.20)$$

The predicted density  $p(X_k | M_{k-1}) \approx \mathcal{N}(X_k; \hat{X}_{k|k-1}, P_{k|k-1})$  is represented by a set of  $N_s$  sample points, given as

$$\mathcal{X}_{k|k-1}^i = A_{k-1} \mathcal{X}_{k-1|k-1}^i, \quad (5.21)$$

the predicted measurement step is given by

$$\hat{M}_{k|k-1} = \sum_{i=0}^{N_s-1} W_{k-1}^i f_k \left( \mathcal{X}_{k|k-1}^i \right), \quad (5.22)$$

and the update step is given as

$$\hat{X}_{k|k} = \hat{X}_{k|k-1} + K_k \left( M_k - \hat{M}_{k|k-1} \right), \quad (5.23)$$

$$P_{k|k} = P_{k|k-1} - K_k S_k K_k^T, \quad (5.24)$$

where

$$K_k = \left( \sum_{i=0}^{N_s-1} W_{k-1}^i \left[ \mathcal{X}_{k|k-1}^i - \hat{X}_{k|k-1} \right] \left[ f_k \left( \mathcal{X}_{k|k-1}^i \right) - \hat{M}_{k|k-1} \right]^T \right) S_k^{-1}, \quad (5.25)$$

$$S_k = C_k + \sum_{i=0}^{N_s-1} W_{k-1}^i \left[ f_k \left( \mathcal{X}_{k|k-1}^i \right) - \hat{M}_{k|k-1} \right] \left[ f_k \left( \mathcal{X}_{k|k-1}^i \right) - \hat{M}_{k|k-1} \right]^T. \quad (5.26)$$

The  $n$  dimensional random variable  $X(k)$  with mean  $\hat{X}(k|k)$  and covariance  $P(k|k)$  is approximated by  $2n$  weighted samples or *sigma* points selected by the algorithm [76]

$$\begin{aligned} \mathcal{X}_0(k|k) &= \hat{X}(k|k) & W_0 &= \frac{\alpha}{(n+\alpha)}, \\ \mathcal{X}_i(k|k) &= \hat{X}(k|k) + \left( \sqrt{(n+\alpha)P(k|k)} \right)_i & W_i &= \frac{\alpha}{2(n+\alpha)}, \\ \mathcal{X}_{i+n}(k|k) &= \hat{X}(k|k) - \left( \sqrt{(n+\alpha)P(k|k)} \right)_i & W_{i+n} &= \frac{\alpha}{2(n+\alpha)}, \end{aligned}$$

where  $\alpha$  is scaling parameter, such that  $\alpha+n \neq 0$ ,  $\left( \sqrt{(n+\alpha)P(k|k)} \right)_i$  is the  $i^{th}$  column of the lower Cholesky factorization of  $(n+\alpha)P(k|k)$ , and  $W_i$  is the weight that is associated with the  $i$ th point.

### 5.2.3 Particle Filter

Particle filter (PF) is a suboptimal filter. It performs sequential Monte Carlo (SMC) estimation based on particle representation of probability densities. In this chapter, we have chosen the modified particle filter, called regularized particle filter (RBF) [62]. Regularization consists of resampling the particles according to a continuous approximation of the target distribution so that all the particles obtained have different locations. The smoothing is performed by convoluting the discrete PF approximation with a kernel whose properties

are provided by the density estimation theory [85]. The resulting continuous approximation takes the following form:

$$\hat{p}(X_k | M_{1:k}) \approx \sum_{i=1}^{N_s} w_k^i K_\beta(X_k - X_k^i), \quad (5.27)$$

where

$$K_\beta(X) = \frac{1}{\beta^n} K\left(\frac{X}{\beta}\right) \quad (5.28)$$

is the rescaled kernel function density  $K(\cdot)$ ,  $\beta > 0$  is the kernel bandwidth (a scalar parameter),  $N_s$  is the total number of particles, and  $w_k^i$ ,  $i = 0, \dots, N_s$  are the normalized weights. The particle system evolves according to an importance-sampling rule; more precisely, the particles are simulated sequentially according to a proposal distribution given as

$$X_k^i \sim q\left(X_k \mid X_{1:k-1}^i, M_{1:k}\right) \quad \text{for } i = 1, \dots, N_s, \quad (5.29)$$

where  $q(\cdot)$  is a proposal density. They are then assigned importance weights to correct for the discrepancy between the proposal and the target distributions given by

$$w_k = \tilde{w}^i / \sum_{j=1}^{N_s} \tilde{w}^j, \quad (5.30)$$

where

$$\tilde{w}^i = \frac{w_{k-1}^i p(M_k \mid X_{1:k}^i, M_{1:k-1}) p(X_k^i \mid X_{1:k-1}^i)}{q(X_k \mid X_{1:k-1}^i, M_{1:k})}. \quad (5.31)$$

According to (5.31), the most likely particles yield high importance weights. A selection step is finally introduced to prevent degeneracy. This selection is performed by resampling the set of particles according to the obtained approximation of the posterior distribution.

However, systematic resampling is known to result in a loss of sample diversity. A measure of degeneracy, called effective sample size and denoted  $N_{eff}$ , has been introduced in [51] to decide whether resampling is useful or not:

$$N_{eff} = \frac{1}{\sum_{i=1}^{N_s} (w_k^i)^2} \quad (5.32)$$

The selection procedure is carried out whenever  $N_{eff}$  is below a given threshold.

For our tracking and estimation problem, the dynamics of interest can be described as follows:

$$x_s[k] = x_s[k-1] + v_x[k-1]\Delta + w_1[k-1], \quad (5.33)$$

$$y_s[k] = y_s[k-1] + v_y[k-1]\Delta + w_2[k-1], \quad (5.34)$$

$$v_x[k] = v_x[k-1] + w_3[k-1], \quad (5.35)$$

$$v_y[k] = v_y[k-1] + w_4[k-1], \quad (5.36)$$

$$R[k] = R[k-1] + w_5[k-1], \quad (5.37)$$

$$\lambda_1[k] = \lambda_1[k-1] + w_6[k-1], \quad (5.38)$$

where  $\Delta$  is the sampling time, and  $w_1, \dots, w_6$  denote the process noises, which are assumed to be uncorrelated. The measurement equation is given by

$$M[k] = F^e(x_s[k], y_s[k], v_x[k], R[k], \lambda_1[k]) + d[k], \quad (5.39)$$

where  $d[k]$  denotes the vector of measurement noises with uncorrelated components.

In this work, we propose a two-stage nonlinear filtering scheme, as illustrated in Fig. 5.3.

In the first stage, five state components, (5.33) – (5.37), are estimated while assuming the shape parameter  $\lambda_1 = 0$ . Correspondingly, the measurement equation for the first stage is obtained by plugging  $\lambda_1 = 0$  in (5.39):

$$M[k] = F^e(x_s[k], y_s[k], v_x[k], R[k], 0) + d[k]. \quad (5.40)$$

In the second stage, the state estimate involves  $\lambda_1$  only (equation (5.38)), while the measurement equation is obtained from (5.39) by plugging in the state estimates from the first stage:

$$M[k] = F^e(\hat{x}_{s,k|k}, \hat{y}_{s,k|k}, \hat{v}_{x,k|k}, \hat{R}_{k|k}, \lambda_1) + d[k]. \quad (5.41)$$

State estimation at each stage is then carried out following the general nonlinear filtering procedure, as outlined earlier.

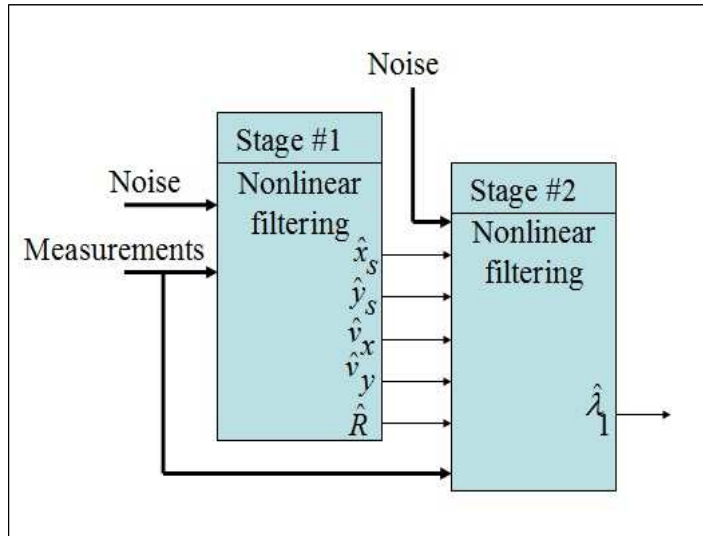


Figure 5.3: Illustration of the two-stage filtering scheme.

There are two motivations for estimating the desired information in two cascaded stages.

First, as discussed in [11], it is likely that a biological lateral line extracts the relevant information in a progressive manner. Second, the proposed scheme leads to reduced computational complexity because of the reduced dimensions for the state dynamics – for example, one only needs to invert  $5 \times 5$  matrices instead of  $6 \times 6$  matrices.

## 5.3 Simulation Results

### 5.3.1 Recursive Information Matrix

Generally, a nonlinear filtering problem does not have a close-form analytical solution, and in all practical applications, nonlinear filtering is performed by some sort of approximation. Despite the absence of a closed-form solution, we would like to find the best achievable error performance for nonlinear filtering; to do so, a theoretical Cramer-Rao lower bound has been formulated for such problems. Consider the system which is described in (5.11), the recursive information matrix  $J_k$  for such system has been derived in [76] as

$$J_k = Q_{k-1}^{-1} + \tilde{H}_k^T C_k^{-1} \tilde{H}_k - Q_{k-1}^{-1} A_{k-1} \left( J_{k-1} + A_{k-1}^T Q_{k-1}^{-1} A_{k-1} \right)^{-1} A_{k-1}^T Q_{k-1}^{-1}, \quad (5.42)$$

where

$$\tilde{H} = \frac{\partial f(X_k)}{\partial X_k}. \quad (5.43)$$

is the Jacobian of  $f(\cdot)$  evaluated at the true value of  $X_k$ .

Fig. 5.4 shows the square root of the CRB,  $\sqrt{CRB}$ , corresponding to the components of the state vector: (i)  $x_s$ -coordinate, (ii)  $y_s$ -coordinate, (iii) size parameter  $R$ , and (iv) shape parameter  $\lambda_1$ , for two-stage and one-stage schemes, respectively. These bounds are obtained

as:

$$CRB(X_k[i]) = J^{-1}[i, i], \quad i = 1, 2, 3, 4. \quad (5.44)$$

The close-form analytical solution for our problem has derived in Appendix B.1. It is clear

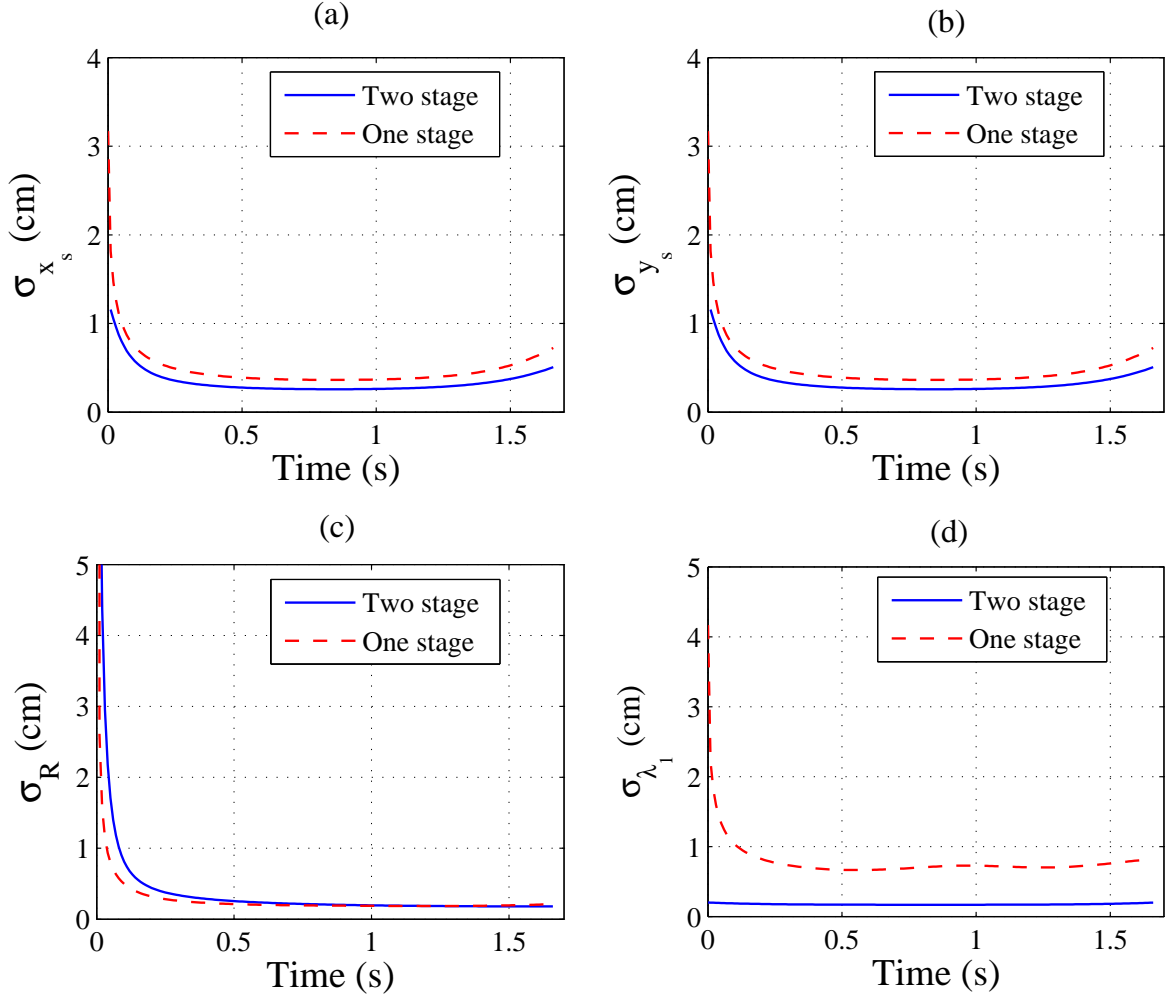


Figure 5.4:  $\sqrt{CRB}$  for: (a) Moving object  $x_s$  coordinate; (b) moving object  $y_s$  coordinate; (c) size parameter  $R$ ; (d) shape parameter  $\lambda_1$ .

from Fig. 5.4 that, a two-stage scheme yields smaller estimation errors than a one-stage scheme. Consequently, we will employ two-stage schemes in our estimation.

### 5.3.2 Simulation Results on Nonlinear Filtering

Fig. 5.5 illustrates the simulation setup. The lateral line system is placed parallel to the  $x$ -axis and centered at  $(5, 0)$  cm. It consists of 6 sensors, with the sensor-to-sensor separation of 2 cm. The ellipsoidal cylinder, with a shape parameter ( $\lambda_1 = 1.5$  cm) and a size parameter  $R = 2.5$  cm, moves from left to right with a constant speed of 6 cm/s. The initial location of the moving object is  $(0, 7)$  cm, and the time duration for the movement is 1.667 s, resulting in a terminal location of  $(10, 7)$  cm. The initial state estimates are set to be  $\hat{x}_{s,0|0} = 0.1$  cm,  $\hat{y}_{s,0|0} = 5$  cm,  $\hat{v}_{x,0|0} = 4$  cm/s,  $\hat{v}_{y,0|0} = 1$  cm/s,  $\hat{R}_{0|0} = 1$  cm, and  $\hat{\lambda}_{1,0|0} = 0.1$  cm. The sampling time  $\Delta$  is chosen to be 0.01 s. Fig. 5.6 shows the simulated measurements of flow velocities ( $x$ -component) at all sensor sites, where a zero-mean, Gaussian noise with a variance of ( $\sigma_m^2 = 0.01$  cm<sup>2</sup>/s<sup>2</sup>) is added to each measurement.

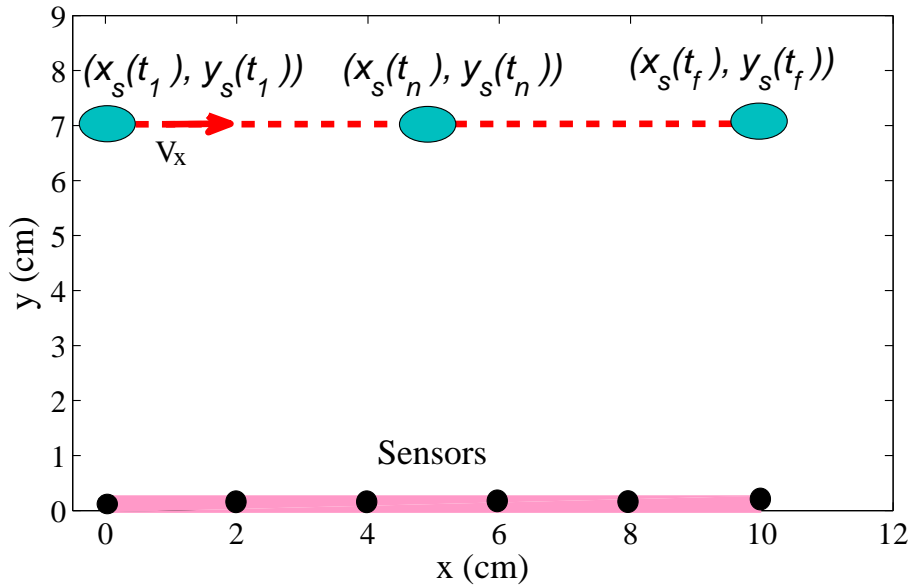


Figure 5.5: Simulation setup for tracking of a moving cylinder.

Fig. 5.7(a) shows the actual object locations and those estimated using the proposed two-stage extended Kalman filtering scheme for a typical run. Here three different val-

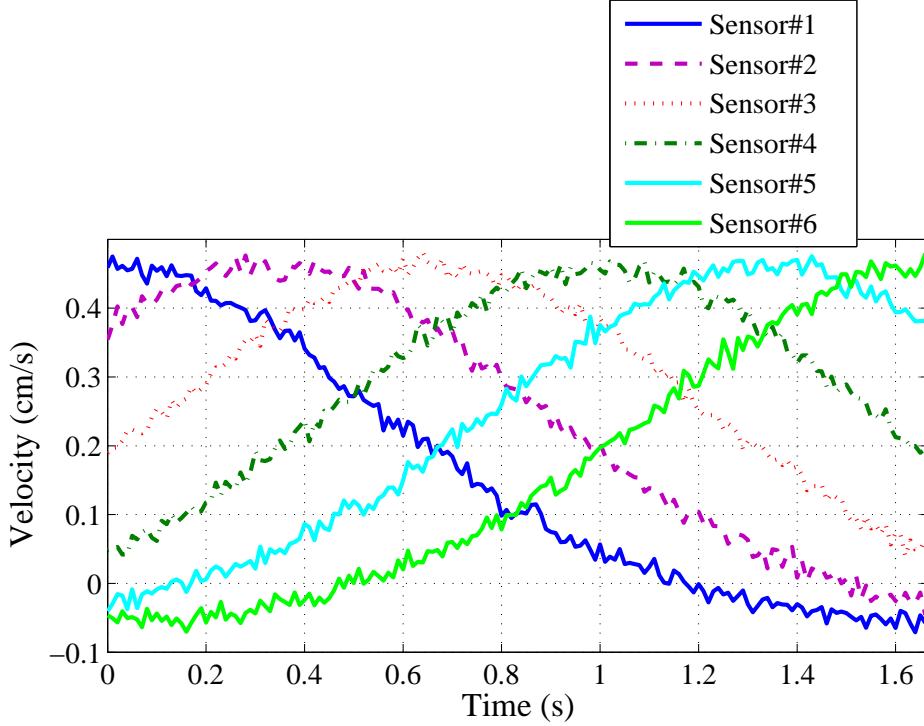
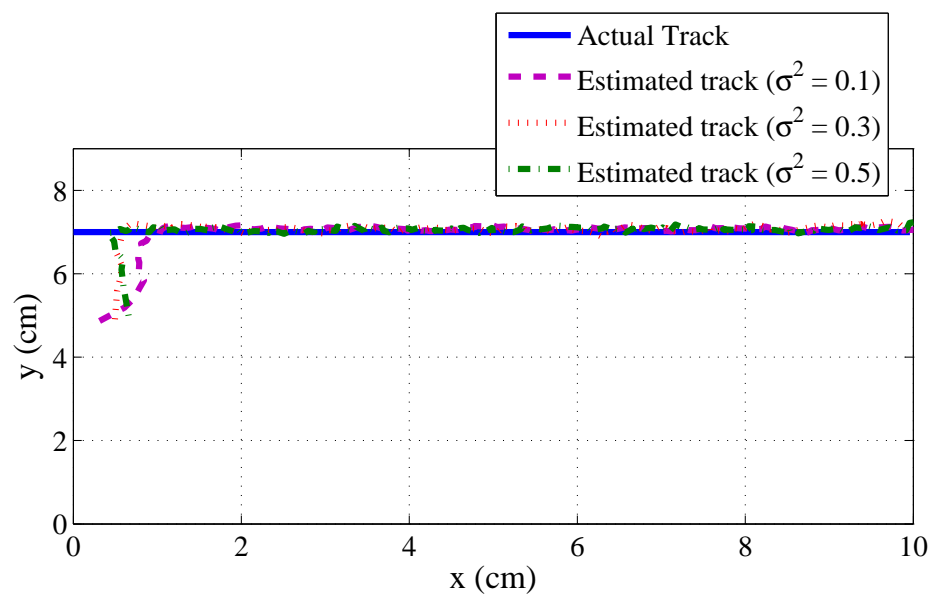


Figure 5.6: Simulated time trajectories of sensor measurements.

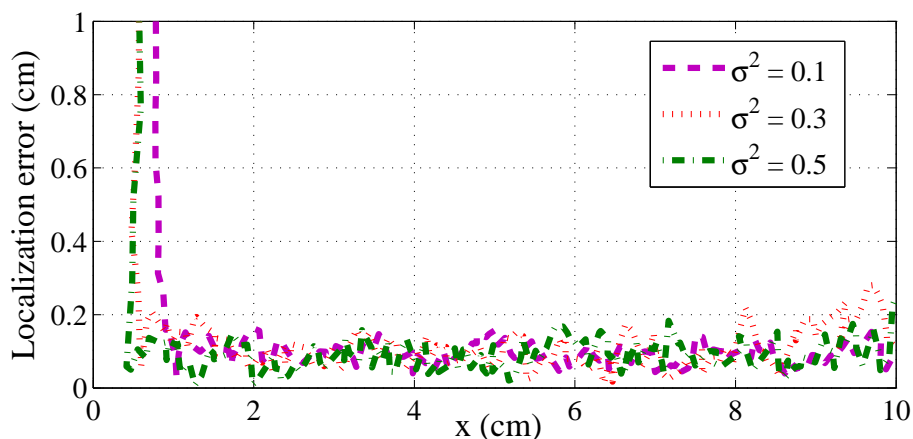
ues of variance  $\sigma^2$  for the process noises  $(w_1, \dots, w_6)$  are tested, to examine the impact of the process noise variance on the estimation results. Fig. 5.7(b) shows the localization error for each actual  $x$ -coordinate  $(x_s[k])$  of the object, where the error is defined as  $\sqrt{(\hat{x}_{s,k|k} - x_s[k])^2 + (\hat{y}_{s,k|k} - y_s[k])^2}$ .

It can be observed that the estimated object location quickly converges to the neighborhood of the actual location after a short transient period (less than 0.15 s). In addition, while the variance of the process noises does influence the transients, its impact on the estimation performance at the steady state is not pronounced. The insensitivity of the estimation performance to the process noise variances is a positive news, since it is difficult to precisely characterize these noise variance values in practice. Table 5.1 summarizes the averages of the estimates for other parameters ( $v_x$ ,  $R$ , and  $\lambda_1$ ), where each average is obtained by taking

the mean of the estimated values over the period  $[0.33, 1.67]$  s. We have further studied



(a)



(b)

Figure 5.7: Simulation results on tracking the ellipsoidal cylinder using two-stage extended Kalman filtering: (a) The estimation of the moving object location for different variance values for the process noises; (b) localization error at each  $x$ -coordinate of the object. The measurement noise variance is held at  $0.01 \text{ cm}^2/\text{s}^2$ .

the impact of the measurement noise variance  $\sigma_m^2$ . Fig. 5.8 shows the localization results for different values of  $\sigma_m^2$ , while the variance for each process noise,  $\sigma^2$ , is held constant at 0.3

Table 5.1: Simulation results: Estimated velocity, size parameter, and shape parameter under different process noise variances. Two-stage extended Kalman filtering is used.

Parameter	Actual	Estimated ( $\sigma^2 = 0.1$ )	( $\sigma^2 = 0.3$ )	( $\sigma^2 = 0.5$ )
Velocity (cm/s)	6	6.22	6.35	6.44
Size R (cm)	2.5	2.34	2.41	2.32
Shape $\lambda_1$ (cm)	1.5	1.23	1.42	1.43

Table 5.2: Simulation results: Estimated velocity, size parameter, and shape parameter under different measurement noise variances. Estimation is done with two-stage extended Kalman filtering.

Parameter	Actual	Estimated ( $\sigma_m^2 = 0.01$ )	( $\sigma_m^2 = 0.03$ )	( $\sigma_m^2 = 0.05$ )
Velocity( cm/s)	6	6.45	7.23	7.24
Size R (cm)	2.5	2.38	2.24	2.258
Shape $\lambda_1$ (cm)	1.5	1.45	1.42	1.63

(in its respective unit), while Table 5.2 lists the averages of estimated values for  $v_x$ ,  $R$ , and  $\lambda_1$ .

It can be seen that, overall, the measurement noise variance has an appreciable impact on the estimation performance; in general, larger measurement noise variance leads to longer transient and larger estimation error, which is consistent with one's intuition. We have further studied the impact of the input and measurement noise variances for a one-stage extended Kalman filtering scheme in Appendix B.2.

Finally, the performance of the three nonlinear tracking filters, designed for this problem, are compared against each other. The considered filters include the extended Kalman filtering (EKF), unscented Kalman filtering (UKF), and regularized particle filtering (RPF). Under two-stage typical run, the results for the actual object locations and those mean estimated and their estimation errors are shown in Fig. 5.9.

From Fig. 5.9, we can see that the three nonlinear filters are unbiased and all of them demonstrate almost similar tracking accuracy. Table 5.3 summarizes the averages of the estimates for other parameters ( $v_x$ ,  $R$ , and  $\lambda_1$ ) for the three nonlinear filters.

Table 5.3: Simulation results: Estimated velocity, size parameter, and shape parameter under three nonlinear filtering algorithms.

Parameter	Actual	Estimated (EKF)	Estimated (UKF)	Estimated (RPF)
Velocity (cm/s)	6	6.45	6.33	6.23
Size $R$ (cm)	2.5	2.83	2.24	2.25
Shape $\lambda_1$ (cm)	1.5	1.45	1.42	1.55

In terms of the computational load of the three algorithms, the following results are obtained (based on MATLAB implementation). The UKF requires 5 times more CPU time than the EKF. The RPF (with 1000 particles) requires 110 times more time than the EKF. Therefore, the EKF is the most efficient scheme among those compared.

## 5.4 Experimental Results

Fig. 5.10 shows the schematic of the experimental setup, while Figs. 5.11(a) and (b) show the picture of the actual experimental system. The artificial lateral line consisted of six IPMC sensors. The sensor-to-sensor separation was 2 cm, resulting in a total span of 10 cm. Each sensor was mounted in such a way that it would bend in the direction parallel to the sensor array, which is denoted as  $x$ -direction. The experiments were conducted in a water tank measuring 6 ft long, 2 ft wide, and 2 ft deep. A digital particle image velocimetry (DPIV) system (LaVision, Ypsilanti, MI), not shown in Fig. ??, which was explained earlier in Chapter 3, was used to measure the flow for model validation. A custom-built, motor-driven conveyor was used to move an object in the water. The system can be driven by a DC

motor or an AC motor. In our experiments, two objects were used, the first one is a circular cylinder with outer radius of 3.02 cm and an ellipsoidal cylinder with the minor and major diameters of 2.5 cm and 5 cm, respectively. Both objects had a height of 10 cm. The speed of the object can be adjusted by varying the voltage to the motor or changing the setup of the gearbox that is associated with the AC motor. The conveyor track was separated from the lateral line system by 7 cm. The signals from the IPMC sensors were conditioned and amplified before the acquisition and processing by a PC equipped with dSPACE (DS 1104, dSPACE).

We first conducted DPIV measurements (using DC motor driving the moving object) to validate the flow model (5.3). Fig. 5.12 shows the comparison of the measured flow velocity ( $x$ -component) with the prediction by (5.3) at a particular sensor site, when the circular cylinder was moved to pass by the sensor site at a speed of 6.67 cm/s. The reasonably good match between the model and the measurement in Fig. 5.12 supports the use of the flow model in this work.

Before running the tracking experiments, we performed the calibration of all IPMC sensors using the mini-shaker. The details of the calibration process are explained earlier in Chapter 3.

Fig. 5.13 shows the measured flow velocities by all six IPMC sensors when the cylindrical and ellipsoidal object traveled by the lateral line system at 6.67 cm/s and 40 cm/s, respectively, which demonstrates a similar shape pattern as in Fig. 5.6.

Fig. 5.14(a) shows the actual trajectory of the moving cylinder and its estimate using the first-stage Kalman filtering shown in Fig. 5.3, and Fig. 5.14(b) shows the tracking error. Since it was known that the cross-section of this cylinder was circular, the shape parameter was

not identified in these experiments. The process noise variances were chosen to be  $\sigma^2 = 0.3$  (in its respective unit of each state component) and the measurement noise variances were set to be  $\sigma_m^2 = 0.01 \text{ (cm/s)}^2$ . Table 5.4 lists the estimated moving speed and size parameter. The tracking error was less than 0.5 cm and the errors in estimating  $v_x$  and  $R$  were less than 25%, which demonstrates the effectiveness of the proposed modeling and estimation approach.

Table 5.4: Cylindrical object experimental results: Estimated velocity and size parameter.

Parameter	Actual	Estimated	Error
Velocity (cm/s)	6.667	8.3	1.6
Size R (cm)	3.02	3.51	0.49

Fig. 5.15 (a) shows the actual trajectory of the moving ellipsoidal object and its estimate using the two-stage Kalman filtering shown in Fig. 5.3, and Fig. 5.14(b) shows the tracking error. The actual size and the shape parameter of the ellipsoidal object were identified to be  $R = 1.5 \text{ cm}$  and  $\lambda_1 = 1.25 \text{ cm}$ , respectively. The process noise variances and measurement noise were chosen as explained earlier in the cylindrical experiment setup.

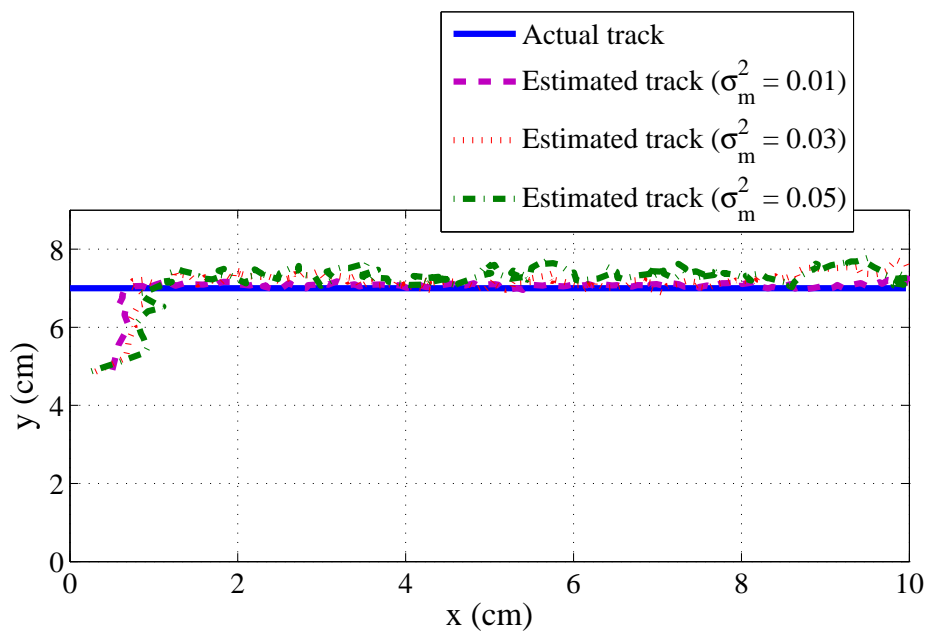
Table 5.5 lists the estimated moving speed, size, and shape parameter. The tracking error was less than 0.45 cm and the errors in estimating  $v_x$  and  $R$  were less than 33%, which demonstrates the effectiveness of the proposed modeling and estimation approach.

Table 5.5: Ellipsoidal object experimental results: Estimated velocity, size parameter, and shape parameter.

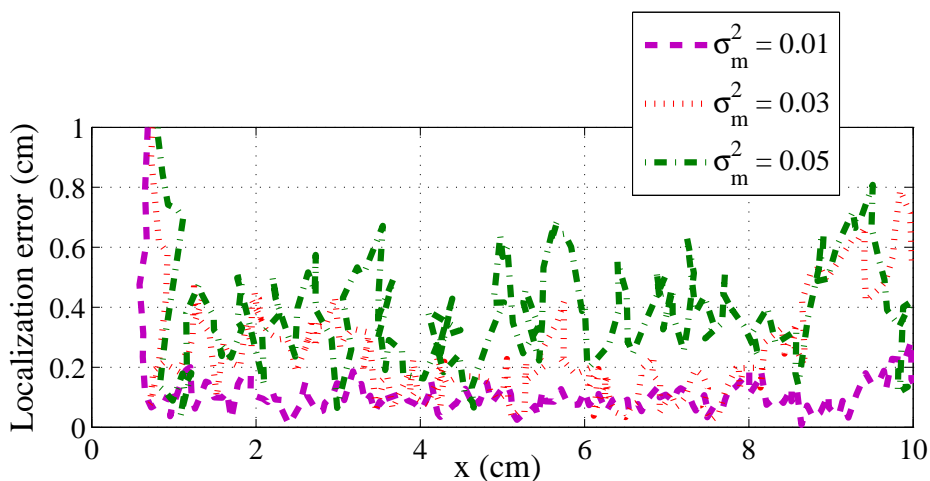
Parameter	Actual	Estimated	Error
Velocity (cm/s)	40	41	1
Size R (cm)	1.5	1.9	0.4
Shape $\lambda_1$ (cm)	1.25	1.6	0.35

## 5.5 Chapter Summary

In this chapter we proposed new nonlinear filtering algorithms for object tracking and estimation using artificial lateral lines. Based on a 2D potential flow model, an estimation problem was proposed and solved with a two-stage nonlinear filtering method. Extended Kalman filtering was shown to have similar tracking accuracy performance as unscented Kalman filtering and regularized particle filtering while having the least computational complexity. Simulation results were presented to illustrate and demonstrate the effectiveness of the proposed approach, where the impacts of process noises and measurement noises were explored. Experimental results were also reported, where an artificial lateral line prototype consisting of six IPMC sensors was used to track and estimate the size and the shape of both a cylinder and an ellipse moving object.



(a)



(b)

Figure 5.8: Simulation results on tracking the ellipsoidal cylinder using the two-stage extended Kalman filtering: (a) The estimation of the moving object location for different variance values for the measurement noises; (b) localization error at each  $x$ -coordinate of the object. The process noise variance is held at 0.3 (in its respective unit for each state component).

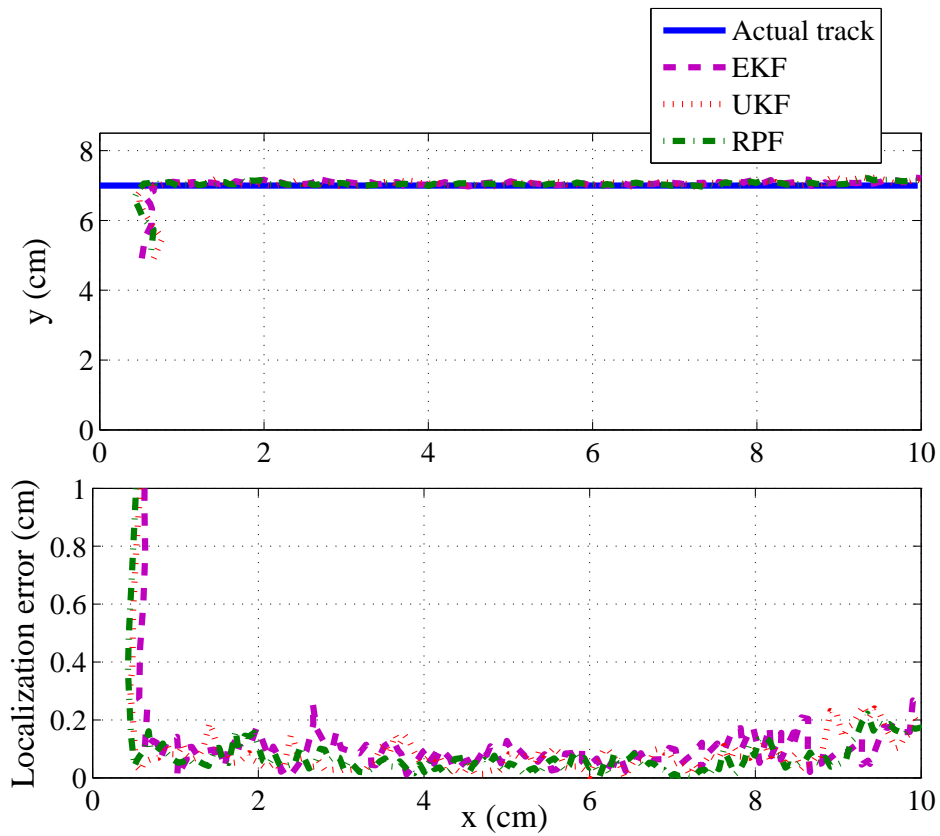


Figure 5.9: Simulation results on tracking the ellipsoidal cylinder for three nonlinear filters: The process noise variance is held at 0.3 (in its respective unit for each state component) and the measurement noise variance is held at  $0.01 \text{ cm}^2/\text{s}^2$ .

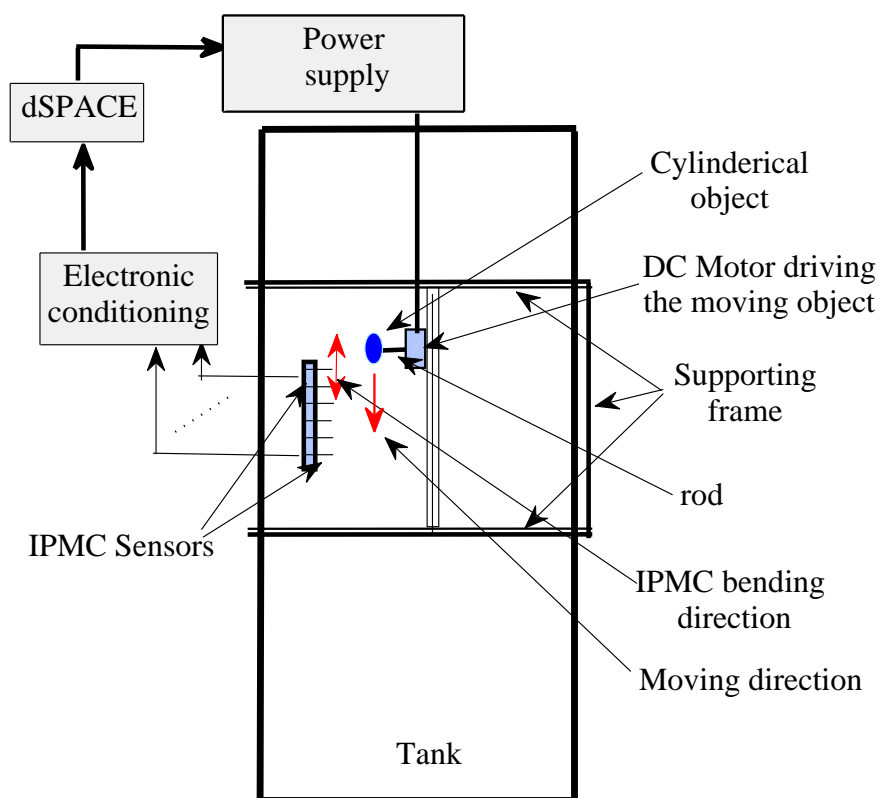
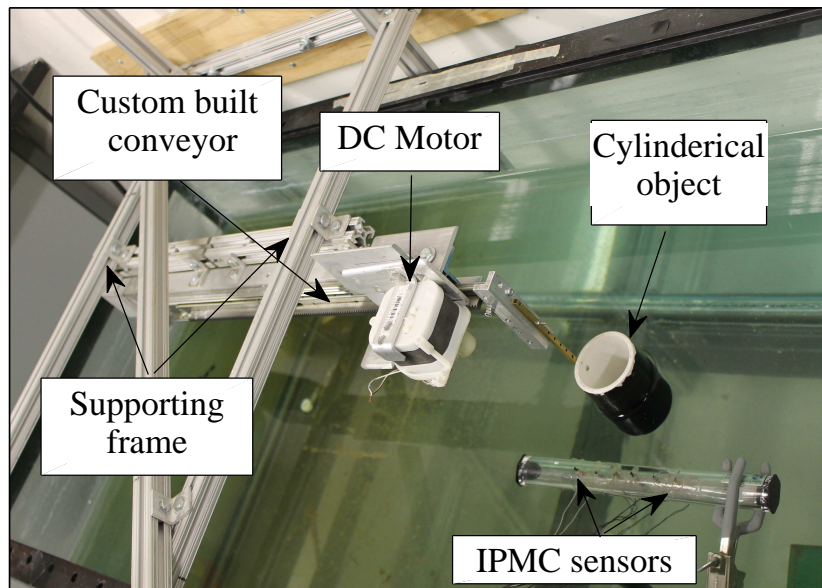
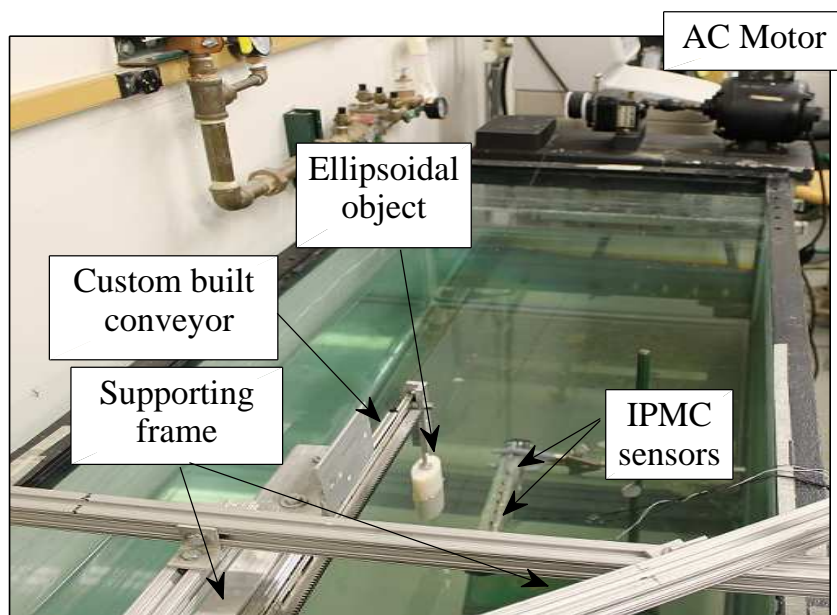


Figure 5.10: Experimental setup: Schematic.



(a)



(b)

Figure 5.11: Experimental setup: (a) Picture of the experimental setup with a circular cylinder; (b) picture of the experimental setup with an ellipsoidal cylinder.

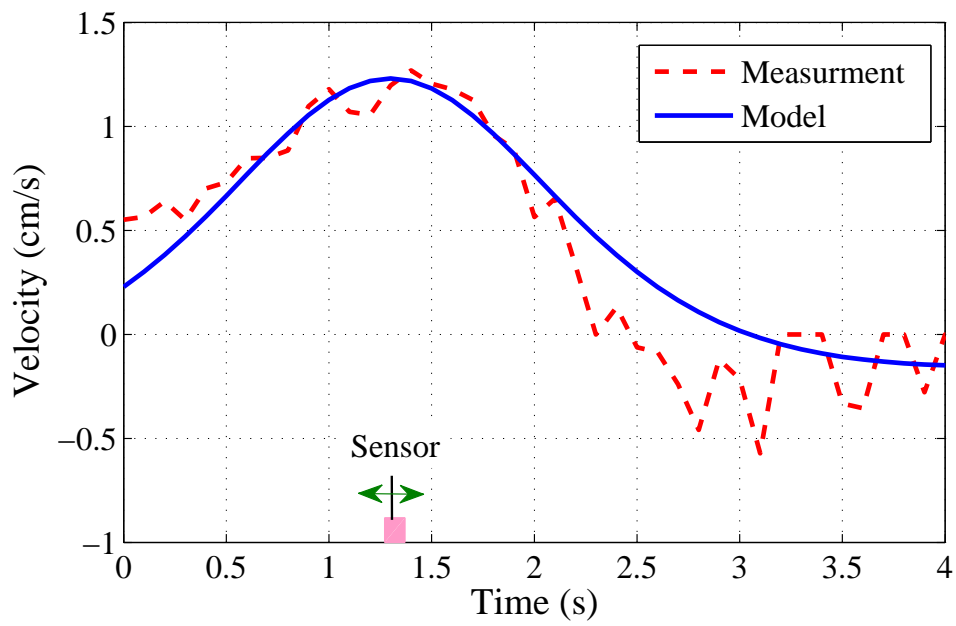
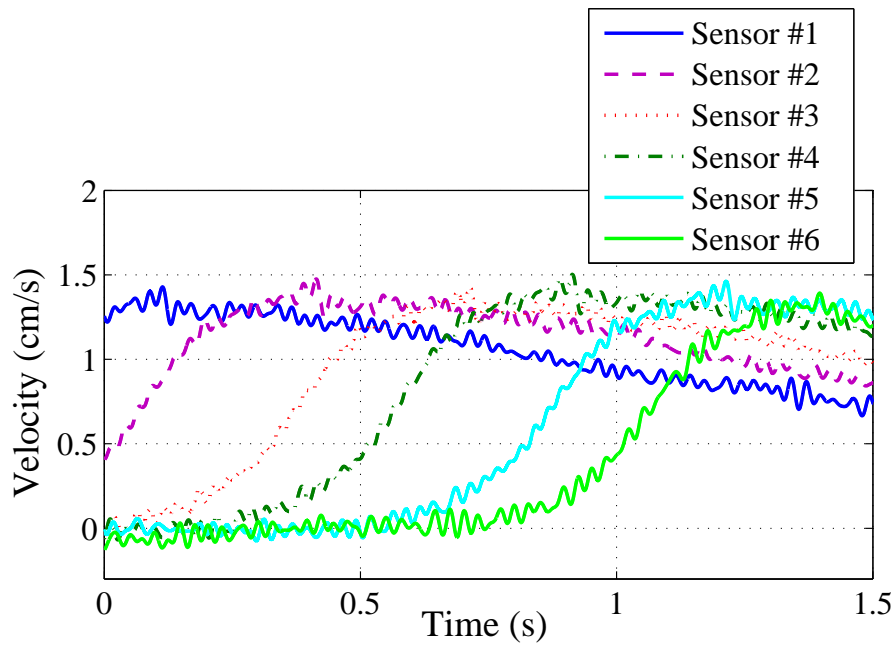
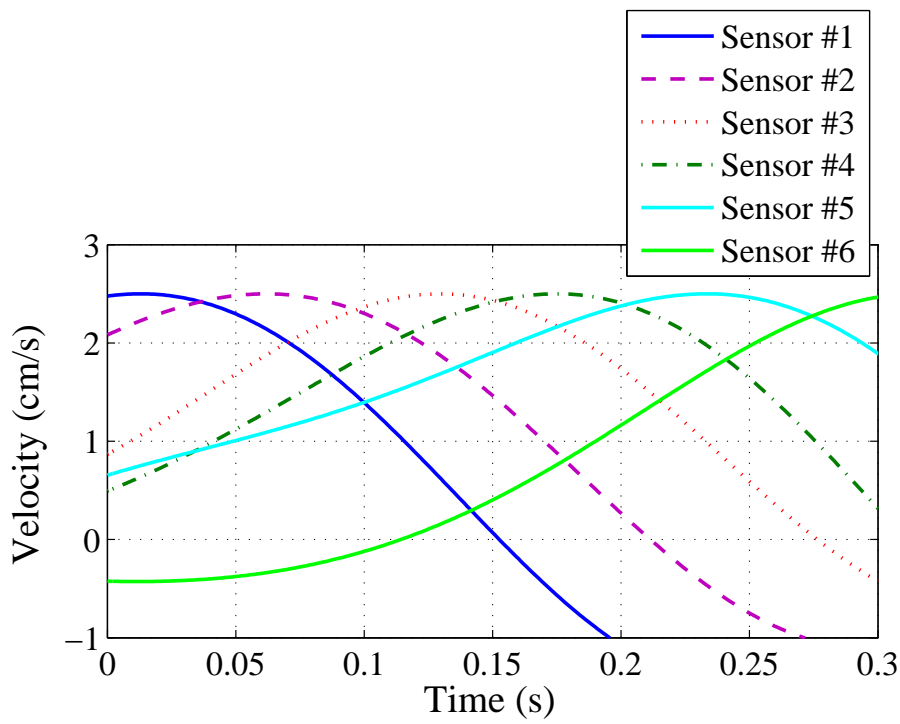


Figure 5.12: Comparison of DPIV-measured flow velocity with the model prediction.

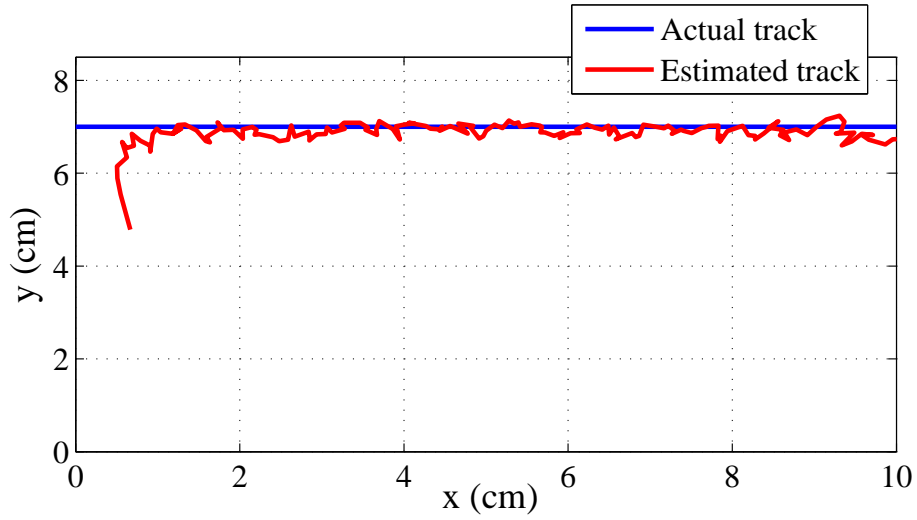


(a)

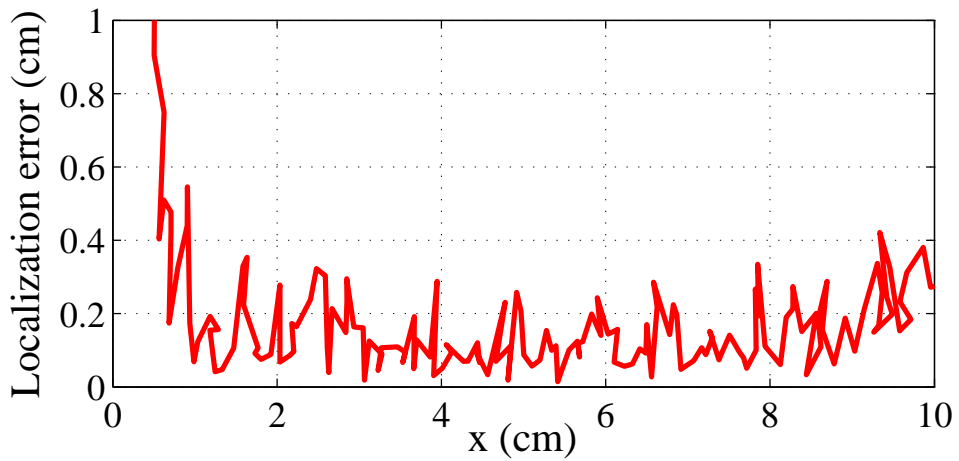


(b)

Figure 5.13: Measured flow velocities by six IPMC sensors: (a) DC motor driving the cylindrical object, with digital low pass filter ( $f_c = 42$ ) Hz; (b) AC motor driving ellipsoidal object, with digital low pass filter ( $f_c = 4$ ) Hz.

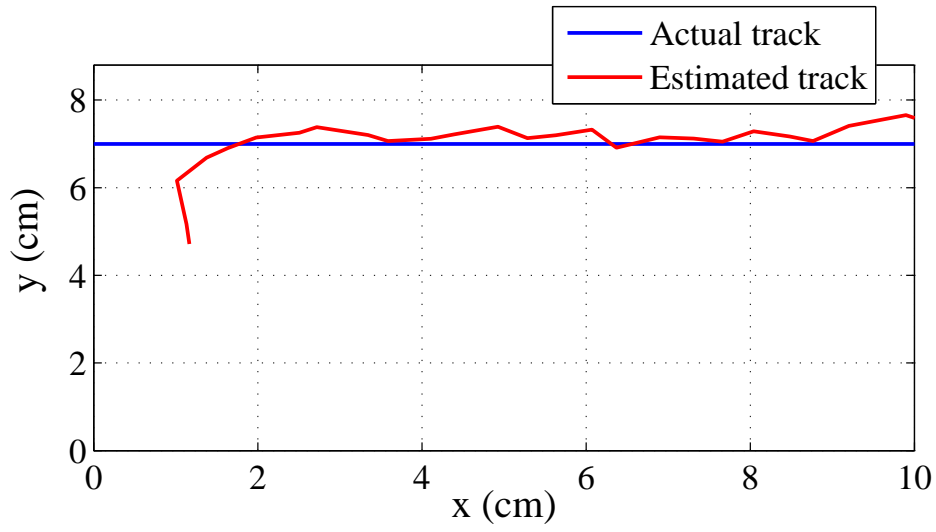


(a)

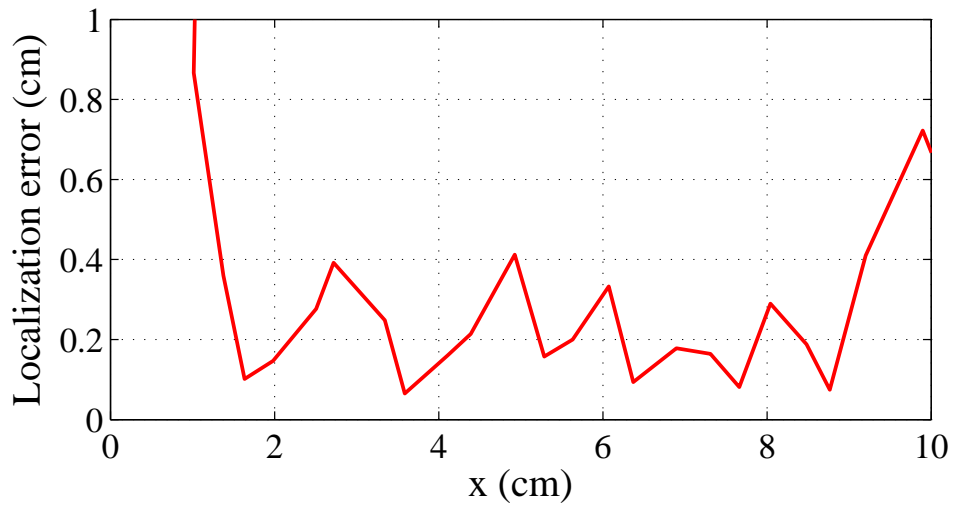


(b)

Figure 5.14: Experimental results on tracking a cylinder with circular profile with two-stage extended Kalman filtering: (a) The estimation of the object location; (b) localization error at each  $x$ -coordinate of the object.



(a)



(b)

Figure 5.15: Ellipsoidal object experimental results on tracking an ellipse: (a) The estimation of the object location; (b) localization error at each  $x$ -coordinate of the object.

# Chapter 6

## Exploration of IPMC Sensors in Vortex Street Sensing

Most fish frequently exploit unsteady forcing of ambient/wake flow to extract energy for efficient locomotion and for obstacle avoidance. In this chapter, we first describe an analytical model for a pair of stable vortices outside an obstacle and then for a Kármán vortex street. Second, with extensive experiments, we explore the problem of identifying hydrodynamic parameters associated with an obstacle in a flow using IPMC sensors. In particular, we show that it is feasible to identify flow velocity and obstacle size based on the measurement of vortex shedding frequency.

The remainder of the chapter is organized as follows. In Section 6.1 the model for a stationary vortex and that for a Kármán vortex street are described. The localization of a static obstacle is discussed in Section 6.2. The experimental setup and results are described in Section 6.3. Finally, chapter summary is provided in Section 6.4.

## 6.1 Stationary Vortex and Kármán Vortex Street

The circle theory reported in [89] proves that any pair of vortices behind a cylinder is stable. Therefore, for every point  $z$  outside the circle of radius  $R$  in the complex plane, there is another opposite point (its complex conjugate),  $\bar{z} = R^2/z$ , which lies inside the circle. Thus, we have two singularities at these points:  $f(z)$ , where a point  $z$  lies outside the circle, and  $\bar{f}(\bar{z}) = \bar{f}(R^2/z)$ , where a point  $\bar{z}$  lies inside the circle. The complex potential  $w(z)$  of these singularities is given by

$$w(z) = f(z) + \bar{f}(R^2/z). \quad (6.1)$$

Generally, the circle theory says that for each vortex outside the circle has a vortex of equal strength but opposite direction inside the circle, which provides an analytical tool for modeling vortex shedding behind a circular cylindrical obstacle. First, we consider two vortices located in the complex plane. The first vortex at position  $p_1$  has a complex coordinate  $z_1$  and strength  $k$ , and the other vortex at position  $p_2$  has a complex coordinate  $\bar{z}_1$  and strength  $-k$ , as shown in Fig. 6.1. The complex potential  $w$  in presence of the cylinder  $|z| = R$  is given as

$$\begin{aligned} w &= ik \ln(z - z_1) + w_z, \\ w_z &= -ik \ln(z - \bar{z}_1) - V \left( z + R^2/z \right) - ik \ln \frac{\left( \frac{R^2}{z} - \bar{z}_1 \right)}{\left( \frac{R^2}{z} - z_1 \right)}. \end{aligned} \quad (6.2)$$

Here  $V$  is the nominal cross flow velocity. The vortex at  $p_1$  will be at rest if  $\frac{dw_z}{dz} = 0$ , which means that its velocity is zero. With this condition, it can be demonstrated [89] that the

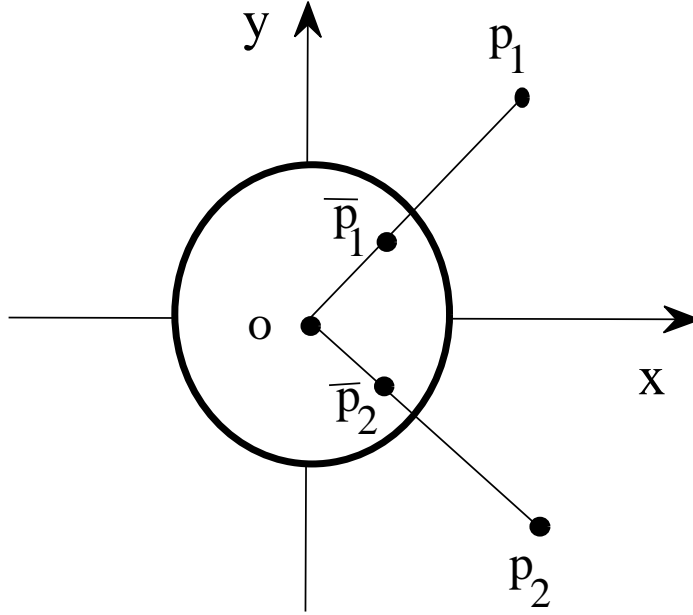


Figure 6.1: Illustration of the analytical model for cylinder-shed vorticity.

vortices behind a cylinder in flow are stable with the vortex strength of  $k$  given by

$$k = V(\|\mathbf{r}\|^2 - R^2)(\|\mathbf{r}\|^2 + R^2) / \|\mathbf{r}\|^5, \quad (6.3)$$

where  $\mathbf{r} = (x, y)^T$ , and  $T$  denotes the transpose. Accordingly, we can find the exact position of the stable vortices behind the cylinder when we use the transformation  $z = \|\mathbf{r}\| e^{i\theta}$ , where  $0 \leq \theta \leq 90^\circ$ , implying

$$\|\mathbf{r}\|^2 = \frac{R^2}{1 - \sin(\theta)}. \quad (6.4)$$

Fig. 6.2 shows the stable vortices behind a cylinder ( $R = 1$  cm) in a flow with nominal velocity of 2 cm/s.

Second, we consider the case of a shed Kármán vortex street which consists of two parallel

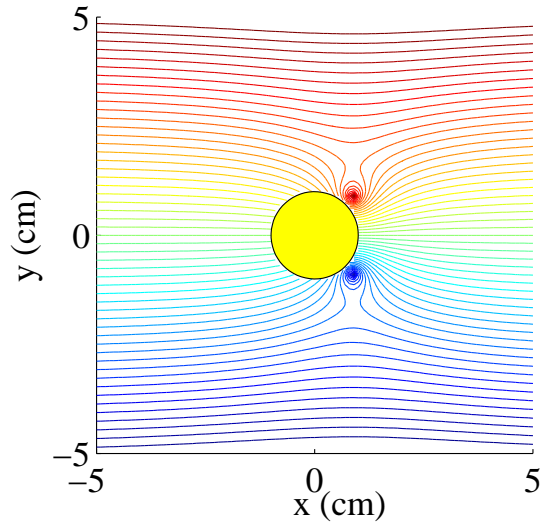


Figure 6.2: Visualization of the flow around a cylinder.

semi infinite columns of vortices of the same spacing, say  $a$ . We denote the vertical distance between the columns as  $b$ . The vortex strength is  $k$  for all vortices with  $y > 0$  and it is  $-k$  for all vortices with  $y < 0$  as shown in Fig. 6.3.

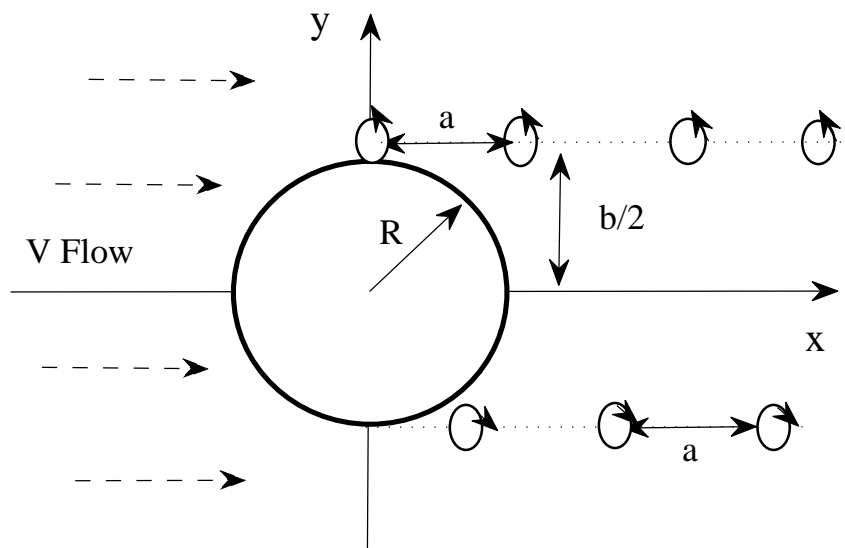


Figure 6.3: Illustration of the analytical model for cylinder-shed Kármán vortex street.

The complex potential for the vortex street at instant  $t = 0$  is given as [89],

$$w_o^c(z) = V(z + R^2/z) + ik \ln \left( \sin \frac{\pi}{a} \left( z - \frac{ib}{2} \right) \right) - ik \ln \left( \sin \frac{\pi}{a} \left( z - \frac{a}{2} + \frac{ib}{2} \right) \right), \quad (6.5)$$

which implies that complex flow velocity  $W_o^c = \frac{dw_o^c(z)}{dz}$  at time  $t = 0$  is given by

$$W_o^c(z) = \left\{ V(1 - (R/z)^2) + \frac{i\pi k}{a} \left\{ \cot \frac{\pi}{a} \left( z - \frac{ib}{2} \right) - \cot \frac{\pi}{a} \left( z - \frac{a}{2} + \frac{ib}{2} \right) \right\} \right\}, \quad (6.6)$$

where  $z$  is outside the region occupied by the cylinder. The complex flow velocity at any instant  $t$  is given by

$$W_o^c(z) = V(1 - (R/z)^2) + \frac{i\pi k}{a} \left\{ \cot \frac{\pi}{a} \left( z - u_v t - \frac{ib}{2} \right) - \cot \frac{\pi}{a} \left( z - u_v t - \frac{a}{2} + \frac{ib}{2} \right) \right\}, \quad (6.7)$$

where  $u_v$ , the velocity of the vortex street, is given by

$$u_v = V - \frac{\pi k}{a} \tanh \left( \frac{b}{a} \pi \right). \quad (6.8)$$

Finally, the relationship between  $a$  and  $b$  is approximately [89]

$$\frac{b}{a} = \frac{1}{\pi} \cosh^{-1} \sqrt{2}. \quad (6.9)$$

The initial configuration will repeat itself after it has moved a horizontal distance equal to  $a$ .

Now, we need to relate this solution to an ellipsoidal obstacle shape. To accomplish this, we use a conformal mapping function called the Joukowski transformation. The Joukowski

transformation transforms circles in the  $\zeta$  plane into shapes that resemble ellipses in the  $z$  plane [77]. In contrast to the usual way, we will not study the flow velocity in the  $\zeta$ -plane, but in the original  $z$ -plane. Consider,  $\zeta(z) := z + \lambda^2/z$  with a real shape parameter  $\lambda$ , which implies that the obtained obstacle shape will be symmetric with respect to the  $x$ -direction. It can be shown that the complex flow velocity  $W_o^e$  around an ellipsoidal obstacle is given by

$$\begin{aligned}
W_o^e(z) &= \underbrace{\left(\frac{dw^c(z)}{dz}\right)}_{W_o^e} \left(\frac{d\zeta}{dz}\right)^{-1} \\
&= \left\{ V(1 - (R/z)^2) + \frac{i\pi k}{a} \left\{ \cot \frac{\pi}{a} \left( z - u_v t - \frac{ib}{2} \right) - \cot \frac{\pi}{a} \left( z - u_v t - \frac{a}{2} + \frac{ib}{2} \right) \right\} \right\} \\
&\quad \left\{ 1 - (\lambda/z)^2 \right\}^{-1}. \tag{6.10}
\end{aligned}$$

In (6.10),  $z \in D$ , the domain outside an ellipsoidal obstacle. Fig. 6.4 shows the visualization of a Kármán vortex street behind an obstacle, where Table 6.1 summarizes the values of the setup parameters.

Table 6.1: Simulation results: Setup parameters.

Parameter	Value
Nominal flow velocity (cm/s)	2
Distance between vortices $a$ (cm)	1
Vortex strength	1
Radius $R$ (cm)	1
Shape parameter $\lambda$ (cm)	0.5

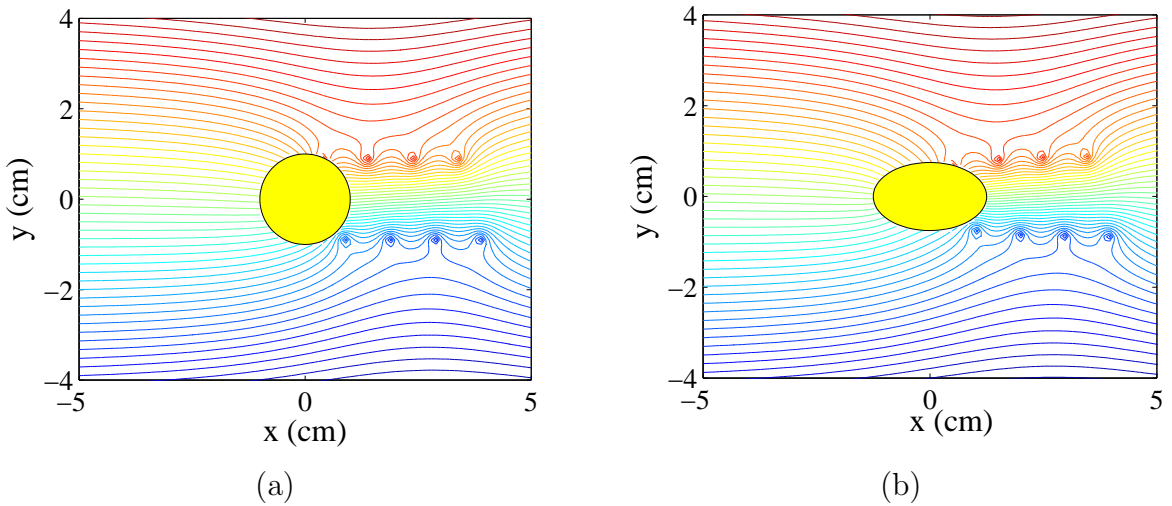


Figure 6.4: Visualization of a Kármán vortex street flow field around: (a) Circular cylinder; (b) ellipsoidal cylinder.

## 6.2 Localization of an Obstacle: Problem Formulation

We now defined the problem in the two-dimensional  $x - y$  plane. As illustrated in Fig. 6.5, suppose that a cylindrical static obstacle is located at  $(x_o, y_o)$ , where  $(z_o = x_o + iy_o)$  is the center of that obstacle and its size parameter (radius of circle) is  $R_o$ , in a flow with constant nominal flow velocity  $V$  that has an angle  $\alpha$  with respect to the  $x$ -axis. It will generate a vortex street with the vortex shedding frequency  $f_{sh}$ . The Strouhal number ( $St$ ) is a dimensionless index, given by

$$St = \frac{f_{sh}(2R)}{v^c}, \quad (6.11)$$

where  $v^c$  is the actual flow velocity in the region behind the cylindrical obstacle. The Strouhal number depends on the Reynolds number; however, it remains at an almost constant value of 0.22 for Reynolds number  $> 2000$  [4]. Consider Fig. 6.5, where an artificial lateral line comprising  $N$  sensors is located in parallel to the  $x$ -axis, with the sensor locations denoted

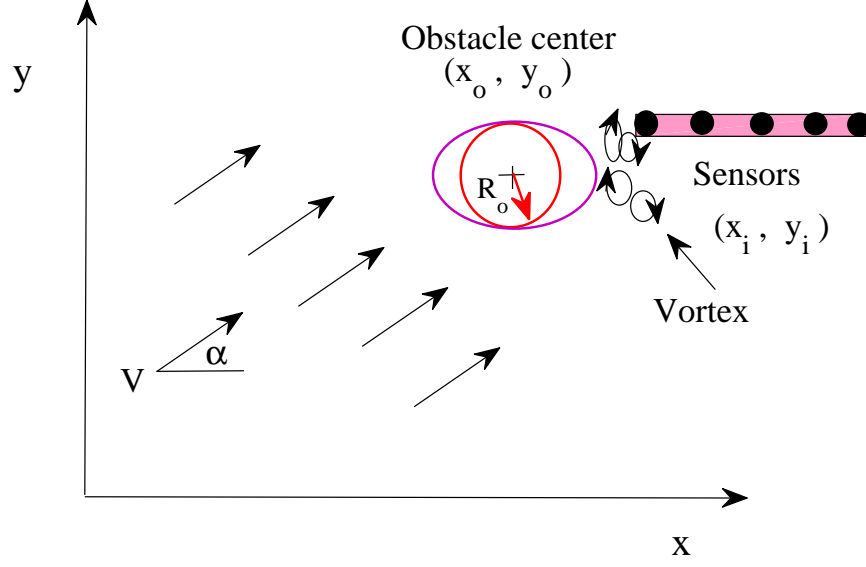


Figure 6.5: Illustration of the problem setup. The obstacle is located at  $(x_o, y_o)$ .

as  $(x_i, y_i)$ ,  $0 \leq i \leq N - 1$ . We assume that the presence of sensors has negligible effect on the flow distribution. For a circular cylinder, we can derive the complex flow velocity  $W_o^c = v_x^c + iv_y^c$  around the cylinder:

$$\begin{aligned}
v_x^c(x_i, y_i, t) = & V \cos(\alpha) \left( 1 + \frac{R_o^2}{(x_i - x_o)^2 + (y_i - y_o)^2} - \frac{2R_o^2(x_i - x_o)^2}{((x_i - x_o)^2 + (y_i - y_o)^2)^2} \right) \\
& + \text{Re} \left( \frac{i\pi k}{a} \left\{ \cot \frac{\pi}{a} \left( (x_i - x_o) + i(y_i - y_o) - u_v t - \frac{ib}{2} \right) \right. \right. \\
& \left. \left. - \cot \frac{\pi}{a} \left( (x_i - x_o) + i(y_i - y_o) - u_v t - \frac{a}{2} + \frac{ib}{2} \right) \right\} \right), \quad (6.12)
\end{aligned}$$

$$\begin{aligned}
v_y^c(x_i, y_i, t) = & -V \sin(\alpha) \left( \frac{2R_o^2(x_i - x_o)(y_i - y_o)}{((x_i - x_o)^2 + (y_i - y_o)^2)^2} \right) \\
& + \text{Im}g \left( \frac{i\pi k}{a} \left\{ \cot \frac{\pi}{a} \left( (x_i - x_o) + i(y_i - y_o) - u_v t - \frac{ib}{2} \right) \right. \right. \\
& \left. \left. - \cot \frac{\pi}{a} \left( (x_i - x_o) + i(y_i - y_o) - u_v t - \frac{a}{2} + \frac{ib}{2} \right) \right\} \right). \quad (6.13)
\end{aligned}$$

Using Joukowski transformation, we can obtain the flow velocity  $W_o^e = v_x^e + iv_y^e$  around an ellipsoidal cylinder:

$$\begin{aligned}
v_x^e(x_i, y_i, t) = & V \cos(\alpha) \left( 1 + \frac{(R_o^2 - \lambda^2)((x_i - x_o) + \lambda)}{2\lambda [(x_i - x_o) + \lambda]^2 + (y_i - y_o)^2} \right. \\
& \left. - \frac{(R^2 - \lambda^2)((x_i - x_o) - \lambda)}{2\lambda [(x_i - x_o) - \lambda]^2 + (y_i - y_o)^2} \right) \\
& + \frac{2\pi k(x_i - x_o)(y_i - y_o)\lambda^2}{a \left( ((x_i - x_o)^2 - (y_i - y_o)^2 - \lambda^2)^2 + 4(x_i - x_o)^2(y_i - y_o)^2 \right)} \\
& Re \left( \left\{ \cot \frac{\pi}{a} \left( (x_i - x_o) + i(y_i - y_o) - u_v t - \frac{ib}{2} \right) \right. \right. \\
& \left. \left. - \cot \frac{\pi}{a} \left( (x_i - x_o) + i(y_i - y_o) - u_v t - \frac{a}{2} + \frac{ib}{2} \right) \right\} \right), \quad (6.14)
\end{aligned}$$

$$\begin{aligned}
v_y^e(x_i, y_i, t) = & -V \sin(\alpha) \\
& \left( \frac{2(R_o^2 - \lambda^2)(x_i - x_o)(y_i - y_o)}{\lambda^4 - 2\lambda^2 ((x_i - x_o)^2 - (y_i - y_o)^2) + ((x_i - x_o)^2 - (y_i - y_o)^2)^2} \right) \\
& + \frac{\pi k ((x_i - x_o)^2 + (y_i - y_o)^2)^2 - \lambda^2 ((x_i - x_o)^2 - (y_i - y_o)^2)}{a \left( ((x_i - x_o)^2 - (y_i - y_o)^2 - \lambda^2)^2 + 4(x_i - x_o)^2(y_i - y_o)^2 \right)} \\
& Img \left( \left\{ \cot \frac{\pi}{a} \left( (x_i - x_o) + i(y_i - y_o) - u_v t - \frac{ib}{2} \right) \right. \right. \\
& \left. \left. - \cot \frac{\pi}{a} \left( (x_i - x_o) + i(y_i - y_o) - u_v t - \frac{a}{2} + \frac{ib}{2} \right) \right\} \right). \quad (6.15)
\end{aligned}$$

Fig 6.6 shows a typical flow velocity behind a circular cylinder ( $R_o = 2$  cm) and an ellipsoidal obstacle shape ( $\lambda = 1.5$  cm), respectively. The obstacle's center is located at  $(x_o = -2, y_o = 5)$  cm. The obstacles are exposed to a cross flow with nominal flow velocity of 15 cm/s, and the vortex strength is set to be  $k = 0.08$ .

Each sensor is assumed to provide a noisy measurement of the local flow velocity  $v_x$  along

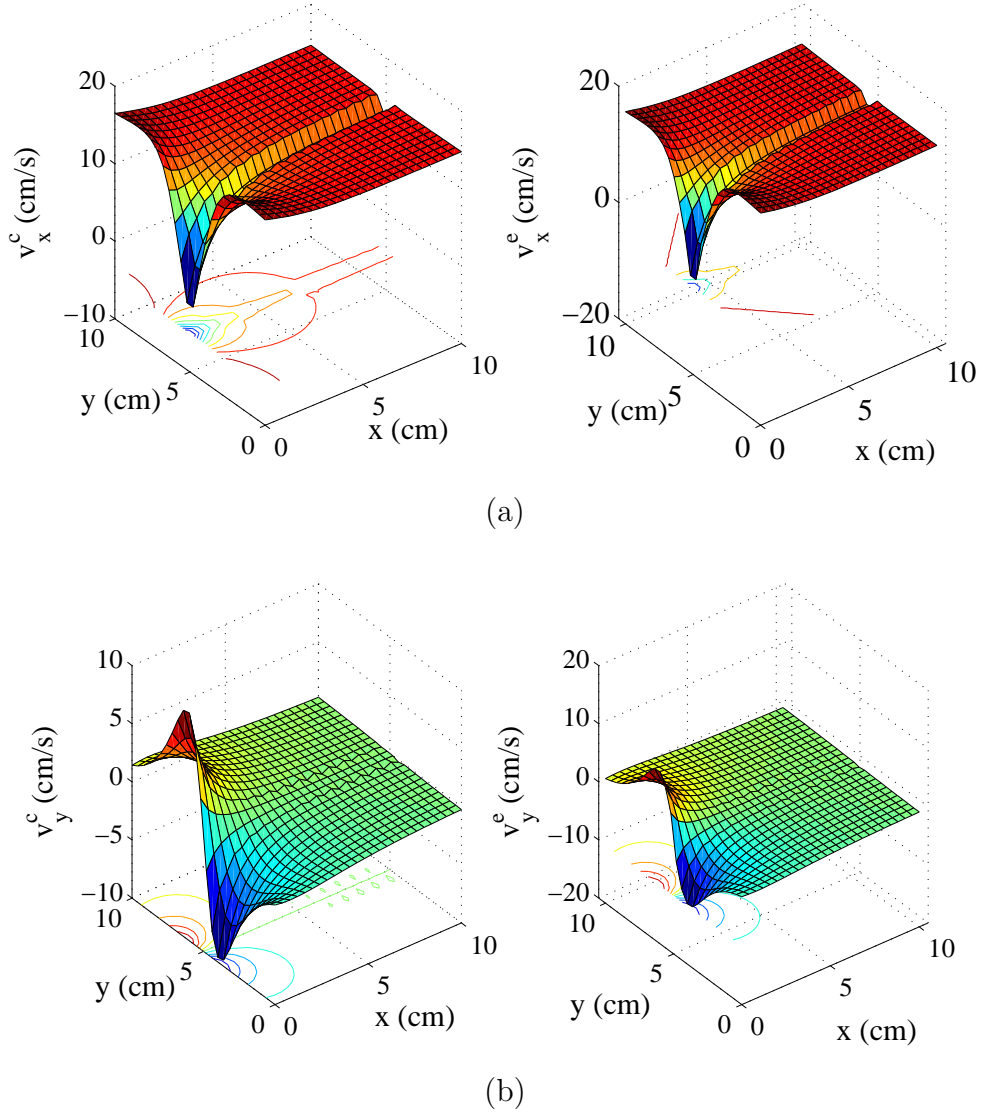


Figure 6.6: Simulation results: 3D illustration of flow velocity behind the obstacles: (a) Along the  $x$ -direction; (b) along the  $y$ -direction. In each subfigure, the left plot shows the velocity for the circular cylinder while the right plot shows the velocity for the ellipsoidal cylinder.

the  $x$ -direction. In particular, the measurement  $m_i(t)$  by sensor  $i$  at time  $t$  is given by

$$m_i(t) = f^e(x_i, y_i, x_o, y_o, V, \alpha, R_o, \lambda, a, b, u_v, k) + d_i(t), \quad (6.16)$$

where the function  $f^e$  follows from (6.14), and  $d_i$  is the measurement noise. We introduce a compact notation for the measurements from all sensors,

$$M(t) = [m_1(t) \cdots m_N(t)]^T = F^e(x_o, y_o, V, \alpha, R_o, \lambda, a, b, u_v, k) + d(t),$$

where  $T$  denotes transpose,

$$F^e(x_o, y_o, V, \alpha, R_o, \lambda, a, b, u_v, k) \triangleq [f^e(x_1, y_1, x_o, y_o, V, \alpha, R_o, \lambda, a, b, u_v, k) \cdots f^e(x_N, y_N, x_o, y_o, V, \alpha, R_o, \lambda, a, b, u_v, k)]^T,$$

and  $d(t) = [d_1(t) \cdots d_N(t)]^T$ .

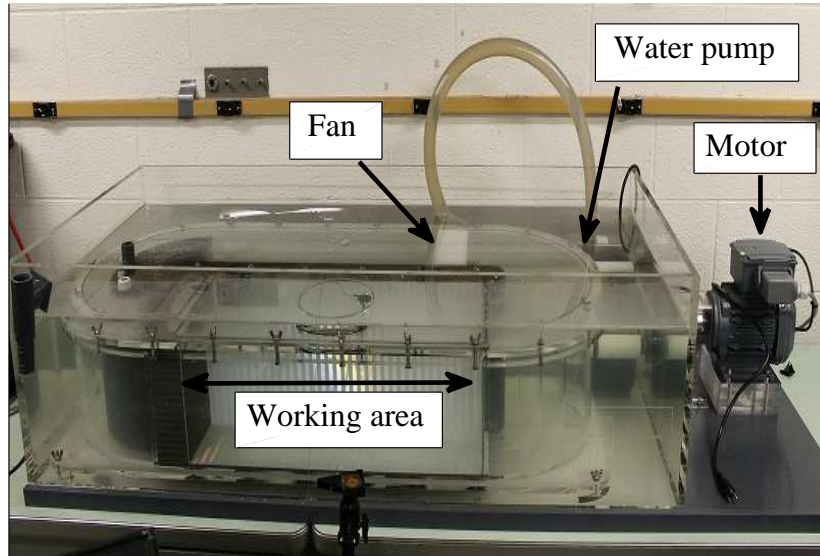
The estimation problem is then formulated as: given the measurements from the artificial lateral line,  $M(\cdot)$ , estimate the obstacle location  $(x_o, y_o)$ , size  $R_o$  and shape parameter  $\lambda$ , flow velocity  $V$ , and angle  $\alpha$ . In the next section, we provide some experimental evidence on how part of the estimation problem can be solved.

## 6.3 Experimental Setup and Results

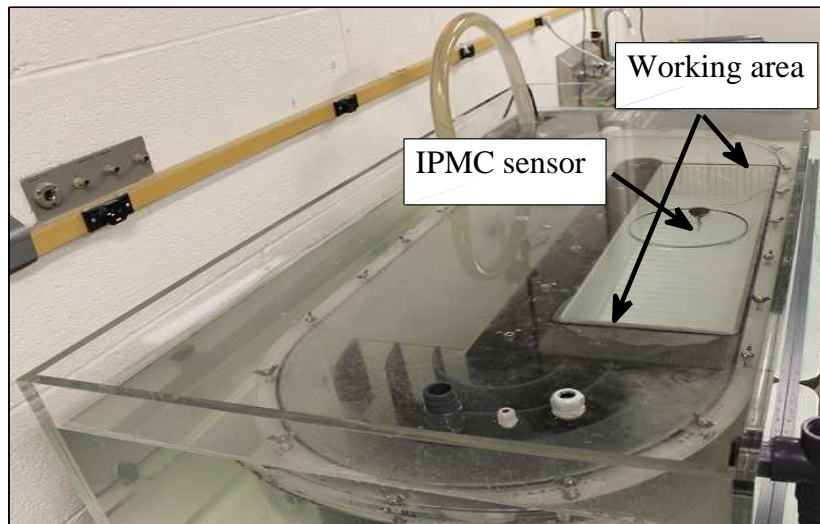
### 6.3.1 Swim Tunnel Flow Calibration

We have conducted experiments in a swim tunnel (Loligo Systems) measuring (length = 146 × width = 68 × height = 35) cm<sup>3</sup>, with a working section of (65 × 20 × 20) cm<sup>3</sup>, as shown in Fig. 6.7.

The nominal flow velocity in the working section of the swim tunnel tank is controlling through a knob. In order to calibrate the swim tunnel, we measured the nominal flow



(a)



(b)

Figure 6.7: Loligo Systems swim tunnel: (a) Side view; (b) top view.

velocity using a 515/2536 Rotor-X paddle wheel flow sensor. We mounted the flow sensor to the swim tunnel as shown in Fig. 6.8. The knob readings of 7 to 30 were used, and the

flow was allowed to stabilize at the new flow speed for a minimum of 3 minutes between the experiments. The calibration curve is shown in Fig. 6.8(c), where we can clearly see an affine relationship between the sensor output (cm/s) and the knob reading.

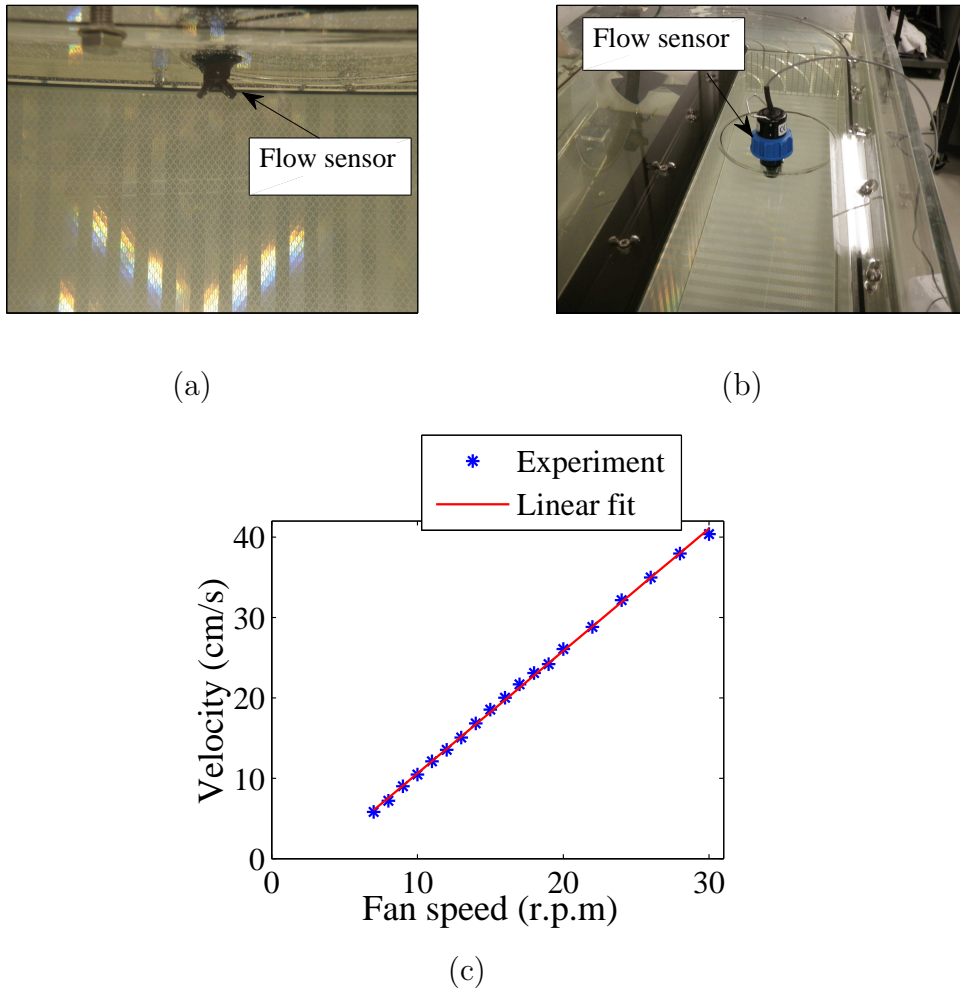


Figure 6.8: Rotor-X flow sensor for swim tunnel calibration: (a) Side view; (b) top view; (c) calibration curve

### 6.3.2 Differentiation of Steady and Unsteady Flow

We first mounted an IPMC sensor measuring (long = 3.5 cm  $\times$  wide = 4 mm  $\times$  thick = 0.25 mm) and used a Cannon digital camera, to visualize each flow regime experimentally.

In the experimental setup, the IPMC sensor was mounted in such a way that it would bend in the direction parallel to the  $x$ -axis. To generate the vortex street, a hollow cylindrical obstacle with a diameter 6 cm was placed upstream the sensor. The IPMC sensor was attached, first, 4 cm behind the obstacle. Second, the sensor was aligned with the obstacle edge, which made the cylinder 5 cm upstream from it.

The authors of [5] have reported that, the flow behind obstacle regime can be divided into three main regions, according to the velocity conditions present in each: (i) base suction region, (ii) vortex formation region, and (iii) vortex street. First, the average flow frequency of region (ii) bigger than that region (iii). Second, the suction region (region (i)) has average flow frequency smaller than those in regions (ii) and (iii). The overall goal is to better understand the sensing environment from the local perspective of a situated sensor. Three sensing tasks will be investigated here, differentiating between steady and unsteady flows, differentiating between suction and shed Kármán vortex region, and finally, differentiating between big and small size obstacles.

Fig. 6.9 shows the image of an IPMC beam in a uniform flow (in the absence of the obstacle). We can see that the beam is deflected with small-amplitude vibration.

Fig. 6.10 shows that the IPMC sensor is sucked toward the cylinder (predominantly negative flow) when the sensor is placed right after the cylinder. Then, when the obstacle is shifted to the right, the sensor bends differently (predominantly positive flow), as shown in Fig. 6.11.

This global analysis is useful to reveal that , first, the differences between the uniform flow and the Kármán vortex street can be captured by the sensor beam. Second, it is clear from Figs. 6.10 and 6.11 that, visually, the IPMC sensor would be able to differentiate the

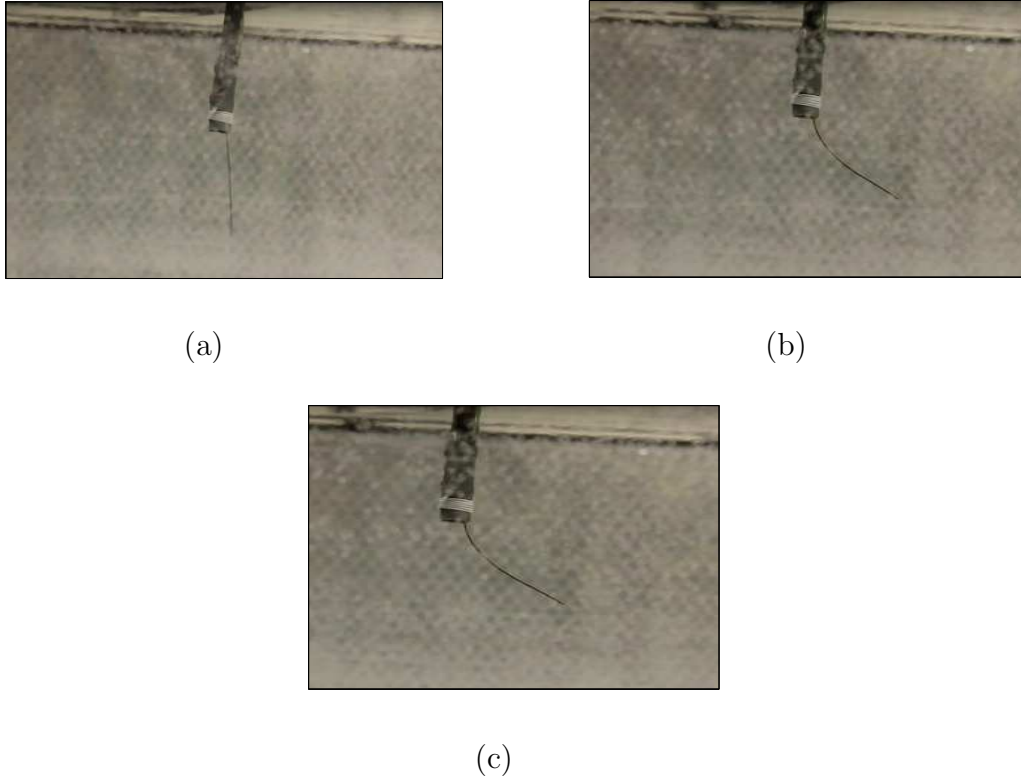


Figure 6.9: IPMC sensor in a uniform flow in the absence of the obstacle: (a) Sensor at  $t_0$ ; (b) sensor at  $t_1$ , (c) sensor at  $t_2$ .

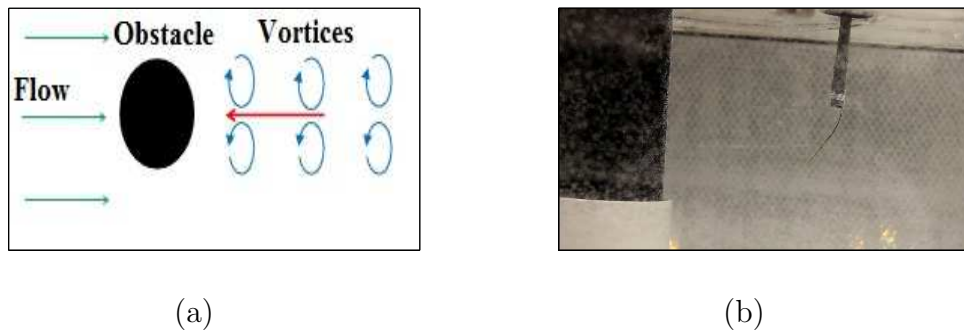
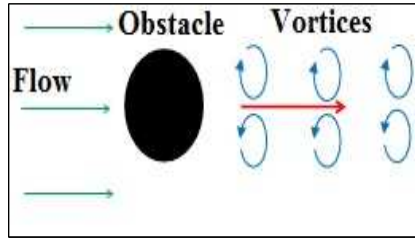


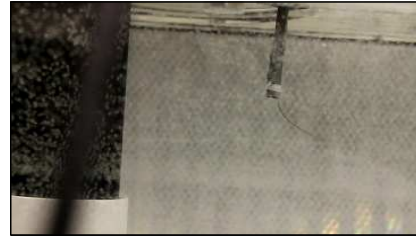
Figure 6.10: IPMC sensor right behind obstacle (predominantly negative flow): (a) Illustration; (b) typical sensor configuration.

suction region from the vortex region.

We further examined the IPMC sensor outputs under different experimental conditions. Fig. 6.12 shows a typical sensor response under various flow conditions with a nominal flow



(a)



(b)

Figure 6.11: IPMC sensor behind obstacle but shifted from center (predominantly positive flow): (a) Illustration; (b) typical sensor configuration.

velocity of 10.6 cm/s. It is clear from Fig. 6.12 that, the water movement behind (at the center or shifted to the right) a cylinder shows much larger fluctuations than in the free stream (running water). The frequency of the suction region is different (smaller) from the frequency of the Kármán vortex region, as expected.

### 6.3.3 Differentiation of Obstacle Size

We tested whether one IPMC sensor could potentially detect and recognize an upstream cylindrical obstacle. For this purpose, we placed an IPMC sensor first behind a cylinder with larger diameter (6 cm) and then replaced the cylinder with another one that has a smaller diameter (4 cm), as shown in Fig. 6.13(b). The center coordinates of both cylindrical obstacles had the same distance away from the IPMC sensor, around 8 cm. The nominal flow velocity was chosen to be 10.6 cm/s in these experiments.

We can observe from the experiments that, the sensor vibrated with different frequencies and amplitudes when the obstacle size was different. Typical IPMC sensor signals for two cases and the corresponding frequency spectra are shown in Fig. 6.14.

From Fig.6.14, we can see that the vortex shedding frequency does vary with the obstacle

size, and the good agreement between the measured and theoretical (Eq. (6.11)) values of  $f_{sh}$  is particularly promising.

### 6.3.4 Differentiation of Flow Velocity

We tested whether an IPMC sensor could be used to estimate the free-stream velocity based on the measurement of vortex shedding frequency. For this purpose, we placed an IPMC sensor behind a upstream cylinder with a diameter of 6 cm, where the obstacle-sensor-separation distance was 5 cm. We used two nominal flow velocities, 7.5 cm/s and 10.6 cm/s. Typical IPMC signals and the corresponding frequency spectra are shown in Fig. 6.15.

It can be observed that, when the flow velocity was increased, the vortex-shedding frequency  $f_{sh}$  increased as well. The observed trend was consistent with that predicted by the model (6.11); however, the discrepancy between the measured and predicted values was relatively large. Quantitative understanding of the relationship between free-stream velocity and the vortex-shedding frequency needs to be pursued further.

### 6.3.5 Two IPMC Sensors

We also conducted preliminary experiments on a pair of IPMC sensors, separated out with a fixed distance (3 cm), to examine the potential of an IPMC array in vortex sensing. In particular, we tested the capability of the sensors in detecting object movement in air. To stimulate the two IPMC sensors, a human finger was moved alongside the sensors at a distance of 1.5 cm. Fig. 6.16 shows the sensor responses when the finger was moved in one direction and then in the opposite direction. It can be observed that there was strong correlation between the responses of the two sensors, based on which one can compute the

time delay between the two responses and consequently the object moving speed.

We conducted further experiments using the two-sensor array, to test whether it could provide more hydrodynamic information than a single sensor. From those experiments, we found that: (i) The two sensors were sucked toward the cylinder if both of them were in the suction region (negatively dominant flow); (ii) they were both bent away from the obstacle if both of them were in the shed Kármán vortex street region (positively dominant flow); (iii) sensor #1 was sucked toward the obstacle and sensor #2 repelled from the obstacle when they were in the suction and vortex regions, respectively. Fig. 6.17 shows the case (iii), where the leading sensor was separated from the obstacle by 4 cm and the nominal velocity was 10.6 cm/s.

Fig. 6.18 shows typical IPMC signals for the latter scenario, where we can see that the vortex-shedding frequency in the vortex region is higher than that in the suction region. These experiments indicate that an IPMC sensor array could potentially be used to map different flow regions in a vortex street.

## 6.4 Chapter Summary

In this chapter we formulated an estimation problem for Kármán vortex street formed by an obstacle in a flow. While we did not provide a full solution to this problem, a number of experiments were conducted in a water tunnel with a single or a pair of IPMC sensors, to shed light on a potential estimation approach. Specifically, we found that one could use the vortex-shedding frequency  $f_{sh}$  to infer the information about the flow region, obstacle size, or the nominal flow velocity. The correlation between the signals from multiple sensors could be used to measure the vortex traveling speed.

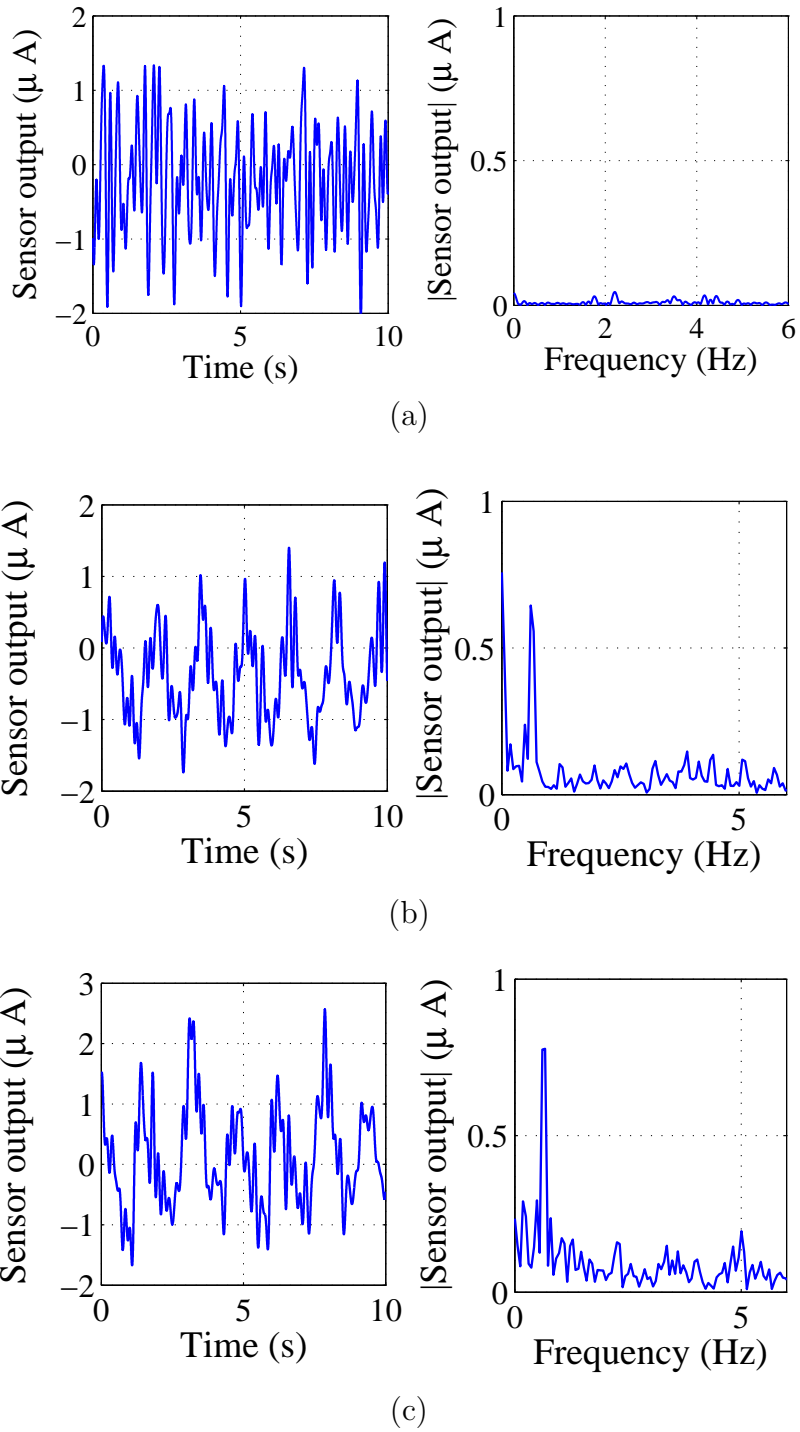


Figure 6.12: Typical IPMC sensor signals and frequency spectrum of the response under different flow conditions with nominal flow velocity of 10.6 cm/s: (a) Running water (free flow); (b) predominantly negative flow (suction region), frequency = 0.61 Hz; (c) predominantly positive flow (vortex region), frequency = 0.67 Hz.



(a)



(b)

Figure 6.13: IPMC sensor was attached behind of the: (a) 6 cm diameter cylindrical obstacle; (b) 4 cm diameter cylindrical obstacle.

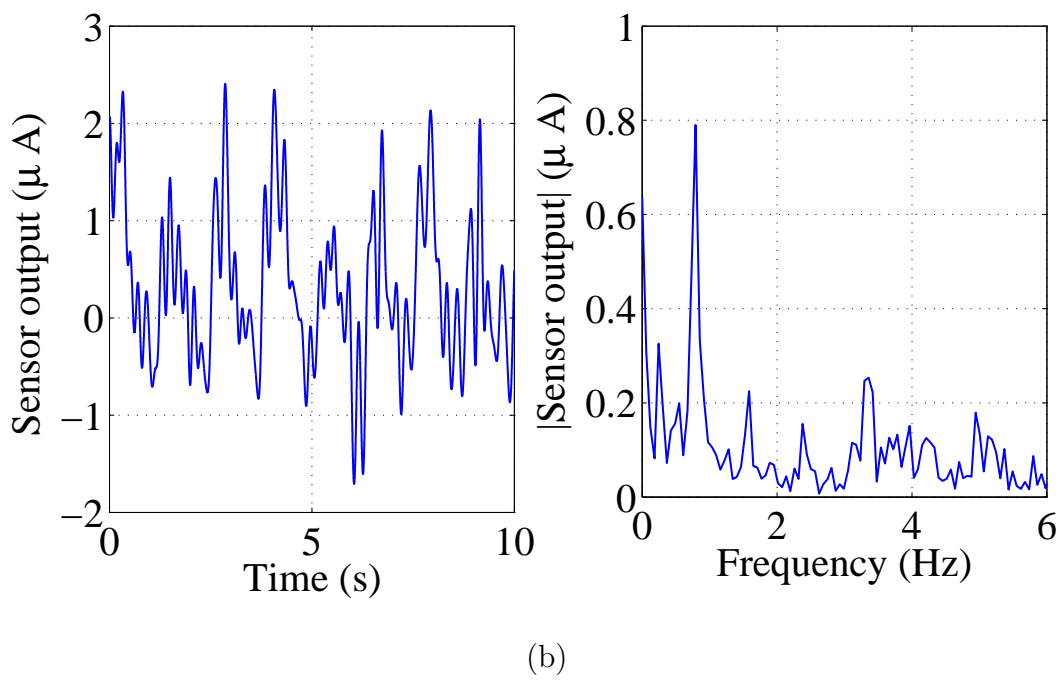
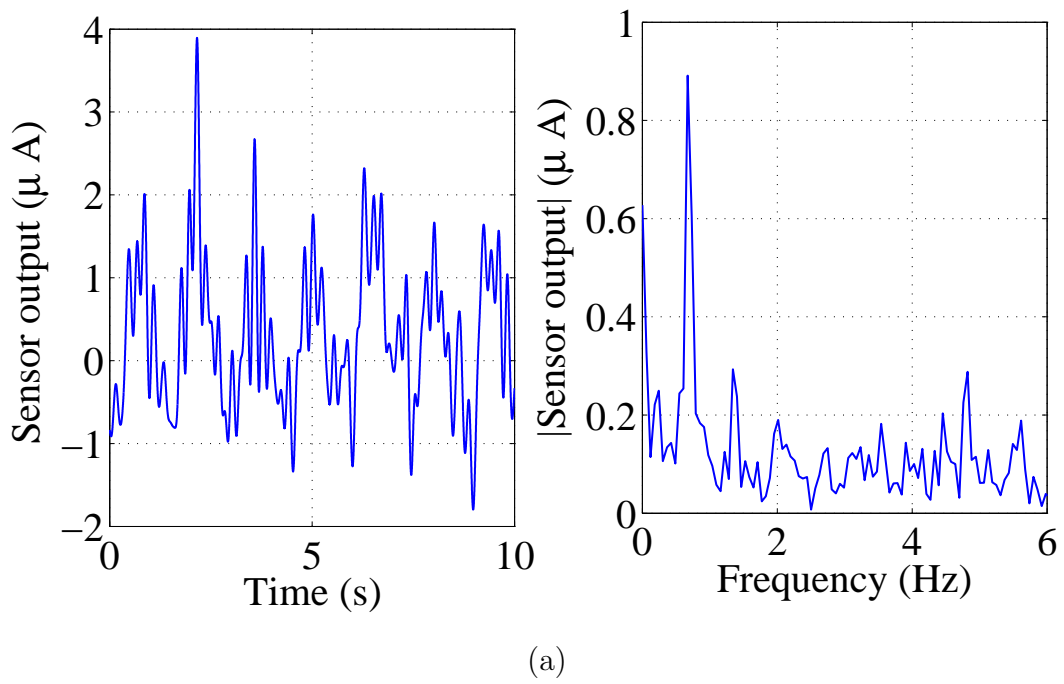
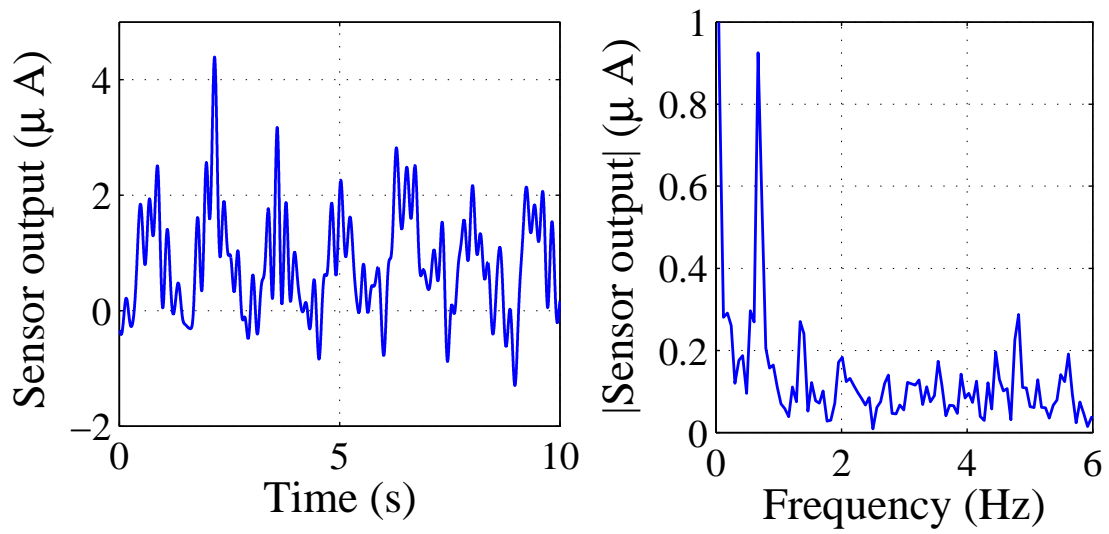
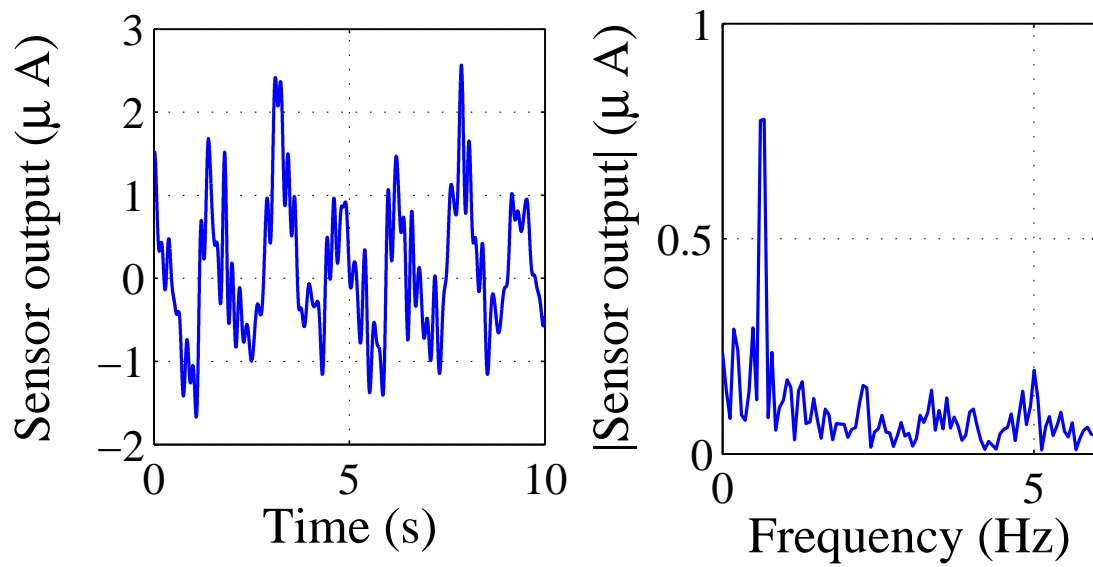


Figure 6.14: Typical IPMC sensor signals for different-size cylindrical obstacles with diameter: (a) 6 cm, theoretical / measured  $f_{sh}$ : 0.56/0.6 Hz; (b) 4 cm, theoretical / measured  $f_{sh}$ : 0.73/0.79 Hz.



(a)



(b)

Figure 6.15: Typical IPMC sensor signals under 6 cm upstream cylinder, the nominal flow velocity of: (a) 7.5 cm/s, Theoretical / Measured  $f_{sh}$ : 0.4/0.61 Hz; (b) 10.6 cm/s, Theoretical / Measured  $f_{sh}$ : 0.56/0.67 Hz.

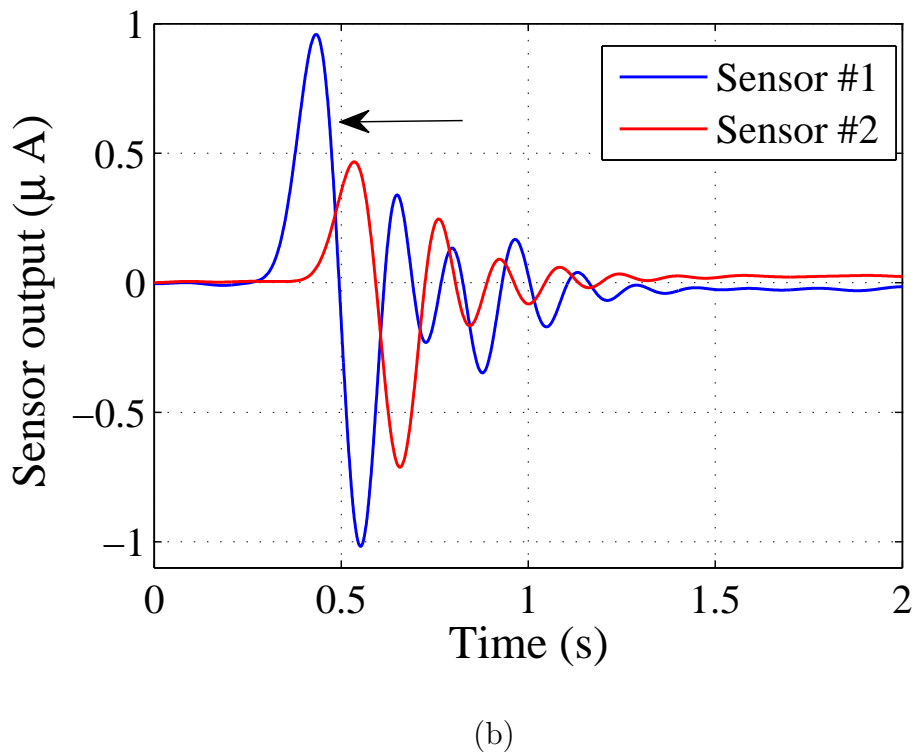
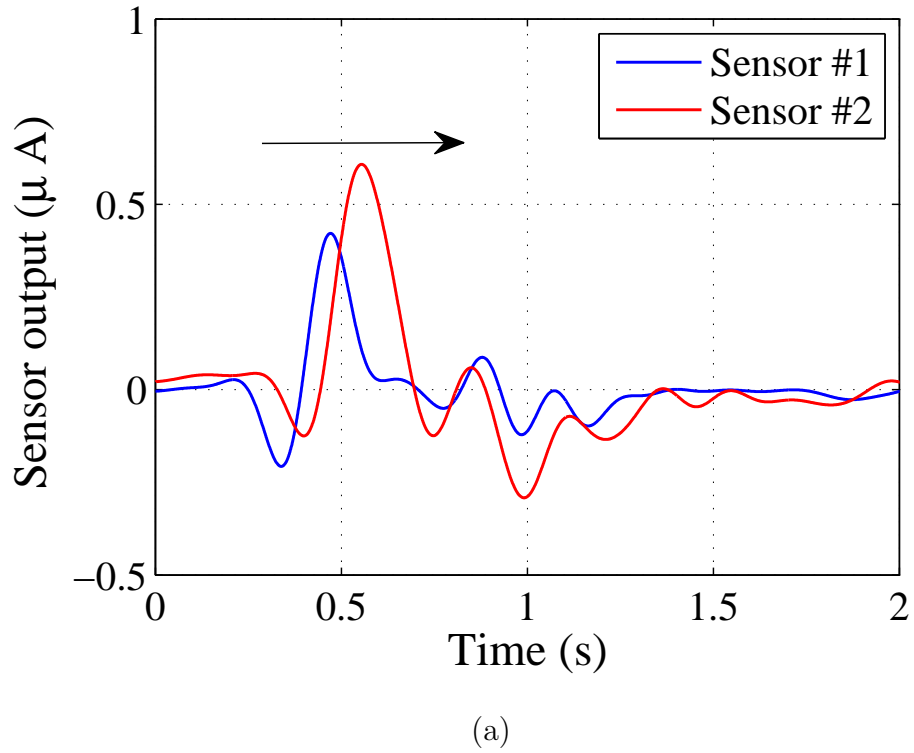
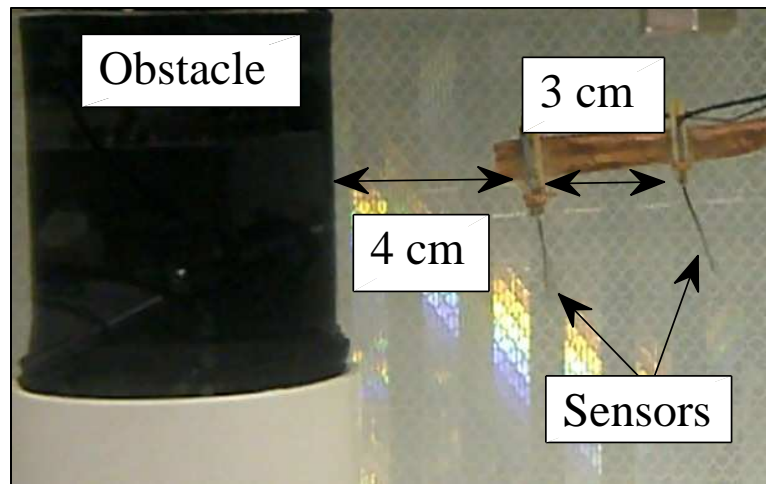
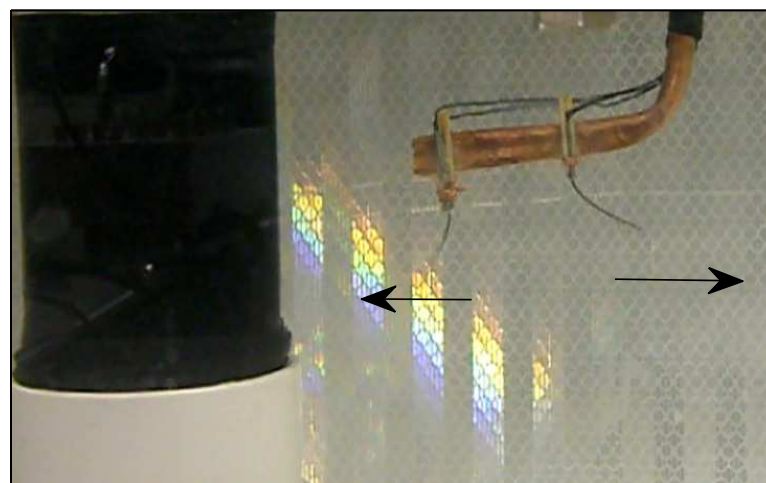


Figure 6.16: Typical IPMC sensor signals to the human fingers that moved alongside the two IPMC sensors with velocity of about 25 cm/s, direction of the movement: (a) Toward positive  $x$ -axis; (b) toward negative  $x$ -axis.



(a)



(b)

Figure 6.17: Two IPMC sensors were attached behind a 6 cm cylinder: (a) Setup at time  $t_0$ ; (b) sensor #1 sucked toward the obstacle, while sensor#2 repelled from the obstacle at time  $t_1$ .

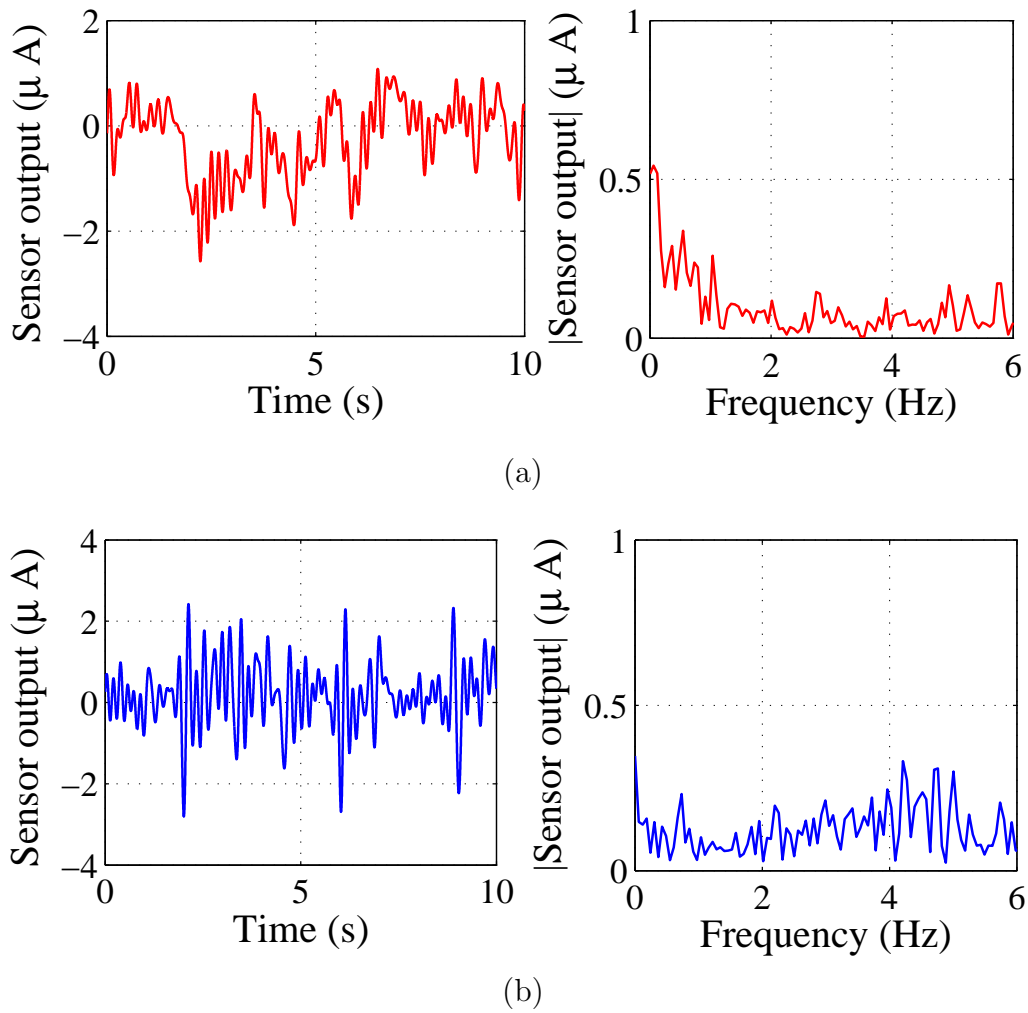


Figure 6.18: Signals from the two IPMC sensors and their frequency spectra: (a) Sensor #1, dominant frequency = 0.55 Hz; (b) sensor #2, dominant frequency = 0.73 Hz.

# Chapter 7

## Conclusion

The first contribution of this dissertation was a new approach to the realization of artificial lateral lines for underwater robots and vehicles that uses IPMC materials as sensing elements. For example, we showed that, with a neural network-based processing scheme, a dipole source can be successfully localized when its vibration amplitude and orientation are known. Experimental results showed that, with relatively few sensor elements, the IPMC-based lateral line was able to localize sources at least 1-2 BLs away, and the localization accuracy at source-sensor separation of 1 BL was comparable to the resolution of manually placing the source (1-2 mm).

Second, we proposed and examined in detail two iterative schemes for dipole source localization based on measurements from an artificial lateral line. The schemes, referred to as Gauss-Newton (GN) algorithm and Newton-Raphson (NR) algorithm, respectively, were derived with a nonlinear estimation perspective to simultaneously estimate the dipole location, vibration amplitude, and vibration orientation. We performed CRB analysis based on the analytical flow model, and demonstrated its use in the design of the lateral line system

via the example of optimizing intra-sensor spacing. The CRB analysis was also used later to confirm the near-optimality of the proposed algorithms. We conducted both simulation and physical experimentation to validate the proposed algorithms. The good consistency between the simulation results and the experimental results does not only suggest the physical relevance of our simulation setup, but also supports the validity of the analytical models and algorithms for the physical system. With a body length (BL) of 10 cm for the lateral line system, simulation and experimental results showed that both the GN and NR algorithms can successfully localize the dipole source and estimate its vibration amplitude and orientation within 1 BL, with the maximum localization error less than 5% of the BL. We also found that, while the GN algorithm did consistently better than the NR algorithm, the overall performance and computational complexity of the two algorithms are very comparable. We also found that the proposed algorithms showed clear advantage over the beamforming algorithm in terms of accuracy and computational efficiency.

Third, we investigated an analytical model-based estimation approach to the localization of a moving dipole source using an artificial lateral line consisting of an array of flow sensors. The moving speed, vibration amplitude, and location of the moving source were assumed to be unknown, and we proposed a Gauss-Newton algorithm to solve the nonlinear estimation problem based on the evolving signal magnitudes obtained with SDFT. The effectiveness of the approach was illustrated with simulation and experimental results.

Fourth, a novel two-stage extended Kalman filter was proposed to track and estimate a moving but non-vibrating object in water. Simulation and experimental results have demonstrated that, with a few IPMC sensors, the ALL was able to identify and estimate the moving object speed, location, size, and shape parameter, respectively.

Fifth, we conducted experimental exploration of using IPMC sensors for detecting hydrodynamic parameters associated with a Kármán vortex street. In particular, our work showed that it was promising to use IPMC lateral line for the estimation of obstacle size, free-stream flow velocity, distance to the obstacle, etc.

Although this work has demonstrated the promise of IPMC sensors in underwater flow sensing, we note that the behavior of IPMCs depends on environmental conditions and could vary over time. While the continuing advances in IPMC fabrication may alleviate such problems, appropriate compensation schemes (see, e.g., [35]) and periodic sensor calibrations are expected to be essential for practical IPMC lateral line systems.

# Chapter 8

## Future Work

The work reported in this dissertation can be extended in several directions. First, in this work we largely ignored the effect of sensor beams on the flow field. On the sensor modeling side, we primarily took the short-circuit current output of the sensor as proportional to the flow velocity. It will be of interest to extend the modeling work on the sensor-flow interaction, which can potentially lead to improved sensing performance for the artificial lateral line.

Second, while we had demonstrated the effectiveness of a two-stage extended Kalman filtering scheme in object tracking and estimation, the convergence and stability properties of such schemes were not examined in this dissertation. The study of these issues, possibly in a more general  $n$ -stage setting (Fig. 8.1), would be of interest.

Third, while we formulated an estimation problem for the case of vortex street sensing, we did not provide a systematic solution to this problem. It would be interesting to develop a complete, analytical approach for the estimation of obstacle location, size, flow speed, and flow direction, and validate the approach experimentally.

Fourth, comparing to the size (less than 1 mm long) of neuromasts in a biological lateral

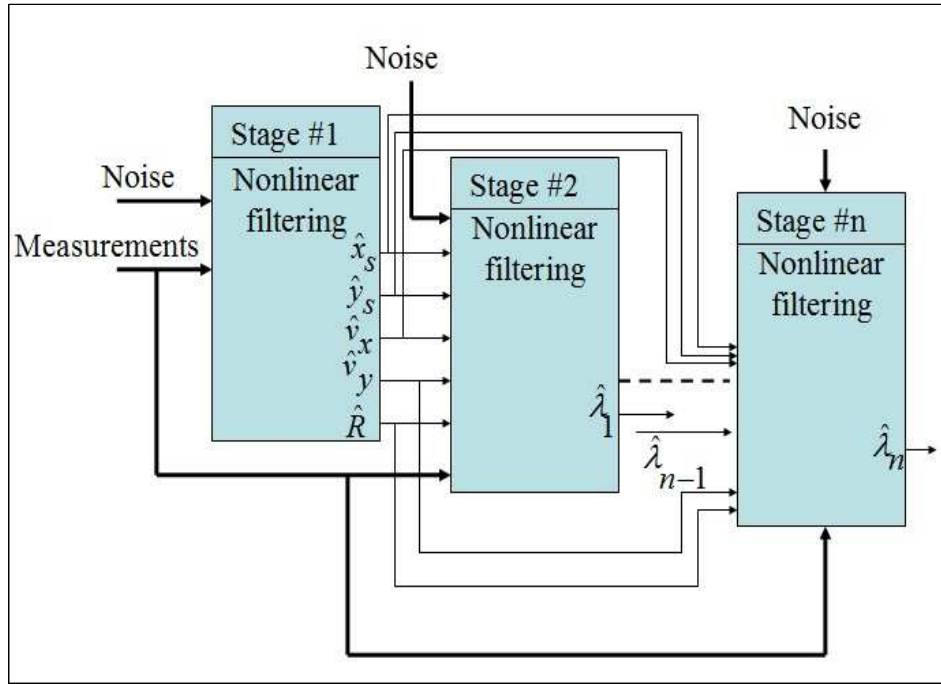


Figure 8.1: Illustration of the  $n$ -stages nonlinear filtering scheme.

line, the IPMC sensors used in this dissertation are relatively big. In addition, a biological lateral line may have many more (from tens to over a thousand [20]) neuromasts. There are many challenges in realizing an IPMC-based artificial lateral line system with sensor size and number comparable to those of a live fish. For example, while the processes for micro fabrication of IPMCs have been reported by a number of groups [18, 101, 32], existing results deal mostly with planar processes, and new polymer MEMS techniques have to be developed to create micro IPMC devices standing on a substrate as in [54]. On the system integration side, the processing of signals from tens to hundreds of IPMC sensors is far from trivial. It will be of interest to extend the signal processing approaches developed in this dissertation to accommodate a much larger number of sensors. To address this challenge, it

will be critical to seek inspiration from how such processing is achieved in biology [21].

Finally, artificial lateral line system can be mounted on a robot, such as a robotic fish, for the investigation of processing schemes that decouple external signals from self-motion-induced flow signals. Such an extension would be particularly relevant for practical applications of artificial lateral lines.

# APPENDICES

# Appendix A

## Artificial Lateral Line Design: CRB

With  $\theta = [x_s, y_s]$ , the first and second derivatives are given as:

$$\begin{aligned} \frac{\partial f_i(\theta)}{\partial x_s} &= \frac{k1}{\|r_i\|^5} [-4(x_i - x_s)\alpha_1 - 3(y_i - y_s)\alpha_2] + \\ &\quad \frac{5k1}{\|r_i\|^7} \left\{ (2(x_i - x_s)^3 - (x_i - x_s)(y_i - y_s)^2)\alpha_1 + (3(x_i - x_s)^2(y_i - y_s))\alpha_2 \right\}, \end{aligned}$$

$$\begin{aligned} \frac{\partial^2 f_i(\theta)}{(\partial x_s)^2} &= \frac{4k1\alpha_1}{\|r_i\|^5} + \frac{5k1}{\|r_i\|^7} \left\{ (-10(x_i - x_s)^2 + (y_i - y_s)^2)\alpha_1 - (9(x_i - x_s)(y_i - y_s))\alpha_2 \right\} \\ &\quad \frac{35k1}{\|r_i\|^9} \left\{ (2(x_i - x_s)^4 - (x_i - x_s)^2(y_i - y_s)^2)\alpha_1 + (3(x_i - x_s)^3(y_i - y_s))\alpha_2 \right\}, \end{aligned}$$

$$\begin{aligned} \frac{\partial f_i(\theta)}{\partial y_s} &= \frac{k1}{\|r_i\|^5} [2(y_i - y_s)\alpha_1 - 3(x_i - x_s)\alpha_2] + \\ &\quad \frac{5k1}{\|r_i\|^7} \left\{ (2(x_i - x_s)^2(y_i - y_s) - (y_i - y_s)^3)\alpha_1 + (3(x_i - x_s)(y_i - y_s)^2)\alpha_2 \right\}, \end{aligned}$$

$$\frac{\partial^2 f_i(\theta)}{(\partial y_s)^2} = \frac{-2k_1\alpha_1}{\|r_i\|^5} + \frac{5k_1}{\|r_i\|^7} \left\{ (-2(x_i - x_s)^2 + 5(y_i - y_s)^2)\alpha_1 + (-9(x_i - x_s)(y_i - y_s))\alpha_2 \right\} \\ \frac{35k_1}{\|r_i\|^9} \left\{ (2(x_i - x_s)^2(y_i - y_s)^2 - (y_i - y_s)^4)\alpha_1 + (3(x_i - x_s)(y_i - y_s)^3)\alpha_2 \right\},$$

$$\frac{\partial^2 f_i(\theta)}{\partial y_s \partial x_s} = \frac{\partial^2 f_i(\theta)}{\partial x_s \partial y_s} \\ = \frac{3k_1\alpha_2}{\|r_i\|^5} + \frac{5k_1}{\|r_i\|^7} \left\{ (-2(x_i - x_s)(y_i - y_s))\alpha_1 - 3((x_i - x_s)^2 + (y_i - y_s)^2)\alpha_2 \right\} \\ \frac{35k_1}{\|r_i\|^9} \left\{ (2(x_i - x_s)^3(y_i - y_s) - (x_i - x_s)(y_i - y_s)^3)\alpha_1 \right. \\ \left. + (3(x_i - x_s)^2(y_i - y_s)^2)\alpha_2 \right\}, \quad (\text{A.1})$$

where  $k_1 = a^3 \pi f$ .

# Appendix B

## Appendix for Chapter 5

### B.1 Derivation of CRB

Based on the measurement equation (5.11), the likelihood function is given by

$$p(M; X) = \frac{1}{2\pi\sigma_m^2} e^{\left(\frac{-1}{2\pi\sigma_m^2} \sum_{i=0}^{N-1} (M_i - f_i(X))^2\right)}. \quad (\text{B.1})$$

Differentiating the log of the likelihood function twice, we get:-

$$\frac{\partial^2}{\partial^2 X} \ln(p(M; X)) = \frac{1}{\sigma_m^2} \sum_{i=0}^{N-1} \left\{ (M_i - f_i(X)) \frac{\partial^2 f_i(X)}{\partial^2 X} - \left[ \frac{\partial f_i(X)}{\partial X} \right] \left[ \frac{\partial f_i(X)}{\partial X} \right]^T \right\}. \quad (\text{B.2})$$

The Fisher information matrix is defined by  $-E \left[ \frac{\partial^2 (\ln p(M; X))}{(\partial X)^2} \right]$ , which is given by

$$F = \frac{1}{\sigma_m^2} \sum_{i=0}^{N-1} \left[ \frac{\partial f_i(X)}{\partial X} \right] \left[ \frac{\partial f_i(X)}{\partial X} \right]^T$$

where  $E[\cdot]$  is the expectation taken over all possible measurement  $M$ . the  $i^{th}$  diagonal of the inverse of  $F$ , which is denoted by  $F_{i,i}^{-1}$ , provides a lower bound on the variance of the  $i^{th}$  element of the state estimate  $\hat{X}$ . Generally,  $Var(\hat{X}) \geq F_{i,i}^{-1}$ . In our case we have four elements and  $F$  is just a  $4 \times 4$  matrix. The Fisher information matrix can be expressed as  $F = [F_{11}, F_{12}; F_{12}^T, F_{22}]$ , where the sub-matrix blocks  $F_{11}$ ,  $F_{12}$ , and  $F_{22}$  are  $2 \times 2$  matrices,

$$F_{11} = \frac{1}{\sigma_m^2} \begin{bmatrix} \sum_{i=1}^N \left( \frac{\partial f_i(\cdot)}{\partial x_s} \right)^2 & \sum_{i=1}^N \left( \frac{\partial f_i(\cdot)}{\partial x_s} \right) \left( \frac{\partial f_i(\cdot)}{\partial y_s} \right) \\ \sum_{i=1}^N \left( \frac{\partial f_i(\cdot)}{\partial y_s} \right) \left( \frac{\partial f_i(\cdot)}{\partial x_s} \right) & \sum_{i=1}^N \left( \frac{\partial f_i(\cdot)}{\partial y_s} \right)^2 \end{bmatrix},$$

$$F_{12} = \frac{1}{\sigma_m^2} \begin{bmatrix} \sum_{i=1}^N \left( \frac{\partial f_i(\cdot)}{\partial x_s} \right) \left( \frac{\partial f_i(\cdot)}{\partial R} \right) & \sum_{i=1}^N \left( \frac{\partial f_i(\cdot)}{\partial x_s} \right) \left( \frac{\partial f_i(\cdot)}{\partial \lambda_1} \right) \\ \sum_{i=1}^N \left( \frac{\partial f_i(\cdot)}{\partial y_s} \right) \left( \frac{\partial f_i(\cdot)}{\partial R} \right) & \sum_{i=1}^N \left( \frac{\partial f_i(\cdot)}{\partial y_s} \right) \left( \frac{\partial f_i(\cdot)}{\partial \lambda_1} \right) \end{bmatrix},$$

$$F_{22} = \frac{1}{\sigma_m^2} \begin{bmatrix} \sum_{i=1}^N \left( \frac{\partial f_i(\cdot)}{\partial R} \right)^2 & \sum_{i=1}^N \left( \frac{\partial f_i(\cdot)}{\partial R} \right) \left( \frac{\partial f_i(\cdot)}{\partial \lambda_1} \right) \\ \sum_{i=1}^N \left( \frac{\partial f_i(\cdot)}{\partial \lambda_1} \right) \left( \frac{\partial f_i(\cdot)}{\partial R} \right) & \sum_{i=1}^N \left( \frac{\partial f_i(\cdot)}{\partial \lambda_1} \right)^2 \end{bmatrix},$$

where

$$\frac{\partial f(\cdot)}{\partial x_s} = v_x R^2 \left\{ \frac{2(x - x_s)}{\left( (x - x_s)^2 - (y - y_s)^2 - \lambda_1 \right)^2 + 4(x - x_s)^2(y - y_s)^2} - \frac{4(x - x_s) \left( (x - x_s)^2 - (y - y_s)^2 - \lambda_1 \right) \left( (x - x_s)^2 + (y - y_s)^2 - \lambda_1 \right)}{\left( \left( (x - x_s)^2 - (y - y_s)^2 - \lambda_1 \right)^2 + 4(x - x_s)^2(y - y_s)^2 \right)^2} \right\},$$

$$\frac{\partial f(\cdot)}{\partial y_s} = v_x R^2 \left\{ \frac{-2(y - y_s)}{\left( (x - x_s)^2 - (y - y_s)^2 - \lambda_1 \right)^2 + 4(x - x_s)^2 (y - y_s)^2} + \frac{4(y - y_s) \left( (x - x_s)^2 - (y - y_s)^2 - \lambda_1 \right) \left( -(x - x_s)^2 - (y - y_s)^2 - \lambda_1 \right)}{\left( \left( (x - x_s)^2 - (y - y_s)^2 - \lambda_1 \right)^2 + 4(x - x_s)^2 (y - y_s)^2 \right)^2} \right\},$$

$$\frac{\partial f(\cdot)}{\partial R} = -2v_x R \left\{ \frac{\left( (x - x_s)^2 - (y - y_s)^2 - \lambda_1 \right)}{\left( (x - x_s)^2 - (y - y_s)^2 - \lambda_1 \right)^2 + 4(x - x_s)^2 (y - y_s)^2} \right\},$$

$$\frac{\partial f(\cdot)}{\partial \lambda_1} = v_x R^2 \left\{ \frac{1}{\left( (x - x_s)^2 - (y - y_s)^2 - \lambda_1 \right)^2 + 4(x - x_s)^2 (y - y_s)^2} - \frac{2 \left( (x - x_s)^2 - (y - y_s)^2 - \lambda_1 \right)^2}{\left( \left( (x - x_s)^2 - (y - y_s)^2 - \lambda_1 \right)^2 + 4(x - x_s)^2 (y - y_s)^2 \right)^2} \right\},$$

and the Cramer-Rao bound is defined as  $F^{-1}$ , where  $F^{-1}$  is given by

$$F^{-1} = \begin{bmatrix} J^{-1} & -JF_{12}F_{22}^{-1} \\ F_{22}^{-1}F_{21}J^{-1} & F_{22}^{-1}(I + F_{21}J^{-1}F_{12}) \end{bmatrix},$$

where  $J = F_{11} - F_{12}F_{22}^{-1}F_{21}$ .  $J$  is a  $2 \times 2$  matrix given by

$$J = \begin{bmatrix} J_{1,1} & J_{1,2} \\ J_{2,1} & J_{2,2} \end{bmatrix},$$

The CRBs for the estimates of  $x_s$  and  $y_s$  are given by  $J_{1,1}^{-1} = |J|^{-1} \cdot J_{2,2}$  and  $J_{2,2}^{-1} = |J|^{-1} \cdot J_{1,1}$ , respectively. Specifically,

$$CRB(x_s) = J_{1,1}^{-1}, \quad CRB(y_s) = J_{2,2}^{-1}. \quad (\text{B.3})$$

## B.2 More Results for One-stage Extended Kalman Filtering Scheme

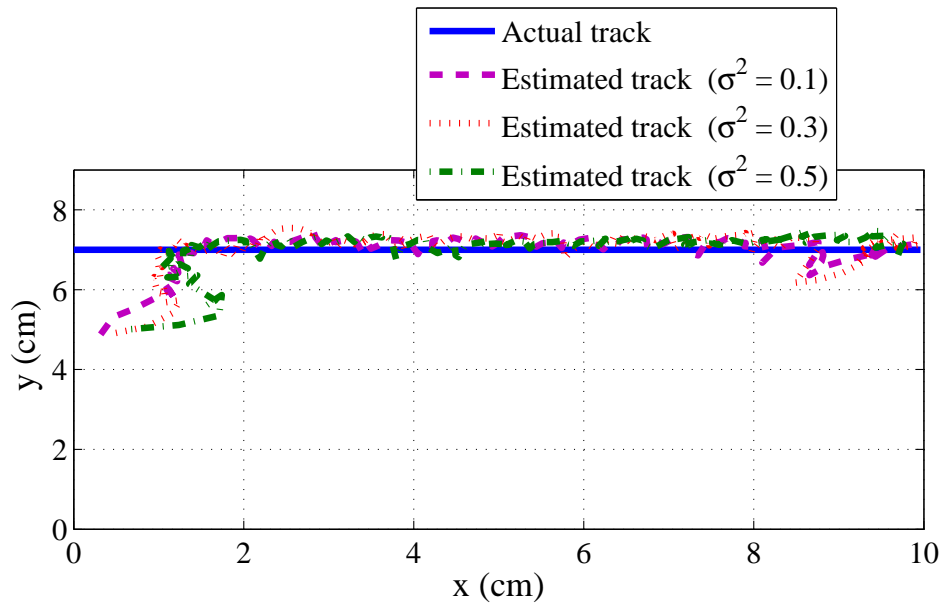
In this appendix we present similar results as in Section 5.3 but with a one-stage extended Kalman filtering scheme. First, we have tested the impact of the process noise on the one-stage scheme as shown in Fig. B.1.

Table B.1 summarizes the other estimated parameters. It is clear from the simulation results of the one-stage scheme that, the model process noise has slight impact on the estimation results.

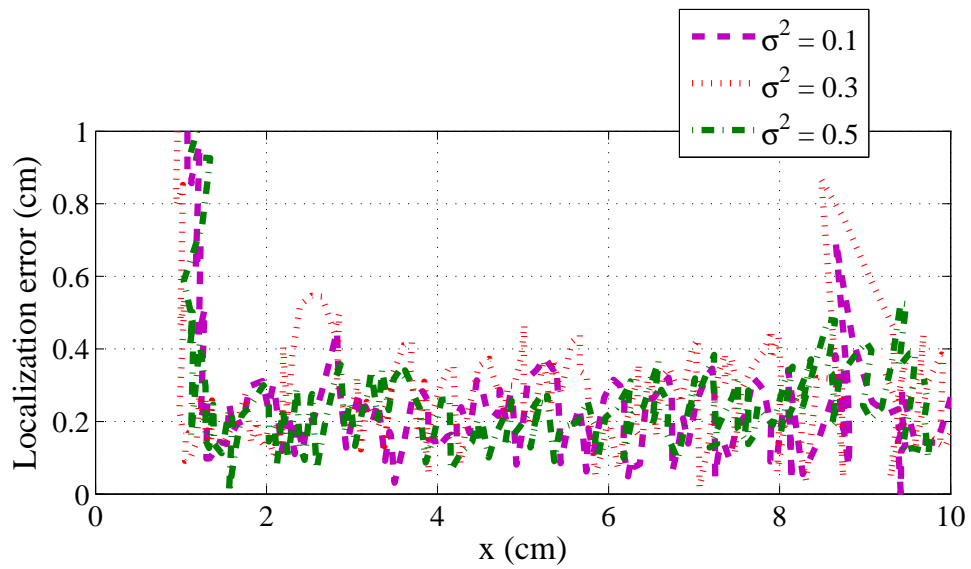
Table B.1: One-stage scheme: Estimated velocity, size parameter, and shape parameter under different process noise variances.

Parameter	Actual	Estimated ( $\sigma^2 = 0.1$ )	( $\sigma^2 = 0.3$ )	( $\sigma^2 = 0.5$ )
Velocity (cm/s)	6	6.33	6.53	6.56
Size R (cm)	2.5	2.45	2.45	2.12
Shape $\lambda_1$ (cm)	1.5	0.63	1.66	0.71

Fig. B.2 shows the impact of the measurement noises on the estimation localization results when the process noise is held at 0.3. Table B.2 lists the other estimated parameters. It can be seen that, overall, the measurement noise variance has a large impact on the estimation performance; in general, larger measurement noise variance leads to much longer transient

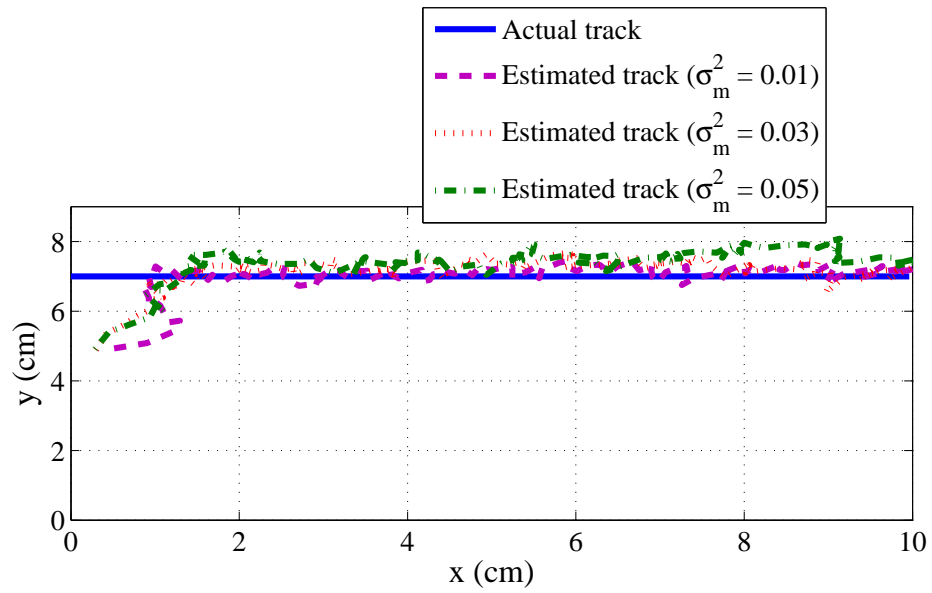


(a)

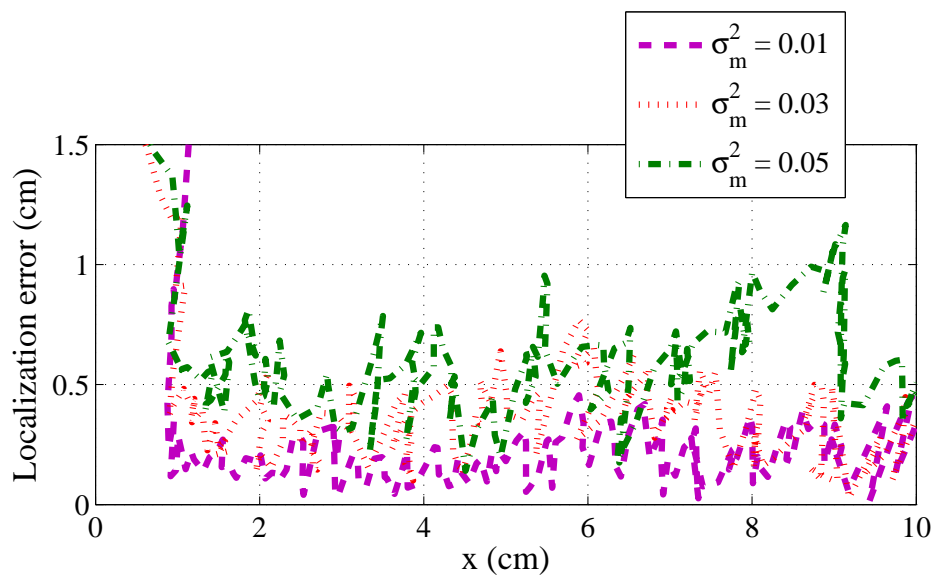


(b)

Figure B.1: Simulation results on tracking the ellipsoidal cylinder for one-stage scheme: (a) The estimation of the moving object location for different variance values for the process noises; (b) localization error at each  $x$ -coordinate of the object. The measurement noise variance is held at  $0.01 \text{ cm}^2/\text{s}^2$ .



(a)



(b)

Figure B.2: Simulation results on tracking the ellipsoidal cylinder for one-stage scheme: (a) The estimation of the moving object location for different variance values for the measurement noises; (b) localization error at each  $x$ -coordinate of the object. The process noise variance is held at 0.3 (in its respective unit for each state component).

and larger estimation error.

Table B.2: One-stage scheme: Estimated velocity, size parameter, and shape parameter under different measurement noise variances.

Parameter	Actual	Estimated ( $\sigma_m^2 = 0.01$ )	( $\sigma_m^2 = 0.03$ )	( $\sigma_m^2 = 0.05$ )
Velocity( cm/s)	6	6.45	6.63	7.23
Size R (cm)	2.5	2.33	2.15	2.64
Shape $\lambda_1$ (cm)	1.5	0.85	0.58	0.42

# BIBLIOGRAPHY

# BIBLIOGRAPHY

- [1] A. T. Abdulsadda and X. Tan. Underwater source localization using an IPMC-based artificial lateral line. In *Proceedings of the 2011 IEEE International Conference on Robotics and Automation*, pages 447–452, Shanghai, China, 2011.
- [2] A. T. Abdulsadda and X. Tan. An artificial lateral line system using IPMC sensor arrays. *International Journal of Smart and Nano Materials*, 2012. to appear, DOI:10.1080/19475411.2011.650233.
- [3] A. T. Abdulsadda, F. Zhang, and X. Tan. Localization of source with unknown amplitude using IPMC sensor arrays. In Y. Bar-Cohen, editor, *Proceedings of Electroactive Polymer Actuators and Devices (EAPAD) XIII*, volume 7976 of *Proceedings of SPIE*, page 797627, San Diego, CA, 2011.
- [4] O. Akanyeti, R. Venturelli, F. Visentin, L. Chambers, W. Megill, and P. Fiorini. What information do kármán streets offer to flow sensing? *Bioinsp. Biomim.*, 6:036001, 2011.
- [5] Otar Akanyeti, Roberto Venturelli, Francesco Visentin, Lily Chambers William Megill, and Paolo Fiorini. What information do kármán streets offer to flow sensing? *Bioinspiration and Biomimetics*, 6:036001:12, 2011.
- [6] B. Akle, M. Bennett, and D. Leo. High-strain ionomeric-ionic liquid electroactive actuators. *Sensors and Actuators A*, 126:173–181, 2006.
- [7] M. Aureli, V. Kopman, and M. Porfiri. Free-locomotion of underwater vehicles actuated by ionic polymer metal composites. *IEEE/ASME Transactions on Mechatronics*, 15(4):603–614, 2010.
- [8] M. Aureli, C. Prince, M. Porfiri, and S. D. Peterson. Energy harvesting from base excitation of ionic polymer metal composites in fluid environments. *Smart Materials and Structures*, 19:015003, 2010.

- [9] H. Bleckmann. Peripheral and central processing of lateral line information. *J. Comp. Physiol. A*, 194:145–158, 2008.
- [10] C. Bonomo, L. Fortuna, P. Giannone, S. Graziani, and S. Strazzeri. A model for ionic polymer metal composites as sensors. *Smart Materials and Structures*, 15:749–758, 2006.
- [11] R. Bouffanais, G. D. Weymouth, and D. K. P. Yue. Hydrodynamic object recognition using pressure sensing. *Proc. R. Soc. A*, 467:19–38, 2011.
- [12] Paola Brunetto, Luigi Fortuna, Salvatore Graziani, and Salvatore Strazzeri. A model of ionic polymer-metal composite actuators in underwater operations. *Smart Materials and Structures*, 17(2):025029:1–12, 2008.
- [13] X. Chen, G. Zhu, X. Yang, D. L. S. Hung, and X. Tan. Model-based estimation of flow characteristics using an ionic polymermetal composite beam. *IEEE/ASME Transactions on Mechatronics*, 2012. to appear, DOI: 10.1109/TMECH.2012.2194300.
- [14] Z. Chen, D. Hedgepeth, and X. Tan. A nonlinear, control-oriented model for ionic polymer-metal composite actuators. *Smart Materials and Structures*, 18:055008:1–9, 2009.
- [15] Z. Chen, S. Shatara, and X. Tan. Modeling of biomimetic robotic fish propelled by an ionic polymer-metal composite caudal fin. *IEEE/ASME Transactions on Mechatronics*, 15(3):448–459, 2010.
- [16] Z. Chen, Y. Shen, N. Xi, and X. Tan. Integrated sensing for ionic polymer-metal composite actuators using PVDF thin films. *Smart Materials and Structures*, 16(2):S262–S271, 2007.
- [17] Z. Chen and X. Tan. A control-oriented and physics-based model for ionic polymer-metal composite actuators. *IEEE/ASME Transactions on Mechatronics*, 13(5):519–529, 2008.
- [18] Z. Chen and X. Tan. Monolithic fabrication of ionic polymer-metal composite actuators capable of complex deformation. *Sensors and Actuators A: Physical*, 157:246–257, 2010.
- [19] Z. Chen, X. Tan, A. Will, and C. Ziel. A dynamic model for ionic polymer-metal composite sensors. *Smart Materials and Structures*, 16:1477–1488, 2007.

- [20] S. Coombs. Smart skins: Information processing by lateral line flow sensors. *Autonomous Robots*, 11:255–261, 2001.
- [21] S. Coombs and C. B. Braun. Information processing by the lateral line system. In S. P. Collin and N. J. Marshall, editors, *Sensory Processing in Aquatic Environments*, pages 122–138, New York, 2003. Springer-Verlag.
- [22] S. Coombs and R. A. Conley. Dipole source localization by mottled sculpin. I. Approach strategies. *J. Comp. Physiol. A*, 180:387–399, 1997.
- [23] S. Coombs and R. A. Conley. Dipole source localization by mottled sculpin. II. the role of lateral line excitation patterns. *J. Comp. Physiol. A*, 180:401–415, 1997.
- [24] S. Coombs, M. Hastings, and J. Finneran. Modeling and measuring lateral line excitation patterns to changing dipole source locations. *J. Comp. Physiol. A*, 178:359–371, 1996.
- [25] T. M. Cover and J. A. Thomas. *Elements of Information Theory*. John Wiley & Sons, Inc., New York, 1991.
- [26] B. Curcic-Blake and S. M. van Netten. Source location encoding in the fish lateral line canal. *Journal of Experimental Biology*, 209:1548–1559, 2006.
- [27] A. M. K. Dagamseh, T. S. J. Lammerink, M. L. Kolster, C. M. Bruinink, R. J. Wiegerink, and G. J. M. Krijnen. Dipole-source localization using biomimetic flow-sensor arrays positioned as lateral-line system. *Sensors and Actuators A*, 162(2):355–360, 2010.
- [28] P. de Gennes, K. Okumura, M. Shahinpoor, and K. Kim. Mechanoelectric effects in ionic gels. *Europhys. Lett.*, 50(4):513–518, 2000.
- [29] M. Dijkstra, J. J. van Baar, R. J. Wiegerink, T. S. J. Lammerink, J. H. de Boer, and G. J. M. Krijnen. Artificial sensory hairs based on the flow sensitive receptor hairs of crickets. *J. Micromech. Microeng.*, 15:S132–S138, 2005.
- [30] A. F. Emery and A. V. Nenarokomov. Optimal experiment design. *Measurement Science and Technology*, 9(6):864–876, 1998.
- [31] Z. Fan, J. Chen, J. Zou, D. Bullen, C. Liu, and F. Delcomyn. Design and fabrication of artificial lateral line flow sensors. *Journal of Micromechanics and Microengineering*, 12:655–661, 2002.

- [32] G.-H. Feng and R.-H. Chen. Fabrication and characterization of arbitrary shaped  $\mu$  IPMC transducers for accurately controlled biomedical applications. *Sensors and Actuators: A physical*, 143(1):34–40, 2008.
- [33] V. I. Fernandez, A. Maertens, F. M. Yaul, J. Dahl, J. H. Lang, and M. S. Triantafyllou. Lateral-line-inspired sensor arrays for navigation and object identification. *Marine Technology Society Journal*, 45(4):130–146, 2011.
- [34] J.-M. P. Franosch, A. B. Sichert, M. D. Suttner, and J. L. van Hemmen. Estimating position and velocity of a submerged moving object by the clawed frog *xenopus* and by fish: A cybernetic approach. *Biol. Cybern.*, 93:231–238, 2005.
- [35] T. Ganley, D. L.S. Hung, G. Zhu, and X. Tan. Modeling and inverse compensation of temperature-dependent ionic polymer-metal composite sensor dynamics. *IEEE/ASME Transactions on Mechatronics*, 16(1):80–89, 2011.
- [36] J. M. Gardiner and J. Atema. Sharks need the lateral line to locate odor sources: Rheotaxis and eddy chemotaxis. *Journal of Experimental Biology*, 210:1925–1934, 2007.
- [37] Stokes G.G. On the effect if the internal friction of fluids on the motion of pendulums. *Trans. Camb. Philos Soc.*, 1201:9:8–106, 1951.
- [38] Batchelor G.K. *An introduction to fluid dynamics*. Cambridge University Press, New York, 1967.
- [39] J. Goulet, J. Engelmann, B. P. Chagnaud, J.-M. P. Franosch, M. D. Suttner, and J. L. van Hemmen. Object localization through the lateral line system of fish: theory and experiment. *J. Comp. Physiol. A*, 194:1–17, 2008.
- [40] E.-S. Hassan. Mathematical analysis of the stimulus for the lateral line organ. *Biol. Cybern.*, 52:23–36, 1985.
- [41] E.-S. Hassan. Mathematical description of the stimuli to the lateral line system of fish derived from a three-dimensional flow field analysis: I. The cases of moving in open water and of gliding towards a plane surface. *Biol. Cybern.*, 66:443–452, 1992.
- [42] E.-S. Hassan. Mathematical description of the stimuli to the lateral line system of fish derived from a three-dimensional flow field analysis: II. The case of gliding alongside or above a plane surface. *Biol. Cybern.*, 66:453–461, 1992.

- [43] E.-S. Hassan. Mathematical description of the stimuli to the lateral line system of fish derived from a three-dimensional flow field analysis: III. The case of an oscillating sphere near the fish. *Biol. Cybern.*, 69:525–538, 1993.
- [44] E. Jacobsen and R. Lyons. The sliding dft. *IEEE Signal Process. Mag.*, 20(2):74–80, 2003.
- [45] Gere J.M. *Mechanics of materials*. Nelson Thornes Ltd, Cheltenham, 2001.
- [46] A. J. Kalmijn. Hydrodynamic and acoustic field detection. In J. Atema, R. R. Fay, A. N. Popper, and W. N. Tavolga, editors, *Sensory Biology of Aquatic Animals*, pages 83–130, New York, 1988. Springer-Verlag.
- [47] S. M. Kay. *Fundamentals of Statistical Signal Processing: Estimation Theory*. Prentice Hall, Upper Saddle River, New Jersey, 1993.
- [48] K. J. Kim, D. Pugal, and K. K. Leang. A twistable ionic polymer-metal composite artificial muscle for marine applications. *Marine Technology Society Journal*, 45(4):83–98, 2011.
- [49] K.J. Kim and M. Shahinpoor. Ionic polymer-metal composites: II. manufacturing techniques. *Smart Materials and Structures*, 12:65–79, 2003.
- [50] A. Klein and H. Bleckmann. Determination of object position, vortex shedding frequency and flow velocity using artificial lateral line canals. *Beilstein Journal of Nanotechnology*, 2:276–283, 2011.
- [51] A. Kong, J. S. Liu, and W. H. Wong. Sequential imputations and bayesian missing data problem. *Journal of the American Statistical Association*, 89(425):278–288, 1994.
- [52] A. B. A. Kroese and N. A. M. Schellart. Velocity- and acceleration-sensitive units in the trunk lateral line of the trout. *Journal of Neurophysiology*, 68(6):2212–2221, 1992.
- [53] H. Lamb. *Hydrodynamics*. Cambridge University Press, Cambridge, 1932.
- [54] H. Lei, W. Li, and X. Tan. Microfabrication of IPMC cilia for bio-inspired flow sensing. In Y. Bar-Cohen, editor, *Electroactive Polymer Actuators and Devices (EAPAD) XIV*, volume 8340 of *Proceedings of SPIE*, page 83401A, Bellingham, WA, 2012. SPIE.

- [55] J. C. Liao. Neuromuscular control of trout swimming in a vortex street: Implications for energy economy during the kármán gait. *Journal of Experimental Biology*, 207:3495–3506, 2004.
- [56] J. C. Liao, D. N. Beal, G. V. Lauder, and M. S. Triantafyllou. Fish exploiting vortices decrease muscle activity. *Science*, 302:1566–1569, 2003.
- [57] James C Liao. A review of fish swimming mechanics and behaviour in altered flows. *Phil. Trans. Royal Society*, 2082:1973–1993, 2007.
- [58] C. Lim, H. Lei, and X. Tan. A dynamic, physics-based model for base-excited IPMC sensors. In Y. Bar-Cohen, editor, *Electroactive Polymer Actuators and Devices (EAPAD) XIV*, volume 8340 of *Proceedings of SPIE*, page 83400H, Bellingham, WA, 2012. SPIE.
- [59] C. Liu. Micromachined biomimetic artificial haircell sensors. *Bioinsp. Biomim.*, 2:S162–S169, 2007.
- [60] M. E. McConney, N. Chen, D. Lu, H. A. Hu, S. Coombs, C. Liu, and V. V. Tsukruk. Biologically inspired design of hydrogel-capped hair sensors for enhanced underwater flow detection. *Soft Matter*, 5:292–295, 2009.
- [61] M. J. McHenry, J. A. Strother, and S. M. van Netten. Mechanical filtering by the boundary layer and fluidstructure interaction in the superficial neuromast of the fish lateral line system. *J. Comp. Physiol. A*, 194:795–810, 2008.
- [62] C. Musso, N. Oudjane, and F. LeGland. *Improving regularity particle filters*. Springer-Verlag, New York, 2001.
- [63] S. Nemat-Nasser and J. Li. Electromechanical response of ionic polymermetal composites. *J. Appl.Phys.*, 87(7):3321–3331, 2000.
- [64] NeuroSolutions. <http://www.neurosolutions.com/>.
- [65] Nam Nguyen, Douglas L. Jones, Yingchen Yang, and Chang Liu. Flow vision for autonomous underwater vehicles via an artificial lateral line. *EURASIP Journal on Advances in Signal Processing*, 2011:806406:1–11, 2011.
- [66] A. V. Oppenheim and R. W. Schaffer. *Discrete-Time Signal Processing*. Pearson Higher Education, Inc., Upper Saddle River, New Jersey, 3rd edition, 2010.

- [67] Y. Ozaki, T. Ohyama, T. Yasuda, and I. Shimoyama. An air flow sensor modeled on wind receptor hairs of insects. In *Proceedings of the 13th IEEE International Conference on Micro Electro Mechanical Systems*, pages 531–536, Miyazaki, Japan, 2000.
- [68] S. Pandya, Y. Yang, D. L. Jones, J. Engel, and C. Liu. Multisensor processing algorithms for underwater dipole localization and tracking using MEMS artificial lateral-line sensors. *EURASIP Journal on Applied Signal Processing*, 2006, 2006. Article ID 76593, 8 pages, 2006. doi:10.1155/ASP/2006/76593.
- [69] T.J. Pitcher, B. L. Partridge, and C. S. Wardle. A blind fish can school. *Science*, 194:963–965, 1976.
- [70] K. Pohlmann, J. Atema, and T. Breithaupt. The importance of the lateral line in nocturnal predation of piscivorous catfish. *Journal of Experimental Biology*, 207:2971–2978, 2004.
- [71] M. Porfiri. Charge dynamics in ionic polymer metal composites. *J. Appl.Phys.*, 104(10):104915:1–10, 2008.
- [72] D. Pugal, K. J. Kim, and A. Aabloo. Modeling the transduction of IPMC in 3D configurations. In *Behavior and Mechanics of Multifunctional Materials and Composites 2010*, volume 7644 of *Proceedings of SPIE*, page 76441T, San Diego, CA.
- [73] D. Pugal, K.Jung, A. Aabloo, and K. J. Kim. Ionic polymer-metal composite mechano-electrical transduction: Review and perspectives. *Polymer International*, 59:279–289, 2010.
- [74] A. Qualtieri, F. Rizzi, M.T. Todaro, A. Passaseo, R. Cingolani, and M. De Vittorio. Stress-driven AlN cantilever-based flow sensor for fish lateral line system. *Microelectronic Engineering*, 88(8):2376–2378, 2011.
- [75] Z. Ren and K. Mohseni. A model of the lateral line of fish for vortex sensing. *Bioinspir. Biomim.*, 7:036016, 2012.
- [76] Branko Ristic, Sanjeev Arulampalam, and Neil Gordon. *Beyond the Kalman Filter*. Artech House, London, 2004.
- [77] Panton RL. *Incompressible flow*. Wiley, New York, 1985.

- [78] M. M. Sadeghi, R. L. Peterson, and K. Najafi. Micro-hydraulic structure for high performance bio-mimetic air flow sensor arrays. In *Proceedings of the 2011 IEEE International Electron Devices Meeting*, pages 29.4.1–29.4.4, 2011.
- [79] Sandhya Samarasinghe. *Neural Networks for Applied Sciences and Engineering: From Fundamentals to Complex Pattern Recognition*. Auerbach, Boca Raton, FL, 2007.
- [80] S. A. Sarles, P. Pinto, and D. J. Leo. Hair cell sensing with encapsulated interface bilayers. In *Proceedings of Bioinspiration, Biomimetics, and Bioreplication*, volume 7975 of *Proceedings of SPIE*, page 797509, San Diego, CA, 2011.
- [81] M. Shahinpoor and K.J. Kim. Ionic polymer-metal composites: I. Fundamentals. *Smart Materials and Structures*, 10:819–833, 2001.
- [82] S. Shatarra and X. Tan. An efficient, time-of-flight-based underwater acoustic ranging system for small robotic fish. *IEEE Journal of Oceanic Engineering*, 35(4):837846, 2010.
- [83] A. B. Sichert, R. Bamler, and J. L. van Hemmen. Hydrodynamic object recognition: When multipoles count. *Physical Review Letters*, 102:058104, 2009.
- [84] A. B. Sichert and J. L. van Hemmen. How stimulus shape affects lateral-line perception: analytical approach to analyze natural stimuli characteristics. *Biol. Cybern.*, 102:177–180, 2010.
- [85] B.W. Silverman. *Density Estimation for Statistics and Data Analysis*. Chapman and Hall, 1986.
- [86] K. Takagi, Y. Nakabo, Z. Luo, T. Mukai, M. Yamamura, and Y. Hayakawa. An analysis of the increase of bending response in IPMC dynamics given uniform input. In *Smart Structures and Materials 2006: Electroactive Polymer Actuators and Devices (EAPAD)*, volume 6168 of *Proceedings of SPIE*, page 616814, San Diego, CA.
- [87] K. Takagi, M. Yamamura, Z. Luo, M. Onish, S. Hirano, K. Asaka, and Y. Hayakawa. Development of a rajiform swimming robot using ionic polymer artificial muscles. In *Proceedings of the 2006 IEEE/RSJ International Conference on Intelligent Robots and Systems*, pages 1861–1866, Beijing, China, 2006.
- [88] Xiaobo Tan. Autonomous robotic fish as mobile sensor platforms: Challenges and potential solutions. *Marine Technology Society Journal*, 45(4):31–40, 2011.

- [89] Milne Thomson. *Theoretical hydrodynamics*. Macmillan Company, New York, USA, 5th edition, 1955.
- [90] M. S. Triantafyllou, D. K. P. Yue, and G. S. Triantafyllou. Hydrodynamics of fishlike swimming. *Annu. Rev. Fluid Mech.*, 32:33–53, 2000.
- [91] R. Venturelli, O. Akanyeti, F. Visentin, J. Jezov, L. D. Chambers, G. Toming, J. Brown, M. Kruusmaa, W. M. Megill, and P. Fiorini. Hydrodynamic pressure sensing with an artificial lateral line in steady and unsteady flows. *Bioinspir. Biomim.*, 7:036004, 2012.
- [92] Y. Wang, C. Lee, and C. Chiang. A MEMS-based air flow sensor with a free-standing microcantilever structure. *Sensors*, 7:2389–2401, 2007.
- [93] D. Weihs. Hydrodynamics of fish schooling. *Nature*, 241:290–291, 1973.
- [94] S. P. Windsor, D. Tan, and J. C. Montgomery. Swimming kinematics and hydrodynamic imaging in the blind Mexican cave fish (*astyanax fasciatus*). *Journal of Experimental Biology*, 211:2950–2959, 2008.
- [95] T. Y. Wu. Hydromechanics of swimming propulsion. Part 1. Swimming of a two-dimensional flexible plate at variable forward speeds in an inviscid fluid. *Journal of Fluid Mechanics*, 46:337–355, 1971.
- [96] Y. Yang, J. Chen, J. Engel, S. Pandya, N. Chen, C. Tucker, S. Coombs, D. L. Jones, and C. Liu. Distant touch hydrodynamic imaging with an artificial lateral line. *Proceedings of the National Academy of Sciences*, 103(50):18891–18895, 2006.
- [97] Y. Yang, A. Klein, H. Bleckmann, and C. Liu. Artificial lateral line canal for hydrodynamic detection. *Applied Physics Letters*, 99:023701, 2011.
- [98] Y. Yang, N. Nguyen, N. Chen, M. Lockwood, C. Tucker, H. Hu, H. Bleckmann, C. Liu, and D. L. Jones. Artificial lateral line with biomimetic neuromasts to emulate fish sensing. *Bioinspir. Biomim.*, 5:016001, 2010.
- [99] W. Yim, J. Lee, and K. J. Kim. An artificial muscle actuator for biomimetic underwater propulsors. *Bioinspiration & Biomimetics*, 2:S31–S41, 2007.
- [100] U. Zangrilli and L. M. Weiland. Prediction of the ionic polymer transducer sensing of shear loading. *Smart Materials and Structures*, 20:094013:1–9, 2011.

- [101] J. W. L. Zhou, H.-Y. Chan, A. K. H. To, K. W. C. Lai, and W. J. Li. Polymer mems actuators for underwater micromanipulation. *IEEE/ASME Transactions on Mechatronics*, 9(2):334–342, 2004.